Development of Advanced Material Modelling for Metal Additive Manufacturing

A thesis submitted for the degree of Doctor of Structural Integrity by

Madie Allen

Department of Engineering, Brunel University London

NSIRC Ltd.

Supervised by: James Campbell[1], Tyler London[2], Kevin Hughes[1], Jan Pryzydatek[3]

Affiliations: [1]Brunel University, [2]TWI Ltd., [3]LRF

Abstract

Additive manufacturing (AM) is becoming an increasingly popular manufacturing process due to its design freedoms and material efficiency. However, the use of AM in industry is limited by the reliability of the deposited parts. Process-microstructure-property relationships are of paramount importance to increasing understanding and consistency within additive processes.

Within this work, thermal and microstructure modelling methods are investigated to develop an efficient approach to the simulation of solidification microstructure. Finite element thermal models are considered as well as the implementation of analytical solutions. Cellular automata methods are used to simulate grain growth, 2D models are implemented for computational efficiency.

The established approach is applied to three case studies within this work. The first is the application to laser scans on a bare nickel superalloy substrate, followed by the application to direct energy deposition techniques. Within the second study the capability of the modelling approach to capture changes in microstructure as a result of a change in process parameters is investigated. Finally, the modelling approach is applied to functionally graded materials through in situ changes in process parameters.

Acknowledgements

With thanks to Tyler London and Dr James Campbell, for their supervision and guidance throughout this process. Also, thanks goes to all the staff at TWI Ltd for their involvement within this project.

This publication was made possible by the sponsorship and support of the Lloyd's Register Foundation. The work was enabled through, and undertaken at, the National Structural Integrity Research Centre (NSIRC), a postgraduate engineering facility for industry-led research into structural integrity established and managed by TWI through a network of both national and international Universities. Lloyd's Register Foundation helps to protect life and property by supporting engineering-related education, public engagement and the application of research.

A special thanks goes to my family for their constant support.

Contents

Table of Figures

Table of Tables

1 Introduction and Background

1.1 Additive Manufacturing

Additive manufacturing (AM) is the process of creating products by depositing material in a layer-by-layer manner. It is officially defined as “a process of joining materials to make objects from 3D model data, usually layer upon layer, as opposed to subtractive manufacturing methodologies” (ASTM International, 2013). The process works by breaking down 3D geometries into 2D layers or slices. Each layer is then deposited sequentially to build the full part. There are numerous methods that can be used to deposit each layer, with varying heat sources and material feedstocks. For additive manufacture of metals, these techniques can be broken down into two main groups, direct energy deposition and powder bed fusion. Experimental examples of both of these types is shown in Figure 1.

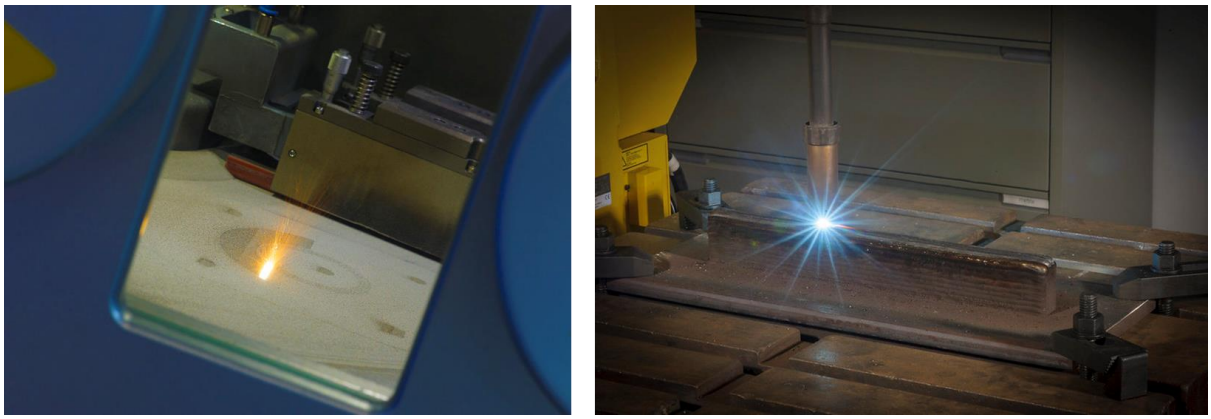

Figure 1: Images of the experimental set up for powder bed fusion (left) and direct energy deposition (right). Images courtesy of TWI Ltd.

Powder bed fusion (PBF) methods take place within a build chamber. A thin layer of powder is spread across the build plate (or substrate) within the chamber, from the material reservoirs within the AM machine. Throughout the build of the geometry, the required 2D geometry of each layer is traced within the powder using the heat source (laser or electron beam). Upon completion of each layer, the build plate is lowered by the specified layer height and another layer of powder is swept across the top of the previously deposited material. A number of process parameters, including hatch spacing, scan speed and layer height, need to be specified for each deposition. The two main powder bed fusion techniques include laser-powder bed fusion (L-PBF), also referred to as selective laser melting (SLM), and electron beam melting (EBM). The heat source for each method is a laser and an electron beam respectively. The inert atmosphere when using a laser heat source is normally nitrogen or argon gas (Yap, et al., 2015), whilst a vacuum is normally used when working with an electron

beam (Gibson, et al., 2015). PBF is more suitable for small scale parts, as it usually uses reasonably small layer heights on an order of 10μm (Gibson, et al., 2015). This means a good resolution of geometry can be achieved, at a cost of longer build times. Furthermore, limitations on geometry size are imposed by the size of the build chamber.

Direct energy deposition (DED), on the other hand, refers to AM techniques that deposit molten material directly from a nozzle on to a substrate. The ASTM standard defines them as “an additive manufacturing process in which focused thermal energy is used to fuse materials by melting as they are being deposited” (ASTM International, 2013). Popular DED methods include laser metal deposition (LMD) and wire-arc additive manufacturing (WAAM). As expected, the heat source used within LMD is a laser, whilst WAAM applies traditional welding techniques in an additive way and therefore an arc is used as the heat source, similar to that in Gas-Metal Arc Welding (GMAW) (Williams, et al., 2016). Additionally, a wire feedstock is used in WAAM, whereas LMD can be performed using both a powder or wire feedstock. DED methods offer higher deposition rates and component size than PBF, but this is normally at the expense of part resolution. In particular, WAAM can produce parts with build rates up to 10kg/hr (Williams, et al., 2016) and with sizes on the order of metres. Moreover, due to the increased freedom of the procedure, techniques such as LMD can be used for part repair.

Over recent years, additive manufacturing has seen high levels of interest from industries such as aerospace, automotive and biomedical. There has seen a number of successful applications within the aerospace industry including the GE LEAP fuel nozzle and GE9X engines, both now in service (Sher, 2020; GE, 2018) As an industry, AM is expected to be worth $21.5 billion by 2025, after reaching $7.336 billion in 2017 (AM-motion, 2016). This is due to the wide range of benefits that AM processes can offer.

One of the most attractive benefits of AM is the more efficient material usage. As the process is based on the principle of depositing material in the required location, this means that there is significantly less waste material compared to more conventional subtractive methods, such as machining. Consequently, this results in a higher buy-to-fly ratio for industries, making the parts more cost efficient and economical. Furthermore, AM offers more customisation options as the need for costly moulds and dies is no longer required, as well as the ability to create more complex geometries. As a consequence of removing the need for component dies, a number of constraints on the geometry imposed as a result of using a die are also removed. For example, through the use of PBF one can create lattices and complex internal channels. This also presents opportunities for part consolidation, leading to simplified production lines and optimised geometries. Other benefits include, part repair opportunities presented by DED techniques, topology optimisation and tailoring of material properties. Functionally graded

materials are materials that are tailored for specific purposes, be that through the deposition of multiple materials or the tailoring of microstructure to induce certain material properties. This adds another element of customisation and design to additive processes.

However, as with any relatively new technology there are a number of challenges and disadvantages. These can be things as small as the constraints posed by build chamber size or limitations on deposition speed. Furthermore, stair stepping effects can be introduced to the geometry. This is as a result of discretising 3D geometries into a number of 2D slices. If the layer height is not suitably small, the geometry cannot be resolved well and stair like effects may be seen on the surface as a result. Consequently this can lead to surface roughness, and subsequently fatigue initiation sites, and can be limited by the control of layer height. This effect can be visualised in Figure 2.

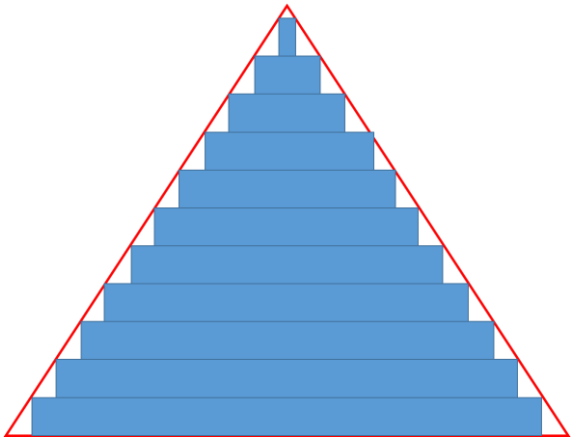

Figure 2: Demonstration of the stair step effect.

Further challenges include lack of fusion and porosity. Lack of fusion can be caused by unsuitable process parameters, meaning that not all of the required material is fully-fused within each layer. Although most AM processes achieve a nearly fully dense component, porosity can also be caused as a result of entrapped gases during the build process. Part distortion is also experienced within AM processes, caused as a result of the rapid heating and cooling cycles the material is subjected to. The thermal process, inherent to the layer-by-layer deposition, results in the build-up of residual stress within the component and consequently part distortion, particularly upon removal of the build plate.

One of the more significant challenges for industries looking to implement AM technologies is the repeatability and reliability of the process. Reliability and structural integrity is obviously of paramount importance for all industries from biomedical to aerospace, without this assurance components cannot be used with confidence within their designed roles. Lack of knowledge surrounding the resultant properties of additive manufactured parts is at the root of this

challenge. Furthermore, the level of repeatability of parts between machines and even between each individual builds with a given machine is not fully understood (Dowling, et al., 2020). All of this means that there is a significant uncertainty to whether each AM part that is designed and manufactured will be fit-for-purpose. Recently, there has been a focus on increasing understanding of links between process parameters, microstructure and material properties to try and address these problems. A full review of the research gaps in the field of additive manufacturing will take place in the literature review in Chapter 2.

1.2 Metals for AM

A number of materials can be used in the additive manufacturing process including ceramics, plastics and metals. However, throughout this work, the focus will solely be on metal AM. Metals for additive manufacture need to have good weldability (Bourell, et al., 2017). This is because, as AM is a joining process, many of the same properties are required as those that are required for welding. According to ISO/TR 581 a material is said to be weldable, for a specific process, when subject to a suitable weld procedure, metallic continuity can be achieved and metallurgical and mechanical properties comply with specified requirements (ISO, 2005) . A material's weldability is therefore affected by a number of properties including its melting point, conductivity and thermal expansion, as well as its susceptibility to cracking and behaviour within the heat affected zone (Dwivedi, 2022). For this reason, the list of metals currently used within AM is reasonably limited. Common materials include, titanium alloys, stainless steels, aluminium alloys and nickel alloys. In particular there has been significant focus on Ti-6Al4V, AlSi10Mg and nickel superalloys, such as Inconel 718 and 625 (Bourell, et al., 2017).

Superalloys are specific metal alloys that have had their alloy composition chosen in order to achieve increased performance. Nickel superalloys is a term used for alloys whose base element is nickel (Ni). These were initially developed for use in gas turbines (McLean, 1995), but are of particular interest in the aerospace industry. This is due to their increased performance at high temperatures (Andersson, 2011; Debroy, et al., 2018). Specifically, nickel superalloys boast increased strength as well as corrosion and oxidation resistance, increased creep strength and wear resistance (Attallah, et al., 2016; McLean, 1995; Graybill, et al., 2018). Examples of common nickel superalloys include Inconel alloys, Hastelloy-X and Waspaloy. Inconel 718 and 625 have become increasingly popular in relation to additive manufacturing. The nominal composition of each of these can be seen in Table 1.

Although it has been shown that some mechanical properties of additively manufactured nickel superalloys surpass those of their cast counterparts, after heat treatment (Xu, et al., 2019), there are still a number of challenges with processing nickel superalloys using additive

methods. These include the build-up of residual stress and poor surface finish (Seetharaman, et al., 2016). Moreover, nickel alloys can be susceptible to defects and cracking, due to their alloy composition (Tang, et al., 2021; Attallah, et al., 2016). It has been observed, that there is also significant anisotropy of mechanical properties within additively built Ni-superalloy components. This is as a direct result of anisotropy within expitaxial solidification microstructures (Attallah, et al., 2016). Until these problems are understood, nickel superalloys cannot be used confidently within industry (Graybill, et al., 2018).

Composition (%)	Alloy 718	Alloy 625
Ni	(Plus Co) 50.0-55.0	58.0 min
Cr	17.0-21.0	20.0-23.0
Fe	Bal.	5.0 max
Mo	2.8-3.3	8.0-10.0
Nb (plus Ta)	4.75-5.5	3.15-4.15
C	0.08 max	0.1 max
Mn	0.35 max	0.5 max
Si	0.35 max	0.5 max
P	0.015 max	0.015 max
S	0.015 max	0.015 max
Al	0.2-0.8	0.4 max
Ti	0.65-1.15	0.4 max
Co	1.0 max	1.0 max
B	0.006 max	N/A
Cu	0.3 max	N/A

Table 1: Nominal composition of popular Inconel alloys, 718 (Special Metals, 2007) and 625 (Special Metals, 2013).

1.3 Numerical Modelling Methods for Additive Manufacturing

Numerical modelling methods are becoming increasingly popular, especially with the birth of industry 4.0 and digital manufacturing (Rodic, 2017). Industry 4.0 focuses on the digitalisation of industry, with key areas of interest including data analytics, autonomous systems, additive manufacturing and the internet of things (Rodic, 2017). Inherently, simulation is also of high interest in relation to industry 4.0, through its application of digital technologies to develop and progress industrial processes.

Modelling methods make use of underling physical equations to simulate and predict physical scenarios, including manufacturing processes such as additive manufacturing. By modelling a situation by its fundamental laws, this allows one to predict and gather required information,

and provide understanding to complex systems (Velten, 2009). This can significantly reduce costs and lead times by reducing the number of experimental tests that would otherwise be required (Rodic, 2017). Furthermore, simulation can be used as a tool for optimisation to improve part performance or the manufacturing process itself. This could be achieved through process parameter optimisation, design optimisation or even operations optimisation (Cruz-Mejia, et al., 2019; Hinsen, 2020).

There are a number of various modelling methods, typically these can be stochastic or deterministic (Marion, 2008). Stochastic methods include statistical or probabilistic features, resulting in varying results for each run. On the other hand, deterministic results have no statistical dependence and therefore produce a single, repeatable outcome. Examples of stochastic models include Monte Carlo and Cellular Automata methods, which can both be used to simulate microstructure growth and are explained in further detail later on in this work. Furthermore models can be mechanistic or empirical - mechanistic models take into account underlying causes directly, whereas empirical models use mathematical relationships to approximate any changes that may take place.

When modelling industrial manufacturing processes, mechanistic models are normally implemented. This involves solving the underlying partial differential equations (PDEs) that define the problem, such as the heat transfer equation, mass conservation and conservation of momentum. PDEs can be extremely complex to solve analytically, especially when there are a large number of variables. However, they can be solved using a variety of techniques based on discretisation and approximation, namely finite difference, finite volume and finite element methods. Whilst these methods are similar in that they all use discretisation methods to approximate PDEs, they have some distinctive differences. The finite difference method is by far the easiest to implement and most suited to uniform meshes (Tadmor, 2012). The method makes use of Taylor series to approximate the solution. An example of the application of this to the heat equation can be found here (Recktenwald, 2011). On the other hand, finite volume methods use conservation equations to monitor the flux in and out of a volume surrounding each node (Versteeg & Malalasekera, 2007). This technique is closely linked with computational fluid dynamics (CFD) and best suited for determining fluid flow. The final approach is the finite element method, which is the most popular method within industry and one of the main numerical modelling methods that will be implemented within this work. It allows application to more complex geometries with irregular meshes and advanced problems that require multi-physics approaches (Tadmor, 2012). Further detail on the finite element method is given in the next section, as the method will feature heavily within the work presented here.

1.4 The Finite Element Method

The finite element method (FEM) has been used frequently throughout the engineering industry since its implementation at Boeing between 1950 and 1962 (Felippa, 2004). It was originally established for use in structural analyses and is widely used throughout the engineering industry today. The theory used within FEM dates back as early as the 1800's with connections to work developed by Raleigh and Ritz (Pepper & Heinrich, 2017). A brief overview of the theory of the finite element method is given here. A number of resources can be used to understand the theory of the finite element method including (Fish & Belytschko, 2007; Moatamedi & Khawaja, 2018; Rao, 2005)

The main aim of the FEM (with regard to linear elastic static mechanics) is to solve the equilibrium equation, given in Equation 1. Here F is the external loads, K the global stiffness matrix and u the resulting displacements. The displacements are the degrees of freedom within this problem. A degree of freedom is a variable of interest within the analysis. This equation ensures internal and external loads are balanced and can be compared to the spring equation.

$$\underline{F} = \boldsymbol{K}\underline{u}$$

Equation 1: Finite element method equilibrium equation.

The first step of the FEM is to discretise the computational domain into a number of elements. This will define the shape of the elements and the nodal connectivity used within the computation. Furthermore, Gaussian quadrature is used to determine a number of integration points, with weightings, within the element. These integration points are a fundamental aspect of the finite element method for two reasons. Firstly, through the use of Gaussian quadrature they allow a simple and convenient calculation of integrated components over the whole element through the use of weightings and summation. Furthermore, they provide a convenient location for the calculation of derivatives, for example when calculating strain, as the derivatives are not necessarily continuous at the nodes.

After discretising the domain and determining the element and nodal connectivity, the next stage is to decide on the order of the elements, usually linear or quadratic. This will determine the shape functions which define how values are interpolated within the element. Shape functions are determined as polynomials of the required order that are equal to 1 at the node in consideration and 0 everywhere else. Figure 3 shows an example of a 2D fully integrated,

linear quadrilateral element, with the corresponding shape function for each node. These shape functions can then be used to interpolate between nodes and the integration points within the elements through the use of Equation 2, where N_i represents the shape function for node i.

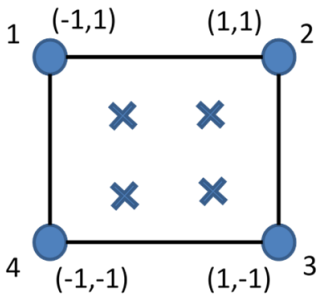

$$N_1 = \frac{1}{4}(1 - x + y - xy)$$
$$N_2 = \frac{1}{4}(1 + x + y + xy)$$
$$N_3 = \frac{1}{4}(1 + x - y - xy)$$
$$N_4 = \frac{1}{4}(1 - x - y + xy)$$

Figure 3: Example linear quadrilateral element and corresponding shape functions.

$$u(x,y) = \sum N_i(x,y)u_i$$

Equation 2: Use of shape functions to interpolate displacement.

The other two key components required to solve the problem statement and complete the system of equations are the compatibility and constitutive equations. The compatibility equations define the relationship between strain and displacement, whilst constitutive provide the relationship between stress and strain.

$$\underline{\varepsilon} = \begin{pmatrix} \varepsilon_x \\ \varepsilon_y \\ \gamma_{xy} \end{pmatrix} = \begin{pmatrix} \frac{\partial u}{\partial x} \\ \frac{\partial v}{\partial y} \\ \frac{\partial u}{\partial y} + \frac{\partial v}{\partial x} \end{pmatrix}$$

Equation 3: Strain-displacement relationship in 2D.

The compatibility equations are closely related to the shape functions as the shape functions describe the displacement across the element. The relationship between strain and displacement within a 2D analysis is given in Equation 3, where u and v are the displacements in the x and y directions respectively. The derivatives of u and v are calculated through the use of the shape functions and the chain rule as demonstrated in Equation 4a. This allows us to construct the compatibility matrix, **B,** seen in Equation 4b.

$$\begin{pmatrix}\varepsilon_x\\ \varepsilon_y\\ \gamma_{xy}\end{pmatrix}=\begin{pmatrix}\frac{\partial u}{\partial x}\\ \frac{\partial v}{\partial y}\\ \frac{\partial u}{\partial y}+\frac{\partial v}{\partial x}\end{pmatrix}=\begin{pmatrix}\frac{\partial N_1}{\partial x} & 0 & \frac{\partial N_2}{\partial x} & 0 & \frac{\partial N_3}{\partial x} & 0 & \frac{\partial N_4}{\partial x} & 0\\ 0 & \frac{\partial N_1}{\partial y} & 0 & \frac{\partial N_2}{\partial y} & 0 & \frac{\partial N_3}{\partial y} & 0 & \frac{\partial N_4}{\partial y}\\ \frac{\partial N_1}{\partial y} & \frac{\partial N_1}{\partial x} & \frac{\partial N_2}{\partial y} & \frac{\partial N_2}{\partial x} & \frac{\partial N_3}{\partial y} & \frac{\partial N_3}{\partial x} & \frac{\partial N_4}{\partial y} & \frac{\partial N_4}{\partial x}\end{pmatrix}\begin{pmatrix}u_1\\ v_1\\ u_2\\ v_2\\ u_3\\ v_3\\ u_4\\ v_4\end{pmatrix} \quad \text{(a)}$$

$$\underline{\varepsilon}=\boldsymbol{B}\underline{u} \quad \text{(b)}$$

Equation 4: Compatibility equations, (a) using shape functions and chain rule and (b) in matrix form (Moatamedi & Khawaja, 2018).

Equation 4 gives the compatibility matrix, **B**, with respect to the global coordinate system (x,y). However, chain rule can be used to more easily calculate this with respect to the local coordinate system (ξ,η), through the transformation shown in, where J is the Jacobian.

$$\begin{pmatrix}\frac{\partial N_i}{\partial \xi}\\ \frac{\partial N_i}{\partial \eta}\end{pmatrix}=\boldsymbol{J}\begin{pmatrix}\frac{\partial N_i}{\partial x}\\ \frac{\partial N_i}{\partial y}\end{pmatrix}$$

$$\boldsymbol{J}=\begin{pmatrix}\frac{\partial x}{\partial \xi} & \frac{\partial y}{\partial \xi}\\ \frac{\partial x}{\partial \eta} & \frac{\partial y}{\partial \eta}\end{pmatrix}$$

Equation 5: Coordinate transformation through the use of the Jacobian (Liu & Quek, 2014).

Once the compatibility matrix is determined, the constitutive matrix can then be calculated. This is done using the stress-strain relationship defined by the problem statement and material properties. The general relationship between stress and strain can be seen in Equation 6, where **D** is the constitutive matrix, whilst Equation 7 shows an example constitutive matrix for plane stress and plane strain.

$$\underline{\sigma}=\boldsymbol{D}\underline{\varepsilon}$$

Equation 6: General stress-strain relationship.

$$\boldsymbol{D} = \frac{E}{1-v^2}\begin{pmatrix} 1 & v & 0 \\ v & 1 & 0 \\ 0 & 0 & 0.5(1-v) \end{pmatrix} \quad \text{(a)}$$

$$\boldsymbol{D} = \frac{E}{(1+v)(1-2v)}\begin{pmatrix} 1-v & v & 0 \\ v & 1-v & 0 \\ 0 & 0 & 0.5-v \end{pmatrix} \quad \text{(b)}$$

Equation 7: Example constitutive matrices for (a) plane stress and (b) plane strain (Fish & Belytschko, 2007).

Once the compatibility and constitutive matrices have been determined, these can be used to calculate the local stiffness matrix for the element. This is defined by Equation 8, further background on the formulation of this equation can be found here (Fish & Belytschko, 2007). However, as a consequence of the Gaussian quadrature implemented to define the integration points, the integral can be determined by computing the matrix multiplication at each integration point and summing the resulting matrices with appropriate weightings.

$$\boldsymbol{K^e} = \int_V \boldsymbol{B^T D B}$$

Equation 8: Calculation of elemental stiffness matrix.

Again, this integration can be made simpler by performing this with respect to the local coordinate system. This can be done through the application of the Jacobian using the relationship shown in Equation 9 (Liu & Quek, 2014).

$$dV = \det(\boldsymbol{J})\, d\xi d\eta d\zeta$$

Equation 9: Transformation of integrals to the local coordinate system.

Finally, the global stiffness matrix can be found by combining all of the elemental stiffness matrices. The global stiffness matrix has dimensions NxN, where N is the number of degrees of freedom within the system. Any boundary conditions are then applied to the problem statement and Gaussian elimination can then be used to solve Equation 1.

1.5 Heat Transfer

Heat transfer mechanisms are extremely important in any experimental process where large temperature changes occur. In particular, within additive manufacturing concentrated heat sources are used and rapid heating and cooling is experienced throughout the course of the build. For this reason understanding the heat transfer mechanisms that take place is key to understanding AM processes.

Heat transfer can take place in any physical scenario through three mechanisms; conduction, convection and radiation. Each of these mechanisms follows certain physical laws that can be described by mathematical equations. Firstly, conduction is the process of heat energy transferring from particle to particle through vibrations of these particles, and hence undertaking a transfer of kinetic energy (Annaratone, 2010). It can be represented by Fourier's Law, as seen in Equation 10. Here, q represents the heat flux, k the materials thermal conductivity and T the temperature.

$$q = -k\nabla T$$

Equation 10: Fourier' law for conduction of heat (Lienhard IV & Lienhard V, 2019).

On the other hand, convection is the transfer of heat between a solid and a fluid. It can be thought of as conduction in the presence of fluid motion (Lienhard IV & Lienhard V, 2019). Heat transfer due to convection can be determined using Newton's law of cooling, given in Equation 11, where h represents the heat transfer coefficient of the solid, and T_{amb} the temperature of the surroundings.

$$q = h(T - T_{amb})$$

Equation 11: Newton's law of cooling.

The final heat transfer mechanism is radiation. This term refers to heat transfer through electromagnetic waves and is determined using Stefan-Boltzmann's law. This is presented in Equation 12. Here, ε is the emissivity of the material and σ the Stefan-Boltzmann constant. All other variables remain as previously defined.

$$q = \varepsilon\sigma(T^4 - T_{amb}^4)$$

Equation 12: Stefan-Boltzmann law for radiation (Jiji, 2009).

All three mechanisms must be taken into consideration when considering a system in which heat transfer plays a key role. The overall heat transfer equation can be seen in Equation 13.

$$\frac{\partial T}{\partial t} = \alpha\Delta T + \frac{Q}{c\rho}$$

Equation 13: Overall heat transfer equation (Han, 2012; Naterer, 2022)

Within the heat equation, c and ρ represent the materials specific heat and density respectively and α represents the materials thermal diffusivity, which can be calculated as $k/c\rho$. The equation is derived by determining the total amount of energy coming in and out of the domain and using the values of specific heat and density to calculate the corresponding changes in temperature. Fourier's law is used directly in the derivation to determine how much heat is

being conducted into and out of the region under consideration. Meanwhile, the Q in Equation 13 represents any external heat sources or sinks, and therefore any convective or radiative heat losses are accounted for within this term.

1.6 Solidification

The thermal profiles experienced by additive manufactured material are unique when compared with traditional manufacturing methods, and consequently unconventional microstructural features occur (Attallah, et al., 2016). In order to help understand these concepts throughout this work, some basic solidification theory is presented here. A lot of the understanding here was taken from (Kou, 2003) and (Dantzig & Rappaz, 2016). These sources can be referred to for further detail.

Most solidification within materials, and metals in particular, takes place by nucleation and growth. Nucleation is the establishment of a collection of particles within the molten material that is above a critical size, so as to be energy preferential. There are 2 main methods of nucleation; homogenous and heterogeneous. Homogeneous nucleation refers to nucleation that takes place within the molten region of pure material, whereas, heterogeneous nucleation takes place in the presence of foreign particles such as the mould wall or particles present within the material. The critical size of a nucleus depends on temperature, or more specifically undercooling. This is the temperature below the liquidus point (T_f) as shown in Equation 14.

$$\Delta T = T_f - T$$

Equation 14: Calculation of undercooling.

Athermal nucleation assumes that there exists a predetermined amount of nuclei that all have a required undercooling to form. Upon reaching the required magnitude of undercooling for a certain nucleus, that nucleus is created instantaneously. This is often demonstrated with a Gaussian distribution, defined by the critical undercooling and the standard deviation (Dantzig & Rappaz, 2016; Rappaz, 1989).

Once a nuclei is formed, the nuclei continues to grow within the molten material. If stable, a grain continues to grow spherically until impinged upon by other grains, this is equivalent to a planar microstructure. Other structures include cellular and dendritic. These are formed when the interface becomes unstable as a result of constitutional supercooling due to solute redistribution. This is common in alloys, as the material composition is effected upon solidification, this is known as solute redistribution. When this takes place this means there is a local effect on the local undercooling, as a result of alterations in composition, known as

constitutional supercooling. This leads to instabilities within the interface allowing for the formation of dendrites. The total undercooling, as shown in Equation 15Equation 14, can be broken down into a number of different components namely, concentration-induced, curvature-induced, thermal and kinetic undercoolings, respectively.

$$\Delta T = \Delta T_C + \Delta T_R + \Delta T_T + \Delta T_K$$

Equation 15: Equation for undercooling (Kou, 2003).

The solidification microstructure is highly dependent on the magnitudes of the thermal gradient, G, and the solidification velocity, R. As discussed by Kou, the type of structure is determined by the ratio G/R and the product of G and R, which is actually the cooling rate. This can be represented by a solidification diagram, or G-R diagram (Kou, 2003), such as that shown in Figure 4. This gives a graphical representation of when a material forms columnar, equiaxed or mixed grain structures based on the values of G and R. Typically for large thermal gradients a columnar structure is formed as the solidification takes place more rapidly than bulk nucleation can take place, and epitaxial growth occurs instead. Similarly, at lower thermal gradients it is more likely that equiaxed grains will form as sufficient time for nucleation and growth takes place.

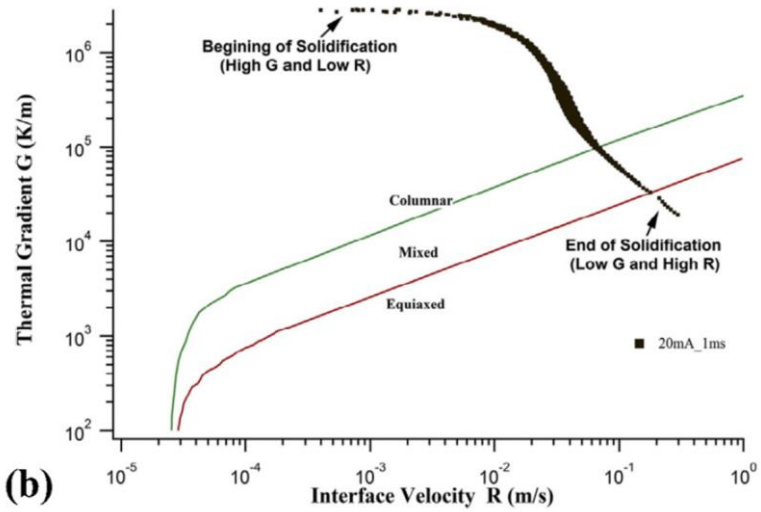

Figure 4: Example G-R diagram for IN718, taken from (Debroy, et al., 2018).

Metal alloys tend to exhibit dendritic microstructures. The dendrite tip velocity, determines the rate of solidification of each grain, and is again dependent on the local undercooling. Metals solidify as crystalline structures. Depending on the alloy in consideration, a number of different structures are observed. The most common are face-centred cubic (FCC), body-centred cubic (BCC) or hexagonal close packed (HCP) crystals (Groover, 2020). These are shown in Figure 5.

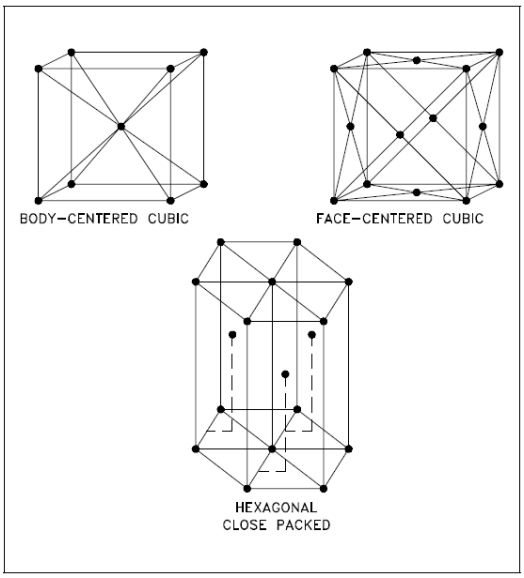

Figure 5: Common crystallographic structures, image from (Engineer Educators, 2022) .

1.7 Objectives and Aims

This chapter has highlighted the benefits that additive manufacturing processes have to offer for industry. However, it has also summarised some of the main challenges being faced in the AM industry. In order to increase the potential for the adoption of AM within industry these challenges must be addressed, particularly the part reliability and repeatability. It is thought that this could be achieved through the increased understanding of the thermal history of AM processes, as well as the resulting microstructure and mechanical properties, as it is understood that mechanical properties are directly related to the microstructure which is in turn related to the thermal profile (Malinov, et al., 2001; Malinov, et al., 2001). Modelling methods are presented, within this work, as a cost effective solution to investigating these types of physical phenomena. A more detailed review of the research gaps in AM and the modelling methods available is presented in the following chapter, along with the research objectives of this project.

2 Literature Review

This chapter starts by identifying the research needs and challenges within the industry of additive manufacturing, focusing on those addressed within the current work. Following this, existing modelling approaches are reviewed for both thermal and microstructure prediction within AM processes. The chapter concludes by outlining the aims and objectives for this work.

2.1 Research Needs in Additive Manufacturing

Developments in additive manufacturing have been of great interest in recent years. As discussed in section 1.1, AM offers a wide variety of benefits for industry and it is for this reason that AM is a key component in the development of industry 4.0 (Khanpara & Tanwar, 2020). However, the lack of understanding regarding certain aspects of the process, mean that the current applications of additive manufacturing in industry are limited. A number of roadmaps and reviews have been developed to help identify and address the key challenges in the manufacturing process (Fielding, et al., 2016; Energetics Incorporated, 2013; Lloyd's Register Foundation, 2016; Additive Manufacturing Center of Excellence, 2020; AM-motion, 2016). Amongst these reports there are a large number of research gaps and challenges presented, however they are frequently grouped into smaller topic groups relating to specific stages of the manufacturing process, such as:

- Design
- Materials
- Process
- Post-processing
- Non-destructive evaluation (NDE)
- Knowledge transfer
- Standardisation and qualification

Firstly, there are a number of challenges presented relating to the design process of additively manufactured parts, in particular the desire for clear design guidelines, including the determination of whether AM is a suitable manufacturing method for a given component and application, and if so, which process would be most advisable along with guidelines surrounding process parameters and features such as support structures (America Makes & ANSI Additive Manufacturing Standardization Collaborative (AMSC), 2017; Additive Manufacturing Center of Excellence, 2020). This also includes design guidelines for more complex structures and functional materials. In general, readily available guidelines describing suitable approaches for additive methods would significantly help increase the use of AM in

industry. The roadmap presented by LRF discussed the benefits of design optimisation and the need for further work to maximise the benefits and ensure safe implementation (Lloyd's Register Foundation, 2016). Furthermore, there is currently a limitation on the materials available for AM processes and consequently there is a desire within industry to expand this range. Moreover, it is clear that there is a need to understand the properties of AM materials and how certain properties, such as spreadability (for power bed processes) and flowability (for powder based, direct energy deposition processes), impact the build. Specifications and standards for raw materials are also required if AM is to become widely adopted. With regards to the added concept of materials-by-design and functionally graded materials, it has been observed that further research is required to fully understand and most efficiently utilise the additional design capabilities AM offers (National Institute of Standards and Technology, 2013). This relates closely to the process-structure-property relationships that will be discussed later.

The next range of challenges relate to the additive process itself. They include parameter control and machine calibration. In particular, it has been highlighted by a number of sources that there is a significant requirement for in-situ monitoring and control throughout AM builds (Additive Manufacturing Center of Excellence, 2020; AM-motion, 2016). The aim of this would be to reduce variability with additive builds and increase reliability. Similarly, there is a need to understand and address the variations introduced between different machines in order to further increase part repeatability. There is also a substantial need for standards on post-processing, as well as non-destructive evaluation methods (Additive Manufacturing Center of Excellence, 2020; National Institute of Standards and Technology, 2013). NDE plays a vital role in validation of part quality, but suitable NDE methods and standards are required for this. In addition, understanding of the impact of defects and their implications on part quality is crucial to determining a part’s safety and suitability.

A key step in the adoption of AM in industry is knowledge dissemination. This includes development of training courses to ensure there is a suitably qualified work force to undertake the required tasks. This is already being introduced through projects such as CLLAIM (CLLAIM, 2021). Furthermore, knowledge transfer and education is an important part of initiating the cultural changes that are instrumental to any wide spread adoption of new technologies. Both companies and consumers need to be assured of functionality and safety before AM can truly be accepted as a reliable manufacturing process.

A common goal that appeared amongst the majority of the reviews and reports cited here was the need for reliable, certified parts that are fit for purpose. Standards play a large role in the achievement of this goal, by ensuring safe, dependable procedures are available for all

aspects of the additive manufacturing process (Additive Manufacturing Center of Excellence, 2020). The core task that needs addressing in order to produce these standards is an increase in the fundamental understanding of the intricate mechanisms and relationships involved. This was captured by a number of the reports reviewed as part of this work (Energetics Incorporated, 2013; Lloyd's Register Foundation, 2016; Bourrel, et al., 2009). The additive manufacturing roadmap presented by the Lloyd's Register Foundation in 2016, in particular, discussed how an increase of understanding, resulting in the development of new standards could lead to a reduction in the excessive testing currently needed for the implementation of AM parts. The roadmap also highlighted the importance of developing an understanding of AM materials and their behaviour for the safety of AM components. One area, specifically, that has consistently been identified as requiring a significant increase in understanding is the resultant material properties of additively manufactured parts. The work presented here aims to contribute to the understanding of this by establishing methods of investigating relationships between process parameters and the resultant microstructure.

A discussion of the anisotropy and heterogeneity of the material properties in AM parts was undertaken within the work completed by Kok et al. (Kok, et al., 2018). As determined within their work, such material properties can be induced as a result of the complex thermal histories imposed upon the material during additive processes, which are significantly different to those experienced in other manufacture methods. In a recent review of metal additive manufacturing in aerospace, Zhang and Liang identified one of the primary challenges to be the stability of mechanical properties (Zhang & Liang, 2019). Ngo et al. also identified anisotropic microstructure and mechanical properties as a key challenge in their review of AM (Ngo, et al., 2018). Further works also investigated the resultant microstructure of additively manufactured including the work by Parimi et al (Parimi, et al., 2014) and Alhuzaim et al (Alhuzaim, et al., 2021), both undertaken at the University of Birmingham. The prior work presented by Parimi et al investigated the influence of deposition strategy and power on laser DED processes. The influence of power was further investigated by the Alhuzaim et al. The results of this study showed that the laser power had significant influence on both the morphology of the grains and their size.

A number of reports have identified the development of comprehensive relationships between process parameters, microstructure and mechanical properties as an important aspect for the advancement of AM. A review of additive manufacturing for aerospace by Singamneni et al., identified a number of key aspects that require further development (Singamneni, et al., 2019). These included further evaluation of the physics involved within additive manufacturing processes as well as the development of material-process-structure-property relationships. These relationships between raw material, manufacturing process, microstructure and

resultant properties are also in the technical focus areas given in (Additive Manufacturing Center of Excellence, 2020). Bourrel et al. also presented the need for understanding these relationships and being able to use these predictively, possibly with the assistance of multiscale modelling (Bourell, et al., 2009). Likewise, it was established by ASTM, among others, that simulation of AM processes to establish material-process-structure properties is an area that needs further development in order to establish suitable standardisation techniques (Additive Manufacturing Center of Excellence, 2020).

Many of the challenges discussed here can be addressed or supported through the use of numerical modelling. As discussed in section 1.3, simulations are a useful tool to provide insight and increase understanding on the mechanisms involved in the process. As noted in the work by Ghobakhloo (Ghobakhloo, 2018), numerical modelling will play a key role in the successful implementation of industry 4.0, by providing capabilities of efficient design and optimisation, as well as digital twins and in-situ monitoring. The metal based additive manufacturing review presented by the National Institute of Standards and Technology in 2013, also discussed the need for simulation methods in order to increase design capabilities and part certification (National Institute of Standards and Technology, 2013). Moreover, the need for microstructure models as well as both low and high fidelity physics based models. A similar AM roadmap also highlighted the need for modelling and simulation methods for AM in order to help additive processes reach their full potential (AM-motion, 2016).

2.2 Advances in Numerical Modelling for Additive Manufacturing

As noted, numerical modelling and simulation techniques are vital to the advancement of AM. A significant increase in the number of published papers related to models in additive manufacturing has been seen in recent years (Figure 6). This is owing to the ability of modelling methods to provide insight and understanding, with a significant reduction in experimental testing. This is particularly useful in AM due to the large amount of process parameters involved. Simulation and modelling methods have been used within additive manufacturing to investigate, predict and understand a wide variety of different phenomena, from defect and melt pool geometry prediction to residual stress and distortion simulations.

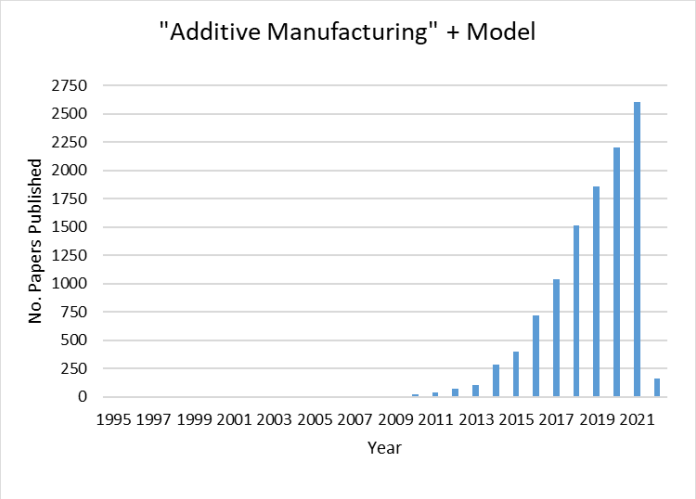

Figure 6 Frequency of published papers relating to modelling of additive manufacturing over recent years (when using the search *"Additive Manufacturing"* + *Model* on Web of Science).

An extensive review of the modelling progress within additive manufacturing was given in the open source report produced by Wei et al. (Wei, et al., 2021). The report was extremely thorough and presented a great deal of insight on the modelling of AM processes from residual stress to microstructure predictions. Research gaps for each topic were discussed, including the need for efficient models and open access models, as well as the wider integration of certain complex physical laws. This built on the modelling aspects of the additive manufacturing review presented by the same team (Debroy, et al., 2018). Within this report a thorough review of both experimental and modelling aspects of the process, structure, property links in additive manufacturing was given. Here, the need for openly available modelling methods was identified to help improve the understanding surrounding these relationships ultimately leading to increased reliability and part validation. Other modelling needs, such as access to temperature dependent material properties are also identified. A collection of the literature undertaken within modelling of AM, for various processes, with varying objectives can be seen in the review presented by (Stavropoulos & Foteinopoulos, 2018).

Furthermore, Peter et al. provided a comparison of a number of specifically designed additive manufacturing software tools (Peter, et al., 2020). The capability of each package to predict and suggest a number of different features was assessed, including; orientation and support optimisation, part distortion and recoater contact. This was done through the comparison of simulated parts against experimentally manufactured IN718 parts built using the EOS M290 system. Three numerical methods were presented as the underlying mechanisms used within the software packages discussed; namely, the finite element, inherent strain and thermal

circuit network methods. Each method was used in an attempt to allow computationally efficient part scale models.

Recently, in 2018, an additive manufacturing benchmark was held by the National Institute of Standards and Technology (NIST) in order to accelerate the development of additive manufacturing models. The benchmark consisted of a number of challenges with extensively measured experimental tests. Each was then opened to blind simulation submissions. A thematic series relating to the challenges within this benchmark was published in Integrating Materials and Manufacturing Innovation (IMMI). A number of the papers within this series will be discussed later on within this work, when individual challenges within the benchmark are discussed in more detail. The organisers of the benchmark also published a paper reviewing the overall outcomes (Levine, et al., 2020). A subsequent benchmark is to be undertaken in 2022.

More specific examples of the literature for thermal and microstructure modelling within additive manufacturing are given in the subsequent sections.

2.3 Review of Thermal Modelling for Additive Manufacturing

Thermal modelling of additive manufacturing processes has been a topic of great interest over the past years. This is owing to the multiple uses of the thermal profile from process parameter optimisation to residual stress, distortion and microstructure prediction. Thermal models play an extremely important role in microstructure prediction and must be as accurate as possible to ensure the best simulation of grain growth achievable (Li, et al., 2020). In order to accurately represent the process there are a number of features that need to be accounted for within the simulations. These include moving heat sources, material deposition and heat loss. Furthermore, due to the intensity of the heat source within AM builds, AM thermal models can be highly computationally expensive and therefore this also has to be taken into account within the modelling approach. How all of these factors are taken account within the current literature is detailed below. Within this section an overview of the current literature available on thermal models in additive manufacturing is provided. Due to the large amount of literature available for AM models, as can be seen in Figure 6, it is unfeasible to review all the relevant papers here. Instead a selection of relevant papers highlighting the important features will be presented. The literature discussed will be broken down into powder bed fusion and direct energy deposition processes, owing to the different approaches that need to be undertaken as a result of the physical processes involved in the respective manufacturing methods.

Firstly, a review of some of the work undertaken in the simulation of thermal history for powder bed fusion processes is covered. A 3D thermo-mechanical model of laser powder based

processes with metals and ceramics within the dental industry was presented by Dai and Shaw (Dai & Shaw, 2004). Most notably within this work, there was a significant focus on the adaptation of material properties to account for the transition of material from powder to solid material. Equations were provided to determine the effective thermal conductivity of the powder bed as well as the contributions to heat loss from the powder material. The implementation of material properties for powder as well as solid material is one of the aspects of thermal models of particular interest for powder bed fusion processes. Huang et al. also provided similar equations for the effective thermal conductivity in their work on selective laser melting of Ti-6Al-4V (Huang, et al., 2016). However, much simpler relationships between material properties of the solid and powder materials are found elsewhere within literature. In particular, Foroozmehr et al. utilised a scaling factor of 0.01 to convert between bulk and powder material properties (Foroozmehr, et al., 2016). Moreover, within the work presented by Roberts et al the level of porosity within the powder bed was used to determine the scaling factor for material properties (Roberts, et al., 2009). The same approach was applied by Hussein et al. in their sequentially coupled thermo-mechanical models of single layers, representative of overhangs within complex geometries (Hussein, et al., 2013).

Roberts et al. presented a 3D thermal model for the simulation of L-PBF with Ti6Al4V. A Gaussian heat source was implemented, along with element birth techniques to simulate material deposition (Roberts, et al., 2009). This is by far the most common material activation method within powder bed fusion processes, as it is a convenient method to activate a layer of material at a given time. The model proposed within the work by Roberts et al. utilised quarter symmetry, for efficiency, to validate the modelling approach against experimental data within literature. The approach was then applied to a multilayer model. The same experimental results were used to validate the modelling approach developed by Huang et al. also (Huang, et al., 2016). The authors within this work also implemented a Gaussian heat source, within their simulation of a single layer deposition process. The validated approach, developed within this work, was then used to investigate the influence of process parameters on the predicted thermal history and melt pool dimensions. Fu and Guo also used a Gaussian heat source in their simulation of a 5 layer, Ti6Al4V, SLM build (Fu & Guo, 2014). The models were validated against experimental melt pool measurements, and used to investigate the influence of laser power. Similarly, the modelling approach presented by Foroozmehr et al was used to investigate the effect of the scanning speed on the melt pool shape (Foroozmehr, et al., 2016). However, this work presented an alternative heat source method based on the optical penetration depth, in which a uniform flux was applied over a volume. On the other hand, a Goldak heat source was used by Song et al. within their 2D fully coupled, thermo-mechanical simulations. Although it was unclear if any of the surrounding powder bed was accounted for

within this model. Denlinger et al. also used the implementation of a Goldak heat source (Denlinger, et al., 2017). A sequentially coupled thermo-mechanical model was undertaken, with a combination of quiet and element birth techniques being applied to simulate material activation, with respect to the mechanical properties. Mesh coarsening was also used to increase efficiency of the approach.

A wide range of work has been undertaken at Lawrence Livermore National Laboratory, on the modelling of powder bed fusion models (King, et al., 2015; Khairallah & Anderson, 2014; Hodge, et al., 2014). Typically this was done on a multiscale approach, where by 2 in house software packages, ALE3D and Diablo were used. First ALE3D was used to model the process on the melt pool scale. The information from this was then transferred into the part scale models in Diablo. However, the software used within these works will not be considered any further here.

Within DED processes, as with the PBF models, a number of attributes must be taken into account within the thermal modelling process, including material deposition, dynamic heat sources and temperature dependent properties. Firstly, whereas the material in PBF models is deposited as a layer of powder and then selectively melted according to the geometry, with either the laser or electron beam, the material in WAAM is deposited as a molten melt bead at the location of the heat source. Therefore, it is not as physically representative to initiate material on a layer by layer manner as in the PBF simulations. Both element birth/ death techniques and quiet element methods can be used as a method of representing this alternative deposition technique. However, if element birth techniques are implemented, elements are often activated within smaller sub regions in a layer, to try and more accurately replicate material deposition with the moving heat source. Michaleris provided a comprehensive comparison of both the quiet and inactive element activation methods (Michaleris, 2014). Furthermore, different heat sources are typically used for DED processes to the common Gaussian heat source seen in the PBF models. Various different heat sources were discussed by Wei et al (Wei, et al., 2021), and also within the review of heat sources which covers Gaussian surface models as well as both Gaussian and Goldak volumetric models (Hamahmy & Deiab, 2020). Moreover, temperature-dependent properties and heat loss boundary conditions must still be taken into account, however the models are made simpler by the lack of powder in the process. A review of some of the current literature, for DED applications, is given below.

There are a number of papers that look at the finite element simulation of the thermal history of WAAM processes. Element birth and death techniques were implemented along with a Goldak heat source by Xiong et al. (Xiong, et al., 2017), as part of their work looking at the

effects of substrate preheating on the resultant thermal profile within a cylindrical build. As previously stated, Goldak heat sources are a popular choice of heat source model for wire-arc processes and have been used multiple times within WAAM thermal simulations and can be seen in work such as (Ding, 2012; Li, et al., 2019) as well, whilst some other authors still implement a Gaussian distribution (Bonifaz, 2018; Hejripour, et al., 2019). Montevecchi et al. looked at the development of a new heat source that takes into account both the heat dissipated from the molten metal as well as the welding arc (Montevecchi, et al., 2016). This was done through the combination of both a body and surface heat flux and was implemented along with the quiet element approach for material deposition. The model was experimentally validated for a single bead wall and showed much better agreement with experimental displacement results than a model using the more traditionally used Goldak heat source. More recently, Hejripour et al. (Hejripour, et al., 2019) studied the effect of cooling rate on phase formation through the use of thermal modelling in duplex stainless steel WAAM builds using a Gaussian heat source. A domain activation technique, similar to element birth, was implemented within this work to account for material deposition. Heat loss due to radiation and convection are often taken into account through the implementation of boundary conditions on exposed surfaces, however Bonifaz et al. (Bonifaz & Palomeque, 2020) made use of a FILM subroutine within their stress analysis of a single bead wall. This was to replicate the heat loss effects within the bead caused by the arc (Bonifaz, 2018).

Furthermore, another feature of interest within WAAM is the shape of the deposited weld bead. In contrast to the finite domain of a powder bed, as molten material is deposited with the heat source in WAAM the geometry is much less predictable. The work carried out by D. Ding et al. (Ding, et al., 2015) focused on a model to accurately represent the bead shape through the use of mathematical functions such as parabolic and cosine equations. However, this work focused purely on shape and did not give any insight into the thermal profile of the bead. Similarly, Bai et al. (Bai, et al., 2018) also predicted the bead geometry through the use of a fluid flow model. Within most finite element thermal models, a layer within the WAAM build is represented as an idealised division of the geometry, ie. a rectangle within a wall or circle within the cylindrical builds (Hejripour, et al., 2019; Montevecchi, et al., 2016; Bonifaz & Palomeque, 2020), although some alter the geometry to try and account for the bead curvature. For example Graf et al. (Graf, et al., 2018) modelled the weld beam by semi-circular and sickle shaped layers, within their thermo-mechanical finite element model. A similar shape was undertaken in the work by Wang and Wang (Wang & Wang, 2016).

A project that focused on the development of a more computationally efficient steady state thermal model, was presented by Ding (Ding, 2012). However, he also successfully implemented a detailed Lagrangian approach achieving a strong agreement with

experimentally obtained thermal data. The steady state model has since been used in their subsequent publications, but will not be used here due to the assumption of a continued steady state. Symmetry has been used in multiple papers as an alternative method to reduce computational cost, by reducing the size of the computational domain (Ding, 2012; Ou, et al., 2018). Fluid flow models are taken into account by both Ou et al. and Ogino et al (Ogino, et al., 2018). However, these are beyond the scope of this work as fluid flow models will not be incorporated as they are generally too computationally expensive and complex to model the thermal history on larger domains, such as the full size of the build part.

A review of modelling approaches for laser metal deposition processes, up to 2015, was given by Andrew Pinkerton (Pinkerton, 2015). It summarised the then current modelling approaches being undertaken to simulate the LMD process on a range of scales from the powder stream to final build properties. Furthermore, it highlighted the ultimate goal of modelling in AM which is to be able to predict the resultant properties of the build. Some of the current work in LMD modelling is discussed here.

Zhan et al. presented a recent study on the application of LMD processes to the repair of a trapezoidal groove in a 316L stainless steel plate (Zhan, et al., 2019). Within this study a Gaussian conical heat source was applied along with modified thermal conductivity to account for Marangoni effects. Whilst the model predicted melt pool geometry reasonably well, when compared to an experimental macrograph, there was a lack of experimental validation for the transient temperature values. The report concluded by considering the effect of the thermal history on microstructure and consequently microhardness. Whilst this does not seem like a typical AM application, the ability for part repair is one of the benefits of DED processes and a lot of the principles required to model the process is the same as the deposition of a new part. Additive manufacturing simulations, and in particular DED processes, involve a lot of the same principles as those involved in traditional weld simulations (Lindgren, et al., 2016) and so we can also consider the established methods for welding and cladding applications, when simulating AM methods. Nevertheless, these will not be covered here as the review focuses on work within AM.

A multi-physics approach was undertaken by Zhang et al. to simulate the thermal history of thin walls produced by LMD, and investigate the effects of certain process parameters including deposition strategy, deposition velocity and laser power (Zhang, et al., 2017). The approach involved a number of complex physical laws and considered both a simulation of the laser-powder interaction zone and the full 3D geometry. A multilayer build, with a total of 6 layers was simulated and a strong level of agreement was obtained for the predicted shape of the build for 4 different sets of process parameters. However, a quantitative comparison of

thermal history values was not given. The bead geometry is of great interest within LMD processes, and the accurate prediction for this features heavily across literature. The shape of the bead surface was also predicted by Peyre et al. and compared against in-situ melt pool imaging (Peyre, et al., 2017). Also within this work, different values of travel speed and power were investigated and the thermal gradient and solidification rates were evaluated to determine columnar or equiaxed growth. Whilst the thermal models were validated with experimental data, the microstructure morphology predictions were not accurate for all process parameter combinations. Ahsan and Pinkerton implemented an iterative analytical model to predict thermal history, bead shape and cooling rate, as well as a prediction of grain size based on the cooling rate values (Ahsan & Pinkerton, 2011). The analytical model implemented is the Cline and Anthony's equation based on the Gaussian heat source. Varying values of flow rate and power were investigated.

A 3D sequentially coupled thermo-mechanical analysis was undertaken by Mukherjee et al., however fluid flow aspects were also accounted for within this work (Mukherjee, et al., 2017). Nevertheless, contrarily to the works presented previously that focused on bead shape, flat surfaces were assumed for the bead deposits. Half symmetry was also implemented as single track walls were simulated. Despite the assumption of flat surfaces, a good level of agreement was achieved between the simulated and experimental thermal measurements. Knapp et al. also considered the effect of assuming a flat bead geometry (Knapp, et al., 2017). This was shown by comparing the flat surface model to a curved surface model with and without the inclusion of convection within the melt pool. Very little difference was seen between the flat surface and curved surface models, whilst a much clearer variation was seen by not including convection. The curved shape of the bead was defined by an ellipsoidal equation and a combined surface and volumetric heat flux was implemented, similar to that in the WAAM work by Motevecchi et al. (Montevecchi, et al., 2016). A strong level of agreement was achieved with experimental images of the melt pool shape.

Heigel et al. investigated the assumption of free convection within finite element models of direct energy deposition (Heigel, et al., 2015). Sequentially coupled thermo-mechanical models of the deposition of Ti-6Al-4V walls were compared against experimental results. The Goldak heat source was assumed and a forced convection model, based on measured heat transfer coefficient values, was suggested. It was determined that the forced convection model proposed achieveed more accurate results, for both the thermal and residual stress predictions, than the common assumption of free convection. In the thermo-mechanical model presented by Kumar and Vedrtnam, a combined heat transfer coefficient has been implemented (Kumar & Vedrtnam, 2018). This has been used widely within literature (Yongjie, et al., 2012). Kumar and Vedtram implemented a Gaussian heat source for their single track

multilayer model, however they suggested that the use of volumetric heat sources would be more suitable in future works. Furthermore, it appears there was a lack of inclusion of material deposition methods within this study. Single track wall deposits have featured prominently within the literature reviewed here. However, the work presented by Lundbäck and Lindgren presented the application to much more complex geometries, with the implementation of a Goldak heat source and activation based on a defined path for the heat source (Lundbäck & Lindgren, 2011).

In more recent works, Doux and Phillipe applied a calibrated Goldak heat source, with the built-in element progressive activation feature in Abaqus (made available in the 2018 release), to simulate the thermal history and residual stresses in an IN718 wall (Doux & Philippe, 2019). Although comparative experimental results for the thermal history were provided at 6 thermocouple positions, it was difficult to draw a direct comparison with simulation results due to how the two are presented. The comparison presented within the work suggests that the overall shape of the thermal profile was accurately represented, whilst peak and final temperature values were under predicted. Experimental data for comparison of residual stress predictions was not yet provided. Li et al. also made use of a Goldak heat source and progressive element activation within their recent multi-scale analysis of a 42 layer LMD deposit in a binary nickel-copper alloy (Li, et al., 2020). The thermal history simulated here was used to provide both residual stress and microstructure predictions through the implementation of a multi-phase field model. Whilst the work provided a modelling approach for the microstructural and residual stress developments as a result of the thermal history, it did not provide any form of experimental validation for the modelling approach proposed. Furthermore, thermal modelling approaches have been applied to single track, wall builds with functionally graded materials within the work by (Li, et al., 2020). Within this work a circular heat source was implemented and element birth techniques applied, with a single element width being deposited in each step. This approach could be very labour intensive during the model development of large AM builds.

Physically representative numerical simulations can be extremely computationally expensive. Typically, the more physical phenomena accounted for within the model, the more computationally expensive the model is. On the other hand, computational expense is also significantly influenced by the size of the simulation domain and the fidelity of the mesh and incrementation strategies implemented. Certain works have focused on the development of efficient modelling strategies within AM. As previously discussed, Ding et al presented an efficient model for the simulation of WAAM (Ding, 2012). Yan et al. also focused on the development of a computationally efficient model capable of predicting the transient thermal profile (Yan, et al., 2018). The model used a combination of thermal flux density and volume

heat generation. Both layer based and track based approaches were compared against experimental results. As is expected, a direct trade-off was seen between the accuracy of the model and the computational time.

Similarly, Yang et al (Yang, et al., 2021) attempted to address the computational expense of part-scale additive manufacturing simulations through the implementation of a semi-analytical heat source model, based on the commonly used Goldak heat source, leveraging the principle of superposition. Within this study, the significant reduction in computational expense was largely attributed to the coarse mesh size that could be used, as smaller mesh sizes are not required to resolve the heat source. Adaptive remeshing is another technique that has been used within literature to increase computational efficiency. For example, Olleak and Xi presented a modelling approach that simulated the deposition of a single layer within each model, allowing for mesh refinement in the layers of interest (Olleak & Xi, 2019). Moreover, inherent strain approaches have also been used in an effort to increase computational efficiency of thermo-mechanical models, however this technique is not really applicable to the application of microstructure simulations.

Analytical solutions have also been applied as an efficient method of approximating thermal problems. As discussed by Lu, (Lu, 2021), the computational efficiency provided by the implementation of analytical thermal models allows for a fast and simple approach to investigate processes at the design level, such as process parameter optimisation. This could be particularly beneficial for AM, due to the large amount of process parameters and design freedoms such as functionally graded microstructures. By far, the most popular analytical heat source used in literature is the Rosenthal solution which has been used widely in welding applications. This will be the primary analytical solution used within this work, although other analytical methods such as Green's function (Steuben, et al., 2019) have been seen within literature.

Obviously, the efficiency of the analytical solutions come at a cost. Namely, this is due to the simplification of the physics involved. Physical phenomena such as Marangoni effects and latent heat of fusion are not typically accounted for within these types of solution. Furthermore, temperature independent properties are usually implemented, therefore limiting the accuracy of the predictions. However, a detailed comparison of the application of the finite element method and this analytical approach, for the simulation of thermal history in L-PBF processes with IN718, was provided by Promoppatum et al (Promoppatum, et al., 2017). A Gaussian surface heat flux was implemented within the finite element model. On the other hand, the Rosenthal solution could only account for a point heat source and temperature-independent material properties. Influence on the melt pool geometry, thermal history and microstructure

were considered. The predicted melt pool width was compared against experimental data in literature. A good agreement was achieved by both heat source approaches for small energy density values. Similarly, both approaches obtained similar thermal gradient values and predicted columnar grain growth, whilst there was a larger difference in cooling and solidification rates. The work presented by Steuben et al. aimed to enhance the analytical methods, for specific use with AM processes, by introducing a number of capabilities to account for temperature dependent properties, representative computational domains and accounting for material deposition (Steuben, et al., 2019). The methods developed showed a significant improvement in the accuracy of the model when compared to a corresponding FE model, particularly through the inclusion of temperature dependent properties.

One of the benefits of using analytical solutions is the ability to derive other quantities associated to the thermal model, such as melt pool width and length. A number of these are given in the works by Tang (Tang, 2017) and Lu (Lu, 2021). Similarly, Bertoli et al, utilised the Rosenthal solution to determine the thermal gradient and solidification velocity for L-PBF processes (Bertoli, et al., 2019). This information was leveraged to investigate the expected grain structure within these AM parts. The prediction of melt pool geometry using the Rosenthal is validated against experimental measurements in the work presented by Reese et al. (Reese, et al., 2018). The approach was then used to predict melt pool geometry as a function of velocity and power. However, very little detail on the modelling approach was provided, such as material properties and efficiency values. In the works presented by Walker et al. (Walker, et al., 2019; Walker, et al., 2020) a combined analytical and finite element analysis was used to predict track profile, thermal history and residual stress in single track deposits of IN718. The analytical model was based on that presented by Ahsan and Pinkerton (Ahsan & Pinkerton, 2011), and was used to predict the track profile. In their most recent work the modelling approach was used to predict these features with an in-situ change of process parameters within the scan.

2.4 Microstructure Modelling Methods in Literature

There are four primary methods of microstructure modelling seen within literature. These include empirical, kinetic Monte-Carlo (kMC), Cellular Automata (CA) and Phase Field (PF) models. A brief overview of each technique and its applications is given here.

Empirical methods include methods such as the Johnson-Mehl-Avrami-Kolmogorov (JMAK) and Koistinen-Marburger equations (Bhadeshia, 2022). These analytical equations determine phase fraction based on a given temperature profile and information about the phase transitions of the material under consideration. Relevant information pertaining to this kind of phase information is usually found in TTT or CCT diagrams, where the specific phase

transformations of an alloy are displayed as a function of temperature. The JMAK equation is used to model the diffusional transformation of phase α to β under isothermal conditions. The equation originates from the work performed by Kolmogorov in 1937 and the theory of the kinetics of phase transformations can be found in the series of works published by Avrami (Avrami, 1939; Avrami, 1940; Avrami, 1941). An application of the models to isotherm cooling of Ti6Al4V can be seen in the work by Malinov et al. (Malinov, et al., 2001; Malinov, et al., 2001). Meanwhile, the Koistinen-Marburger equation is used to model martensitic transformations. These methods are extremely efficient, however, they can only supply a limited amount of data. Results from such an analysis would be in the form of a phase fraction for each representative element. Leblond and Devaux present an adaption of the models for anisothermal phase transformations in steels (Leblond & Devaux, 1984). These methods have also seen implementation with manufacturing processes. An example of this is the work presented by Mi et al. (Mi, et al., 2014). In this paper, JMAK equations were coupled with a 3D finite element model to predict phase transformations in a TIG welding process. However, one of the main drawbacks of the approach is that it is unable to give any visual representation of the grain size, morphology or orientation, unlike other methods such as Cellular Automata and kinetic Monte Carlo simulations.

Cellular automata was introduced as a method of modelling solidification, primarily, by Rappaz and Gandin in their seminal work for the application of cellular automata methods to casting processes (Rappaz & Gandin, 1993; Rappaz, et al., 1996; Gandin, et al., 1999; Rappaz & Thevoz, 1987; Gandin & Rappaz, 1994; Gandin & Rappaz, 1997). The technique is based on basic principles of nucleation and capture. Rappaz first presented improved models for nucleation in his preliminary work (Rappaz, 1989). A Gaussian distribution was suggested as oppose to the almost discontinuous representation used previously. In their more notable work, a 2D growth envelope model was developed to represent crystal growth within the material (Rappaz & Gandin, 1993). This was later modified establishing what is now a commonly implemented modelling method, the 2D decentred square algorithm (Gandin & Rappaz, 1997). This work also presented the 3D decentred octahedron algorithm for the representation of 3D FCC crystals. The 2D growth envelope technique was initially applied with a uniform temperature field. The CA- FE coupling was introduced in later work (Gandin & Rappaz, 1994), with weak and full couplings being presented here (Gandin, et al., 1999). The methods developed here are renowned within the implementation of CA for solidification mechanisms and form the basis for all other CA applications presented within this thesis, making the work presented by these authors one of the most significant developments for the simulation of microstructural development.

In more recent work, Guillemot et al. presented an improvement to the CA-FE coupling through the implementation of a front tracking method and compared this against the coupling approach presented by Rappaz and Gandin (Guillemot, et al., 2004). This work was developed further by Carozzani et al. (Carozzani, et al., 2012), where by an iterative 3D fully coupled model was implemented by reducing memory usage. The authors provided experimental validation of this approach in subsequent work (Carozzani, et al., 2013), as well as efficient parallelisation methods for the simulation of large scale parts (Carozzani, et al., 2014). Furthermore, Chen et al. then presented a detailed description of the application of the 3D cellular automata finite element coupling for the application of arc-welding (Chen, et al., 2016). A level-set function was implemented to model the gas-liquid interface, along with a concise algorithm of five main rules for the implementation of the Rappaz-Gandin growth envelope algorithm. Moreover, it was also assumed that nucleation was not included within the melt pool. The work successfully simulated microstructure development for an arc welding process, but was not supported by experimental validations. Further works have been presented by Zinovieva and Zinoviev et al. for the application of solidification. In their early work, they demonstrated a 2D fully coupled cellular automata – finite difference model for the solidification of a nickel based superalloy (Zinovieva, et al., 2015) . The authors also presented an alternative approach to the reduction of mesh anisotropy, to the decentred algorithm suggested by Gandin & Rappaz, using two correction factors, one for the correction of grain shape and one to remove staggered boundary effects. (Zinovieva, et al., 2015). However, again, neither work was supported with experimental validations.

The next method, of microstructural prediction, is the kinetic Monte Carlo approach, or Potts model as it is sometimes referred to. Monte Carlo simulations are statistical models that can be applied to a wide range of applications. For the application of microstructure predictions, kMC is very similar to the CA approach in that a discrete grid of cells is used to assign a state variable, or spin as it is more commonly called within kMC methods. One key difference is the rules used to update this variable, whilst the CA method uses solidification laws, kMC focuses on the implementation of the least energy principle. This approach sees a site change grain ID, with a given probability, if this configuration is more energetically preferential (Holm & Battaile, 2001). Nevertheless, some work has also demonstrated the incorporation of the least energy principle within CA methods (Ding, et al., 2006). Spittle and Brown presented some of the first uses of Monte Carlo methods for the application of solidification (Spittle & Brown, 1989; Spittle & Brown, 1989). Incrementally, Spittle and Brown introduced the effects of thermal field as well as solute redistribution within their work. The current leader in the application of the kinetic Monte Carlo is arguably the Sandia National Laboratories, whom have developed and released open source software, SPPARKS (Stochastic Parallel Particle

Kinetic Simulator), for the implementation of kMC models. Examples of the implementation of this software for welding applications are given here (Rodgers, et al., 2016; Rodgers, et al., 2017). Steady state melt pools were implemented to prescribe the temperature profile and steps were taken to relate the MC simulation to physical measures of both time and space through calibration. Temperature-dependence of the grain growth was implemented through the use of a grain boundary mobility function. In their later work, the effects of weld speed and laser mode (pulsed or continuous) were considered.

The final method discussed here is the phase field method. This is probably the most physically accurate modelling technique, presented here, but is consequently also the most computationally expensive method. Phase field methods work by tracking a number of continuous field variables, known as order parameters, as they vary between 0 and 1 in accordance with a number of physical laws based on thermodynamics and the conservation of energy at the interface (Singh, 2015). The common method implemented in phase field models is the diffuse interface approach, where the order parameter varies continuously across the interface (Bhadeshia, 2010). This is different from the sharp interface method where a discrete change in order parameter occurs (ie. the order parameter can take on the value of 0 or 1). Further details on the phase field method can be found here (Singh, 2015). These methods generally take place on a much smaller scale, than the other methods discussed here, simulating microstructure development on the scale of single dendrites. The approach has been implemented by a number of authors within literature, some of these works are referenced here (Steinbach, et al., 1996; Fan & Chen, 1997; Krill III & Chen, 2002).

Each of these established methods have their benefits and limitations. For this reason, all 4 methods have seen exposure to the application of metal additive manufacturing processes. The next sections focus on presenting the current state of the art for this area, as well as comparing the positives and drawbacks of each modelling approach in order to assess the suitability of each technique.

2.5 Literature for Microstructure Prediction in Additive Manufacturing Processes

The interest in microstructure prediction for additive manufacturing has become of increasing interest in recent years. To that end, all of the mechanisms presented above have been used to investigate a number of different processes, phenomena and materials, with an aim of providing a better understanding of solidification mechanisms in metal additive manufacture.

Empirical approaches have been applied by a wide range of authors for the application of AM. As additive processes involve highly non-uniform temperature profiles, the additivity rule is implemented for the implementation of the empirical approaches with such complex,

anisothermal temperature histories (Charles Murgau, 2016). This technique essentially sees the discretisation of the thermal profile into very small individual isothermal segments. Some of the more important works in this area are presented by Kelly and Charles. Kelly and Kampe presented an extensive analysis of the resultant microstructure of laser metal deposited Ti-6Al-4V (Kelly & Kampe, 2004). The authors' subsequent work presented a modelling approach that accompanied the experimental investigation (Kelly & Kampe, 2004). A simple 2D thermal model, perpendicular to the scanning direction, was implemented, whereby each new layer was deposited at a fixed temperature and the heat source shape was neglected. This thermal model was then used to determine the phase evolution within the material. Further details can be found in the thesis completed by Kelly (Kelly, 2004). Similarly, Charles presented a modelling approach for the prediction of phase composition in TIG wire metal deposition of Ti6Al4V (Charles, 2008). The approach undertaken is very similar to that of Kelly and Kampe, and focused on the time and spatial discretisation of the empirical equations. A detailed description of the JMAK and Koistinen-Marburger equations, as well as the incremental additivity approach was given in the later work by Charles Murgau et al. (Charles Murgau, et al., 2012).

There has been a heavy accent on the use of empirical models for the prediction of microstructure development in the titanium alloy, Ti-6Al-4V. This is likely due to the popularity of the alloy within AM applications but also as a result of the complex phase transformations undertaken by the alloy, meaning that empirical approaches are more suitable for capturing all aspects of the phase transformations involved. The principles developed by Kelly and Charles have been implemented by a number of subsequent works by other authors. These include the work presented by Vastola et al. whereby empirical equations accounting for the formation and dissolution of α phase, as well as martensite were used to predict microstructure formation for Ti6Al4V produced by both SLM and EBM (Vastola, et al., 2016). The microstructure model presented here is coupled with a 2D finite element thermal model, and shows a clear difference in the microstructural phases formed by the two processes. Irwin et al., similarly, implemented the methodology, suggested by Kelly and Charles, to Ti6Al4V LENS production (Irwin, et al., 2016). A 3D finite element thermal model was used as the input for the microstructural model. The work optimised the material properties implemented, through experimental validation and compared them against the material properties suggested by Kelly and Charles. However, the model did not consider the effects of martensitic transformations separately. Both diffusion and diffusionless transformations were accounted for in the work presented by Suarez et al., for the application of laser metal deposition of Ti6Al4V (Suarez, et al., 2011). In a more recent work, Yang et al. used similar methods to

simulate phase transformations in powder bed fusion of Ti-6Al-4V but with an added capability to determine dislocation density within the martensitic phases (Yang, et al., 2020).

Whilst the application to Ti-6Al-4V heavily dominates the current literature, application to other alloys have also been seen in the literature. Zhang et al. applied similar methods in their recent work presenting a framework for the simulation of phase transformation in AM (Zhang, et al., 2019). As the work presented a generic framework that could be applied to alternative alloys and AM processes, application for steel 5140 was demonstrated, whilst the model was also applied to powder bed fusion of Ti-6Al-4V, with calibration and validation against experimental samples. Lindgren et al. also applied empirical methods for the prediction of phase formation in Ti-6Al-4V and IN718 (Lindgren, et al., 2016). Computational welding mechanics were exploited within the modelling approach and flow stress models were implemented to determine mechanical behaviour. Further work was presented by the authors that expanded on the implementation of the modelling approach with Ti-6Al-4V (Babu, et al., 2019). Similarly, phase transformation kinetics were implemented within the work by Lu et al to predict the development of precipitates within IN718 WAAM builds (Lu, et al., 2021).

Furthermore, a number of papers within literature have focused on the assessment of microstructural development through the quantification of the solidification parameters: thermal gradient, G, and solidification velocity, R. As discussed within chapter 1, these parameters control solidification mechanisms and determine the grain morphology. This phenomena can be exploited through investigation of the thermal history. Firstly, Liu et al. investigated the effect of laser power and scan speed on the solidification parameters of a single melt pool in selective laser melting of AlSi10Mg (Liu, et al., 2018). 3D thermal models were developed using finite element software. This allowed the authors to predict where in the melt pool columnar to equiaxed transitions were likely to take place. Furthermore, Sabau et al. also investigated the thermal gradient and solidification velocity distributions in single track models of laser powder bed fusion with IN625 (Sabau, et al., 2020). Two modelling approaches were used for the thermal model, heat transfer only and heat transfer coupled with fluid dynamics. The difference in solidification parameters provided by the two methods were discussed. Moreover, Hunt's model was also used to predict primary dendrite arm spacing.

Phase field models can also be used to predict microstructure on the scale of dendrite arm spacing. Sahoo and Chou modelled the development of a single grain as the result of electron beam powder bed fusion of Ti6Al4V (Sahoo & Chou, 2016). The model used a 3D finite element thermal model to calculate the thermal gradient and solidification velocity, which were then imported into the phase field model. Finite difference methods were implemented to solve

the required phase field and concentration equations on a 100μm x 100μm domain. Notably, the effects of thermal gradient and scan speed on the grain growth were investigated. The results were compared with experimentally and analytically obtained microstructures and a reasonable level of agreement was achieved, although no quantitative measurements were obtained experimentally. Similar work for laser powder bed fusion of IN625 was undertaken by Keller et al. (Keller, et al., 2017). Cellular growth was successfully simulated using a 2D phase field model following a 3D thermal analysis. However, unlike the nucleation of a circular seed in the work presented by Sahoo and Chou, Keller et al. initiated a planar solid-liquid interface. Furthermore, the frozen temperature approximation was implemented, whereby a linear thermal profile was assumed that moved along the growth direction with a given speed and maintained a constant thermal gradient. A 2D phase field model was also used by Acharya et al. due to the computational expense of 3D models, although the model was undertaken in both the longitudinal and transverse planes to give a more thorough analysis of the microstructural evolution (Acharya, et al., 2017). A CFD analysis was undertaken to estimate the melt pool and solidification region, whilst the seeding method applied within this work allowed for multiple seeds to be applied at both the bottom and top of the melt pool. In the work by Kumara et al. they also applied multiple seeds with a distance equivalent to the primary dendrite arm spacing (Kumara, et al., 2019).

Unlike Archarya et al., whom assumed a binary system for IN718, in the more recent works presented by Kumara et al. the alloy was represented by a seven component system (Kumara, et al., 2019; Kumara, et al., 2019). This obviously provided a more accurate representation of the alloy system. Within this work the commercial software MICRESS was implemented to undertake the phase field models. There were two stages to the phase field model, first the solidification model and then a subsequent model that simulated microstructure development as a result of in situ heat treatment. Experimental microstructures were analysed and the simulation results were also compared with comparative simulations of a casting scenario. However, unlike other works, a thermal analysis was not undertaken within this work. Instead a representative cooling rate was assumed, and the heat treatment temperature was taken from experimental thermocouples. It should be noted that the domain size modelled in each of the authors works was extremely small, with one being 6μm x 6μm and another 25μm x 25μm. This gives the reader an idea of the small scale to which phase field models can be applied. For this reason other mesoscale modelling approaches need to be applied to give a more global representation of the grain morphology.

The application of kMC methods to additive manufacturing has also been seen. Ge et al. presented a process-structure-property modelling approach, that utilised Monte Carlo methods to simulate the microstructure development in Ti-6Al-4V (Ge, et al., 2019). The kMC

method was used on a multi-scale basis to provide simulation of the development of β grains, whilst a single grain scale model simulated the development of α phase within the prior β grains. The thermal aspects of this work were discussed in an earlier section. The most notable work in this area is that presented by Rodgers et al. Building on their application of kMC to welding, (Rodgers, et al., 2016; Rodgers, et al., 2017), Rodgers et al. used kinetic Monte Carlo techniques to investigate grain structures in metal additively manufactured parts (Rodgers, et al., 2017). As part of the Sandia National Laboratories, this was done through the use of the SPPARKS software. The model was used to simulate microstructural development within LENS processes and compared against experimental studies in literature. An idealised melt pool and heat affected zone were used to replicate the thermal field, whilst this was not exactly representative of the process it was beneficial for the computational efficiency of the model. Inactive material was hidden from the simulation to replicate material deposition. Qualitative and quantitative comparisons were undertaken. Results showed how grain structures could be altered by scanning strategy, although with a reasonably low resolution. The authors commented on the simplifications made in the model and the need for future work in this area. In their more recent work, Rodgers et al. applied the developed modelling approach to investigate the effect of process parameters on mechanical properties (Rodgers, et al., 2020).

Within the work provided by Rodgers et al., a comparison of microstructure modelling methods was also given (Rodgers, et al., 2017). Within the comparison CA-FE, CA-Lattice Boltzmann (CA-LB), Monte Carlo and empirical methods were evaluated. Whilst the benefits of the kMC method identified included, the availability of the open source software SPPARKS, the ability to account for solid-state transformations and being slightly more computationally efficient than both CA-FE and CA-LB, its limitations were also presented. These included the inability to account for crystal orientation as well as difficulties drawing quantitative links to experimental conditions. This point was also acknowledged in the comparison of CA and kMC techniques, for the application of recrystallisation, given by Sieradzki and Madej (Sieradzki & Madej, 2013). Rodgers et al. also identified empirical methods as the most computationally efficient, however it was also noted that even this is still relatively expensive for the simulation of full AM build parts. The overall opinion given within this work is consistent with the conclusions drawn in a number of other critical reviews of microstructure modelling methods. Zhang et al. presented a comparison of microstructure models for laser AM and in this work they considered Monte Carlo, Cellular Automata and Phase field. However, the CA approach applied in this work was a more probabilistic approach than that presented by Rappaz and Gandin. In this work, the CA approach presented appeared to be more computationally

efficient than the MC, but will not be considered any further due to the lack of physical relevance.

More recently, Tan et al. compared phase field, kinetic Monte Carlo and Cellular Automata approaches, as well as a very recent modified Cellular Automata approach that applied CA methods on a scale of dendrite shape, akin to the phase field approach. Conclusions drawn included the necessity of either kMC or CA modelling for the prediction of material properties, due to the larger scale of simulation, as well as the more accurate grain size predictions obtained through CA. Similar work was undertaken by Korner et al. (Korner, et al., 2020). As in other works, the accuracy of phase field models at the expense of efficiency was highlighted. However, it was stated that whilst PF methods are computationally expensive, they could be used to give insight into the dendrite growth velocity for implementation in more efficient CA models. Furthermore, the review also commented on the inability of Monte Carlo approaches to simulate grain texture. Similar conclusions can be seen in the work presented by Gatsos et al. and Li et al. (Gatsos, et al., 2020; Li, et al., 2020). Whilst Rodgers et al. identified the limitation of CA to be the inability to account for simulation of solid state transformations, accounting for subsequent work presented by Yang et al. (Yang, et al., 2018), Gatsos et al. identified this as one of the benefits of CA methods. Moreover, it is established by Korner et al. that the common challenge across all the modelling approaches is the simulation of new grain nucleation, as well as ensuring the development of well-established nucleation parameters for independent alloys. Li et al. also identified nucleation methods as an open question within microstructure simulations and identified the lack of microstructural simulations that validate thermal/melt pool models prior to the completion of grain growth predictions (Li, et al., 2020).

Within this work, we will focus on the application of cellular automata methods for metal AM processes. This choice has been made as it offers a visual representation of the grain morphology which is not achievable using empirical, transformation kinetics, based models. Furthermore, it is more physically accurate than kinetic Monte Carlo methods whilst remaining more computationally efficient than the phase field approach and provides a simulation on a larger scale. Li et al. drew the same conclusion that these attributes make CA the most suitable modelling technique for this application (Li, et al., 2020). Figure **7** demonstrates the visual differences between these three modelling techniques. Moreover, there is a wide range of literature demonstrating the successful application of CA methods. For example, the work by Gu et al, presents the application of 3D CA methods to predict grain structure and porosity for casting applications with a good level of agreement with experimental tests (Gu, et al., 2019). The following sections aim to present some of the key works in the application of CA for the

prediction of microstructure in metal additive processes and identify current limitations and possible areas for development within the literature.

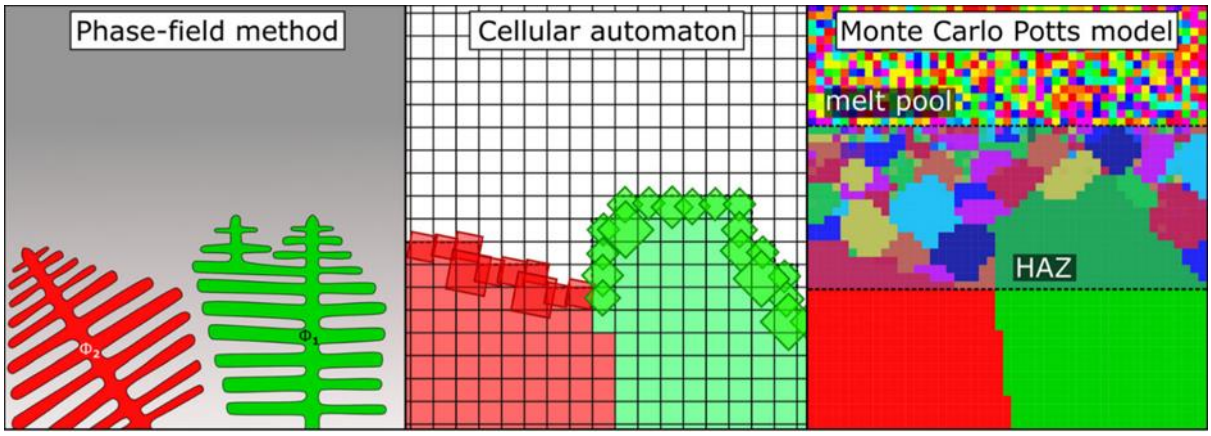

Figure 7: Schematic of different microstructure modelling approaches. Sourced from (Korner, et al., 2020)

2.6 Use of Cellular Automata for Simulation of Microstructure in AM

Following the decision to implement cellular automata methods within this work, an in-depth review of the current literature on applications of CA within additive manufacturing is provided. As previously mentioned, cellular automata models are often coupled with a supplementary modelling approach that provides the thermal results of the analysis. Rai et al. coupled a CA microstructure model with a lattice Boltzmann model (Rai, et al., 2016). The 2D model was used to simulate grain development in powder based processing of IN718. The 2D decentred square algorithm, developed by Rappaz and Gandin, was implemented with automatic incrementation. A rain drop model was used to generate powder particles. Meanwhile, Lopez-Botello et al. implemented the more commonly used Cellular Automata – Finite Element (CAFE) method (Lopez-Botello, et al., 2017). In this particular work an approximation of the Gaussian heat source was used to simulate the thermal history in a 4 layer SLM build using the aluminium alloy AA-2024. A weak coupling between the FE and CA models was used with the Von Neumann neighbourhood condition. A good level of agreement was achieved when comparing the predicted grain size against those seen experimentally. Powder bed fusion processes were also considered in the work presented by Yang et al., (Yang, et al., 2018) . A 2D CA model was implemented within the commercial software MATLAB. The prior beta grain structure in Ti-6Al-4V was simulated as well as the prediction of solid-state transformations. A good qualitative agreement was achieved between the model results shown and experimental samples.

On the other hand, Zhang et al. looked at the application of a fully coupled 2D CA-FE method for the application of LMD. Element activation was achieved through the use of element birth techniques and a Gaussian heat flux was assumed, although no experimental validation of

the thermal history was undertaken within this work, simulated microstructures were compared against experimental samples both quantitatively and qualitatively. Both clearly showed columnar grains of a similar magnitude. This work was built upon in their later work, where the authors implemented a new growth envelope model, the modified decentred polygon (Zhang, et al., 2018). This approach was thought to be more suitable for the non-uniform thermal fields seen in additive manufacturing, as well as being more computationally efficient. However, the details of implementation were not presented. The study focused on a single deposition scan and showed good agreement with both experimental thermal measurements and microstructure. A columnar to equiaxed transition was predicted within the melt pool.

As discussed previously, whilst nucleation methods among models remain reasonably similar, whether the inclusion of nucleation techniques is necessary, and how they can account for different aspects, is often in question. The effect of nucleation mechanisms was explored in the work presented by Li and Tan (Li & Tan, 2018). Within this work a number of simulations were carried out on both single scans and multiple layer builds to assess the effect of nuclei density and critical undercooling on microstructure predictions. The modelling approach undertaken was a weakly coupled finite volume – CA approach. A significant alteration in the microstructure was seen as a result of the changes in both nuclei density and critical undercooling. Akram et al. (Akram, et al., 2018) implemented a cellular automata based microstructure prediction model in order to demonstrate the effects of scanning strategy on resultant microstructure within additively manufactured parts. A 2D model was implemented to show the final microstructure in all 3 planar directions. The model only allowed for nucleation on interface regions, such as the melt pool boundary, and used an alternative model to the Gaussian approach implemented by Rappaz (Rappaz, 1989). Out of plane nucleation was artificially accounted for through additional nucleation sites. A good visual agreement was achieved with experimental images reported in literature and a clear change was witnessed between the different scanning strategies. However, within this work fixed thermal gradients were imposed, the microstructure model was not coupled with any thermal models. Furthermore, the results shown here were independent of any particular alloy. Rolchigo and Le Sar also suggested that a correction to the nucleation mechanisms within 2D CA models was required to accurately model the columnar to equiaxed transition (Rolchigo & LeSar, 2019). The adaption of nucleation methods has also been considered by Mohebbi and Ploshikin, where the authors recently investigated the development of new nucleation methods to account for specific microstructural features in aluminium alloys (Mohebbi & Ploshikhin, 2020). This particular study focused on the grain nucleation along the fusion boundary witnessed in additive manufacturing of AlSi10Mg and other aluminium alloys. Three nucleation methods, each with sound justification, were implemented and compared against

experimental images. The most suitable method of nucleation was determined by direct comparison with the experimentally obtained microstructures. Simulated microstructures have also been compared against alternative aluminium alloys, although fully calibrated and validated models have not yet been undertaken on alloys other than AlSi10Mg.

Following on from their early work, Zinovieva and Zinoviev et al. adapted their modelling approach for the application of powder bed fusion AM in their more recent publications. In 2016 the group presented a study implementing a 2D CA- finite difference (CAFD) method for the simulation of 316L processed by SLM (Zinoviev, et al., 2016). Adaptive time incrementation was undertaken and it was assumed, within this work, that due to the rapid cooling within the process, nucleation did not take place within the melt pool. Variations of the Goldak parameters were investigated and it was determined that the 2D model more accurately simulated grain growth within shallower melt pools, whilst it would be beneficial to include 3D aspects for deeper melt pools. The use of 2D and 3D models have both been seen in literature. It has been identified that 3D models are required to account for all aspects of microstructural evolution, including out of plane growth and 3D texture (Lian, et al., 2019 ; Gandin & Rappaz, 1997). However, as expected, a 3D CA model comes with an increase in computational expense. For this reason, Rolchigo and LeSar investigated the effects of including the third dimension, in their recent work applying CA to simulate grain growth in scenarios similar to LENS (Rolchigo & LeSar, 2019). The work concluded that a change from 2D to 3D resulted in a difference in the amount of grain impingement within the model, as well as the ability to accurately represent the columnar to equiaxed transition. The primary reason for this is the considerably smaller range of orientations available in the 2D model. It should be noted that within this work, growth rates were prescribed at a constant rate and as such, the modelling approach was not strictly representative of the manufacturing process. However, the literature clearly demonstrated the need for 3D CA approaches to fully capture microstructure characteristics.

The more recent work, presented by Zinovieva et al., implemented a 3D CAFD model, using a modified decentred octahedron growth envelope, for the application of Ti6Al4V (Zinovieva, et al., 2018). A sub volume was modelled in order to reduce computational efficiency. Both works provided comparisons of the grain structures produced in the CAFD model against experimentally manufactured microstructures, however, there was no validation of the thermal profile implemented. Koepf et al. focused on the computational efficiency of 3D powder bed fusion models (Koepf, et al., 2018; Koepf, et al., 2019). In the earlier work (Koepf, et al., 2018) the Rosenthal solution was used to analytically represent the thermal profile. This served to improve computational cost, along with the reduced simulation domain implemented within this work. Simulations were compared against experimental results of manufactured, cuboid,

samples. A good agreement was seen in both EBSD images and pole figures. In the following work, a more representative thermal profile was used (Koepf, et al., 2019). A finite element model was used to model the thermal history of a single layer within the additive process. The thermal profile was then stored locally and reused, rotated by the required angle for each new layer. Simulated microstructures were again compared with experimental images, with good agreement. Whilst these works focused on the improvement of computational efficiency the 3D models still required 200 hours of computing time on 720 cores. This would be an unfeasible amount of computational power for the majority of industrially relevant applications.

It has been widely recognised that one of the biggest challenges of microstructure modelling is the trade-off between accuracy and computational efficiency. In an attempt to address this issue Liu and Shin presented a coupled 2D cellular automata-phase field model (Liu & Shin, 2020). The purpose of the work was to combine the accuracy of a PF approach with the efficiency of CA methods. A 2D CA model was implemented to model the dendrite growth, whilst a 1D PF model was used to determine the dendrite growth kinetics. The modelling approach was applied to DED of Ti6Al4V and was compared against 2D PF and 3D CA models as well as experimental results. Whilst a good agreement was achieved with experimental results, some aspects of the grain morphology was lost by the use of the 2D model compared to the 3D CA. It was also more computationally expensive than the 3D CA model, but more efficient than the 2D PF whilst still being able to simulate sub grain structure.

Moreover, one of the key reasons for establishing microstructure modelling methods for additive manufacturing is to be able to understand and predict the effect of process parameters on the resultant microstructure and hence material properties. Herriott et al. developed a multi-scale framework for the simulation of material properties in additively manufactured parts (Herriott, et al., 2019). The framework presented implemented a finite volume - 3D CA method for the simulation of resultant microstructure. The domain was then split into subvolumes that were used as input for an elasto-viscoplastic fast Fourier transform (EVPFFT) model, for the simulation of mechanical properties. The microstructure was simulated using 4 different nucleation conditions. Each approach returned reasonably different results, accenting the need for established nucleation parameters as discussed by Korner et al. (Korner, et al., 2020). Furthermore, whilst the obtained stress-strain curves were compared with experimental results, simulated microstructures were not compared with those achieved experimentally. Similar work was undertaken previously by Yan et al. (Yan, et al., 2018). Here, a CFD thermal model was used to determine the thermal history used as an input for the 3D CA grain growth model. Microstructure outputs were then used in a self-consistent clustering analysis (SCA) crystal plasticity model.

A number of works focused solely on the link from process parameters and resultant microstructure. The authors of the process-structure-property framework proposed by Yan et al, (Yan, et al., 2018), also presented a subsequent work focusing solely on the grain growth predictions. Lian et al. presented a recent work that investigated the effects of laser power, scan speed and scanning strategy on the resultant microstructure of IN718 LMD deposits (Lian, et al., 2019). The model made use of a weakly coupled finite volume – cellular automata model. A decrease in grain size was observed with an increase in scan speed or decrease in laser power. Whilst the paper demonstrated the capability of the modelling approach to capture these changes, the results were not validated with experimental tests. Rolchigo and LeSar also noted the importance of being able to understand the relationship between process parameters and microstructure development (Rolchigo & LeSar, 2019). As mentioned earlier, their work looked at the use of 2D and 3D CA for microstructure predictions in Laser Engineered Net Shaping (LENS) and demonstrated the effects of thermal gradient and solidification velocity on the resultant microstructure, as well as solute concentration. In a similar approach, Shi et al. made use of ALE3D, a hybrid finite element and finite volume code, along with CA to investigate the effects of beam shape and consequently melt pool geometry on the resultant microstructure in a single track powder bed fusion deposit. A total of 3 different beam shapes were explored, and a 3D CA method was implemented with the use of DREAM3D software to generate an equiaxed initial substrate microstructure. The effect of beam shape on nucleation and epitaxial growth, as well as its effects on thermal gradient and solidification velocity were investigated. Among other things, it was concluded that the amount of nucleation is correlated to the width of the melt pool when the laser is on and depth when the laser is off. However, both the work presented here and that by Rolchigo and LeSar, lacked support from experimental investigations. Whilst Shi et al. discussed the calibration of the thermal model against absorptivity values and melt pool depth, the study was largely a numerical study of the modelling approach, independent of a physically representative AM scenario. In particular, the computational domain was reasonably small and nucleation densities had been artificially increased above those witnessed experimentally in order to investigate the effects of bead shape on nucleation. Some small comparisons were drawn to previous experimental work undertaken by the authors (Roehling, et al., 2017). Whilst this supported some conclusions drawn in the work, other conclusions drawn through the model investigations were not in agreement with those seen experimentally. Meanwhile, the work presented by Rolchigo and LeSar was limited by the thermal assumptions made. The work presented here imposed a frozen temperature approximation, which is more commonly used in phase field models due to the small domain (Li, et al., 2020). This is where the thermal field is defined by prescribing a fixed cooling rate and thermal gradient. Therefore, the work was not representative of an experimentally observed thermal profile.

The most recent works within this area include those presented by Wang (Wang, 2021) and that by Teferra and Rowenhorst (Teferra & Rowenhorst, 2021). Wang used a 2D CA model combined with a CFD thermal model to investigate all 3 principal planes, similarl to Akram et al. (Akram, et al., 2018), for powder bed fusion of IN718 . The effects of scan strategy, laser power and scan speed were investigated, however, experimental validation of these studies is required. Similarly, Teferra and Rowenhorst, simulated microstructural developments using a 3D CA model with an analytical thermal model to simulate powder bed fusion of 316L SS. Significant effort within this work was taken to investigate parallelisation techniques to improve computational efficiency. Two different scan strategies were simulated, initially with varying nucleation densities on a smaller domain, with simulations taking approximately 6.5 hours with 132 cores. The nucleation density was chosen based on experimental results, taken from literature, and larger domain simulations were undertaken taking approximately 65 hours on 144 cores.

The literature discussed here represents the current state-of-the-art in the use of cellular automata methods to simulate grain growth in additive manufacturing processes. Whilst it clearly presents a wide range of applications and developments of the methodology, it also shows a range of limitations and challenges available within the current scope of work developed. Below, a table summarising some of the key papers and the limitations and challenges presented within each work is provided.

Authors	Year	Key Features	Limitations
Akram et al.	2018	• 2D CA simulation in PBF. • Simulation with 3 principal planes. • Investigates influence of scan strategy, thermal gradient and cooling rate.	• No coupling with thermal model. • Constant thermal gradients/cooling rates imposed. • No association to any particular alloy.
Zinovivea et al.	2018	• 3D CA finite difference model for PBF. • Experimental validation of microstructure.	• No bulk nucleation. • No validation of the thermal model is given.
Koepf et al.	2019	• 3D weakly coupled CA-FE model for PBF. • Compared against experimental microstructures. • Iterative use of thermal model for computational efficiency.	• High performance cluster computers used, which may not be accessible within industrial application. • Lack of inclusion of nucleation effects, other than from the surrounding powder.

Lian et al.	2019	• Application to DED processes with IN718 • 3D CA and finite volume methods. • Laser power, scan speed and scan strategy investigated.	• Lack of experimental validation for both thermal and microstructure models.
Teferra and Rowenhorst	2021	• 3D CA PBF model with analytical thermal model. • Investigates 2 scan strategies. • Focus on computational efficiency.	• Although computational efficiency is investigated the hardware used is still much more sophisticated than that typically available in industry. • Analytical thermal model implemented.
Wang	2021	• Simulation using 2D CA within 3 planes for PBF of IN718, with CFD thermal model. • Investigates the effects of various process parameters.	• Limited experimental validation. • In particular experimental validation for the effects of process parameters is required.

Table 2: Table summarising the current state-of-the-art in microstructure prediction for metal AM.

The next section within this work outlines the research challenges and objectives addressed within the scope of this project.

2.7 Research Aims and Objectives

It is clear from the literature reviewed above that there is a great need for increased understanding within the additive manufacturing industry. The main aim of this work is to contribute to this by investigating the link between process parameters and microstructure to increase reliability of additive manufacturing. Taking into consideration the key features and limitations of the work available in the current literature, the work presented here aims to contribute through the following objectives:

- Contribute to the smaller catalogue of work available for the application of CA to direct energy deposition processes, particularly for multi-layer builds.
- Implement cellular automata methods with experimentally-validated thermal models.
- Improve computational efficiency of the required models to achieve sensible run times with practical hardware requirements, suitable for use in industry.
- Apply CA models to investigate the influence of process parameters, with experimental validation.

3 Thermal Modelling Activities

The first stage to predicting microstructure development, is to be able to simulate the thermal history experienced. As discussed within the literature review, there are a number of different aspects that need to be accounted for when developing a finite element model of an additive manufacturing process. These include moving heat sources, temperature dependent behaviour and material deposition. Within this chapter some of the work completed in order to develop an understanding of thermal models for additive manufacturing, early on within this project, is presented. We first discuss the work undertaken as part of the additive manufacturing benchmark study and conclude with other work undertaken as part of projects undertaken by TWI Ltd and linked to this PhD. Note, the results of this chapter are not directly relevant to the conclusions and results of this thesis, but are presented here as a background and examples of development in the field of thermal modelling.

At the start of this project one of the main priorities of the work was to establish the current state of the art for modelling within the additive manufacturing industry. For this reason, the 2018 National Institute of Standards and Technology (NIST) additive manufacturing benchmark (National Institute of Standards and Technology, 2018), provided an ideal opportunity. It was my privilege to work as part of a team with TWI and Dassault Systèmes to complete a submission to the first challenge, for residual stress predictions. Whilst the focus of this thesis is on thermal and microstructural model development, residual stress predictions are also highly-dependent on the thermal history. Therefore, this provided a good opportunity to both familiarise myself with modelling techniques for additive manufacturing as well as test and validate thermal modelling approaches.

As discussed in section 2.2, the NIST 2018 AM benchmark, gave global access to 4 heavily monitored, AM based, experimental trials. For each, a challenge outlining a number of objectives for numerical predictions was given. Submissions of numerical predictions were entered as blind studies, before the experimental measurements were released. The data made openly available as part of the benchmark ensured high quality experimental trials were completed and extensively monitored. Furthermore, this was all completed using equipment available at a globally renowned laboratory, with resources and associated costs that could otherwise not have been feasible within the scope of this work. The first challenge, which will be the subject of this section, requested predictions for the residual stress profile, distortion measurements and microstructure predictions of the manufactured geometry. Within the earlier stages of this work, the focus remained on the thermal history predictions prior to the development and implementation of microstructure codes. Therefore, the numerical predictions undertaken as part of this challenge were of residual stress and distortion. Data

from this benchmark was used in subsequent work, chapter 5, to test and validate the microstructure modelling methods.

The test article was manufactured through laser powder bed fusion in both Inconel 625 (IN625) and stainless steel 15-5; however, only the IN625 samples have been modelled within this work. This is relevant as nickel-base superalloys feature heavily in this project. The geometry was designed as single cantilever with additional ridges on the top surface for accurate measurement of part deflection upon removal from the substrate. This can be seen in Figure 8. A detailed report of the process parameters and scan strategy were provided in the challenge description (National Institute of Standards and Technology, 2018). This included details of both contour and infill strategies throughout the total build height of the geometry. A layer height of 20um was used throughout the manufacturing, meaning a total of 625 layers were manufactured during the build of the test specimen. For this reason special considerations need to be made in order to model the geometry at the part scale.

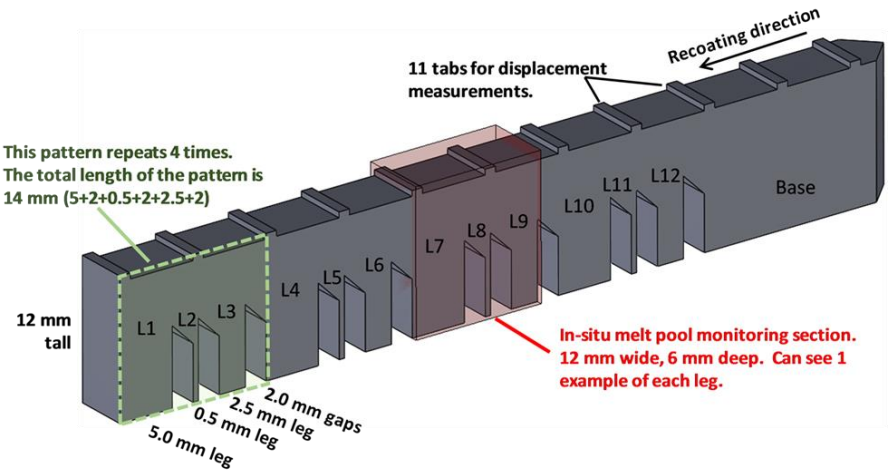

Figure 8: Geometry specified for challenge AMB2018-01 (National Institute of Standards and Technology, 2018).

As highlighted, there are a wide range of factors that need to be accounted for within thermal models for additive manufacturing: material deposition, scan strategy, heat source characteristics and heat loss. During the development of the models, the (then recently released, beta version) Abaqus AM app, that was made available to TWI, was used for efficiency. The app combines the ability to apply element birth techniques and a moving heat source through the definition of an event series. An event series is a table of data defining the path of the heat source by specifying the power and location of the heat source at various time points. Linear interpolation is used between the specified points to find the required details

between these times. The AM app utilises this information within user subroutines to activate the material as specified by the “recoater event series” and apply a moving concentrated point heat source in accordance with the “laser event series”. A visual representation of the event series within the AM app is shown in Figure 9. Within the app, the toolpath-mesh intersection module is used to identify all the elements that are intersected by the heat source within a given time increment. The energy delivered by the heat source during this increment is then distributed uniformly over these elements. Heat loss due to convection and radiation were also accounted for within the model.

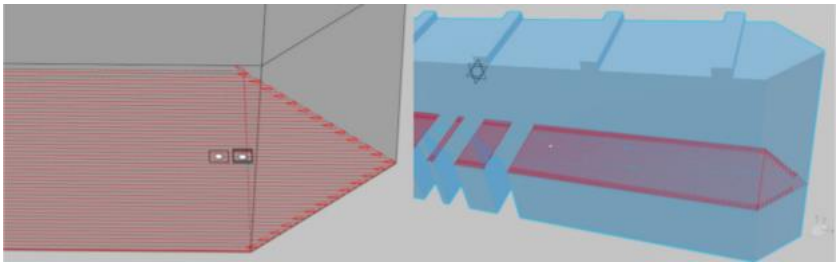

Figure 9: Visual demonstration of the application of the event series within the AM app (Yang, et al., 2019).

Specifically my role within this work focused on the development of finite element thermal models utilising the AM app within Abaqus with temperature-dependent material data. The use of the AM app was beneficial within this work as it removed the need for defining individual steps for each layer of new material, which would otherwise need to be defined through the use of a model change. Furthermore, the development process also involved calculation of an event series, for the geometry, based on the details of the scan strategy given as part of the challenge description. The models created were then compared to similar thermal models developed by other team members, and ultimately a more efficient technique of layer aggregation was implemented due to the large number of layers.

Layer aggregation is a method where multiple layers are deposited in the model at once, as if they are a single layer. The final models represented averagely 10 layers within each individual element. The layer aggregation technique applied here is an acceptable approach when simulating residual stress due to the resolution needed on the part scale as opposed to the macro or micro scale. However, this would not be a suitable technique when trying to simulate the solidification microstructure. Similarly, the fidelity of the heat source model for this simulation would not be appropriate when looking on at the micro scale; however the work provided a good demonstration of both the use of moving heat sources and event series. Temperature-dependent material properties were used for both the thermal and mechanical models. As the focus of this thesis is thermal and microstructural modelling for any further

details of the mechanical model the reader is asked to refer to the resulting paper (Yang, et al., 2019).

The resulting submission to the challenge was completed by a team from Dassault Systèmes and TWI and ultimately received 1st place for residual stress predictions out of a total of 6 submissions for this category worldwide. The team were invited to write a journal article detailing the model as part of a special issue on the AM benchmark, which one contributed to significantly within the writing and submission procedure (Yang, et al., 2019). The resulting residual strain predictions and corresponding experimental measurements can be seen in Figure 10 and Figure 11 respectively. As presented by Levine et al in the review of the benchmark outcomes (Levine, et al., 2020), the distortion predictions submitted for this challenge worldwide were consistently over or under predicted. Interestingly, half of the submissions predicted extremely similar results above the experimental distortion values and the other half provided very similar predictions below the experimental curve, highlighting that despite significant efforts within literature to predict part level distortions, accurate models for additive manufacturing are still required.

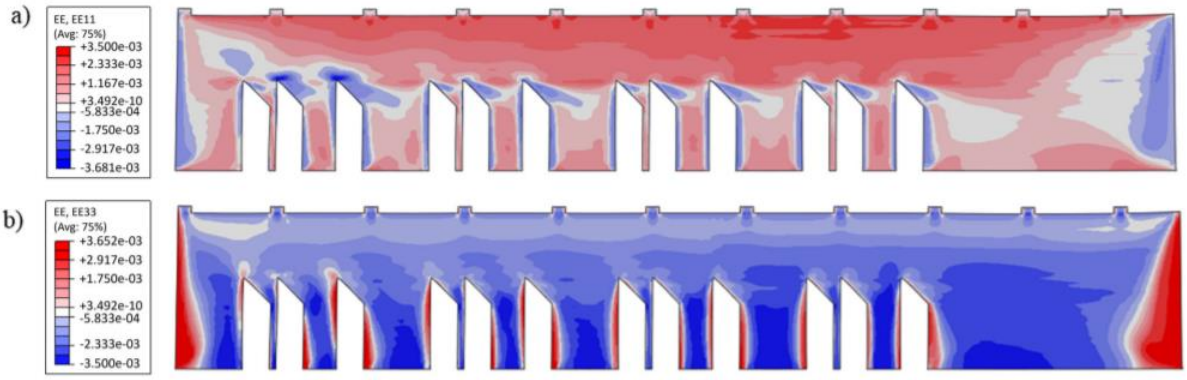

Figure 10: Predicted residual strain profiles a) EE11, b) EE33 (Yang, et al., 2019).

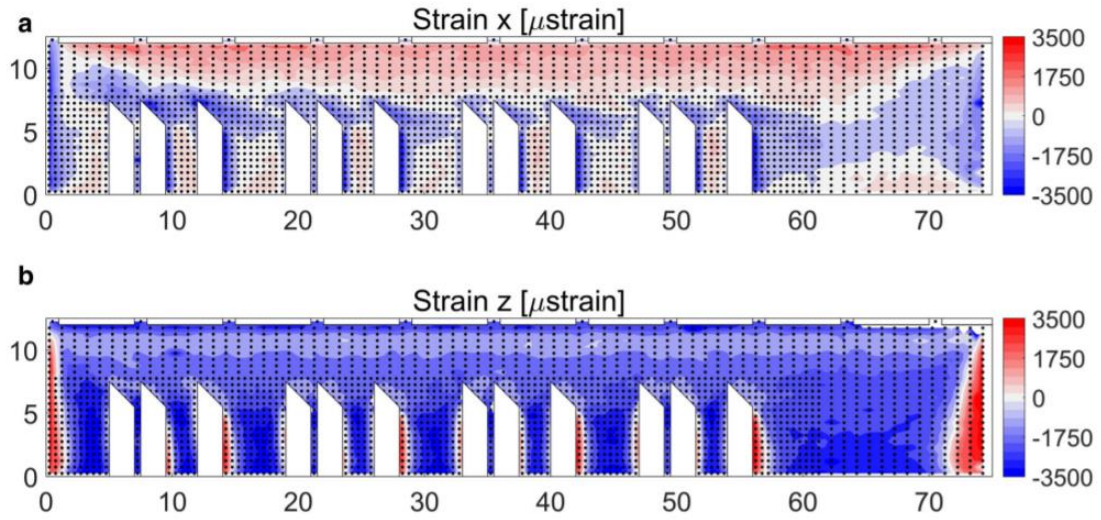

Figure 11: Experimentally observed residual strain profiles a) EE11 b) EE33 (National Institute of Standards and Technology, 2019).

Subsequent work was undertaken as part of another project within TWI, involving the thermal modelling of L-PBF of AlSi10Mg. This was performed as part of the European Comission-funded project PASSPORT (European Commission: CORDIS, 2020). This was done in order to determine the effectiveness of using the specific point energy and power factors as design parameters in laser powder bed fusion. Modelling work was used to support these investigations, by using thermal models to predict the influence of various process parameters.

Within this work I worked closely with colleagues to develop finite element models involving the development of user defined subroutines to prescribe moving heat sources. The use of an event series to define the heat source location was also leveraged within this work and material activation was modelled through the use of the model change function within Abaqus to define element birth within various steps. Further detail on the outcomes of this work can be found in the paper, published in 2019, summarising this work (Zavala-Arredondo, et al., 2019).

Overall, the work completed within both of these exercises provided an opportunity to gain familiarity and knowledge of specific techniques required for thermal modelling of AM procedures, in order to establish modelling methods to produce thermal profiles which can be used to drive the solidification models. Whilst the results from these studies will not be used directly within this work, they have provided a means to implement and validate the use of certain approaches, such as the implementation of event series and the use of user subroutines to define heat source movement, which can be carried forward and adapted into subsequent thermal models within this work. Particularly, the methodology used within the Abaqus AM app, is useful when considering efficient modelling approaches later on within this

work. Nevertheless, fine scale models, with higher fidelity, need to be undertaken for the simulation of solidification microstructure. For example, implementing Goldak or conical Gaussian heat source models in order more accurately predict the melt pool, as seen in more detail within later sections of this work. This level of fidelity cannot be achieved using the Abaqus AM app implemented within the NIST benchmark study. The corresponding papers, for works discussed here, can be found within the Appendix.

4 Microstructure Model for AM Processes

Within this chapter we will discuss the background behind the modelling methods implemented in this work. This will include an overview of the Cellular Automata (CA) technique as well as detailed information regarding its application to grain growth predictions and the implementation methods used within this work. The chapter will conclude with a discussion of techniques that can be used to determine the success of the model.

4.1 Cellular Automata

Cellular Automata is a modelling technique that was developed in the 1940's by John Von Neumann and Stanislaw Ulam (Shiffman, 2012). One of its initial implementations was actually for the simulation of grain growth as well as self-replicating robots. This application eventually lead to the most famous application of the CA modelling technique - James Conway's game of life created in 1970 (Shiffman, 2012). This is a zero-player game that uses CA to determine if a cell is living or dead. The notable feature of the game is that, no matter the initial configuration of the game, a number of specific shapes and images are produced within the simulation. Cellular automata is an efficient way of simulating complex phenomena by discretising a spatial domain. It has numerous applications and can be tailored to a wide range of phenomena, including the simulation of growth of numerous substances; leaves, shells and snowflakes (Andrews, 2008; Wolfram, 2002), fluid flow models , application in intrusion sensors (Navid & Aghababa, 2013) as well as uses in cryptography (Wolfram, 1994). Within this work we focus solely on the application of CA to the simulation of crystal growth.

The technique makes use of a grid of cells, or elements, the two terms will be used interchangeably throughout this work due to the coupling with finite element models. The gird of cells is usually a uniform structure, however techniques can also be applied to irregular grids (Navid & Aghababa, 2013). The cells, within a uniform CA grid, can be any regular, tessellating shape for example, squares, triangles or even hexagons. For simplicity throughout this chapter we will assume each cell to be a square. Each cell, within the domain, is assigned a number of state variables. These are updated throughout the analysis using a set of prescribed rules. Colours or shading can be assigned to variables allowing for visual representations of the scenario. The rules are typically dependent on the value of state variables within previous steps of both the cell of interest and its neighbouring cells. Therefore, we must also define the neighbourhood of each element at the beginning of the analysis. There are two common types of neighbourhood; Moore's and Von Neumann's. The Von Neumann neighbourhood was established in 1952 by John von Neumann himself, whilst Edward Moore developed the Moore neighbourhood in 1962 (Wolfram, 2002). Representations of these two neighbourhoods can be seen in Figure 12. Whilst these are two

of the more common neighbourhood definitions, the neighbourhood of a cell can in fact be defined in any manner that the user so wishes.

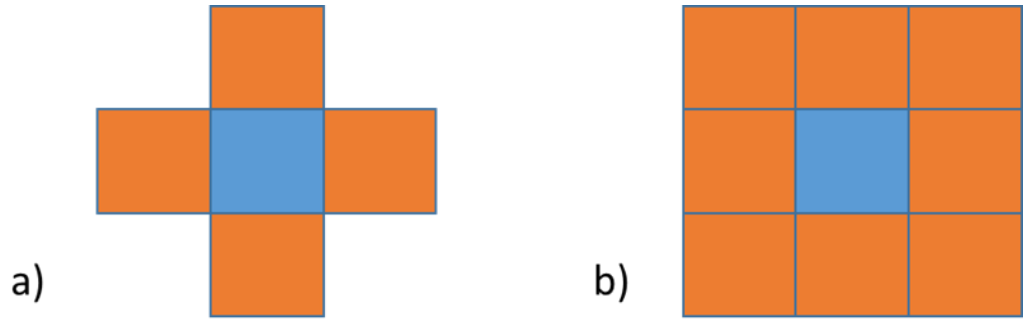

Figure 12: Diagrammatic representation of a) Von Neumann and b) Moore neighbourhoods.

Every individual cell is updated at the same time using the state variables from previous steps. Each time this occurs, this is known as a CA step. The step is typically time independent, but depending on the application it can be associated with real time increments. The concepts described here can be seen in the following simple example (Figure 13). Imagine we have a domain that has been divided into 25 uniform cells and the state variable applied to each cell (v) is its colour (C_v); B (blue) or O (orange). We assign the rule that if a blue cell has an orange neighbour then the cell also becomes orange. This can be written in an algorithmic form, using standard mathematical notation, as below, in Table 3. Within this formulation we describe the cell under consideration as v and its neighbourhood as Ω.

Initial State	Final State	Condition
$C_v = B$	$C_v = O$	$\exists\ \mu \epsilon \Omega\ s.t. C_\mu = O$

Table 3: Example formulation of a CA rule.

Within this example, we will show the effects of applying the same CA rules to the same initial configuration, but applying different neighbourhood definitions. Figure 13a) shows the application of the rules with the implementation of the Von Neumann neighbourhood and Figure 13b) with the Moore neighbourhood.

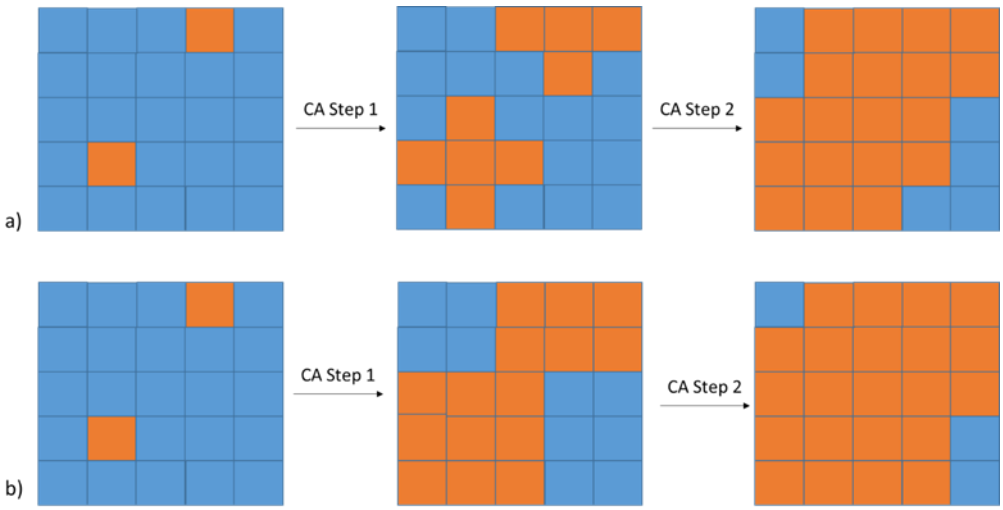

Figure 13: Example of a CA process with a) Von Neumann and b) Moore neighbourhoods.

As you can see the neighbourhood chosen has an obvious impact on how the CA model develops. Within the work of this thesis, the Moore neighbourhood will be implemented as it best represents the continuous surroundings experienced within solidification mechanisms. This is also demonstrated through an analytical comparison in the work by Rappaz and Gandin, (Rappaz & Gandin, 1993). The modelling techniques and transition rules used to replicate physical solidification mechanisms are explained below.

4.2 Nucleation Mechanisms

Solidification, within metals, takes place through nucleation and growth mechanisms. A detailed description of the background of solidification laws and mechanisms can be found in section 1.6. The rest of this chapter focuses on the modelling techniques used to replicate these solidification mechanisms. One of the first cellular automata grain growth models was developed by Rappaz and Gandin for the application of castings (Rappaz & Gandin, 1993), and many of the techniques presented herein have been developed from their seminal work. Firstly, the modelling mechanisms used to replicate physical nucleation processes will be examined. The following section will then describe the techniques employed to simulate grain growth.

Heterogeneous nucleation is modelled by Rappaz in his early work (Rappaz, 1989) where he presents a nucleation model, for the application of equiaxed casting. The model represents the rate of change in nucleation density as a function of the undercooling. In this paper, the author summarises why the previous model suggested by Turnbull and Fisher insufficiently represents the complexities of nucleation mechanisms and fails to predict grain size correctly. The main reason for the discrepancies in the Turnbull and Fisher method originates from the extremely rapid increase in nucleation density for a significantly small interval in undercooling.

Consequently, due to the discreteness of the distribution, the majority of nucleation sites would be initiated within the same increment. The work presented by Rappaz proposed a new nucleation model that more accurately represented physical nucleation mechanisms. The work utilised the theory suggested by Oldfield and has been widely accepted as well as implemented successfully within the large majority of cellular automata microstructure models. Within the model, nucleation probability is described as a Gaussian distribution. Figure 14 shows diagrammatic representations of the nucleation model proposed.

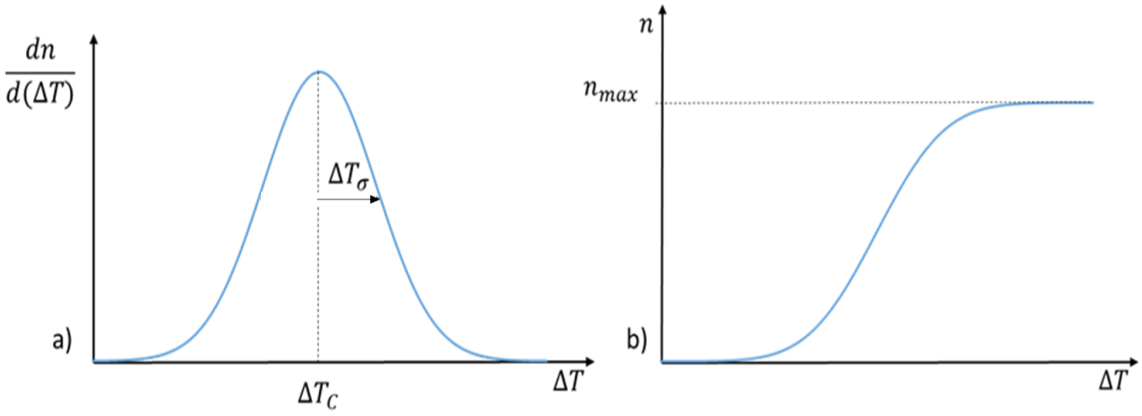

Figure 14: Gaussian nucleation model (Rappaz, 1989).

Figure 14a) represents the rate of change in nucleation density as a function of undercooling. It assumes a Gaussian distribution where ΔT_C represents the critical undercooling, the mean of the distribution, and ΔT_σ the standard deviation of the distribution. The same model is shown in Figure 14b) as a cumulative distribution, where n_{max} is the maximum grain density of the material. The 3 parameters ($\Delta T_C, \Delta T_\sigma, n_{max}$), can be determined experimentally. The model can be adjusted to account for different sites of nucleation by assigning two different nucleation models with different parameters to allow for the difference in critical undercooling required for a nucleus to form in the bulk liquid or the mould wall (Rappaz & Gandin, 1993). This is more appropriate for casting applications, but less so for additive techniques and hence only a single distribution will be modelled in this work. This is common in other cellular automata models for additive manufacturing. It is a reasonable assumption as there is no mould wall within additive manufacturing applications and other rules are applied to account for epitaxial growth from existing crystal material, as can be seen in Section 4.3.

The modelling approach described above can be implemented within the cellular automata through a number of different mechanisms. The first is by calculating the change in nucleation density that occurs as a result of undercooling for each time increment and then distributing the required number of nucleation sites within the domain. This method is implemented by (Zinovieva, et al., 2015; Zhan, et al., 2018). However, it poses issues within processes such

as additive manufacturing where a non-uniform thermal profile is experienced. This is because, at any given time the molten region is moving or changing profile and a different degree of undercooling is seen throughout, making it difficult to determine an exact value of nucleation density throughout the domain. In order to resolve this problem another method is employed within papers such as (Lopez-Botello, et al., 2017; Lian, et al., 2019 ; Li & Tan, 2018). This technique involves prescribing a probabilistic undercooling to a number of cells at the start of the analysis.

The latter method of applying the nucleation model was applied within this work. At the start of each analysis each cell is given a value of probabilistic undercooling. Once the undercooling of the cell exceeds this value, the cell is nucleated. An initial approach was implemented whereby every cell within the CA domain was assigned a probabilistic undercooling from the Gaussian distribution at the beginning of the analysis or whenever a cell became liquid. However, this method is not physically representative of the nucleation density as the density becomes dependent on mesh size. As a consequence of this, this method introduces a degree of mesh dependency into the model. For this reason, other methods were considered, throughout the course of this project, which were physically representative of the experimentally determined nucleation density. In order to do this the required number of nucleation sites was calculated at the start of the analysis. The sites were then assigned randomly among the CA cells within the domain. Each nucleation site was prescribed a random probabilistic undercooling from the Gaussian distribution as before. However, all cells which were not a nucleation site were assigned artificially large probabilistic undercooling values to prevent them from nucleating within the analysis.

Within additive manufacturing, there is a common assumption made within solidification models that nucleation does not occur within the melt pool during these processes. This assumption has been made in a large number of papers (Akram, et al., 2018; Chen, et al., 2016; Zinoviev, et al., 2016). Zinoviev et al. explain the reasoning behind this assumption, by arguing that due to the large thermal gradients, experienced in additive manufacturing, epitaxial growth from existing grain structures will occur before a high enough degree of undercooling is reached to initiate bulk nucleation. However, Li and Tan investigated the effects of bulk nucleation in such models and found it can have a large effect (Li & Tan, 2018). Whilst there is an obvious influence on the final microstructure, the comparison to experimental processes is less clear, whilst highlighting there is a strong need for calibration of nucleation parameters against experimental results. Within the earlier parts of this work we will undertake the assumption that nucleation does not occur within the melt pool. In later studies the inclusion of nucleation and necessary nucleation densities are investigated.

4.3 Solidification and Growth Techniques

Once a nucleus has been generated within the molten region, growth mechanisms then determine the development and expansion of the grain. In order to replicate solidification mechanisms within cellular automata grain growth models, Rappaz and Gandin developed the growth envelope mechanism (Rappaz & Gandin, 1993). This involves assigning an intrinsic shape, representative of the materials crystal structure, to each growing cell. For example, within this work we will focus primarily on FCC crystals which can be represented by a regular octahedron in 3D or a square in 2D, the 2D projection of an octahedron. The geometry is used to model the development of the envelope, or convex hull, formed by the dendrite tips within the crystal. Once the centre of a liquid cell falls within the growth envelope of a neighbouring growing cell, the cell is captured and becomes part of the growing crystal. A growth envelope is then associated with the captured grain to ensure the continued development of the crystal. To explain the concept behind the growth envelope, we will first discuss the most simple 2D case available and then discuss adaptations that have been made in order to make the method more physically representative.

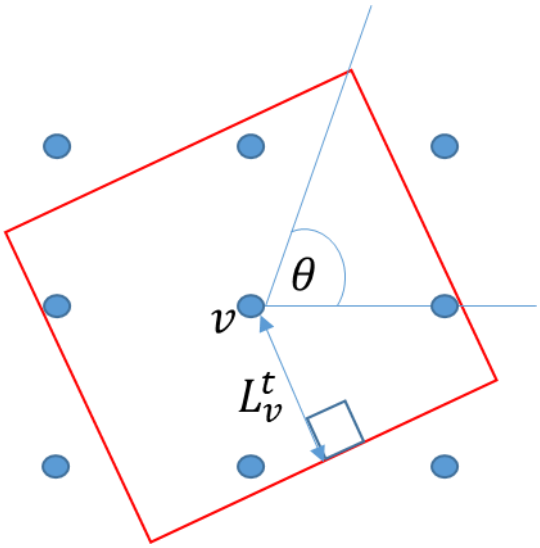

Figure 15: Example of centred 2D grain capture.

For 2D applications, the growth envelope is represented by a square, as this is the 2D projection of an octahedron (FCC crystals) or cube (BCC crystals), as mentioned previously. The square is geometrically defined by two parameters; orientation and size, seen in Figure 15. In 2D, orientation can be described by a single angle, θ, in the range $0 < \theta \leq \frac{\pi}{2}$, due to the

quarter symmetry of the geometry (Rappaz & Gandin, 1993). This defines the preferential growth directions of the crystal. The size of the shape is defined using the kinetic growth laws given by Kurz, Giovanni and Trevdi (Kurz, et al., 1986). As shown in Equation 16, the envelope size can be determined from the integral of the dendrite growth velocity, with respect to time, from the time of nucleation to the current time. Here, L_v^t represents the envelope size at time t as shown in Figure 15, t_n is the time of nucleation and v is the dendrite growth velocity. Dendrite growth velocity is given as a function of the local undercooling. This function is often approximated by a polynomial function. This can be seen in a number of works using third order polynomials (Lian, et al., 2019 ; Li & Tan, 2018; Yang, et al., 2018). Rappaz and Gandin (Gandin, et al., 1996) use the approximation $v = A \cdot \Delta T^2$, where $A = 10^{-4}\left(\frac{m}{sK^2}\right)$, this representation has been successfully used within other works (Rai, et al., 2016; Koepf, et al., 2019) and will be used here.

$$L_v^t = \frac{1}{\sqrt{2}} \int_{t_n}^{t} v[\Delta T_v(\tau)]\ d\tau$$

Equation 16: Grain growth kinetics in 2D (Gandin & Rappaz, 1997).

In 3D, the same principles can be applied, only in this case the envelope is represented by the full 3D geometry (Figure 16). For the case of an FCC grain this would be an octahedron. In order to specify this geometry a total of 4 parameters must be given. These describe the size and orientation of the geometry, as before, however in 3D three Euler angles must be specified in order to fully define the crystal orientation.

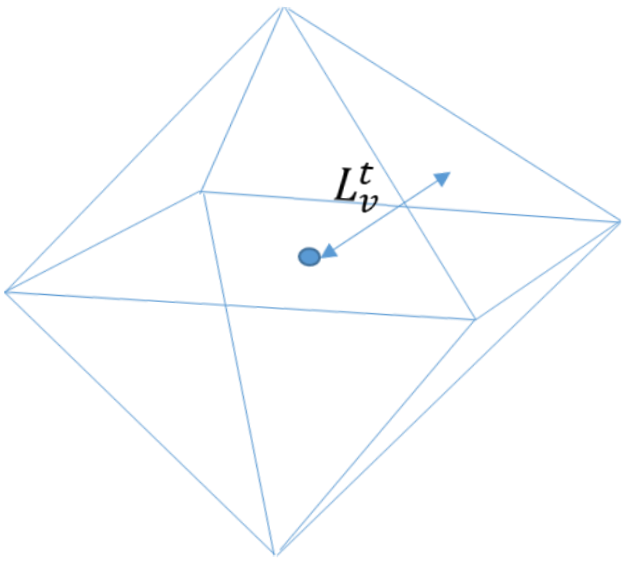

Figure 16: Example of 3D octahedral growth envelope.

Euler angles are used commonly throughout mathematical and engineering disciplines. They describe a composition of three rotations $(\theta, \varphi_1, \varphi_2)$ that uniquely describe a 3D orientation. Within this work the Bunge convention is used to describe the Euler angles, as it is a common definition that is also used within software to produce inverse pole figures from angle data. This convention is described within the work of H.-J. Bunge (Bunge, 1982). This convention dictates that the 3 rotations consist of a rotation of φ_1 about the z- axis, followed by a rotation of θ about the new x-axis and finally a rotation of φ_2 about the rotated z- axis. Here φ_1 and φ_2 are in the interval $0 < \varphi_1, \varphi_2 \leq 2\pi$, whilst θ is limited by 0 and π, $0 < \theta \leq \pi$. A visual representation of these three rotations can be seen in Figure 17.

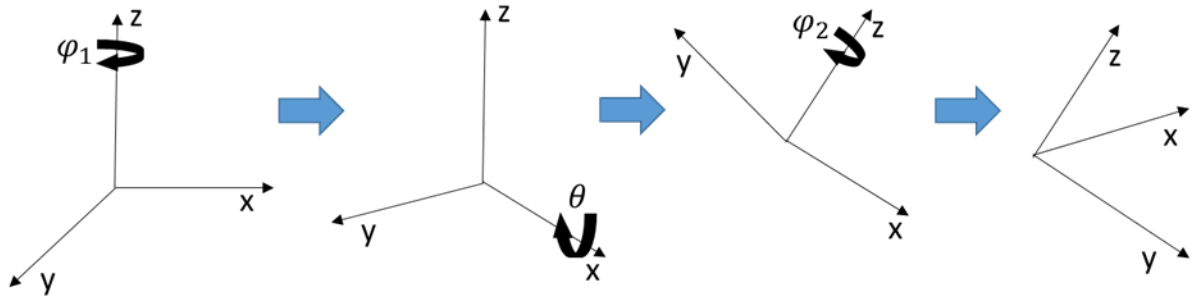

Figure 17: Bunge Euler angle convention (AZO Materials, 2015).

The size of the envelope is defined in a similar fashion to that of the 2D geometry, using the kinetic growth laws. This is shown in Equation 17, where L_v^t represents the normal distance from the octahedron to each face (Figure 16).

$$L_v^t = \frac{1}{\sqrt{3}} \int_{t_n}^{t} v[\Delta T_v(\tau)] \, d\tau$$

Equation 17: Grain growth kinetics in 3D (Gandin & Rappaz, 1997).

Whilst the work shown by Rappaz and Gandin et al. shows the successful implementation of the initial 2D methods, there are still a number of discrepancies within the model. A number of considerations have been made within the seminal work of Rappaz and Gandin, in order to adjust the physical accuracy of the modelling approach. This includes evaluation of neighbourhood effectiveness as well as a dendrite tip correction. Their most recent modelling approach, presented in 1997, introduces a decentred grain growth algorithm (Gandin & Rappaz, 1997). In initial approaches, the growth envelope associated with a newly captured cell was the same as that of the capturing cell, only continued growth calculations were undertaken using the new undercooling values associated with the captured cell. The decentred method presented here calculates a new growth centre for each captured cell in

order to more accurately represent the crystal shape and reduce mesh anisotropy. Figure 18 represents how the calculations for each cell capture are undertaken.

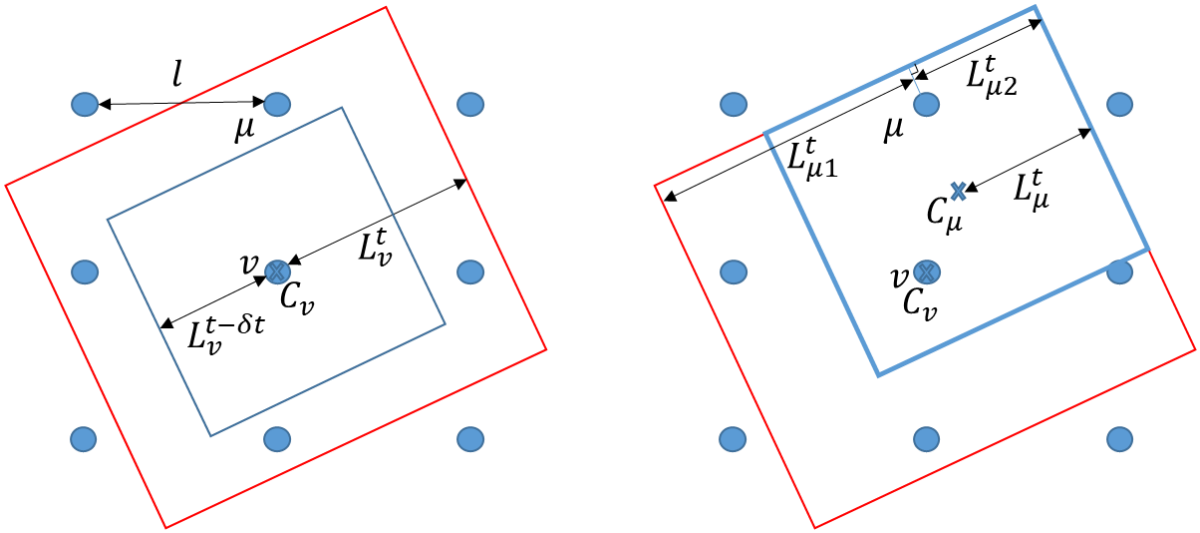

Figure 18: Decentred growth algorithm (2D) (Gandin & Rappaz, 1997).

We consider a cell, v, which has been nucleated within the molten region. Upon nucleation the growth envelope is activated. As the cell has been nucleated independently, the growth centre, ie. the geometric centre of the prescribed shape, is coincident to the cell centre. After a certain amount of time, t, the growth envelope reaches a size of L_v^t and a neighbouring cell, μ, is captured within the envelope and changed to a growing cell. In order to be able to continue with the calculations of the growth algorithm, we then need to know the growth envelope associated with μ. This requires an orientation, size and centre. Orientation, as before, is obtained from the capturing cell. The centre and size must be calculated as below.

Firstly, the capturing face of the envelope is identified. This can be determined reasonably easily by dividing the square diagonally into quadrants or by identifying the face with the smallest normal distance to the cell centre. Once this has been determined, the two distances that are obtained by dividing this edge by the normal to the captured cell centre (Figure 18) are calculated, $L_{\mu 1}^t$ and $L_{\mu 2}^t$. The values are used to determine the size of the growth envelope associated with μ using Equation 18. Here, L_μ^t is the size of the growth envelope associated with μ at time t, whilst l represents the cell spacing.

$$L_\mu^t = \frac{1}{2}\left[Min\left(L_{\mu 1}^t, \sqrt{2}\cdot l\right) + Min\left(L_{\mu 2}^t, \sqrt{2}\cdot l\right)\right]$$

Equation 18: Decentred growth envelope size calculation.

The final parameter required to define the envelope is the growth centre. This is determined by defining a square of side length $2L_\mu^t$, with the same orientation as the capturing envelope,

such that the corner of this envelope is coincident to the nearest corner of the capturing envelope. A diagrammatic representation of this can be seen in Figure 18. The centre of this square delimits the growth centre associated with μ, L_{μ}^{t} denotes the initial envelope size and additional growth can be calculated, as before, using Equation 16.

The same decentring can be applied to the 3D octahedral envelope. The growth centre of the captured cell can be calculated in a very similar manner. A detailed algorithm of the calculations required can be found in the original work (Gandin & Rappaz, 1997).

Whilst the 2D model is efficient and reasonably representative of the in plane crystallographic morphology, it does make the assumption that all grains are growing perpendicular to the plane in consideration. This is due to the fact that whilst a square is the 2D projection of an octahedron, it is only achieved as an intersection of a plane and an octahedron along the central axis of the octahedron. If an octahedron is intersected along any plane, that is not one of the 3 principal planes, a hexagon is obtained. Therefore, within this work a code for a 2.5D model considering only the 8 in plane neighbours, but utilising the 3D growth envelope was tested, as well as the a code for the 3D model. However both the 2.5D and 3D models proved to be too computationally expensive and will not be used any further within this work.

4.4 CA Algorithm

In order to simulate the nucleation and growth mechanisms presented in the previous sections state variables and algorithmic rules representative of the underlying modelling theory must be used. Firstly, two main state variables are assigned to each cell; physical state, I, and grain orientation, θ (or $\theta, \varphi_1, \varphi_2$ in the 3D model). The physical state monitors the state of each cell. This is achieved by assigning a different value depending on the state of the material. Namely, a value of 0 defines the cell as liquid, 2 a solid cell and 1 a growing cell. For the case of additive manufacturing we also require a value that assumes a cell is inactive and not to be take into account within the simulation. That is a cell that exists within the computational domain but has not yet been deposited within the additive process. In finite element models, this can be achieved through the implementation of element birth and death techniques. However, for a CA analysis we require details regarding the neighbours of each element. For this reason, as well as other meshing limitations described later, it is easier to establish a fixed domain within the simulation. Therefore, in these CA simulations, material deposition is modelled by assigning a physical state value of -2 to any inactive material, ie. material that has not yet be deposited. Furthermore, for processes involving a static powder bed, eg. L-PBF, powder materials are given a physical state of -1. Grain orientation is a state variable that stores the angles assigned with the grain envelope. In 2D, a single array is used to store the θ value assigned to the square envelope. However, in 3D three separate arrays are used to store the

three Euler angles of the octahedral envelope. The grain orientation variable is also used to determine which cells belong to the same grain. Any neighbouring cells with the same grain orientation are assumed to be part of the same grain. This is a reasonable assumption because, due to the randomness in orientation assignment, it is probabilistically unlikely that any two cells that have nucleated separately or captured from different growing grains would have identical grain orientations.

The state variables are then updated according to a number of rules that represent the nucleation and growth modelling techniques. There are five main rules within the CA algorithm that can be seen in a mathematical formulation within Table 4. These do not include any mechanisms with regards to inactive or powder material. These will be discussed separately further on in the work. The main rules presented here are based on those seen in the work presented by Chen et al. (Chen, et al., 2016). Within the formulation seen below, v represents the cell for which the calculations are taking place and μ a cell within the neighbourhood of that cell, Ω_v. Furthermore, I_v and θ_v are the physical state and grain orientation of cell v respectively. Similarly, T_v represents the current temperature at the cell, ΔT_v the current undercooling and ΔT_{pu} the probabilistic undercooling assigned to that cell. Finally, the growth envelope of cell v, described in Section 4.3, is given here by A_v.

Rule	Initial State	Final State	Condition
M1	$I_v \neq 0$	$I_v = 0, \theta_v = 0$	$T_v \geq T_{liq}$
M2	$I_v = 2$	$I_v = 1$	$\exists\, \mu \in \Omega_v\ s.t.\ I_\mu = 0$
N1	$I_v = 0,\ \theta_v = 0$	$I_v = 1$ $\theta_v = \theta_{rand}$ & A_v initiated	$\Delta T_v \geq \Delta T_{pu}$
S1	$I_v = 0,\ \theta_v = 0$	$I_v = 1$ $\theta_v = \theta_\mu$ & A_v initiated	$\exists\, \mu \in \Omega_v\ s.t.\ v \in A_\mu$
S2	$I_v = 1$	$I_v = 2$	$\nexists\, \mu \in \Omega_v\ s.t.\ I_\mu = 0$

Table 4: CA algorithm rules.

The first two rules presented within Table 4 describe the methods of melting within the algorithm, hence the nomenclature M1 and M2. The first of these rules represents the physical state change experienced by the metal when liquidus temperature is obtained. The rule specifies that any cell that is not already liquid, becomes liquid upon reaching or surpassing the liquidus temperature. The second melting rule then states that if any solid cell obtains a liquid neighbour, the cell becomes growing as it now has a neighbouring liquid region into which it could grow. This is the key rule that allows for epitaxial growth from existing grains. Following this, there is a nucleation rule that works by initiating growth within any cell that surpasses the probabilistic undercooling assigned to it at the start of the analysis. Upon

nucleation the cell is given a random grain orientation and the grain envelope is initiated. For the 2D implementation this is a value within the range $0 \leq \theta < \frac{\pi}{2}$, due to the four fold symmetry of the square envelope. In 3D, three random values are assigned to the three Euler angles described in Figure 17.

The final two rules in the model implement the solidification mechanisms. The latter of these rules ensures the termination of a growing cell, by specifying that any growing cell with no liquid neighbours becomes a fully solid cell. Grain capture using the grain growth envelope technique is implemented through S1. This rule states that if a liquid cell falls within the growth envelope of a neighbouring cell then the cell is caught. Grain envelopes are defined geometrically within the model and Equation 16 is used to determine the grain size. However, since the analysis is undertaken in discrete steps, the integral must also be discretised. Therefore, the current envelope size, L_t, is determined as follows. Equation 19 represents the discretisation of the 2D equation for a time increment of length δt from t-δt to t. The same can also be applied to the 3D equation.

$$L_t = L_{t-\delta t} + \frac{1}{\sqrt{2}} v(\Delta T_{t-\delta t}) \cdot \delta t$$

Equation 19: Discretised envelope size calculations.

Upon capture, the cell in consideration assumes the grain orientation for the cell it has been caught by, and the growth envelope for the captured cell is initiated. In the event that a cell is caught by multiple cells within the same time increment a number of approaches can be undertaken. Lopez-Botello et al. implemented a random selection (Lopez-Botello, et al., 2017), whilst Rai et al. compared the difference between three mechanisms, including selection by greatest undercooling and selection based on iteration order, and showed minimal difference in results (Rai, et al., 2016). Within this work a random selection between any capturing grains were assigned. Due to the small size of time increment used throughout the model, this is a reasonable approximation to make. Furthermore, within some CA work, boundary conditions are applied to the edges of the domain (Rappaz & Gandin, 1993; Yang, et al., 2018). Boundary conditions within the CA model are not applied within this work.

In order to model material deposition within the CA models, material can be assigned with an inactive physical state. As previously mentioned, this ensures that these cells are not taken into account within any of the CA calculations, until a time when the cell becomes active. The cells can be activated by assigning an alternative state value within the program to cells on a time or temperature basis. For example, within an L-PBF simulation like the one shown in Chapter 7, material is deposited in layers of powder. Therefore, prior to the deposition of any

powder layers, the corresponding cells are all prescribed an inactive cell state, $I = -2$. Then each subsequent layer is deposited individually according to the appropriate recoat times within the scan strategy. This is achieved by changing the physical state from inactive to powder (-2 to -1) based on a function of time and position. For direct energy deposition methods where material is deposited in a molten state continuously, within a layer, it is less feasible to activate material as a function of time and position. Therefore, is it suggested here that within DED simulations material is activated as a function of temperature. The algorithmic formulation of this can be seen in Table 5.

Rule	Initial State	Final State	Condition
A1	$I_v = -2$	$I_v = 0, \theta_v = 0$	$T_v \geq T_{liq}$

Table 5: CA rule defining temperature-based material activation within DED methods.

The algorithm implemented within microstructure code can be seen as a flow chart in Figure 19. It begins with the assignment of probabilistic undercoolings at the start of the analysis and then shows the various decision loops that are undertaken within each time increment, at each element, to implement the various rules that have been detailed within this section.

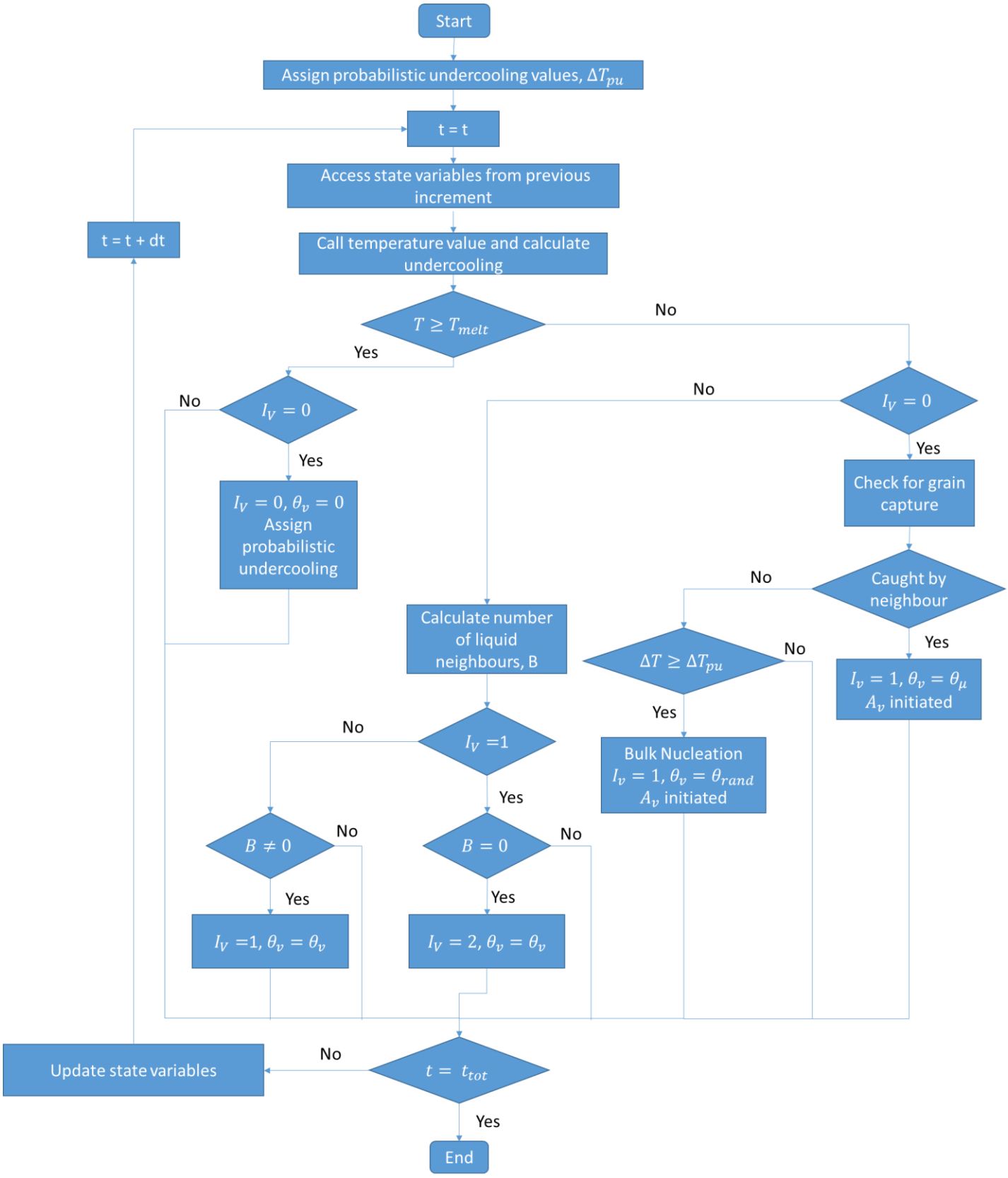

Figure 19: Decision tree representation of the basic CA algorithm occurring within each element.

4.5 Implementation within Abaqus

The algorithm, described in Section 4.4, is implemented through the use of Fortran subroutines with Abaqus standard. Abaqus is a useful tool to use for the implementation of the cellular automata model due to the elemental nature of the software. Firstly, due to the finite element methods employed within the software, calculations are undertaken at each element before moving to the next time increment. This is the same mechanism required within the CA algorithm. In addition, calculations are undertaken independently at each element. More importantly, by using Abaqus to carry out the CA calculations, this makes the coupling between the finite element thermal model and microstructure model easier to implement, as the thermal history can be imported directly from the thermal analysis undertaken in Abaqus. Linear interpolation is also automatically applied within the CA model to determine the temperature at each integration point.

Within this work a weak coupling has been used between the finite element thermal and cellular automata microstructure models. This means that the microstructural developments explained in Section 1.6, such as solute concentrations, are not accounted for within the thermal analysis. Strong coupling approaches, whereby microstructural calculations are fed back into the thermal calculations can be seen in works such as (Zhang, et al., 2018) and a detailed explanation can be found in (Gandin & Rappaz, 1994). These models involve curvature calculations based on solid fractions as well as the constitutional effects on undercooling and more realistically represent all of the physical mechanisms involved within the solidification mechanisms described earlier (section 1.6).

However, weakly coupled models have also been used in a number of works and offer the benefit of a simpler and more computationally efficient model, whilst still providing successful predictions of microstructural features. Computational efficiency of the model is important when trying to simulate larger domains, such as the full build, in an efficient manner, particularly at a design level and is part of the reason the CA approach was chosen. The assumption made here means that the undercooling of each cell is determined as the difference between liquidus temperature and current temperature, calculated on a continuum scale as in Equation 20.

$$\Delta T = T_L - T$$

Equation 20: Undercooling calculations used within weakly coupled models.

Whilst the fully-coupled approach is the most physically accurate, a weak coupling is a reasonable assumption to make due to the large thermal gradients within the additive manufacturing process. Rappaz et al. state that a “semicoupling” can be used, where the

thermal field is pre-calculated, when thermal gradients are particularly large (Rappaz, et al., 1996) and present such a weak coupling approach in their following work (Gandin, et al., 1999). The use of a weak coupling also makes the modelling approach simpler to implement and more computationally efficient. This coupling approach is also seen within the work by Koepf et al. and their implementation of a more computationally efficient model (Koepf, et al., 2019) among others (Rai, et al., 2016; Lian, et al., 2019 ; Lopez-Botello, et al., 2017).

The weak coupling approach means that the thermal analysis and microstructure analysis are undertaken sequentially. Following the completion of the thermal analysis, the microstructure model is implemented within a static, implicit general step in Abaqus. Although this type of procedure is typically used for linear elastic stress problems, the use of this procedure here allows for the prescription of the thermal history as a predefined field. A smaller domain is normally used within the CA model, by using Abaqus the in-built interpolation and mapping capabilities can be used to interpolate the thermal field from the coarse thermal mesh onto the finer CA mesh. Typically this is a 2D cross section of the region of interest, however other domains can be modelled with the application of the 3D algorithm. 3D elements are used within the model regardless of whether the CA algorithm is 2D or 3D, as this allows for the correct interpolation of the 3D thermal field. Reduced integration, 8-node linear stress elements are used. Reduced integration is necessary for the simulation as they have a single central integration point at which all the state variables can be calculated and updated, Figure 20. This represents the centre of each cell within the CA grid. This is important because, as we will describe later, the subroutines used are called at every integration point, and therefore there needs to be a single integration point at the centre of each element in order for them to be used efficiently as CA cells.

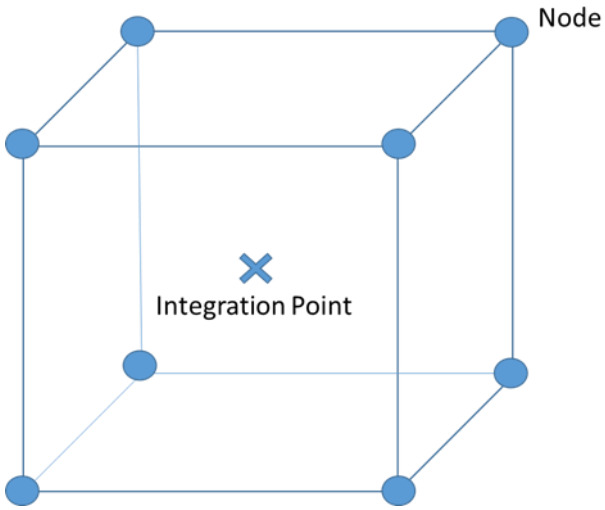

Figure 20: Visual representation of C3D8R elements.

In built meshing techniques, within Abaqus, can also be utilised to prescribe a uniform grid of cells to the domain. Subsequently, Python scripts can be used to determine the neighbourhood for each element. However, throughout this work the mesh has been generated manually in order to determine the relevant neighbourhood of cells more efficiently. In other words, the meshing module within Abaqus/CAE was not used. Instead, by generating the mesh algorithmically, it was possible to uniquely identify the neighbours of each element based on a consistent element numbering strategy. This way the neighbours of each cell can be determined within the calculation of the mesh and stored within a data file. This approach also ensures a more methodical approach to the elemental/cellular numbering than that automatically assigned within Abaqus itself. Data files can then be read into the Fortran subroutines and stored as an array, ensuring the information is easily accessible for every element throughout the calculations.

User subroutines are implemented to carry out the actual calculation required within the CA model. A combination of a USDFLD and a UEXTERNALDB subroutine are implemented with access to a module. The USDFLD subroutine is used to perform the calculations required for the cellular automata algorithm at the centre of each element, whilst the UEXTERNALDB is used to store and update all the required data through the use of arrays. Meanwhile the module allows global access to array data between the two subroutines.

A USDLFD is a subroutine commonly used to allow the definition of a user defined field. It allows for the creation and calculation of field variables and state variables. State variables can be updated, stored and output within the Output Database (odb) file. Field variables are very similar, but can also be used within the analysis to determine a change in the analysis, such as field-dependent material properties. The field and state variables within this subroutine are used to output the variables within the CA algorithm to an odb file so they can be visualised throughout the time step. The subroutine is called for each integration point of each element (in this instance once, due to the choice of element type) for each time increment. There are two other features of the USDFLD that have also been exploited within this model, the ability to access material point data and the ability to specify a new value of time incrementation. The first of these features is used to access the temperature values at the integration point, at each time increment. This is achieved through the use of the utility subroutine GETVRM. Time incrementation can be dictated (Gandin, et al., 1999) through the variable PNEWDT, this is utilised to allow for automatic incrementation within the model. We can then update time incrementation based on mesh size and growth velocity through the use of an identity, such as the one in Equation 21, where α is a scaling factor and l the cell spacing. Similar approaches to automatic incrementation can be seen in a number of papers including within

the work by Gandin et al. (Gandin, et al., 1999) among others (Koepf, et al., 2019; Zinoviev, et al., 2016) .

$$\delta T = \alpha \frac{l}{v(\Delta T)_{max}}$$

Equation 21: Automatic time incrementation.

A UEXTERNALDB is an external database subroutine, its primary purpose is for the storage of arrays that can be accessed in other subroutines, such as the USDLFD. In this case it is used to store arrays of variables and attributes required to be able to carry out the cellular automata algorithm. The subroutine is called at the start and end of the analysis and also at the start and end of each increment. This feature allows us to update all the relevant array values at the end of each increment prior to the analysis in the next time increment. The use of the different subroutines and coupling approach is demonstrated in the flow chart in Figure 21. Within the diagram E represents the element being considered, with E_{tot} representing the total number of elements within the CA analysis and t_{tot} the total time of the microstructure simulation. More details on all of the Abaqus user subroutines can be found in the documentation (Dassault Systèmes, 2015). Within the development of these codes, geometric aspects were utilised from open source code (Burkardt, 2005).

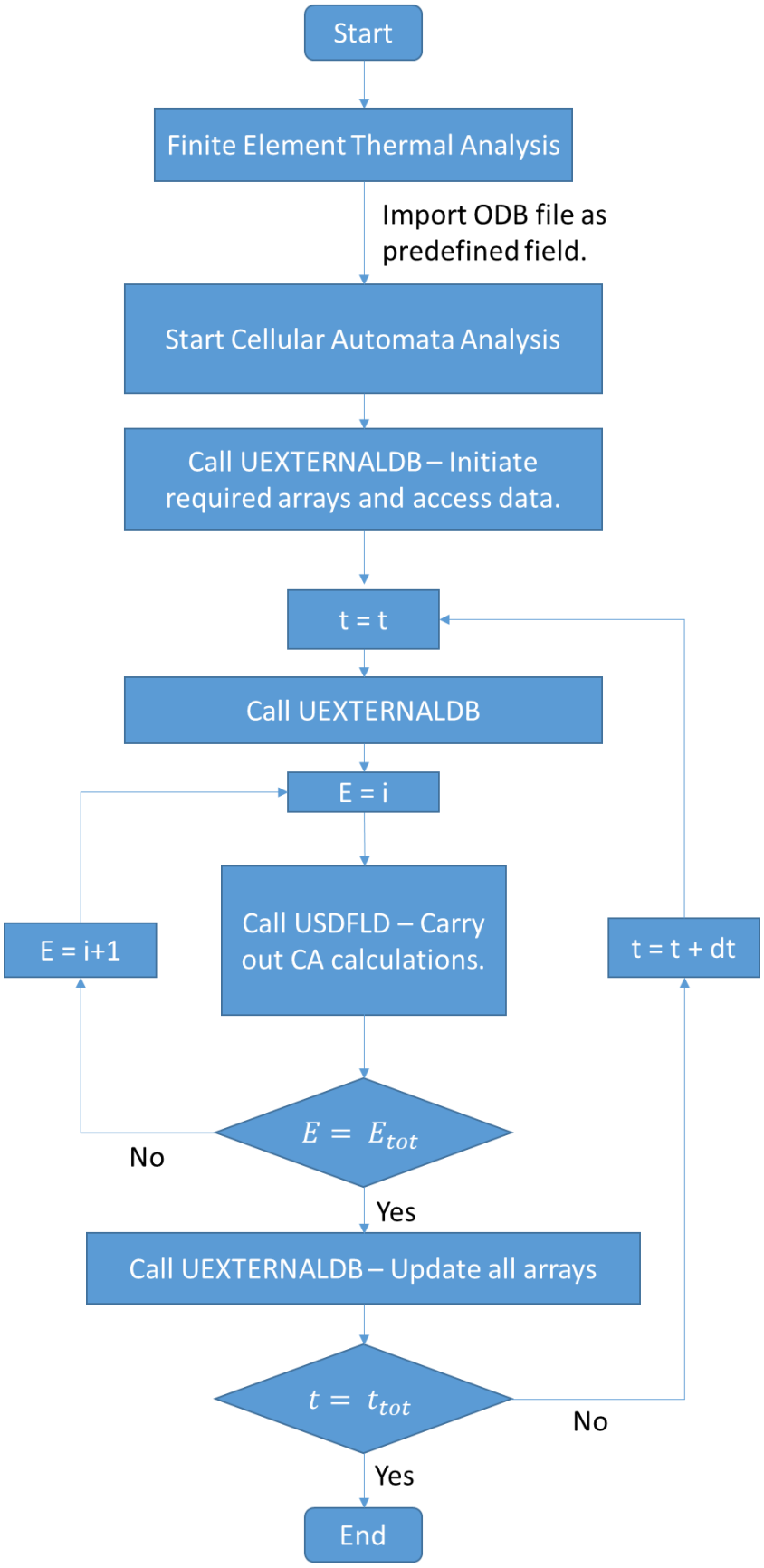

Figure 21: Flow chart of overall subroutine approach.

4.6 Analytical Verification

The implementation through Fortran subroutines, described above, has been developed within this work as open source code is unavailable. Therefore, in order to verify the code developed within this work, an analytical study was undertaken. Within the model, the 2D decentred growth envelope code was applied with a uniform thermal boundary condition. A single cell is assigned with a critical undercooling to allow nucleation of a single crystal. The nucleation, growth and capture mechanisms are then compared against hand calculations to ensure the Fortran subroutines are performing as expected.

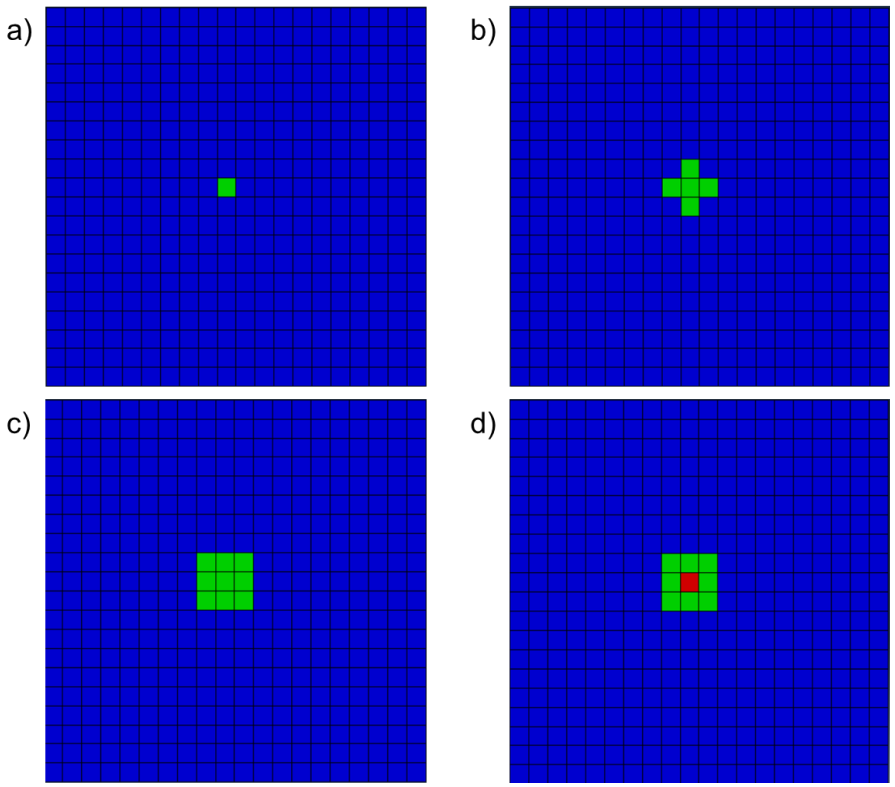

Figure 22: Initial stages of the growth of a single crystal within the CA code.

Within this study, the assumption made by Rappaz and Gandin regarding the growth kinetics were implemented. A cooling rate of 50°Cs^{-1} was imposed. Assuming the domain starts at liquidus, a critical undercooling of 5°C was applied to the nucleation cell with a grain orientation of 30°. Fixed incrementation of 0.01s was applied, to simulate the development of the grain growth. Hand calculations, using the same parameters, were undertaken as a comparison for the developed CA subroutines. The cell nucleated at the expected frame within the analysis, and neighbouring grains were captured within the growth envelope at the expected times. These initial steps can be seen in Figure 22. However, hand calculations become too complex beyond a certain point, so only the initial steps were involved within the analytical verification. An example of further growth beyond this point is shown in Figure 23.

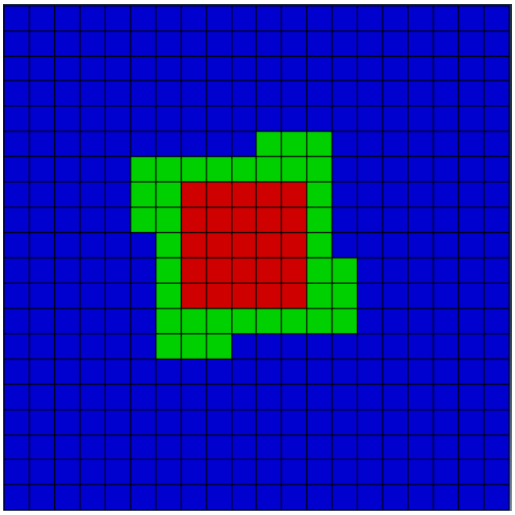

Figure 23: Growth development of a single crystal with a grain orientation of 30°.

4.7 Analysis and Comparison Methods

The CA model presented here gives predictions in the form of a visual representation of the grain structure. In order to be able to validate the capabilities of the model we need to be able to compare the simulated microstructure to experimental results both quantitatively and qualitatively. Qualitative comparisons are relatively easy to undertake as the results show a visual representation of the physical domain. Grains can be coloured by orientation within Abaqus or by a grain number attributed during post processing in MATLAB. This allows us to see the grain boundaries and draw visual conclusions about the morphology of the grains. However, unless a 3D simulation has been undertaken, comparisons that can be made regarding grain orientation are limited. Moreover, due to the finite number of colours available in either Abaqus or MATLAB, a bias of results can be introduced when two similarly orientated or neighbouring grains are assigned the same colour. This is part of the reason why quantitative measurements are an important feature of the analysis.

Quantitative comparisons are based around physical, numerical measurements of features such as average grain size. They allow us to see a numerical measure of how successful the model is. The traditional method of measuring grain size is through the linear intercept method presented in the ASTM standard for determining average grain size (ASTM International, 2013). This involves drawing a line, of length L, across the domain, where L should be long enough to encounter a minimum of 50 intercepts. It is then calculated how many grain boundaries are crossed by the line, each of these events is an intersection. The total number of these is represented by N_L. A numerical relation between the average value of N_L per mm and the ASTM grain size number, G, is then used to give us a value for the average grain size. Within the standard the relationship between G and grain area, A, is given via a tabulated set of values. In order to allow for a continuous set of data a function has been fitted to the set of

the data within Excel. This method of grain analysis is a simple yet effective approach to evaluating average grain size within a sample. However, it is only an accurate measurement for equiaxed structures, which is not a true representation for the grain structures witnessed within some of the additive manufacturing processes seen within this work.

Within the standard (ASTM International, 2013) it is noted that, for non-equiaxed grain structures, measurements should be undertaken in all principal directions and the average grain size estimated from these values. This could still be insufficient for the grain structures experienced within AM, as this would only allow us to determine the average grain size along a given axis and not for the overall plane of material. For example, for the simulation of a single melt pool (as will be seen in Chapter 5) due to the thermal processing, grains are often orientated to the centre of the melt pool as this is the direction of the thermal gradient, Figure 24 . Consequently, there is no one principal direction that would give an overall representation of the average grain size within the melt pool.

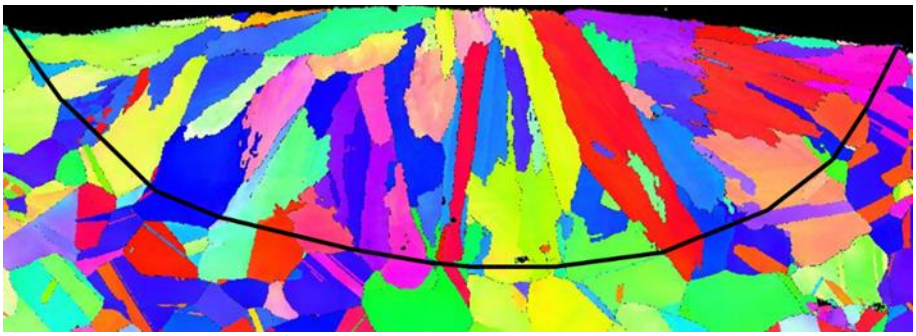

Figure 24: Example grain structure experienced within an AM melt pool (National Institute of Standards and Technology, 2018).

For this reason, alternative methods of quantitative measurements have been implemented within some of the studies undertaken as part of this project. The alternative method involves post processing of the grain structures within MATLAB. Data can easily be extracted from the Abaqus odb file, using a Python script, and imported into MATLAB. Once in MATLAB, an open source function is implemented to fit each grain with a minimum bounding ellipse (Moshtagh, 2005). Examples can be seen within Figure 25. The area, length and width of the minimum bounding ellipse can then be determined and used to give a close approximation of the grain dimensions, irrelevant of orientation or size. Using this method, the length and width can also be used to determine the aspect ratio associated with the grain. The aspect ratio is given by length of the minor axis divided by length of the major axis. This is useful as it provides us with a numerical value associated to the morphology of the grains. For example a grain with an aspect ratio of 1 is perfectly circular and therefore equiaxed. Meanwhile, a columnar grain

would have a much greater length than width and therefore a much smaller aspect ratio would be witnessed.

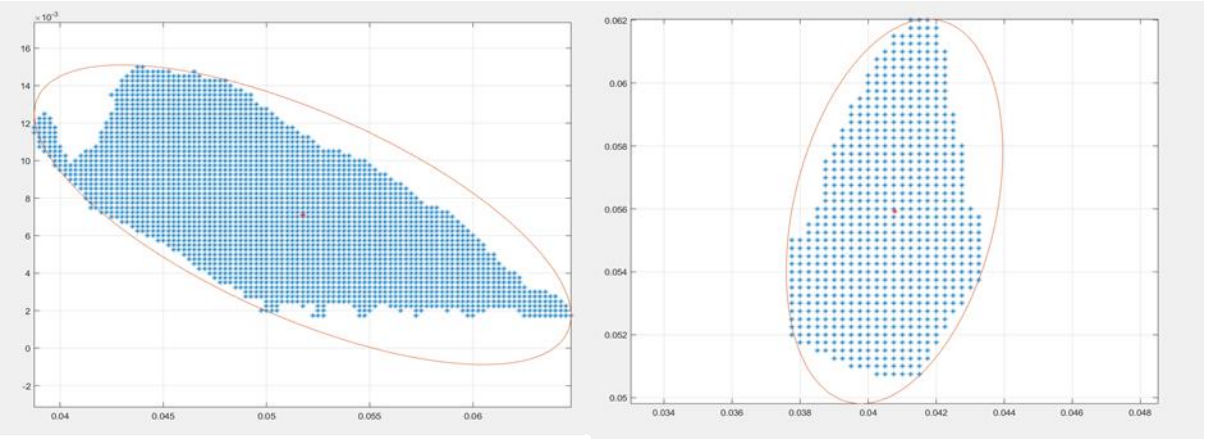

Figure 25: Examples of minimum bounding ellipse fitting.

A comparative study between the linear intercept method and minimum bounding ellipse approach has been undertaken in order to discuss the differences and effectiveness of each technique. This has been done on both experimental microstructures and simulated microstructures.

Three experimental EBSDs were generated from 316L substrate material, an example of one of these can be seen in Figure 26. The microstructure was analysed using both the linear intercept method and minimum bounding ellipse method. Firstly, MTEX was used to extra pixel locations, calculate grain IDs and fill in some of the unindexed data with the EBSD. Once the required data was extracted, the linear intercept method and minimum bounding ellipse approach described above were applied, ignoring any remaining unindexed data. Within the linear intercept method, 500 random lines were applied to each EBSD. The comparison between the methods can be seen in Table 6.

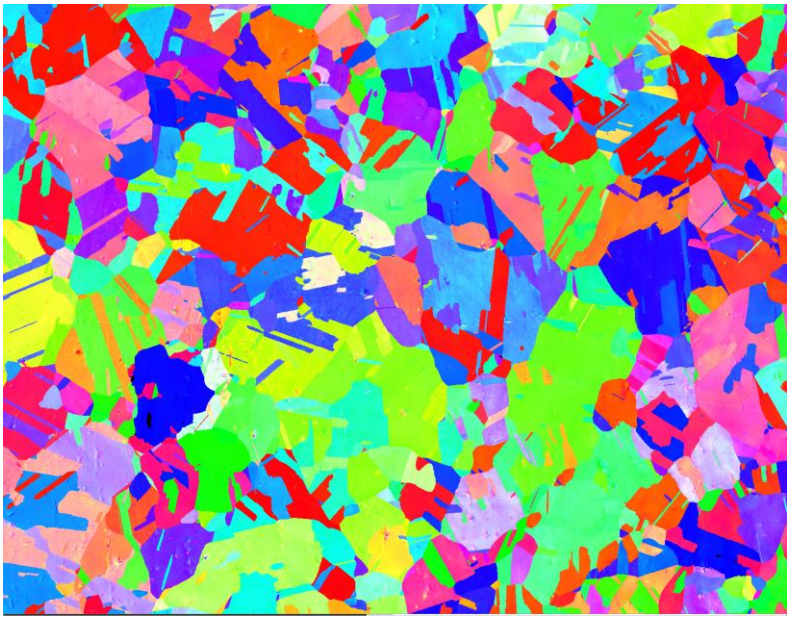

Figure 26: Experimental EBSD of substrate material for grain analysis.

	Linear Intercept			Minimum Bounding Ellipse			
EBSD #	**G**	**A (μm^2)**	**D (μm)**	**Ellipse Area (μm^2)**	**L (μm)**	**W (μm)**	**Aspect Ratio**
1	8.96	258.52	16.02	1100.82	57.53	16.97	0.429
2	9.11	233.83	15.24	1112.08	35.93	15.73	0.414
3	8.87	275.95	16.55	1228.434	40.70	18.70	0.440

Table 6: Comparison of linear intercept and minimum bounding ellipse analysis methods on experimental microstructures.

This study was also undertaken on three numerically simulated, reasonably equiaxed substrates of varying grain size. For the linear intercept approach, a total of 65 random lines were imposed onto the substrate and extended to reach the limits of the domain. The number of lines was chosen after witnessing approximately how many lines it took for the average grain area measurements to stabilise/converge. The results of the comparison of methods for the simulated microstructures can be seen in Table 7.

		Linear Intercept				Minimum Bounding Ellipse			
#	**Cell Area (μm^2)**	**G**	**N_L (mm^{-1})**	**Area (μm^2)**	**D (μm)**	**Ellipse Area (μm^2)**	**L (μm)**	**W (μm)**	**Aspect Ratio**
1	1109.84	7.753	45.892	598.84	24.40	1656.82	48.991	33.274	0.6704
2	1634.91	7.377	40.287	777.03	27.80	2536.32	61.574	40.085	0.6382
3	2309.02	6.802	33.007	1157.53	33.94	3581.09	73.628	48.926	0.6539

Table 7: Comparison of linear intercept and minimum bounding ellipse analysis methods on simulated microstructures.

This comparison allows us to consider the differences between the two results. Within the experimental comparisons, the grain width calculated by the minimum bounding ellipse is very similar to the diameter determined using linear intercept methods. However, the grain area and length (comparable again to the grain diameter assuming reasonably equiaxed grains) are largely overestimated. This is similar to that seen in the simulated microstructures, where the grain area and length are much larger than those calculated via linear intercept methods. Whilst the width is closer in value to the grain diameter, it is still larger. However, within this comparison we were also able to compare cell area. This is calculated by multiplying the number of pixels within a grain by the area of an individual pixel, as such this can be considered the most accurate measure of grain area for the simulate microstructures. In the comparison of methods here it is clear that the linear intercept method consistently underestimates this value whilst the ellipse method overestimates it by a similar amount. Over estimation of the are a is expected form the minimum bounding ellipse approach, as by nature the ellipse contains regions of empty space, as can be seen in Figure 25.

From this exercise we can conclude that both methods give different estimations of grain features such as grain diameter or length. However, while the two methods differ in area estimations, they both give a similar level of accuracy when compared to cell area. Despite the variation in estimations, within this work we will be using the minimum bounding ellipse as it can be applied to non-equiaxed structures, such as those seen within the additive manufacturing process where columnar anisotropic grain structures are seen. Furthermore, it is highlighted that the same measurement process, ie. the minimum bounding ellipse method, will be undertaken on both experimental and simulated microstructures within subsequent case studies, so that the quantitative measurements can be compared like for like between the experimental results and predicted microstructures.

5 AMB2018-02 Validation Study

This chapter presents a case study using open source experimental results, that have been made publically available as part of the National Institute of Standards and Technology (NIST) AM Benchmark 2018, as validation data. The main aim of this study was to validate the overall modelling technique for a reasonably simple experimental set up. All of the experimental details were described thoroughly as part of the benchmark (National Institute of Standards and Technology, 2018) and an overview of these can be found below. Following this the thermal modelling approach will be discussed before looking at the use of the cellular automata models for microstructure prediction. The chapter will conclude with a statistical analysis of the model and a discussion of the accuracy of the results.

5.1 Challenge Description

The focus of this case study was challenge AMB2018-02 of the open benchmark presented by NIST. This involved scanning a bare IN625 substrate with 10 laser scans, of varying power and scan speed. Details of experiments, as well as test data, were found on the Benchmark website (National Institute of Standards and Technology, 2018; National Institute of Standards and Technology, 2019). Diagrammatical representations of the experiment, involved within this case study, can be seen in Figure 27.

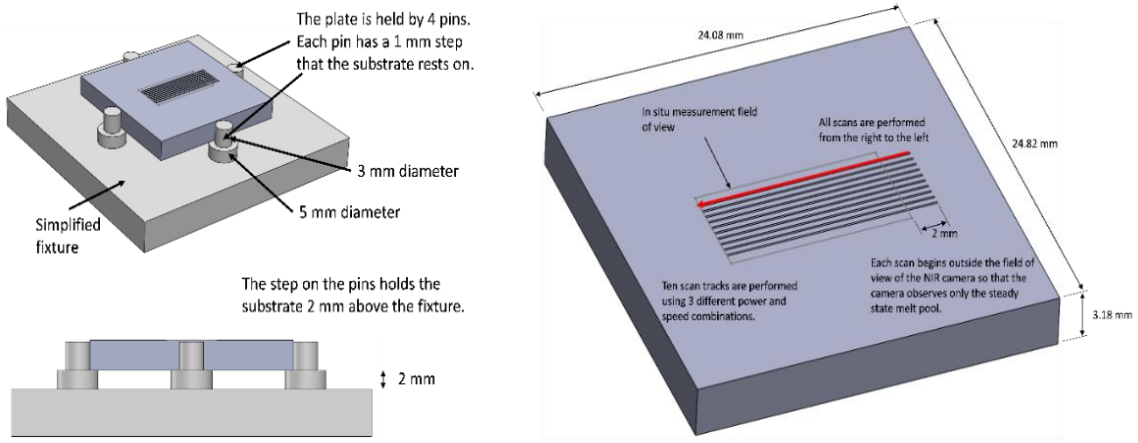

Figure 27: Diagrammatical representations of the experimental set up within AMB2018-02 (National Institute of Standards and Technology, 2018).

The substrate used had dimension 24.82mm x 24.08mm x 3.18mm. Each scan was 14mm with a hatch spacing of 0.5mm between scans. A combination of three different sets of process parameters were used on two different processing machines. In this work we have focused solely on the experiments completed using the NIST Additive Manufacturing Metrology

Testbed (AMMT) machine as the experimental results were more readily available for these tests. The process parameters used with this machine can be seen below in Table 8. Within this work we focus solely on the process parameters of Scan B and use this example to validate the modelling approach. The laser used featured 170µm and 100µm, D4σ and FWHM spot sizes respectively.

Scan	Power (W)	Scan Speed (mm/s)
A	137.9	400
B	179.2	800
C	179.2	1200

Table 8: Process Parameters for each scan.

The melt pool geometry and cooling rate were measured experimentally for each scan through a combination of thermal imaging, scanning electron microscopy (SEM) and electron backscatter diffraction (EBSD) among other techniques. Cooling rate was calculated through thermal imaging, as it was impossible to monitor the temperature within the melt pool directly. The image was used to determine the location of the point along the scan direction at which the temperature was 1290°C (solidus temperature) and 1190°C respectively. The distance between these two points was then divided by the scan speed to determine the time for cooling (Figure 28). Similarly, the melt pool length was calculated from these images by determining the distance between the front and back point of the melt pool at solidus temperature. EBSD maps and SEM images were taken on a cross section of the substrate, perpendicular to the scan direction, and were used to determine the melt pool width and depth as well as expose the resultant microstructure.

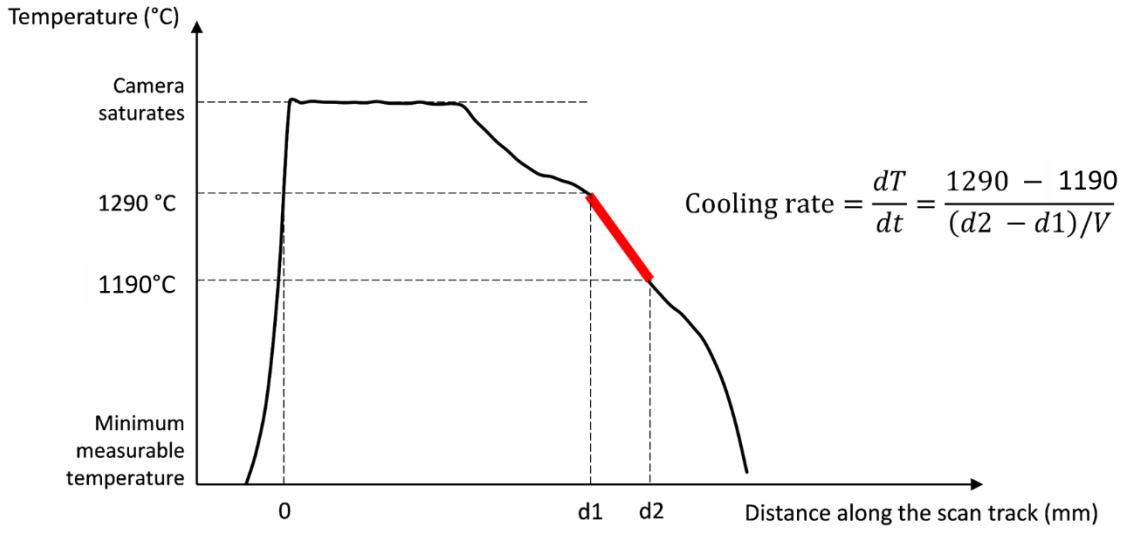

Figure 28: Calculation of cooling rate (National Institute of Standards and Technology, 2018).

Work on this particular challenge can also be seen within a number of thematic papers published as part of the Benchmark (Gan, et al., 2019; Kollmannsberger, et al., 2019; Robichaud, et al., 2019). The work seen in all three of these works varies slightly as each paper focuses on different aspects of the tasks outline. Gan et al. (Gan, et al., 2019) compared three types of thermal models and determined that the most accurate modelling method was the thermal-fluid vaporisation model, accounting for both fluid flow within the melt pool and heat loss due to vaporisation. They then used this thermal profile to look at surface topography and dendrite arm spacing. However, this simulated the process using the CBM machine and not the AMMT machine seen here. Robichaud et al. entered a submission to the benchmark as a team from Applied Optimization inc. (Robichaud, et al., 2019). Their work focused on the prediction of the thermal profile and grain structure, and received 2nd place for their grain structure predictions using a cellular automata method, similar to the work within this thesis. However, their thermal model was also performed using computational fluid dynamics (CFD) techniques. Finally, Kollmannsberger et al. (Kollmannsberger, et al., 2019) focused solely on melt pool geometry and cooling rate predictions. Isotropic and anisotropic conductivity were considered within their work. The anisotropic conductivity appeared to be more successful, as it partially accounts for the fluid flow within the melt pool. However, it is not used within this model as it increased computational expense significantly.

5.2 Thermal Models

As detailed in the previous sections, the modelling approach taken within this work involves two key steps: 1) the development of the 3D thermal model and 2) the application of the thermal model within the microstructure model of a 2D cross section. A 2D model has been chosen in order to reduce computational expense and also to allow for a higher resolution within the plane through the implementation of a finer mesh. The thermal model was calibrated using the experimental melt pool geometry and cooling rate measurements released after the Benchmark.

Thermal modelling was undertaken through the use of commercial FE software, Abaqus. A 3D analysis was performed, however due to computational expense a reduced domain was modelled in order to improve efficiency. The reduced substrate domain focused only on a single Scan B laser scan. It was stated in the challenge description that the time between scans was sufficiently long such that the scans were independent of each other, therefore such a reduction is justified. The reduced domain was representative of the full depth of the original substrate, 3.18mm, but a smaller substrate width and length were used. The width measured 1mm and was used in order to capture the full region affected by the melt pool, whilst minimising excess material. Similarly, the reduced length was taken to be 4mm as to allow time for the melt pool to reach a stable steady state, which is said within the challenge

description to be achieved after the first 2mm. Furthermore, a biased mesh was used to achieve a 10μm element size within the centre of the domain, where the laser scan takes place, in order to achieve accurate results within the region of interest, whilst optimising computational efficiency. Furthermore, a time incrementation of 3.125e-06s was implemented as the result of a convergence study (Figure 29). This incrementation was chosen as the thermal profile was suitably close to that of the finer incrementation within the critical cooling region, but with a reduced run time by approximately half.

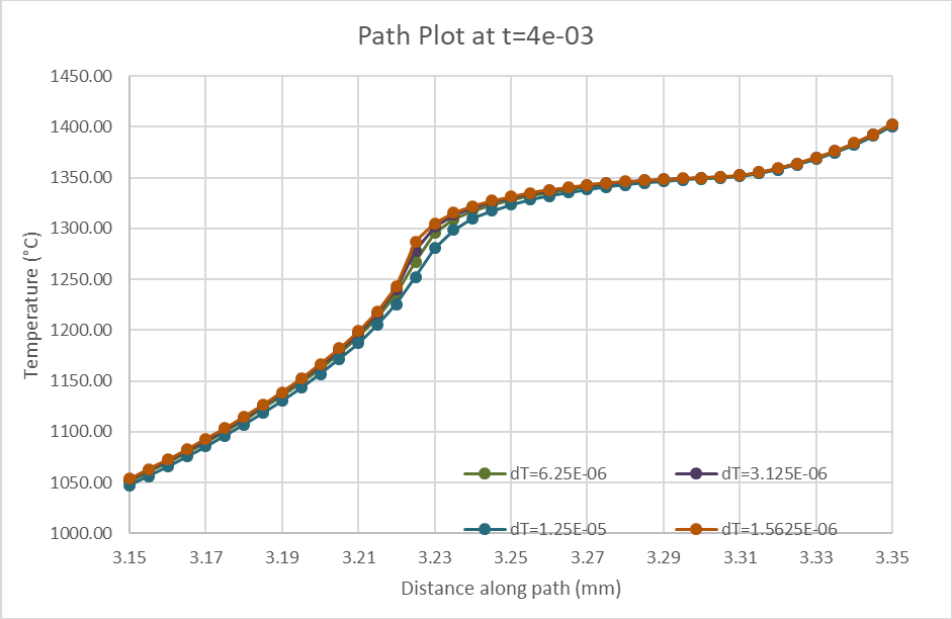

Figure 29: Graph representing the convergence study for the thermal analysis within the critical cooling region.

The moving laser was modelled by a Goldak heat source. The defining equations for this heat sources are given in Equation 22.

$$q_f(x,y,z,t) = \frac{6\sqrt{3}f_f\lambda P}{abc_f\pi\sqrt{\pi}}\exp\left(\frac{-3x^2}{a^2}\right)\exp\left(\frac{-3y^2}{b^2}\right)\exp\left(\frac{-3z^2}{{c_f}^2}\right), z \geq 0$$

$$q_r(x,y,z,t) = \frac{6\sqrt{3}f_r\lambda P}{abc_r\pi\sqrt{\pi}}\exp\left(\frac{-3x^2}{a^2}\right)\exp\left(\frac{-3y^2}{b^2}\right)\exp\left(\frac{-3z^2}{{c_r}^2}\right), z < 0$$

$$f_f = \frac{2}{1+\frac{c_r}{c_f}}$$

$$f_r = \frac{2}{1+\frac{c_f}{c_r}}$$

Equation 22: Goldak heat source (Zinoviev, et al., 2016).

Both radiation and convection boundary conditions were applied to the top and bottom of the substrate to represent heat loss to the surroundings. No boundary conditions were applied to the sides of the substrate, as within Abaqus the lack of a boundary condition represents a zero flux condition, which in turn is representative of a symmetry plane. Therefore, as we are only modelling a small region of a larger substrate the symmetry boundary condition accounts for the other material surrounding the smaller domain. Temperature dependent material properties were used based on those found within a literature review. The material properties used can be seen in Figure 30. A latent heat of fusion of 227 kJ/kg was used between the solidus temperature of 1290°C and the liquidus temperature 1350°C (Shrestha & Chou, 2018).

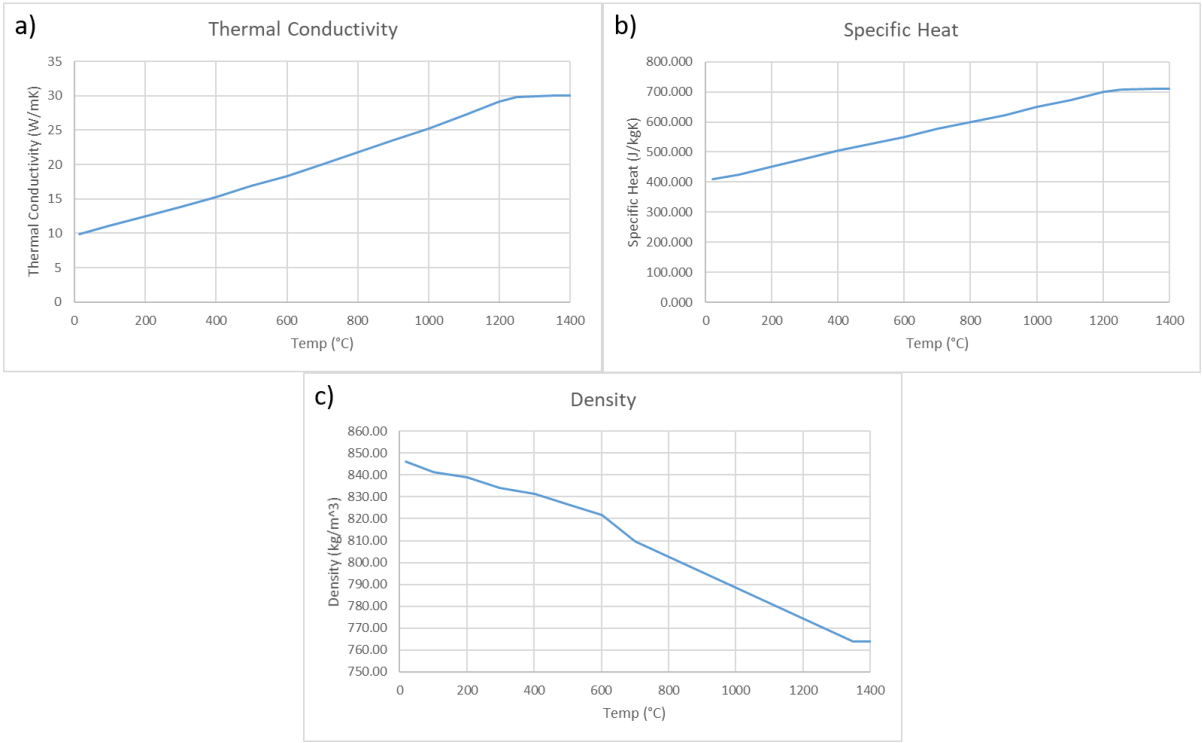

Figure 30: Temperature dependent material properties used for IN625 a) Thermal Conductivity (Shrestha & Chou, 2018; Arisoy, et al., 2019) , b) Specific Heat Capacity (Shrestha & Chou, 2018; Gan, et al., 2019), c) Density (Shrestha & Chou, 2018; Gan, et al., 2019).

The thermal model was calibrated using the experimental measurements. The cooling rate within each simulation was calculated by extracting the thermal profile along the central path once the melt pool had reached a stable state. Calculations were then undertaken as in the experimental analysis with the use of linear interpolation. The length was calculated as in the experiments according to the solidus temperature, whereas width and depth were calculated according to liquidus temperature as these experimental values were measured from the residual melt pool line within the macrographs. An in-depth design of experiments (DoE) was undertaken using DoE software, Design-Expert 12. The aim of this DoE was to optimise the heat source input parameters to reduce the error between the simulated and experimental

melt pool dimensions and cooling rate. A total of 5 variables within the model were optimised, namely; the dimensions of the Goldak heat source (a, b and c, where c is assumed to be equal to c_f+c_r), the ratio between the front and back ellipses within the Goldak heat source (f_f) and the heat source efficiency (λ). Suitable intervals for all variables were chosen based on some preliminary models. An initial 50 models were run, of which, due to the design chosen 7 were duplicate parameter combinations and could therefore be ignored. Optimised solutions were then identified. No solutions were found that allowed for a maximum of 1 standard of deviation for all of the measured variables. Therefore, the equations were set to minimise error for the melt pool geometry and then minimise cooling rate within these results, as cooling rate was the property with the biggest deviation from experimental results. The corresponding models were then run and analysed. If the predicted solutions and simulated solutions were suitably different the runs were added to the analysis and the analysis was undertaken again. A total of 60 models were run and the most suitable of the solutions was used as the thermal profile within the cellular automata analysis.

The final thermal model implemented within the microstructure simulations used the parameters a=0.117, b=0.05, c=0.162, f_f=0.435 and λ=0.357. The relative error between this thermal model and the average measurements over the 10 experimental tests of scan B can be seen in Table 9. It is acknowledged that the Goldak parameter b, is on the boundary of its allowed interval. However, predicted results for an analysis using a larger value than this were consulted and, if the accuracy of length, width and depth are maintained, the predicted variation in cooling rate was minimal. Therefore, the original parameters have been used within the final analysis.

		Length (µm)	Width (µm)	Depth (µm)	Cooling Rate ($°s^{-1}$)
Experiment	Average	359	123.5	36	1080000
	CoV (%)	5.57	5.26	5.28	54.44
Simulation	Value	360.9	125.4	36.4	3964606
	% Error	0.53	1.53	1.04	267.09

Table 9: Error between thermal simulation and experimental measurements.

These results clearly show the close simulation of melt pool geometry using these process parameters. However, there is clearly a large difference in cooling rates between the experimental and simulated results. Although the values are of the same order of magnitude there is a substantial difference in value, with the simulated cooling rate being more than 5 standard deviations faster than that of the experimental measurements. There are a number of reasons why such a large difference is seen. Firstly, cooling rate is naturally a very difficult

attribute to measure accurately within the melt pool, due to the inability to monitor this using thermocouples. The method seen in the NIST benchmark uses thermal imaging and therefore uncertainty errors are introduced by the spatial and temporal resolution of the equipment. Furthermore, in order to attempt to measure the cooling rate within the simulations in the same way, linear interpolation was used within elements. This, again, could introduce a degree of uncertainty within the measurements. However, it is thought that the main source of error between the results is the lack of inclusion of fluid flow effects within the model. Marangoni effects are a well-known physical phenomena that take place within molten material. It accounts for the movement of material within the melt pool and how this alters the effective conductivity. Within literature, these effects can be taken into account through the artificial alteration of thermal conductivity values (Safdar, et al., 2013; Lopez-Botello, et al., 2017). This provides a rough approximation to the effects caused by fluid flow within the melt pool. However, the discontinuity in material properties that is introduced can lead to a significant increase in run time. Such methods were attempted within this work, but were found to be too computationally expensive, with minimal impact on the results. The most accurate results are suspected to be achieved with a computational fluid dynamics (CFD) model, but this is beyond the scope of this project.

5.3 Microstructure Predictions

Following the development of the calibrated thermal model, we now move onto the implementation of the microstructure model. The 3D thermal model is applied to a 2D CA grid, representative of a cross section, with the same dimensions as the EBSD map, perpendicular to the scan direction. The corresponding EBSD map was then used to determine the quality of the final microstructure predictions. Both qualitative and quantitative comparisons were undertaken using the measurement methods outlined in section 4.7. Note, all grain measurements made within this study removed any grain with cell area smaller than 10μm^2, in order to try and replicate the noise reduction seen in the EBSD map.

A visual representation of the overlap between the 3D thermal profile and the 2D cross section used for microstructure predictions can be seen in Figure 31. A mesh size of 0.25μm is used within the CA domain with automatic incrementation techniques. The CA model used in this analysis is a 2D decentred method and does not allow for bulk nucleation within the melt pool, due to the rapid cooling times. Before applying the cellular automata algorithm to the model, one must first establish an initial substrate microstructure. This is done by applying an artificial thermal profile, representative of a casting application, whereby the material is uniformly cooled from a temperature at or above liquidus. Ideally, the resultant microstructure should be representative of that used experimentally.

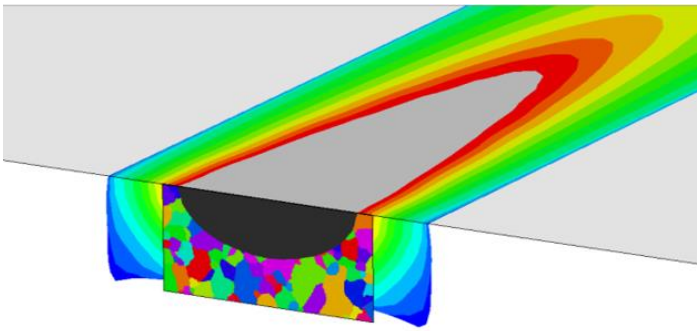

Figure 31: Visual representation of the overlap of 3D thermal and 2D CA models.

Unfortunately, no detail is given within the challenge description regarding the substrate initial microstructure. Therefore, the most detail we can obtain regarding this is from the grains within the resultant EBSD that have not been effected by the laser scan. These grains were analysed within MATLAB and dimensions of the grains were obtained using the minimum bounding ellipses. Note, the grain length and width have been measured in terms of the major and minor axes within this study. The parameters within the microstructure model were then altered to calibrate the initial microstructure. The most suitable parameters for this model were chosen to be a critical undercooling, μ, and standard deviation, v, of 17.5 and 1.0 respectively. Average dimensions of both the experimental and simulated substrate microstructures can be found in Table 10. It can be seen that all measurements made within the simulated microstructure are within 1 standard deviation of those seen experimentally within the EBSD. Therefore, it is determined that the parameters used to create this substrate are suitably accurate enough for implementation within the case study.

		Cell/Pixel Area	Ellipse Area	Half Length (major radius)	Half Width (minor radius)	Aspect Ratio
Experiment	Average	91.67	135.61	7.91	4.45	0.602
	SD	92.47	148.06	4.47	2.09	0.145
Simulation	Average	84.74	131.74	6.84	4.66	0.677
	SD	103.97	168.17	3.68	2.91	0.149

Table 10: Calibration of initial substrate microstructure.

Once the initial microstructure has been developed, the next step of the analysis is to simulate how this existing structure is altered by the laser scan, through the application of the thermal model previously developed. A number of incrementation methods were considered for this application, including 2 values of fixed increment and 2 values of automatic incrementation. These were applied to the same initial substrate microstructure. The results can be seen in Figure 32. An automatic incrementation method with a scaling factor of 0.1 (Figure 32d) was

chosen due to its close similarity to the finest increment choice in Figure 32b whilst being more computationally efficient. For both the simulated and experimental microstructures, in order to compare the effects of the laser scan, the grains affected by the melt pool are separated from those that are not. This is done within MATLAB and allows us to focus solely on grains within the melt pool.

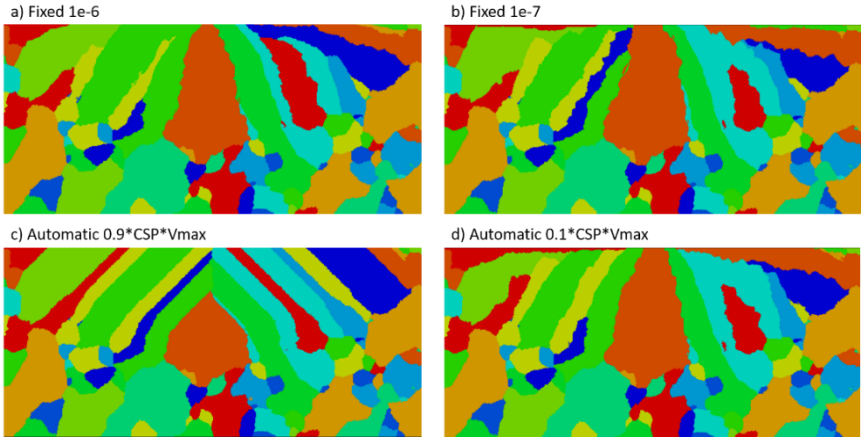

Figure 32: Different incrementation methods, tested on the same initial substrate.

Below we see the comparison of the results of the microstructure model and the experimental EBSD, both qualitatively (Figure 33) and quantitatively (Table 11).

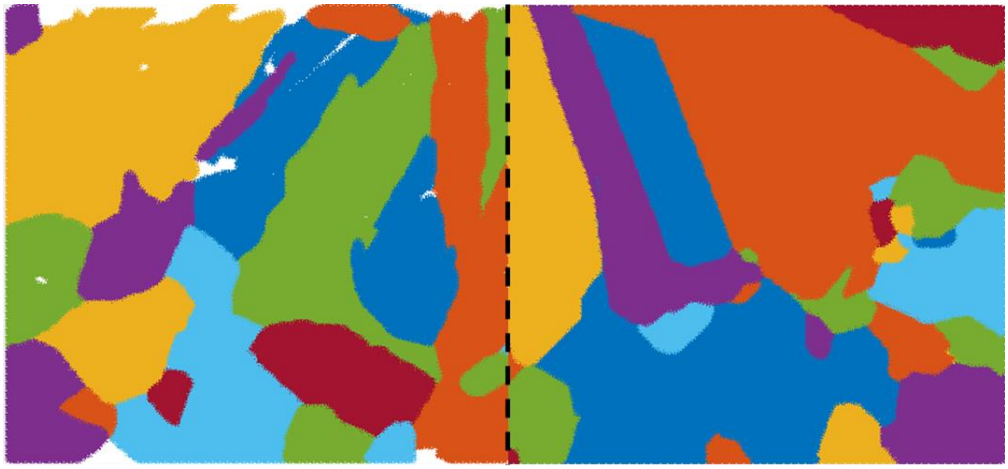

Figure 33: Visual comparison of microstructure predictions (right) against the NIST EBSD (left).

		Cell Area	Ellipse Area	Half Length (major radius)	Half Width (minor radius)	Aspect Ratio
Experiment	Average	188.06	378.15	15.56	5.80	0.347
	CoV (%)	101.12	118.62	53.68	76.6	46.86
Simulation	Average	303.35	568.93	20.28	7.31	0.413
	% Diff	61.30	50.45	30.33	26.05	18.97

Table 11: Quantitative comparison of predicted vs. experimental microstructures.

Visually a good agreement is achieved between the predicted and experimental microstructure. There is clear elongated grain growth, within the melt pool, in the direction of the thermal gradient. The microstructure in the EBSD is slightly more disjoint than that in the simulation, but this will be contributed to by the sensitivity of the EBSD but also by the lack of 3 dimensional growth within the microstructure model. The simulated microstructure is also visually affected by the colour scheme used within Matlab or Abaqus, as only a discrete number of colours are used. This can make grains appear larger than they are by assigning the same colour to two neighbouring grains. Such is the case for the large orange grain seen in the simulation results above, this grain is actually made of at least 2 separate grains, which have unfortunately been given the same colour. For this reason, among others, a quantitative analysis has also been undertaken so that we can eliminate any bias introduced through the presentation of the results. It should be noted that this study was undertaken early on within the thesis, and since alternative contour plots and colour maps have been used within Matlab to reduce the influence of this. The quantitative results can be seen in Table 11. A clear increase in the aspect ratio, in both experimental and simulation results, shows a transition from reasonably equiaxed grains within the substrate to columnar, elongated grains within the melt pool. Moreover, there is a significant increase in average grain size post laser scan for both the microstructures, although the average grain dimensions are slightly larger within the simulated microstructure than those seen experimentally. However, the average values still remain within one coefficient of variation of the experimental microstructure, so it can be concluded that it is a successful prediction of the microstructure properties. Some of the differences of grain structure can be attributed to the uncertainty of the initial substrate microstructure as well as variation of the thermal profile.

In addition, the microstructure model used within this work features a number of probabilistic features, namely the probabilistic nucleation and the probabilistic choice of grain capture, discussed earlier. Within this case study, due to the small time increment used and the lack of bulk nucleation within the melt pool, the main probabilistic impact comes from the variation in initial substrates. Due to the lack of information surrounding the initial substrate microstructure in the experimental studies, it is impossible to replicate the exact substrate and therefore an approximation has been simulated. When using the model to cast this substrate, probabilistic nucleation means a different substrate is created each time and consequently different post melt microstructures. Therefore, a statistical analysis has been undertaken to determine the impact of the probabilistic aspects of these substrates and determine the average results over the entire analysis.

5.4 Statistical Analysis

The statistical analysis featured a total of 25 runs of the microstructure predictions, each using the exact same algorithm parameters, mesh size and incrementation parameters. The microstructure of each initial substrate and resultant melt pool were analysed and compared with the results taken from the experimental EBSD. The mean and standard deviation of the average grain characteristics from each analysis were monitored. A total of 25 runs was chosen as this allowed sufficient runs such that the average standard deviation of the majority of the grain dimensions began to stabilise as can be seen in Figure 34. Table 12 presents the average and standard deviation of the post melt microstructures across the statistical analysis.

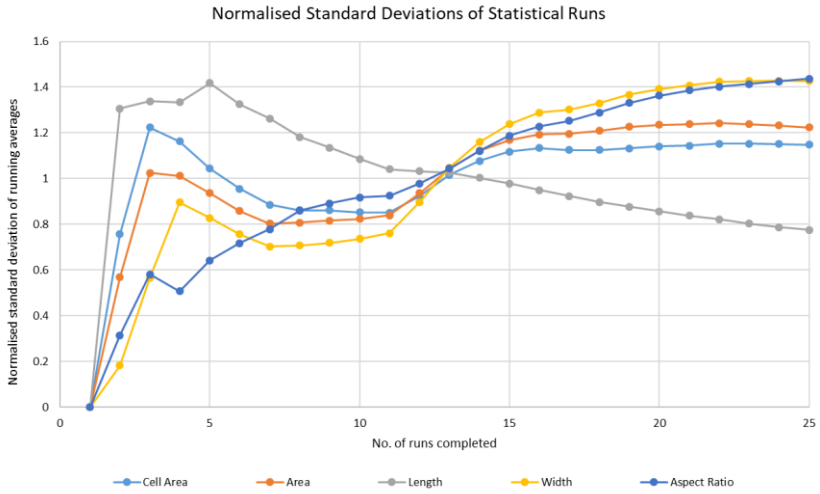

Figure 34: Variability of standard deviation throughout statistical analysis.

		Cell Area	Ellipse Area	Half Length (major radius)	Half Width (minor radius)	Aspect Ratio
Experiment	**Average**	**188.06**	**378.15**	**15.56**	**5.80**	**0.347**
	SD	190.18	448.58	8.35	4.44	0.163
	CoV (%)	*101.12*	*118.62*	*53.68*	*76.6*	*46.86*
Mean of Simulation Measurements	**Average**	**257.12**	**488.20**	**19.96**	**6.74**	**0.366**
	% Diff	*36.72*	*29.10*	*28.31*	*16.29*	*5.49*
	SD	219.95	418.75	8.92	3.79	0.171
	Max value	394.78	735.02	22.78	9.07	0.443
	Min value	158.69	295.83	17.52	4.87	0.311
Best Simulation	**Average**	**197.94**	**378.88**	**19.12**	**5.65**	**0.335**
	% Diff	*5.25*	*0.19*	*22.89*	*-2.54*	*-3.44*

Table 12: Statistical analysis results.

The results, again, show that the mean of the average area, length, width and aspect ratio all lie within one coefficent of variation of the experimental results. Notably, there is a smaller difference on all accounts between the mean values across the 25 runs than those seen in the first simulation (Table 11). As can be seen by the minimum and maximum values for each dimension, the range of average charactersitics clearly varies greatly depending on the initial microstructure used. The range of each variable includes the experimental value, except for that for the grain length. The grain length is consistently predicted longer than seen experimentally, though not by much. This could be due to the 2D aspects of the model. In 3 dimensions, one could expect some new grains to be dragged into the meltpool from the scanning direction that here is the out of plane direction. The introduction of these would hypothetically inhibit further growth of some grains and hence slightly reduce grain length. Despite this, there is only a minimal difference within the length averages and therefore the computaional efficency of implementing the 2D model outweighs the slight difference in measurements. Furthermore, although averages over 10 scans were given for thermal profiles only a single experimental EBSD map was supplied and therefore more experimental information would be useful to fully determine the level of statistical variation within experimental tests.

To summarise, this case study has given us the ability to validate the modelling approach against detailed experimental data. A strong agreement was achieved between the simulated and experimental microstructures. Therefore verifying the suitability of the modelling method. Furthermore, this exercise has highlighted key features within the model that need to be considered within future analyses. For example, the dependence of results on probabilistic elements, such as initial microstructure, and hence the importance of performing a statistical analysis.

6 Direct Energy Deposition (DED) Validations

Following the validation of the sequentially coupled 2D CA-FE modelling approach for a single laser scan in the previous chapter (chapter 5), the main objectives of this chapter are to validate the model for a more complex, additive manufacturing application and to determine if the identified modelling approach is capable of predicting differences in solidification as a result of changes in the deposition process.

Within this section the microstructure modelling methods will be applied to DED processes. The main advantage of validating the model using direct energy deposition rather than powder bed fusion, is the lack of powder deposition. In PBF simulations there is a requirement to model three material phases: solid, liquid and powder, whilst modelling of the deposition in DED only utilises two material phases: liquid and solid material. Thus, there is less room for inaccuracy both in the thermal model through material properties and in microstructure predictions via the assumptions made regarding nucleation from powder material. Furthermore, DED structures are typically built with a much coarser deposition strategy than PBF parts, with fewer layers and larger melt pools. Therefore, thermal models can be used to model the whole domain with accurate deposition strategies more easily and more efficiently. Moreover, larger melt pools means that a slightly larger cell size can be used, whilst maintaining the same level of resolution with respect to the cell size in comparison to the melt pool size. Hence increasing computational efficiency of the microstructure simulations.

This case study aims to provide the required experimental arrangement to address the objectives identified in section 2.7:

- Contribute to the smaller catalogue of work available for the application of CA to direct energy deposition processes, particularly for multi-layer builds.
- Implement cellular automata methods with experimentally-validated thermal models.
- Improve computational efficiency of the required models to achieve sensible run times with practical hardware requirements, suitable for use in industry.
- Apply CA models to investigate the influence of process parameters, with experimental validation.

Originally, plans were made to undertake extensive wire-arc additive manufacturing experiments. However, unfortunately, due to the outbreak of COVID-19 within the UK, the WAAM experiments were suspended due to lack of technical staff. Therefore, due to the loss of time, the decision was made to go ahead with alternate plans to achieve the desired objectives of this study. This involved focusing on existing data available within TWI from some recent LMD experiments.

6.1 Laser Metal Deposition (LMD) Experiments

As discussed above, unfortunately due to staff shortages and the onset of COVID-19, sufficient resources were not available to carry out the desired WAAM experiments. Alternative plans were made to replace the experimental data with IN718 laser metal deposition experiments that had already been carried out as part of another project. Whilst there are some differences within the scope of the experiments to those that were planned, the main concepts remained the same as both processes are direct energy deposition techniques using IN718 as the deposition material. On the other hand, the particular LMD process used within these experiments used a powder fed nozzle, as oppose to a wire feed. However, this will have minimal influence on the modelling process as the raw material, in either case, is melted by the heat source, and is deposited onto the build in a molten form. Other differences include the deposition strategy implemented along with the approximate dimensions of the build, both of which can be accounted for within the modelling process. Also, it should be noted that these samples were deposited on SS 304L substrates, not IN718 substrates as originally planned when developing the WAAM experiments. Whilst IN718 substrates would have provided consistency in microstructure between the substrate and the build part, SS 304L is also a face centred cubic structure and it is expected that this will have little influence on the resultant microstructure predictions. Within the first layer, the microstructure may be influenced by dilution of the composition, but it is expected that the influence of this would be negligible within subsequent layers. Nevertheless, alternative material properties will need to be applied within the thermal model.

Within the project for which the LMD samples were deposited, a wide range of samples were built using various sets of process parameters. Specifically, 32 samples were deposited with varying values of laser power, gas flow rate and powder feed rate, although not all samples were deposited with thermocouple measurements. For this work, 3 samples were identified that were completed with full thermocouple measurements and kept all process parameters consistent except from the travel speed. This was an important choice, as it ensures any variation in microstructure can be attributed directly to the change in travel speed, as opposed to a combination of parameters. Upon detailed analysis of the experimental data, it was

established that there were some queries with regards to the data recording and labelling process, and it was believed that some of the thermocouple labels did not correspond correctly to those expected. Consequently, the three samples were deposited again with increased focus on the data records. This time, three repeats of each sample were completed to provide evidence of repeatability for the samples. The data collected from these nine samples (three builds, each with three repeats) is used within this work. A full description of the LMD samples completed is given within this section.

Element	%
Al	0.57
B	<0.02
Co	<0.02
Cr	19.59
Cu	<0.02
Fe	19.24
Mn	<0.02
Mo	3.18
Nb	5.39
Ni	50.96 (by remainder)
P	<0.005
Si	0.03
Sn	0.02
Ta	<0.02
Ti	0.94
V	0.02
W	<0.02
C	0.04
S	0.001
N	0.01
O	0.01

Table 13: Composition of IN718 powder used.

Firstly, each sample was deposited using IN718 powder onto a 304LSS substrate with approximate dimensions of 200mm x 120mm x 15.75 mm. The powder was characterised, by an external company, and the composition can be seen in Table 13. A particle size distribution of approximately 45-90µm was seen, along with an apparent density of 4.69g/cm^3. The system used for the deposition of the samples was a Trumpf TruLaser Cell 7040+, with a Trumpf Trudisk 3002 3kW disc laser and an ILT multi-jet powder nozzle with 1.5mm inserts. A stand-off distance of 10.6mm was applied. The other key build parameters used for each deposition can be found in Table 14. The z-inc defines the distance in the build direction moved by the nozzle between layers.

Sample	Travel speed (mm/min)	Powder feed rate (g/min)	Nozzle gas flow (l/min)	Track Sep (mm)	Tracks in odd/even layers	Number of layers	Z-inc (mm)
A	2000	35	10	2.4	8/7	13	0.9
B	1000	35	10	2.6	7/6	7	1.7
C	1500	35	10	2.4	8/7	9	1.2

Table 14: Build parameters used within the LMD samples.

A total of 9 samples were built, 3 variations on the travel speed, as can be in Table 14, and 3 repeats of each sample. The number of tracks and layers within each deposition was chosen in order to achieve a similar geometry across all samples. By keeping the geometry consistent as opposed to number of layers and tracks, this is more representative of a scenario where the same part is manufactured using different process parameters. Furthermore as discussed earlier, by keeping all other parameters consistent other than travel speed, this allows us to investigate the ability of the model to capture any variations in microstructure as a direct result of changes to this variable. The only other parameter that changes within Table 14 is the track separation. This is larger for sample B than it is for A and C. This is because the lower travel speed results in a larger melt pool and the overlap between each layer is calculated to be approximately 33%, therefore the track separation increases with an increase in bead width.

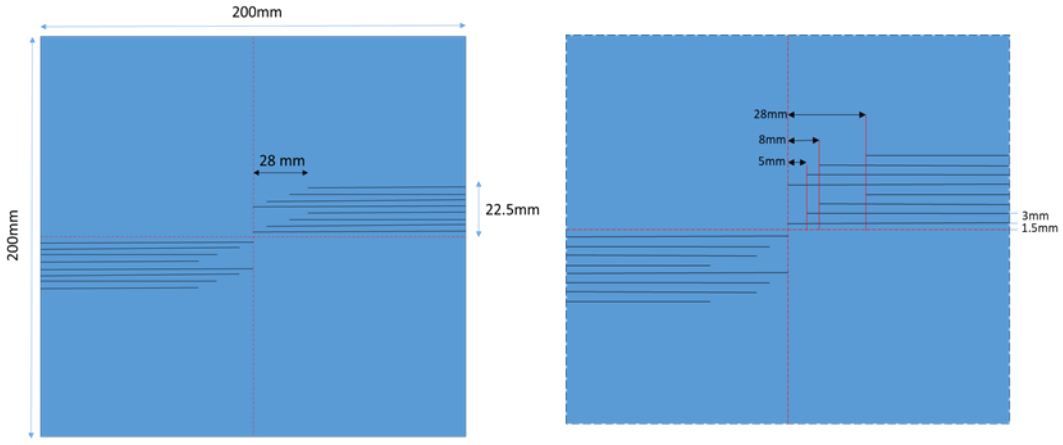

Figure 35: Schematic of thermocouple fixture.

Figure 36: Experimental set up for the LMD samples.

For each build, a thermocouple fixture with 16 channels machined into the surface was used, with a build substrate clamped on top of the fixture. A schematic of the thermocouple fixture can be seen in Figure 35, which clearly shows the different lateral and transverse locations of the channels for thermocouples with respect to the build plate. The experimental set up of the thermocouple fixture and clamped substrate, prior to the deposition of the build, can be seen in Figure 36. As in the originally planned WAAM activities, simple wall geometries have been built. However, the scan strategy used was a bidirectional deposition strategy with an offset on even layers in order to fill in the troughs created as a result of each odd layer, as this had already been established within the design of these samples for the corresponding project, due to manufacturing considerations related to the efficiency of material usage and nozzle movement. A schematic of the deposition strategy can be seen in Figure 38. The representative build dimensions of the builds as a result of the change in build parameters were recorded. These values can be seen in Table 15, along with images of the final builds in Figure 37.

Sample	Build Height (mm)	Build Width (mm)	Build Length (mm)
A	12.5	19.1	140.5
B	12.4	19.0	140.7
C	11.9	19.3	140.7

Table 15: Resultant build dimensions.

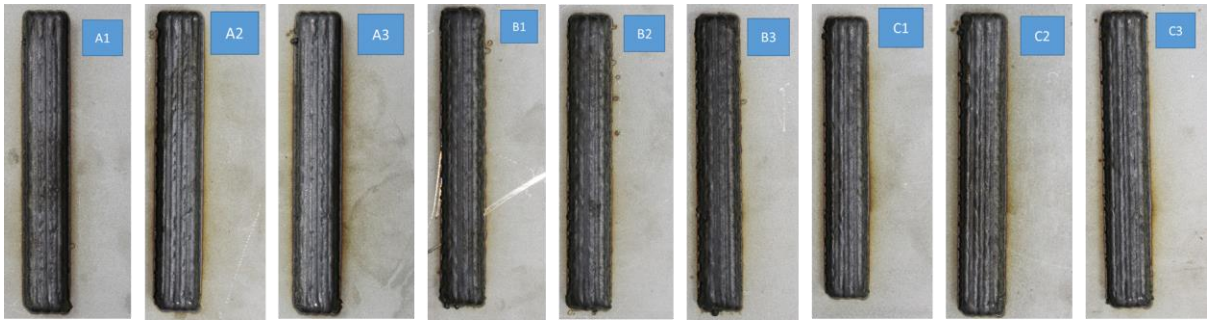

Figure 37: Images of deposited samples.

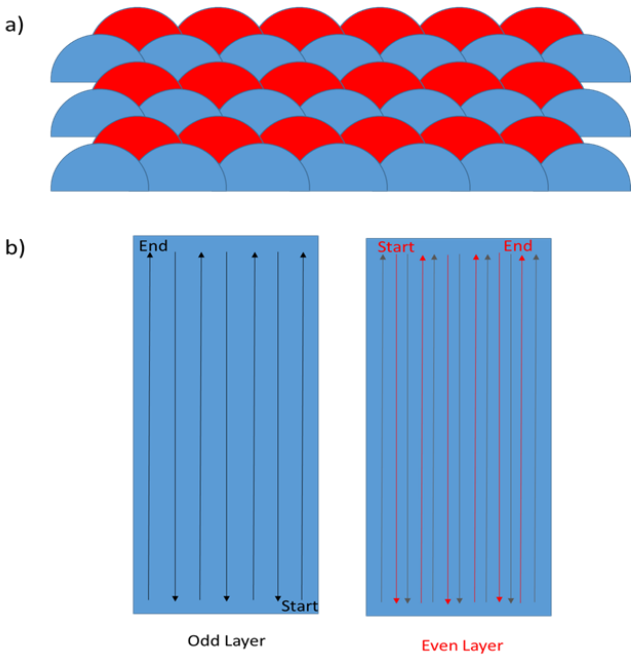

Figure 38: Schematic showing the deposition strategy implemented, a) shows a cross section perpendicular to the deposition direction, b) shows the deposition direction in the build plane.

Thermocouple results were obtained for all repeats of each of the three samples. One of the initial steps in the analysis of the experimental results was the assessment of the repeatability of the thermal profiles for each set of process parameters. Manual post-processing of the data to align the start times of each repeat was undertaken. Due to a large, unexpected change in initial temperature samples (as can be seen in the experimental thermocouple results for sample A in Figure 39), the repeatability of the samples has been compromised. It is expected that this is due to insufficient time between repeated samples to allow the set up to return to room temperature. Therefore, samples A1 and C1 have been discounted from certain aspects of this analysis, such as thermal calibrations, as the initial temperature for these samples were substantially lower than their repeats. Only the two remaining repeats for both samples A and C will be used throughout the work presented here. The thermocouple data for sample A, B and C is shown in Figure 39, Figure 40 and Figure 41 respectively. Only a sample of the

thermocouples are shown for each of the three samples for clarity. For sample A and C, a reasonable level of repeatability is seen within two of the samples, where as one set of data clearly starts at a much lower initial temperature. A schematic of the corresponding locations of each thermocouple reading within the fixture is shown in Figure 42. Consistently thermocouple 0 is lower than the rest of the profiles, which is to be expected as it is the furthest away from the centre of the build. The hotter thermocouples do not always follow the logic that the thermocouples closest to the centre, both longitudinally and laterally, will be the hottest. A level of epistemic uncertainty should be considered due to inability to accurately position the deposit centrally on the build plate.

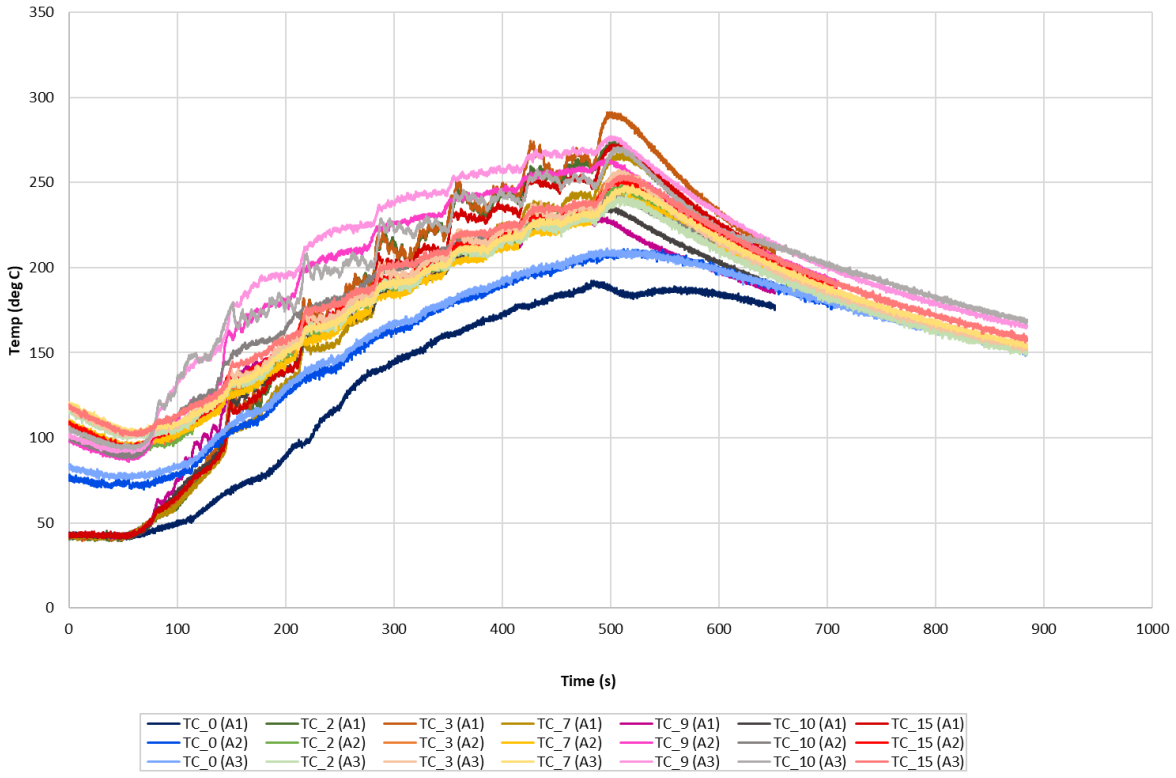

Figure 39: Thermocouple results for sample A.

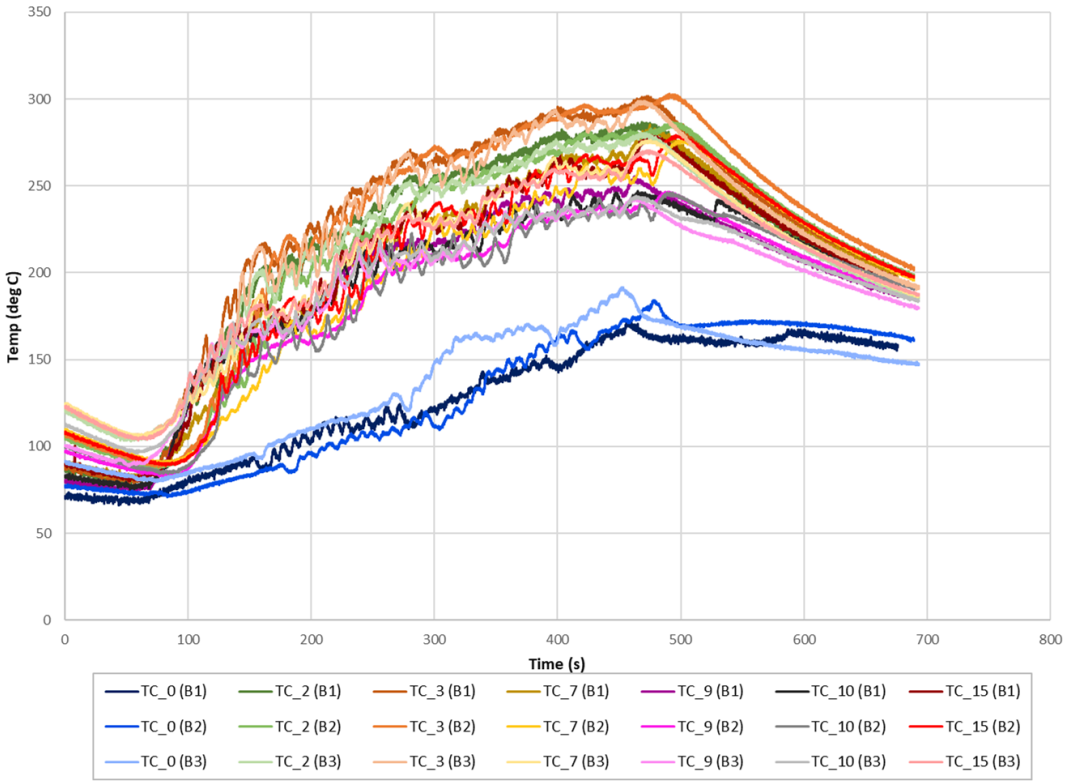

Figure 40: Thermocouple results for sample B.

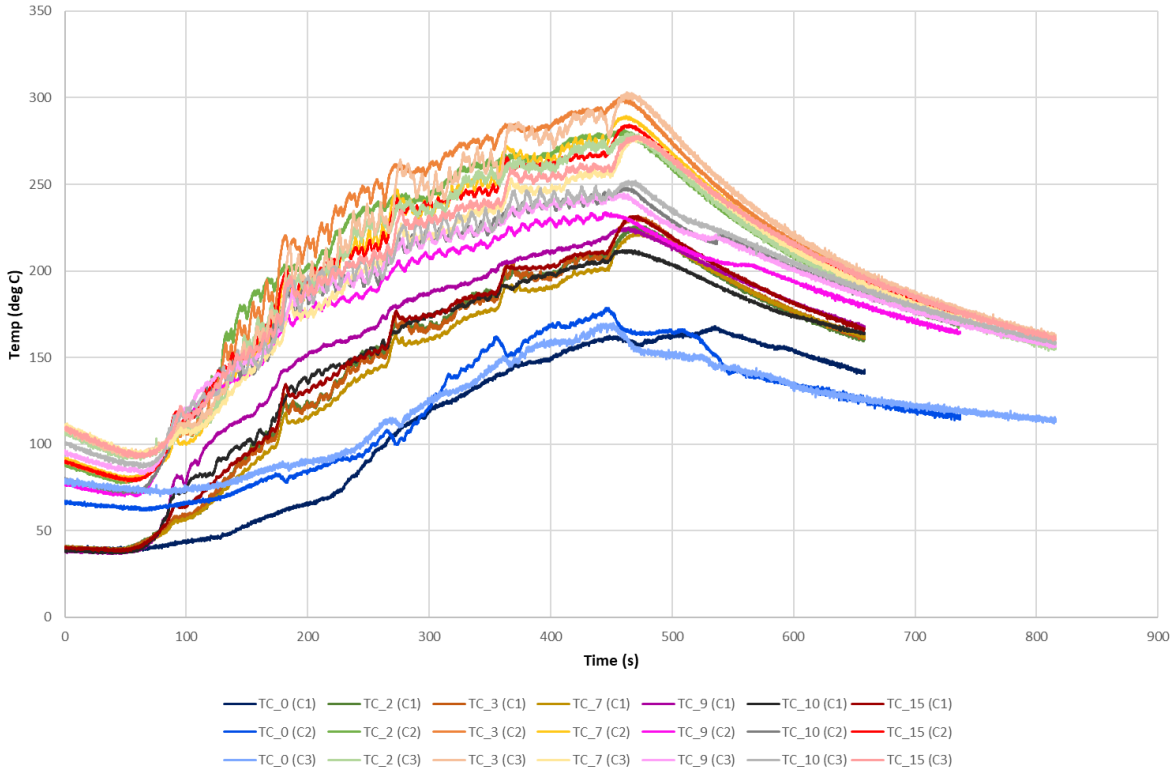

Figure 41: Thermocouple results for sample C.

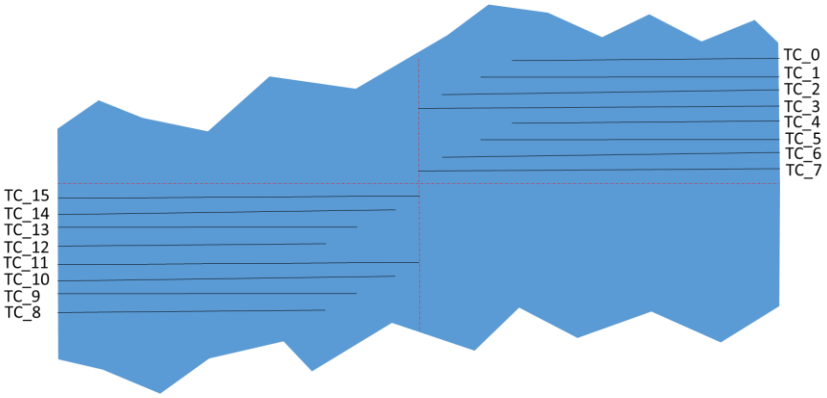

Figure 42: Labelling of thermocouple locations.

6.2 Microstructural Examination

Following deposition, each sample has been cross-sectioned and examined to reveal a number of features of the builds. Firstly, macrographs have been taken of the cross-section normal to the deposition direction in order to reveal the melt pool geometry achieved throughout the build. Figure 43, Figure 44 and Figure 45 show the macrographs for one repeat of sample A, B and C respectively. These images show the clear changes in bead geometry as a result of the change in travel speed. Specifically a much shallower bead geometry is seen for sample A when compared with sample B and C; this is expected due to the higher travel speed.

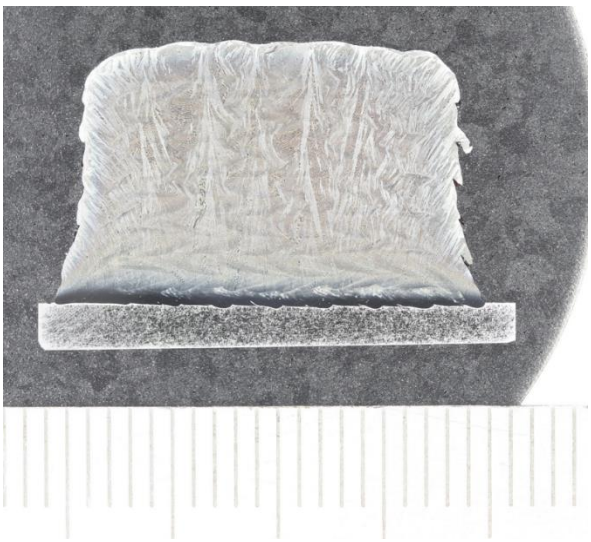

Figure 43: Experimental macrograph of sample A1.

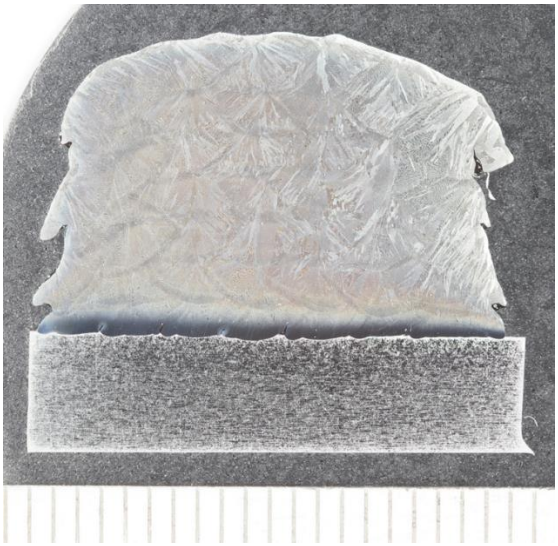

Figure 44: Experimental macrograph of sample B2.

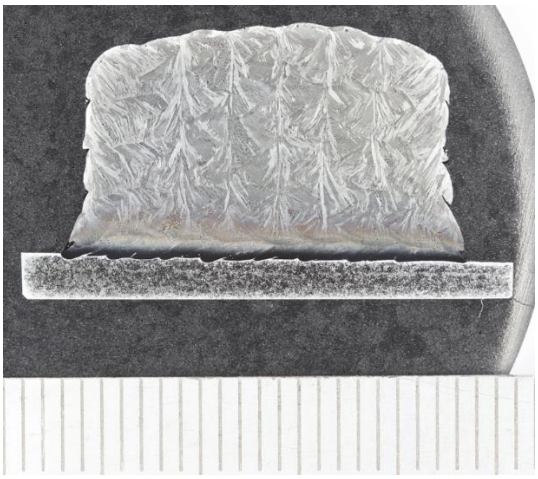

Figure 45: Experimental macrograph of sample C2.

Secondly, EBSD images have been taken on the cross section normal to the deposition direction (XY plane) on each of the 9 samples. This reveals the solidification microstructure of the as-built geometry parallel to the build direction. By completing this on all 9 samples, this gives an indication of the repeatability of the grain morphology between repeats of the same samples. In addition, EBSD imaging was undertaken on both of the other two cross sectional planes (XZ and YZ planes) for one sample of each set of process parameters. This was not completed on all 9 samples due to the resources available. In an ideal scenario microstructural analysis would have been completed in each plane for all 9 samples with additional sections taken throughout the samples to assess repeatability of the grain structure within each individual sample. However, the EBSD images obtained still allow for the analysis of microstructural changes as a result of the change of process parameters within all three principal planes within the as-built material. As EBSD maps visually show the grain

morphology and texture within a material, they are a good source of experimental data for comparison with the microstructural simulations.

All EBSD images were taken as close to the centre of the build as possible to ensure they were taken in a region where the melt pool was relatively stable. Specifically, the XY plane examinations were undertaken approximately half way through the build length. Similarly, YZ plane was taken as close to the centre of the sample as possible and the XZ plane was examined just above mid-point of the build height. In order to achieve large EBSDs that could analyse large domains, such as the full build height, the EBSDs were completed using a relatively large step size of 20μm and a low magnification of 40x nominal magnification. EBSD maps were completed in individual strips using Aztec software produced by Oxford instruments. The final maps were then constructed by stitching individual strips together, such as that seen in Figure 46. These were all completed by staff at TWI Ltd.

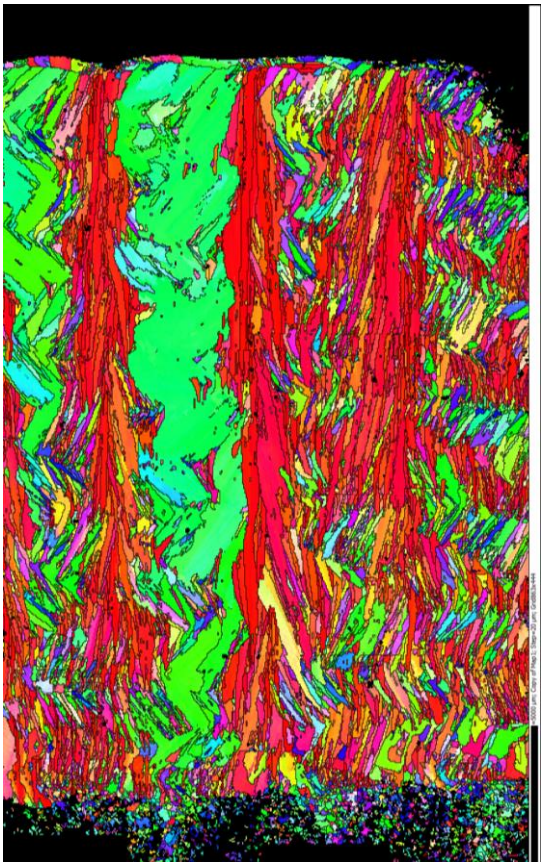

Figure 46: EBSD image of sample A1, XY plane, step size=20um.

The inverse polar figure (IPF) scheme has been chosen for the EBSD images as it showed more distinctly the crystallographic texture and alignment within the various samples than the Euler scheme. This is a common attribute of Euler schemes as a result of how the Euler angles are used to determine the colour of a grain, which can result in similarly orientated grains being prescribed dissimilar colours. The IPF colouring scheme identifies if the <100>, <101> or

<111> symmetry group is in line with a chosen direction, which defines a reference plane. This is explained clearly for cubic materials by UC Riverside by discussing when a plane, face or corner is parallel to the reference plane (UC Riverside, Central Facility for Advance Microscopy and Microanalysis, 2013). Figure 47 demonstrates the corresponding orientation of the octahedron for face centred cubic crystals. The EBSDs presented within this work are consistently displayed using the reference plane normal to the build direction. The legend for this colouring scheme is shown in Figure 48.

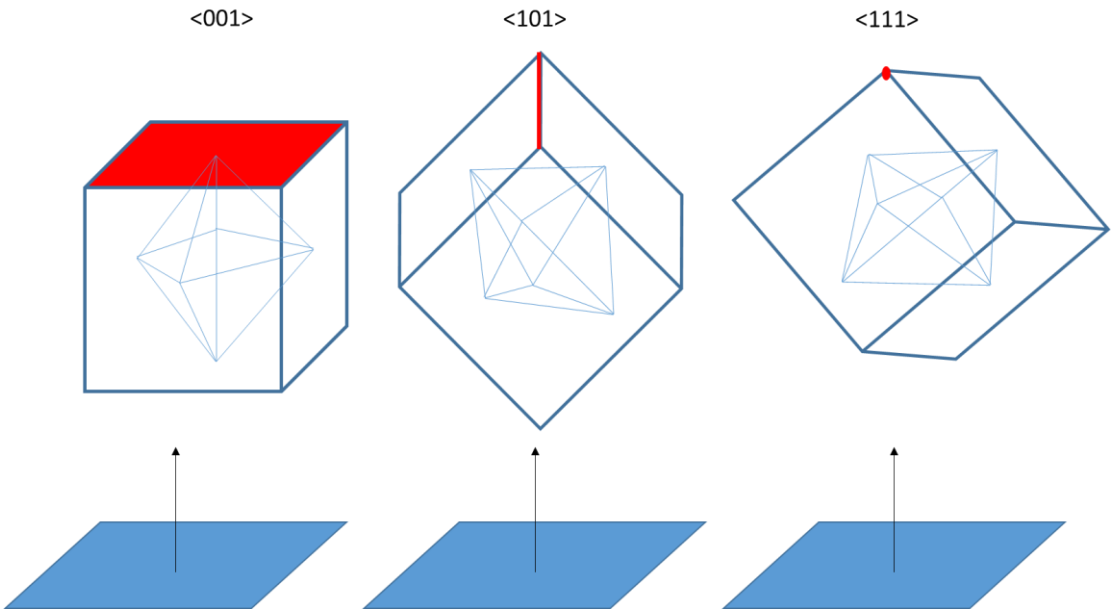

Figure 47: Octahedral crystal orientations within IPF EBSD images.

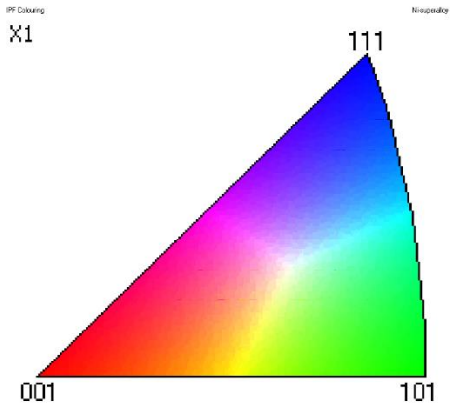

Figure 48: IPF colour scheme legend for EBSD images.

6.3 Planned Thermal Modelling Approach

The finite element methods intended for use in the thermal modelling approach are discussed here. Unfortunately, again due to events out of our control, the resources required to run these models were not available and alternate strategies had to be implemented. High power computing resources were required in order to be able to undertake the 3D finite element thermal models, with sufficient fidelity for use in microstructures, whilst still being able to simulate the complete build height. This section presents the intended finite element approach and preliminary work undertaken.

Finite element models were created in Abaqus 2019 for each sample individually. The geometry was defined as a cuboid of length 140mm. The specific height for each sample was determined by calculating the average experimental layer height by dividing the total height by the number of layers. This varied slightly from the expected z-increment as can be seen in Table 16. The width of the build was determined by the track separation and the number of tracks per layer. For sample A and C, 8 tracks were deposited in each odd layer, with a track separation of 2.4mm. Assuming a bead width of approximately 4mm, as this is the beam diameter, another 2mm is included on either side of the outer most scan locations to account for the width of the melt pool. Therefore, a width of 20.8mm was modelled. Similarly, for sample C a width of 19.6mm was assumed.

Sample	Actual Height (mm)	Expected z-inc (mm)	No. layers	Modelled layer height (mm)	Modelled build height (mm)
A	12.5	0.9	13	0.96	12.48
B	12.4	1.7	7	1.77	12.39
C	11.9	1.2	9	1.32	11.88

Table 16: Table of calculated layer height and build eight for thermal models.

The assembly was created including the IN718 wall deposit, SS 304L substrate and SS 304 thermocouple fixture. This is shown in Figure 49. It should be noted that a single set of stainless steel 304 material properties have been used for both the fixture and substrate. Geometric partitions were created to define individual layers. Similarly, partitions were used within the build substrate to replicate the thermocouple locations on the bottom surface of the substrate. Tie constraints were used at the interface between the deposit and substrate, as well as the interface between the substrate and thermocouple fixture.

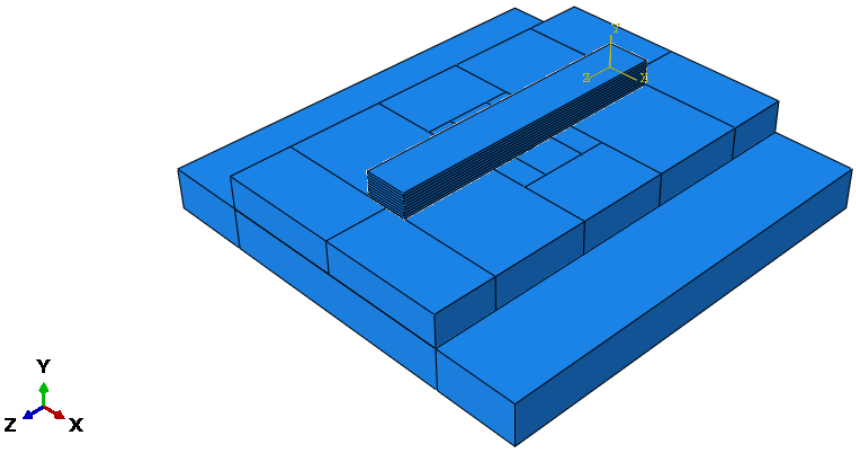

Figure 49: Assembly of sample C in Abaqus 2019.

Temperature-dependent material properties were implemented for both materials within this model. These have been found in literature (Salerno, et al., 2018; Lee & Zhang, 2015; Venkatkumar & Ravindran, 2016; Vakili-Tahami & Ziaei-Asl, 2013) and are show in Figure 50. A value of 227kJ/kg was assumed for IN718 (Rai, et al., 2016) with a solidus and liquidus of 1260°C and 1336°C respectively (Special Metals, 2007). Equivalently, a value of 273.79kJ/kg and a melting range of 1399°C to 1454°C was assumed for the stainless steel (De Moraes & Czekanski, 2017; AK Steel Corporation, 2007) .

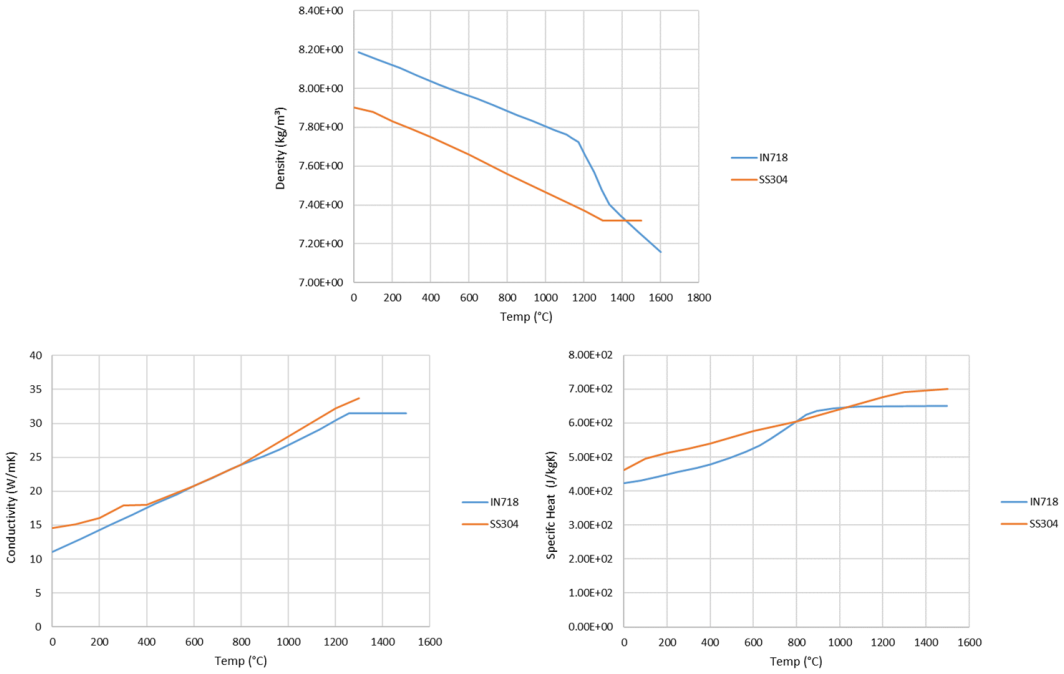

Figure 50: Temperature-dependent thermal properties (Salerno, et al., 2018; Lee & Zhang, 2015; Venkatkumar & Ravindran, 2016; Vakili-Tahami & Ziaei-Asl, 2013)

Material activation was achieved within the models using the new functionality within Abaqus 2019 of progressive element activation. This was implemented through the use of a UEPACTIVATIONVOL subroutine and specific keyword edits that can be found in the Abaqus 2019 documentation (Dassault Systemes, 2019). Progressive element activation allows elements to be activated or deactivated during a given step. Similar to the AM app utilised in section 3 this removes the need for individual steps and model changes when trying to implement element birth techniques. However, LMD models typically require the use of quiet element methods as material is deposited with respect to the movement of the heat source and not in easy to define geometric regions such as powder layers within PBF models. Quiet elements utilise dampened material properties to supress thermal diffusivity within elements which are technically active within the finite element calculations but represent inactive material. Consequently, the sudden change in material properties ahead of the heat source when activating new material can result in convergence errors. The use of progressive element activation avoids the need for this technique and hence also avoids these convergence challenges. Within this work progressive element activation has been used efficiently to combine the highlights of both of these approaches. A new step has been defined for the deposition of each layer for ease and clarity when defining the scan strategy. Within each new step the corresponding layer is specified as the region of activation for the specific step. Activation of elements within the layer is then determined by the value of the heat flux present, and hence material is activated in coordination with the heat source location as required by the LMD process.

There are a number of different heat source models available for the simulation of laser AM processes, as can be seen in some of the presented literature within chapter 2. Within this work, two heat source model approaches were considered. The first was the conical Gaussian heat source. The conical heat source still provides the Gaussian profile typically associated with a laser, but also provides the added benefit of being a volumetric heat source, which is more suitable for a DED process than a 2D Gaussian surface flux. It also has fewer parameters for calibration than the volumetric, Goldak, double ellipsoid model. However, for accurate resolution of this heat source a fine mesh and time increment must be implemented. This is ideal for trying to resolve the melt pool geometry and thermal profile for microstructure models. Nevertheless, it is extremely computationally expensive when trying to model a significantly large domain size, such as the build height and width in consideration here. The model is shown in Figure 51 (although, the labelling for r_0 and r_i should be reversed) and defined in Equation 23. Although, the conical model was never validated and implemented within the completed work presented here, suggested values for the parameters were as follows. The value of r_e is taken to be equal to that of the beam diameter, whilst a ratio of 0.6 between r_e

and r_i was to be undertaken, as in the work presented by Shahabad et al. (Shahabad, et al., 2020) . The difference between z_e and z_i is assumed to be the layer height.

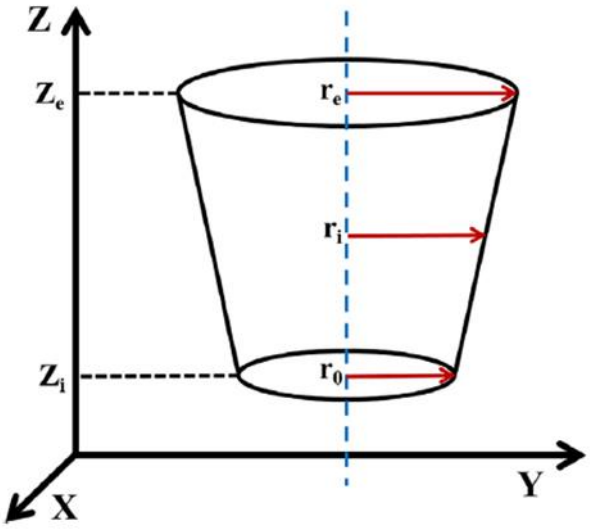

Figure 51: Volumetric conical Gaussian heat source, taken from (Zhan, et al., 2019).

$$q(x,y,z) = \frac{9Q_0}{\pi(1-e^{-3})(z_e - z_i)\left(r_e^2 + r_e r_i + r_i^2\right)} \exp\left(-\frac{3(x^2+y^2)}{r_0^2(z)}\right)$$

$$r_0(z) = r_i + (r_e - r_i)\frac{z - z_i}{z_e - z_i}$$

Equation 23: Conical Gaussian heat source (Zhan, et al., 2015; Agarwal, et al., 2018).

The second heat source considered within this work was built on concepts used within the AM app that was utilised in section 3. However, it has been dev eloped within a stand-alone subroutine within this work to allow flexibility and adaptability within the subroutine. An integrated heat source approach was used which, in a similar fashion to the toolpath-mesh intersection module, determines the elements which are intersected by the specified deposition strategy within a given time increment from a specified event series. The total thermal energy delivered within this time increment is then determined by the power and increment duration. This is then applied uniformly as a volumetric heat flux over the region of newly deposited material. A visual representation of this heat flux model is shown in Figure 52. The primary aim of using this integrated heat source approach was to improve computational efficiency of the models, particularly for iterative efficiency calibrations. The efficiency is a scaling factor applied to the power of a heat source, to account for how much energy is actually absorbed from the source compared to how much energy is delivered by the heat source. It can be calibrated in thermal models.

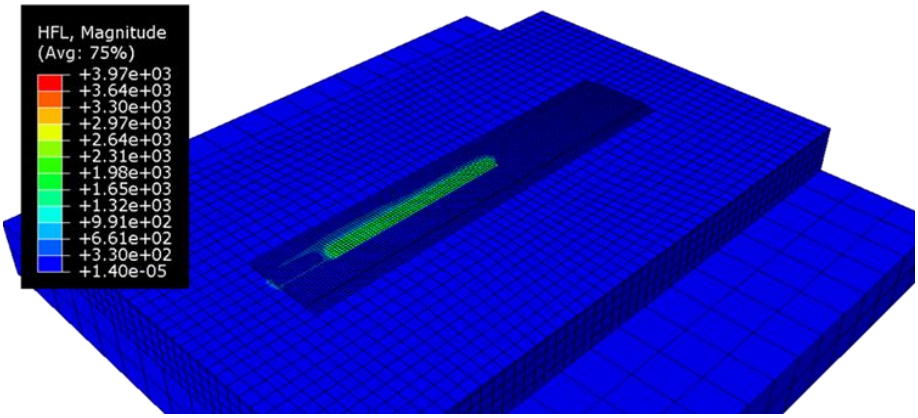

Figure 52: Visual demonstration of the integrated heat source model.

Heat loss is taken into account within the model in two ways – firstly, a user-defined film condition on the exterior surfaces of the fixture and substrate, as well as the evolving surfaces of the build part; and secondly, a temperature-dependent surface film condition on the base of the thermocouple fixture. Film conditions are used within Abaqus to define the heat loss on surfaces or element sets, by prescribing a heat transfer coefficient and sink temperature. The film condition on the evolving exterior surfaces is achieved through the use of progressive cooling by specifying an element based film condition directly within the input file, as described within the Abaqus documentation (Dassault Systemes, 2019). User-defined settings were chosen and a UFILM subroutine was used to implement the combined heat transfer equation, shown in Equation 24, where ε is the material emissivity, and, T is the temperature in degrees Kelvin. This equation has been used in literature (Yongjie, et al., 2012; Hu & Kovacevic, 2003; Alimardani, et al., 2007), and reduced the number of parameters required for calibration.

$$h_c = 2.41 \times 10^{-3} \varepsilon T^{1.61}$$

Equation 24: Combined heat transfer equation (Yongjie, et al., 2012).

A temperature dependent surface film condition was implemented on the base of the fixture to account for heat loss from the fixture to the bench. Temperature dependence was eventually implemented as a result of calibration studies. Initially, constant heat loss coefficients were implemented, however, this did not show the same concavity of the cooling curve as that seen experimentally. It is thought the temperature dependence of the film condition accounts for any variation in temperature within the surface of the bench resulting in how effectively heat is removed from the fixture. For example, as the build is deposited it is clear from the thermocouple data that the temperature at the interface between the substrate and fixture can reach upwards of 200°C. If this influences the temperature of the surface below the fixture, ie. the bench, and causes this to heat up also, this will change the effective ambient temperature below the surface, altering the rate of heat loss. The temperature dependent heat transfer

coefficient, was calibrated along with the material emissivity. The final value of emissivity implemented was 0.3, and the resultant temperature dependent heat transfer coefficient for the bottom surface of the fixture is shown in Figure 53.

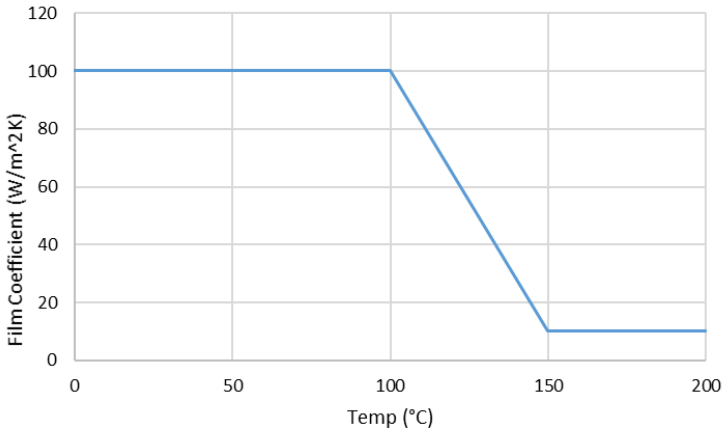

Figure 53: Temperature-dependent heat transfer coefficient.

Following the establishment of modelling methods presented here, the next stage of the modelling process was to calibrate the laser efficiency for each sample. Thermal models using the integrated heat source model were used for this to increase efficiency. Mesh and time increment sensitivity studies were undertaken to determine the suitability of the fixed time increment and mesh size choices. Firstly, a time increment sensitivity study was undertaken to determine a suitable fixed time increment for the integrated heat source model. The results of the thermal profile, at one of the central thermocouple locations is shown for 4 different fixed time increments in Figure 54. There is an obvious lack of accuracy for the largest time increment, however the remaining three are very similar. The model run using the smallest increment did not complete due to convergence errors. Therefore, the second smallest time increment of 2.5s has been chosen as the fixed time increment within these studies.

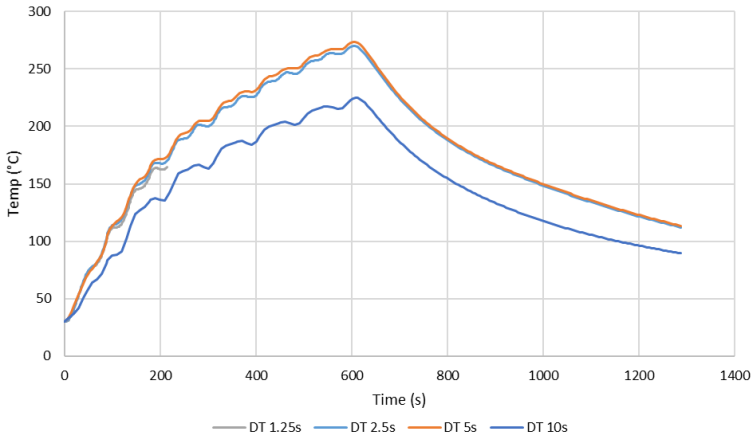

Figure 54: Time sensitivity study for integrated heat source models.

Subsequently, a variety of mesh sizes were tested for each different component of the assembly. The combinations investigated, along with resulting run times (undertaken on the NSIRC-Brunel server with 24cpus) to simulate the full deposition, are shown in Table 17. Again, the resulting thermal profile at a central thermocouple for each mesh combination is shown in Figure 55. The mesh combination used for Model 1 was ultimately chosen for use in the final models.

Model	Wall (mm)	Build Plate (mm)	Fixture (mm)	Run time (hh:mm:ss)
Model 1	1	4	12	00:34:20
Model 2	0.5	4	12	03:32:07
Model 3	1	2	12	01:12:18
Model 4	1	1	12	12:26:24
Model 5	1	8	12	00:37:00
Model 6	1	4	8	00:33:40
Model 7	1	4	4	00:38:00

Table 17: Mesh combinations investigated as part of the mesh sensitivity study.

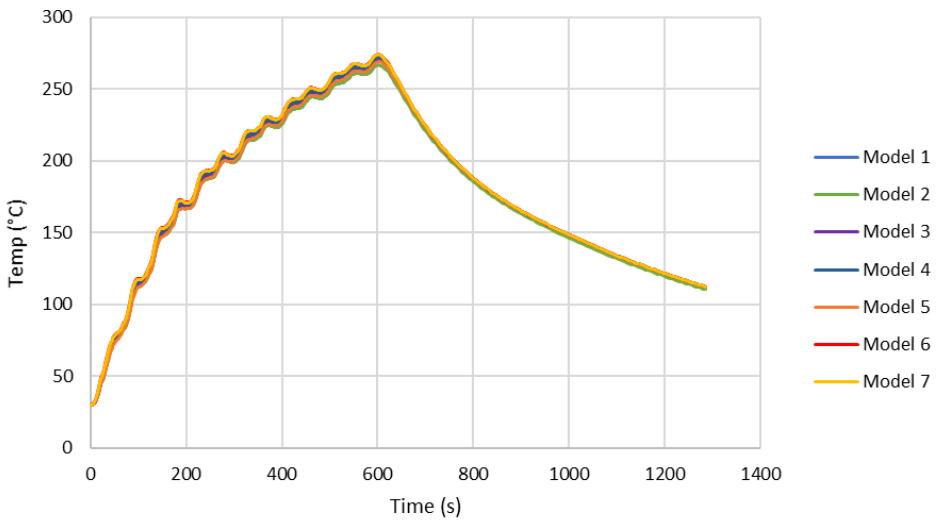

Figure 55: Results of mesh sensitivity study.

Calibration of efficiency was undertaken individually for each step. Upon initial investigations it was discovered that the use of a single value of efficiency throughout the deposition meant that the thermal profile was over predicted in certain layers and under predicted in others. This is sensible as there are a number of reasons absorptivity may differ within the height of the build. For example, the heat sink effect introduced by the substrate and proximity to the substrate within lower layers may lead to an increase of energy lost to the surrounding plate. Furthermore, the material absorptivity may be variable with temperature and therefore, differ throughout the height of the build as the temperature of the part increases. Therefore, it was decided that efficiency would be defined as a function of layers. Calibrations were undertaken with the aid of the design of experiments software, Design-Expert 12 (StatEase, 2022). Five simulations were run with varying values of efficiency. The regression analysis tools within Design Expert were then utilised to predict the most suitable value by comparing the simulated temperature at the end of the layer with the corresponding experimental value for three of the thermocouple measurements. Initially, layers were calibrated individually. This however resulted in excessive over prediction of peak temperatures. Ultimately, the first two layers of each sample were calibrated individually as these were influenced more severely by the presence of the substrate. Subsequent layers were then calibrated in pairs. Given the scan strategy involves offsets within the even layers to fill in the troughs of the previous layer it is natural to consider the layers in sets of 2. The resultant efficiency values are shown in Table 18.

Layer	Sample A	Sample B	Sample C
1	0.189	0.391	0.329
2	0.253	0.614	0.427
3	0.314	0.523	0.561
4			
5	0.457	0.538	0.522
6			
7	0.336	0.503	0.532
8			
9	0.489		0.515
10			
11	0.405		
12			
13	0.67		

Table 18: Calibrated efficiencies as a function of layer for each sample.

The calibrated thermal profiles are shown in Figure 56 to Figure 58. Experimental thermocouples are labelled ‘TC_x’, simulated thermocouple locations are labelled ‘TCx’. The results generally show a good agreement between thermal simulations and experimental data. The rate of increase of temperature at the location of the thermocouples is accurately represented, and the rate of cooling agrees well, particularly for sample B and C. Whilst some thermocouples are over predicted and others under predicted, for example thermocouple 2 and 15 in sample C, the overall spread and peak temperatures of the thermocouples are well represented. Thermocouple 0, is the least accurate amongst the results, but as this is the thermocouple furthest from the centre of the build, it is less representative of the region of interest. Some of the inaccuracies seen could also be influenced by experimental uncertainties such as thermocouple contact, as well as the positioning of the deposition on the build plate. Whilst efforts were made to make this central, a variation in alignment could lead to uncertainty of thermocouple locations with respect to the build.

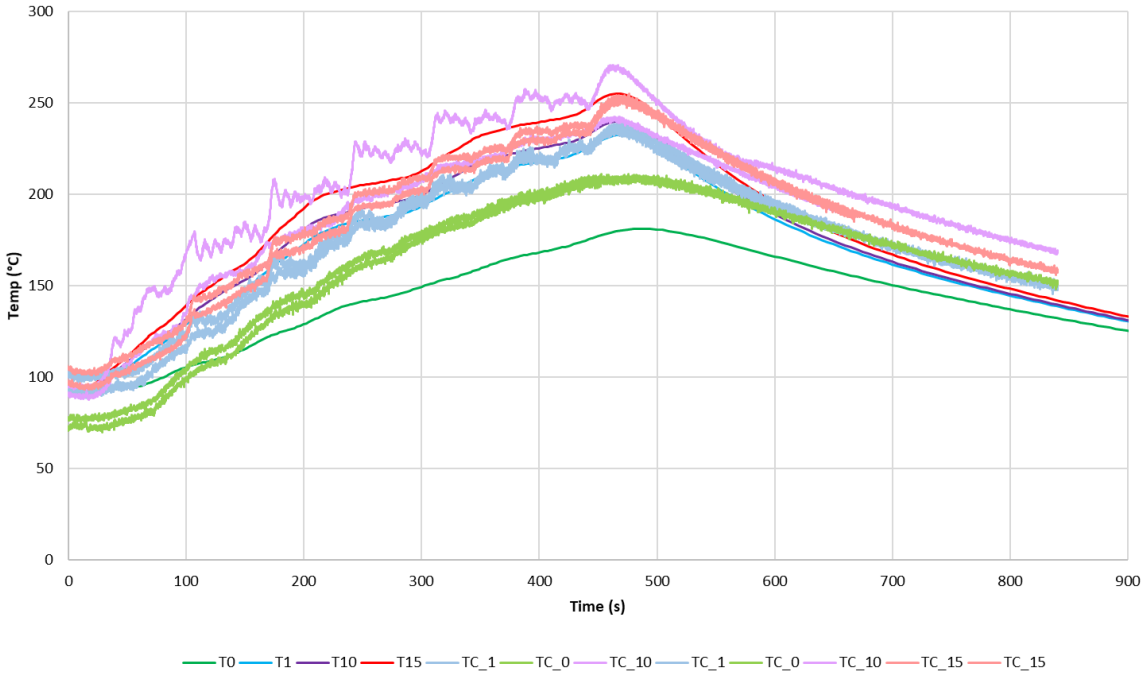

Figure 56: Calibrated coarse-level thermal models for Sample A compared to experimental data.

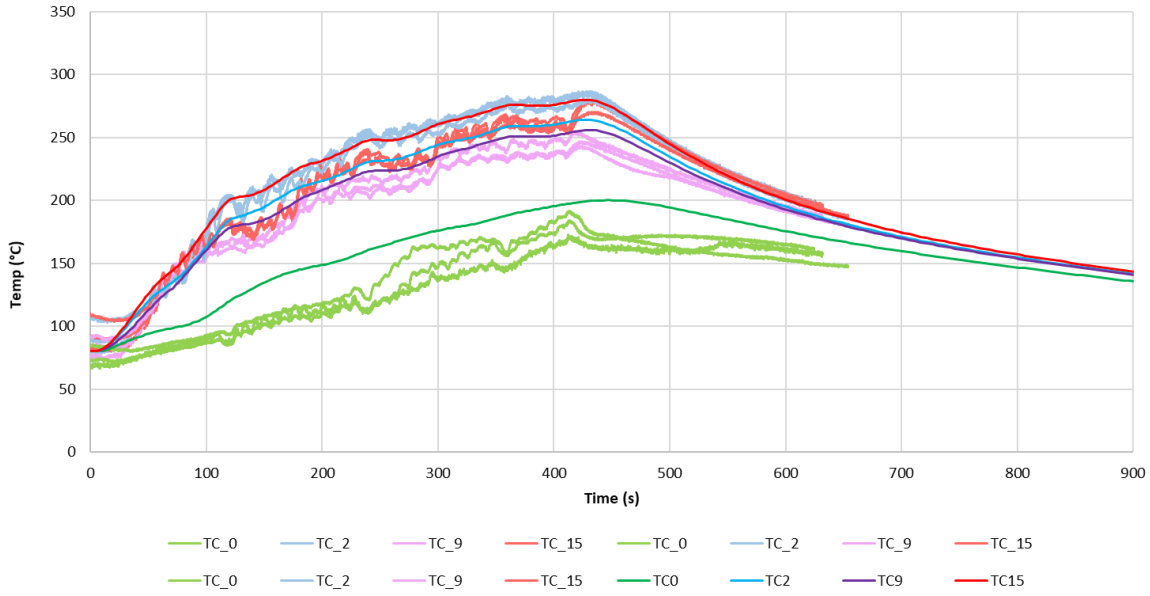

Figure 57: Calibrated coarse-level thermal models for Sample B compared to experimental data.

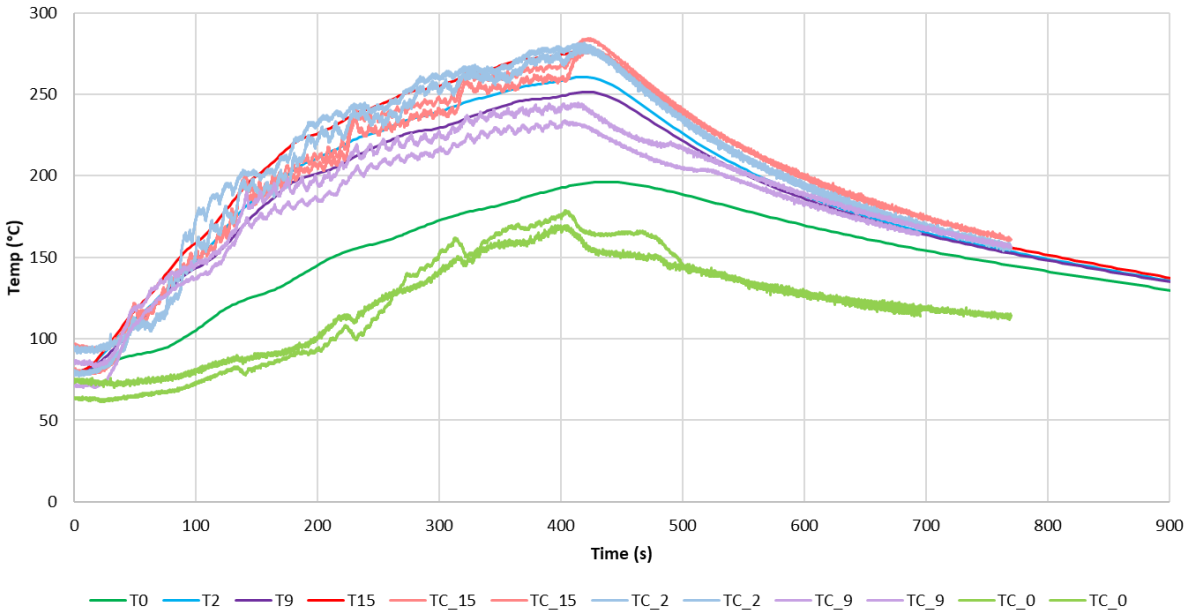

Figure 58: Calibrated coarse-level thermal models for Sample C compared to experimental data.

The intended approach for the fine level thermal models as input for the microstructure simulations, was to combine the two heat source approaches. Within this approach, each layer would be deposited within a separate model, allowing for refined mesh and incrementation methods within the region of interest. The integrated model would be used to provide predefined fields of the thermal field prior to the deposition of the layer of interest. Furthermore, a coarse mesh was used at either end of the build part, whilst a finer mesh was implemented within the central region of the build, based on the principle that there would be a weaker influence, on the region of interest, when the source is further away. Within the coarse region the integrated heat source was used, with a transition into the conical heat source for finer resolution within the central region of interest, where 2D planes were to be taken for solidification predictions. A correction factor would be applied to the calibrated efficiencies when applied to the conical heat source model, in order to account for the difference in thermal profile witnessed when simulating the model through the implementation of an integrated heat source versus a volumetric conical heat source. Preliminary test models were undertaken for this approach and an example can be seen in Figure 59. Whilst the use of the integrated heat source increases computational efficiency, these models still took approximately a day to run a single layer on a computer server with 8 cpus. Whilst this is not uncommon within industry for numerical models, unexpected problems with the computing resources available to this project meant that these models were unable to be completed.

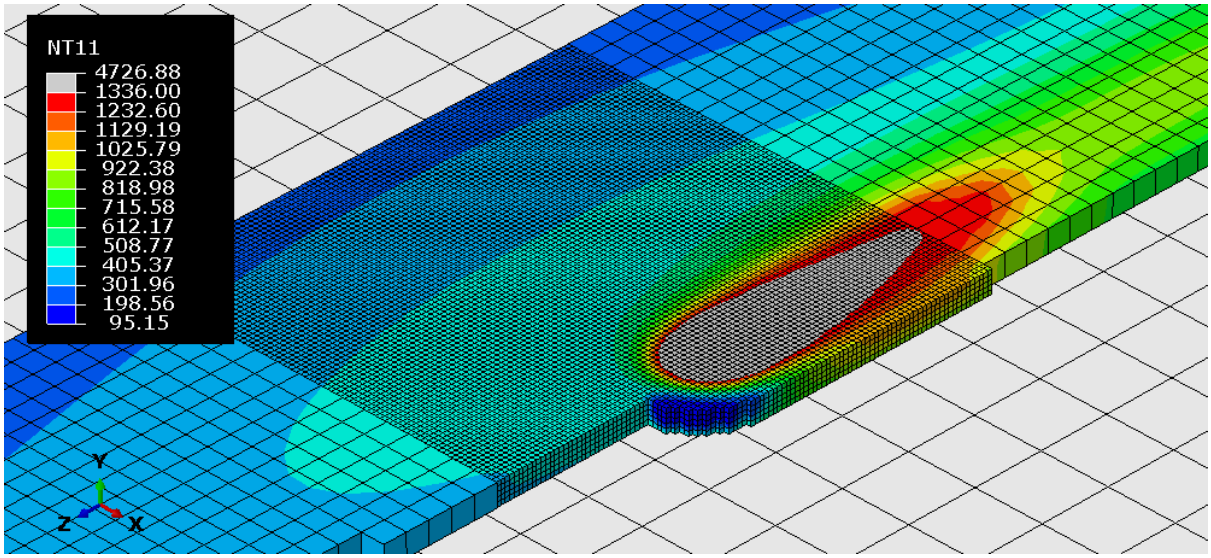

Figure 59: Coarse to fine heat source transition.

6.4 Alternative Thermal Models

Due to a significant lack of available computational resources, simpler, more efficient modelling methods needed to be implemented. As the computational resources were not available to run a finite element model with high enough fidelity within the melt pool for use in the microstructural simulations, an alternative method of predicting the thermal history was required. Therefore, analytical thermal solutions were implemented. This meant that the main objective of this work, to demonstrate and assess the capabilities of the microstructural model, could still be achieved, although more efficiently and with significantly less powerful computational resources.

The Rosenthal solution is by far the most commonly used analytical solution for thermal models of welding and additive manufacturing applications. The defining system of equations, which is given in Equation 25, describes the resulting thermal profile of a stable melt pool based on a moving point heat source. Within these equations the x-axis is assumed to be scan direction, and y and z perpendicular to this, whilst V represents the scan speed, P the laser power and λ the efficiency. The material properties required are the thermal conductivity, k and the thermal diffusivity, α. Finally, the ambient temperature is represented by T_0.

$$T = T_0 + \frac{\lambda P}{2\pi k r}\exp\left(-\frac{V(r+\xi)}{2\alpha}\right) \quad \text{(a)}$$

$$r = \sqrt{\xi^2 + y^2 + z^2} \quad \text{(b)}$$

$$\xi = x - Vt \quad \text{(c)}$$

Equation 25: Equations required to define the Rosenthal solution (Promoppatum, et al., 2017).

The use of the Rosenthal solution provides the much required efficiency to undertaken fast microstructure predictions with limited computational resources. This is because it removes the need for fine-level finite element thermal models to resolve the thermal history within the melt pool, and moreover these do not need to be imported into the microstructure models and interpolated onto the CA mesh. The analytical thermal model can also be implemented in such a way that is representative of the experimental deposition strategy. Techniques such as superposition of the analytical solutions can also be used to adjust the melt pool geometry defined by the model. However, such methods have not been used explicitly within this work, as limited melt pool information is available for calibration, but also by not extensively calibrating the melt pool geometry against experimental measurements, one can assess if the modelling approach could actually be used at the design level, without the need for supporting experimental trials.

Nevertheless, by using an analytical solution there are obviously a number of simplifications and assumptions that are made within the model (Hekmatjou, et al., 2020; Eagar & Tsai, 1983). For the Rosenthal solution, these include:

- The heat source is assumed to be a point heat source.
- Temperature-independent material properties are used.
- The heat source is applied to a semi-infinite domain.
- Heat loss due to convection and radiation is not accounted for.
- Temperature changes as a result of latent heat of fusion is not included.

The assumption of a point heat source means that there is no way to account for the experimental beam diameter or distribution without undertaking calibration of the superposition of multiple sources as mentioned earlier. Furthermore, the use of constant material properties is a simplification on the material properties we have previously identified. Similarly, the lack of inclusion of latent heat of fusion will influence the accuracy of the thermal profile and melt pool geometry. Despite this, Promoppatum et al. (Promoppatum, et al., 2017) displayed the similarity between finite element models of laser powder bed fusion and the Rosenthal solution. Whilst the effects of the assumptions made should be noted and taken into consideration within any model that uses the Rosenthal solution, it is expected that the Rosenthal solution will still provide a suitable level of accuracy to determine changes in solidification grain morphology at the level predicted by the cellular automata approach. This would probably not be the case for phase field predictions that predict microstructure characteristics on a much finer scale and require a much more in depth physical basis. Furthermore, as efficiency is of significant importance, particularly at the design level, this study will identify if the Rosenthal solution can provide enough accuracy to predict solidification

microstructures and their variations as a result of process parameters, to ultimately determine if this efficient modelling approach could be used for the design of AM parts.

An additional benefit of using the Rosenthal solution, is that by the nature of being an analytical solution, equations for a number of features such as melt pool geometry can be derived. The derivative equations used to calculate melt pool width, W, depth, D, and length, L, are presented here within Equation 26. Being able to estimate these characteristics is useful when determining suitable dimensions for models, as well as comparing various characteristics between samples when trying to understand the underlying cause of microstructure variations. In the following equations, in addition to the parameters defined for Equation 25, ρ and C are the material density and specific heat respectively, whilst T_m represents the melt temperature.

$$2D = W \approx \sqrt{\frac{8}{\pi e}\frac{\lambda P}{\rho C V (T_m - T_0)}} \qquad \text{(a)}$$

$$L \approx \frac{\lambda P}{2\pi k (T_m - T_0)} \qquad \text{(b)}$$

Equation 26: Approximation of melt pool width (a) and length (b) (Promoppatum, et al., 2017; Tang, 2017)

Property	Value	Units
Density	8.22	kg/m^3
Conductivity	11.4	W/mK
Specific heat	435	J/kgK

Table 19: Temperature-independent material properties for IN718.

The constant material properties used for the IN718 deposit are shown in Table 19. These values were found within literature (Promoppatum, et al., 2017). Room temperature properties for SS304L were also obtained from MPDB, the material properties database. The melt pool shape as a result of using SS304L properties within the substrate was investigated. Figure 60 shows the resulting melt pool shape under this assumption compared to the shape when the IN718 properties are also assumed for the substrate. The change in material properties clearly results in a disjoint melt pool shape along the interface. Upon implementation of this thermal profile within the microstructure models, it was found to have an adverse effect on the microstructure simulations. This was believed to be because of the discontinuous thermal gradients imposed within the melt pool. Therefore, the final simulations have all been undertaken assuming all material has the same, IN718, material properties. This assumption will have some influence on the first layer of deposition, when compared for example to the equivalent finite element model. However, this influence is expected to be less significant than the simulation using a discontinuous thermal profile.

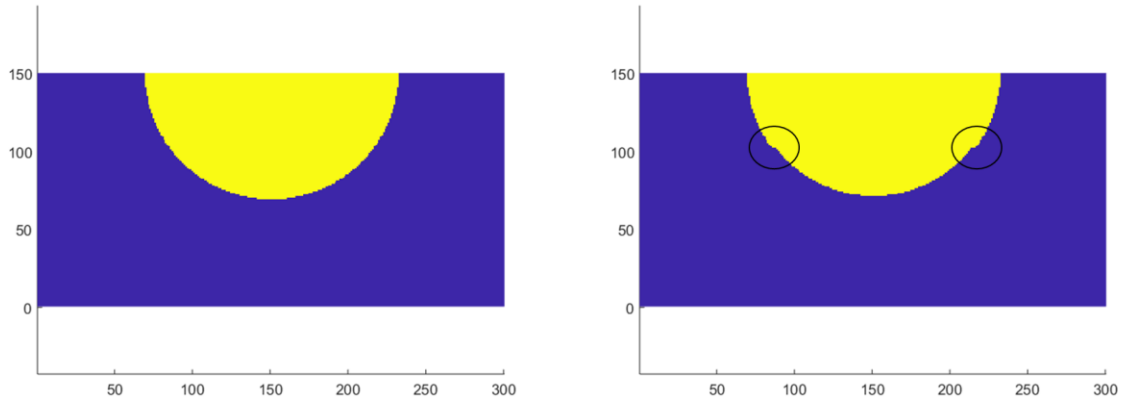

Figure 60: Comparison of melt pool shape, with (left) and without (right) inclusion of stainless steel properties within the build substrate.

The efficiency values determined for the finite element models were considered for the simulations - however not all were suitable for the application of the Rosenthal solution, resulting in lack of fusion. Instead, the approximate depth of the melt pool was determined from the upper most melt pool on each macrograph (Figure 43 to Figure 45). This was used to calculate the expected efficiency using Equation 26. A value of 0.598, 0.614 and 0.596 were calculated for sample A, B and C respectively. Consequently, an average value of 0.6 was used throughout this study. Using this efficiency the resulting approximate melt pool dimensions for each sample is given in Table 20. Various other quantities such as the ratio between horizontal overlap to melt pool width are also calculated to help provide insight into certain aspects of the microstructural development.

Sample	Experimental Depth (mm)	Approx. Depth (mm)	Approx. Length (mm)	Ratio of D to L (%)	Horizontal overlap (mm)	Ratio of overlap to W (%)	Vertical overlap (mm)
A	1.64	1.64	19.168	8.57	0.885	26.94	0.683
B	2.35	2.32	19.168	12.12	2.046	44.03	0.563
C	1.89	1.90	19.168	9.89	1.393	36.73	0.577

Table 20: Simulated melt pool dimensions for all samples.

6.5 Microstructure Modelling Approach

As discussed above, due to issues with modelling resources, the developed cellular automata code was converted from the Fortran user subroutine, implemented within Abaqus, into a MATLAB script. This allowed the microstructure models to be run locally on a personal pc without the need for remote servers. Furthermore, due to the matrix and vectorisation functionalities that can be exploited within MATLAB, this significantly increased the computational efficiency of the CA code and decreased required run time. It should be highlighted that similar analytical predictions of a single grain were completed on the

developed MATLAB code as those presented in section 4.6 for the Abaqus subroutine to validate the implementation of the microstructure model within MATLAB. Typical run times of each plane for sample A is given in Table 21. These are the run times taken to complete the simulations on a personal laptop with a 2.5Ghz cpu and 8GB ram. As models were completed in MATLAB, simulation records detailing run time were not created as with Abaqus files; however the elapsed wall clock time was recorded for the simulation of each plane for sample A. It should be noted that as similar approaches were taken for sample B and C, whilst run times may vary due to differences in travel speeds and cooling rates, they will typically remain of a similar magnitude.

The dimensions of the 2D domains used within the simulations is given in Table 21. The height of the domain was taken to be the number of layers multiplied by the layer height, with an additional two layers included to account for the build substrate. Layer heights were kept as defined in Table 16 except for the layer height within samples C. This was altered slightly to account for the mesh size. A mesh size of 40μm was implemented across all the microstructure models presented here. This was chosen as a step size of 20μm was used within the experimental EBSD images, however when preliminary investigations were being undertaken for the CA simulations within Abaqus, it was determined that at this mesh size for the full build height and width this would be too computationally expensive. Therefore, the decision was made that by doubling the step size, a significant increase in computational efficiency could be achieved for a relatively small loss in resolution. Consequently, for sample C, the layer height of 1.77mm is not divisible by 0.04mm. In fact, the layer height is not divisible by any sensible mesh size of similar magnitude. Therefore, the layer height was reduced slightly to 1.76mm to allow appropriate mesh discretisation. The width of the domain for the XY and XZ were determined to allow four scans on an odd layer, resulting in three infill scans within even layers. This was chosen as it was too computationally expensive to complete the simulation on the full domain, even increasing the domain by an extra scan in each layer results in a run time increase from approximately 3 hours to approximately 15 hours, whilst the added width provided little benefit to the prediction of microstructural characteristics. The run time has since been reduced since this check. Consequently, a four scan width was implemented as it was determined that this provided sufficient material to simulate the effects of melt pool overlap and infill, whilst ensuring enough material was sufficiently far from the boundary to be influenced severely by any boundary effects. A length of 7mm was chosen for the z direction as this allowed sufficient length to simulate enough material within the scan direction such that the overall domain was not heavily influenced by boundary effects, whilst compromising with run time. It should also be noted that run time can be significantly impacted

by the frequency of outputting matrices as images to visually witness the progression of the simulation.

Sample	Plane	X (mm)	Y (mm)	Z (mm)	Cell Spacing (mm)	Total no. of elements	Approx. run time (hh:mm:ss)
A	XY	11.2	14.36	0.0	0.04	101441	01:21:09
	XZ	11.2	0.0	7.0	0.04	49456	00:15:29
	YZ	0.0	14.36	6.96	0.04	63000	00:30:02
B	XY	13.0	15.8	0.0	0.04	129422	
	XZ	13.0	0.0	7.0	0.04	57376	
	YZ	0.0	15.8	6.96	0.04	69300	
C	XY	11.2	14.48	0.0	0.04	102284	
	XZ	11.2	0.0	7.0	0.04	49456	
	YZ	0.0	14.48	6.96	0.04	63525	

Table 21: Dimensions of model domains for each principal plane within each sample, and approximate run times.

The models were assumed to be taken from the centre of the build in each direction as demonstrated by Figure 61. Consequently, within the XY plane models, alternating layers of 4 and 3 scans for the full build height of the geometry were simulated. An offset was applied on even layers to fill in the troughs of the previous layer as shown by the deposition strategy demonstrated in Figure 38. The XZ plane was simulated by modelling the deposition of an odd layer (4 scans) followed by the subsequent two layers, to show the effects of re-melting caused by the deposition of the following layers. Finally, within the YZ plane it was assumed that the plane is taken from the centre of the build. Therefore, as 8 scans are present, within the experimental deposition of sample A and C, within each odd layer two scans, offset on either side of the plane by the hatch spacing, were simulated travelling in opposite directions. The subsequent layer then simulates the deposition of a bead centred on the plane. This is representative of the experimental deposition strategy undertaken.

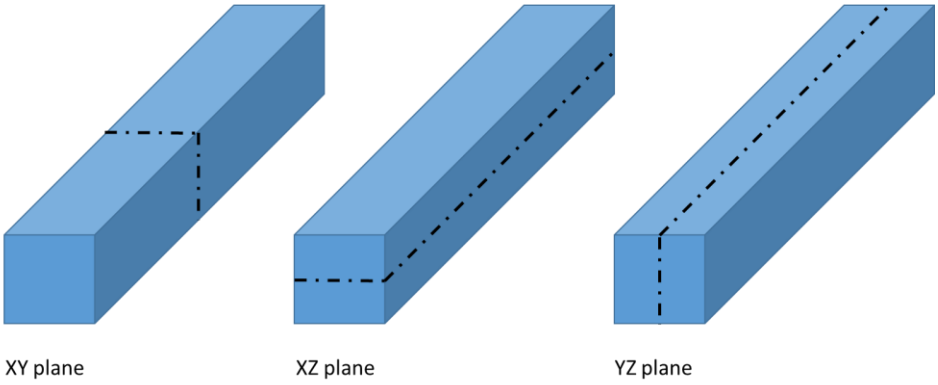

Figure 61: Demonstration of various planes for CA models.

Calibration of substrate microstructure was achieved by altering the nucleation parameters used to initiate the substrate. As experimental data regarding the grain size within the substrate was not readily available, the nucleation parameters were chosen to achieve a suitable level of visual agreement with the grain size seen within the substrate present on the resultant EBSD images. The final parameters used were a critical undercooling of 7.5, a standard deviation of 1.5 and a nucleation density of 1e4. For the substrate initiation a time increment of 0.001s was used. The initial microstructure within the XZ plane was introduced with a much larger grain size, this is because it is assumed that the simulation plane is taken from the middle of the sample, at which point the microstructure will have coarsened significantly from the substrate microstructure. A critical undercooling of 17.5 was used for this.

For the simulation of the actual additive process, a critical undercooling of 9.5 has been applied with a standard deviation of 2.0, as reported in literature for microstructure modelling of IN718 (Lian, et al., 2019). Various values of nucleation density have been investigated within the study. The automatic incrementation approach, seen in Equation 21 with a scaling factor of 1, was applied during deposition, limiting the time increment by growth velocity and cell spacing whenever liquid cells were present.

6.6 Results

Within this section the results of the microstructure simulations are shown and compared to the experimental EBSD images. For clarity, the simulated and experimental results for each of the principal planes will be presented within a separate section. Post-processing of the simulation results has been undertaken, within MATLAB, to provide the visual results presented here. Namely, the resulting matrix of grain orientation values has been converted into a visual representation of the grain structure through the use of the contourf function. The colour map ‘hsv’, Figure 62, has been implemented, as this is offers a wide range of colours to help distinguish between various grains. Furthermore, the colouring is similar to that of the

EBSD imaging. However, perhaps most importantly, the colour distribution is continuous and therefore, the assumption can be made that similarly coloured grains have similar orientations, within the 2D plane making it easier to draw conclusions based on grain orientation. As the 2D grain orientations vary from 0 to π/2, these will be the approximate limits of the colour scheme. A total of 314 divisions have been requested for this colour map, resulting in approximately one colour per 0.005 radians. Within these results, qualitative comparisons will be undertaken. Quantitative comparisons, such as those given in chapter 5, will not be undertaken due to the complexity of the grain morphologies and images compared.

Figure 62: MATLAB hsv colour map (MathWorks, 2021).

One of the main objectives within this section is to investigate the capabilities of the 2D CA model. Solidification, by nature, is a 3D mechanism, however, as discussed, a fully 3D CA-FE model is too computationally expensive to be undertaken here. For this reason, 2D cross-sections in all 3 principal planes, similar to that in the work by Akram (Akram, et al., 2018), are simulated to determine if the 2D approach can be used in this way to capture 3D aspects. This is particularly important as certain 3D aspects such as out of plane growth cannot be accounted for intrinsically within the 2D models. Whilst the results of chapter 5 validate the use of the 2D model without bulk nucleation, the inclusion of nucleation was deemed necessary throughout this study and results with and without nucleation will be discussed.

6.6.1 XY Plane

Firstly, the simulations of the solidification microstructure within the XY plane are presented for all samples with and without nucleation (as discussed above). Some regions of the modelling domain have been cropped from the models shown below, to remove regions significantly influenced by boundary effects. Approximately the width of one melt pool has been removed from either side of the domain to focus on the more representative material within the centre of the domain.

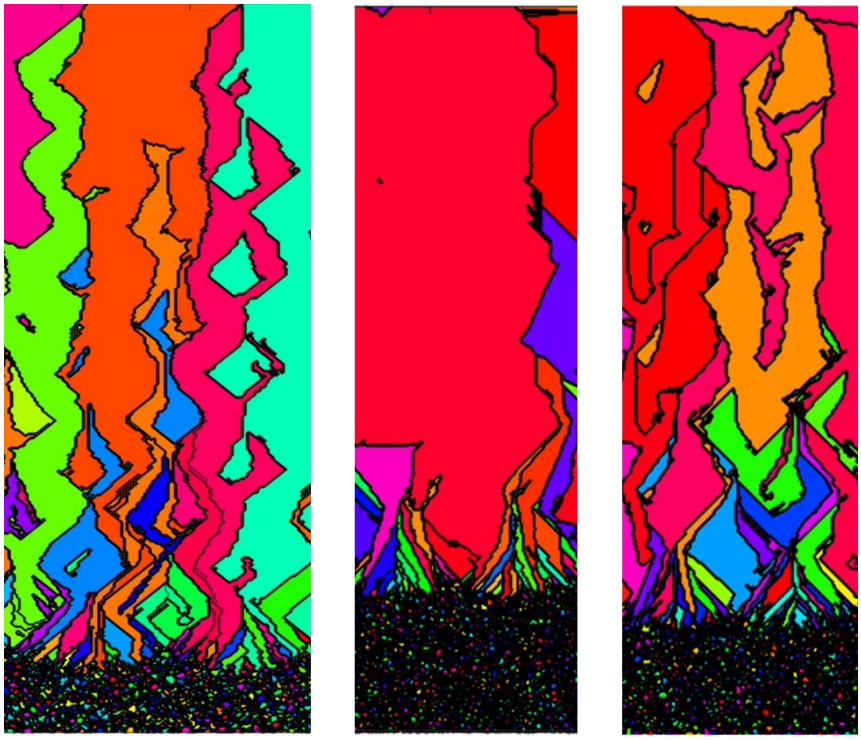

Figure 63: Microstructure predictions in XY plane without nucleation; sample A (left), B (middle), C (right).

The numerical results shown in Figure 63 already show clear changes within the microstructure as a result of the changes in travel speed. In particular, all samples clearly demonstrate elongated columnar growth. This occurs through grain growth competition. As the grains with larger grain envelopes, due to orientation and undercooling, capture surrounding cells, other grains seize to grow and the number of grains present dramatically reduces from that seen within the substrate. Whilst in sample A and B these are seen throughout the entire length of the build height, the columnar grains within sample C are shorter. Elongated columnar grains are consistent with the experimental images for all three sample A builds, as shown in Figure 64. The individual images shown here, show a good level of repeatability of grain structure across the repeated samples of the deposition. However, elongated columnar grains throughout the height of the build are not witnessed in sample B, Figure 65, where grains have a smaller morphology typically contained within discrete melt pools. Sample C, Figure 66, almost shows a combination of the two structures, which is logical as sample C was deposited using a travel speed that is the mean of the travel speed for sample A and B.

Throughout all three experimental samples, columnar grains, in red, are shown in vertical lines throughout the sample. These become more prominent with an increase in scan speed, with sample A demonstrating large strips of similarly aligned vertical grains. According to the legend of the EBSD, red denotes alignment of the octahedron with the build direction. Green shows an orientation approximately at 45 degrees to the build direction. Therefore, it is

expected that the red strips are developed through growth vertically from the base of the melt pool, whilst the green strips (clearly seen in Figure 64) are a result of growth from the sides of the melt pool, as the melt pool solidifies radially inwards. Similarly, within the simulated microstructures, grains displayed in a red tone show grains with an angle close to 0 degrees (or π/2 by symmetry), in accordance with the colour scheme shown in Figure 62, ie. with the corner of the grain envelope aligned with the build direction. As can be seen in Figure 63 the grains that are typically elongated within each of the simulations are red (or similar tones). This corresponds to grain growth competition - that the grains aligned with the build direction and hence the thermal gradient, at the centre of the melt pool, are those showing favoured growth.

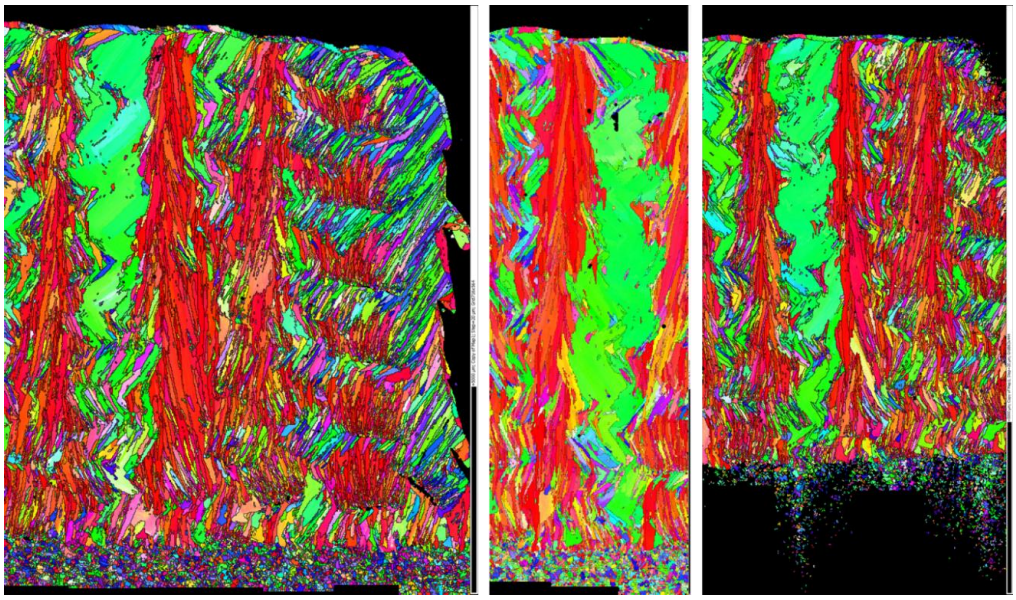

Figure 64: EBSD images for sample A in the XY plane; A1 (left), A2 (middle) and A3 (right).

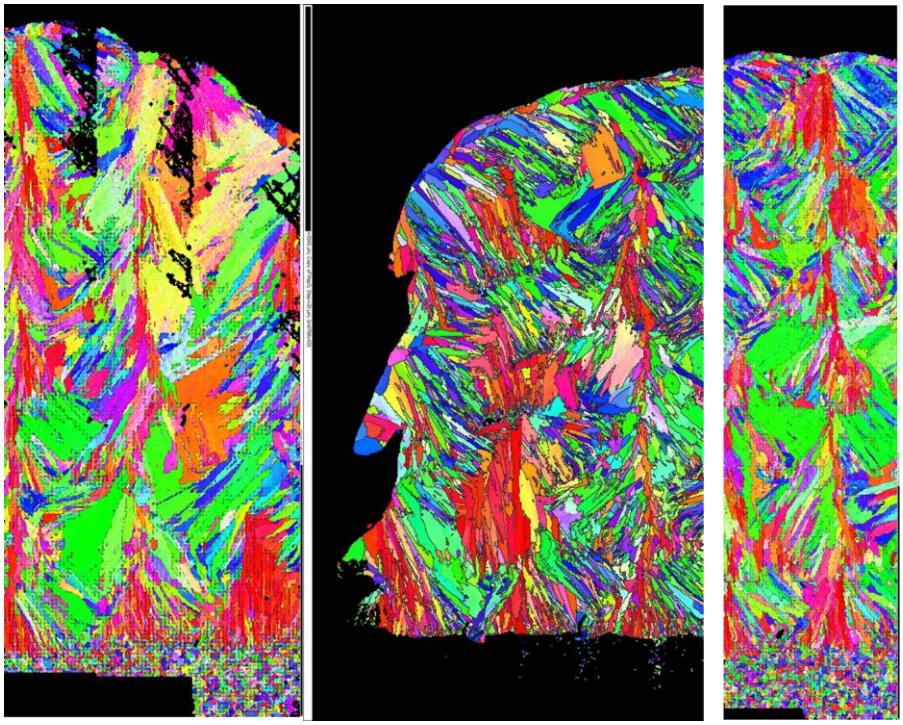

Figure 65: EBSD images for sample B in the XY plane; B1 (left), B2 (middle) and B3 (right).

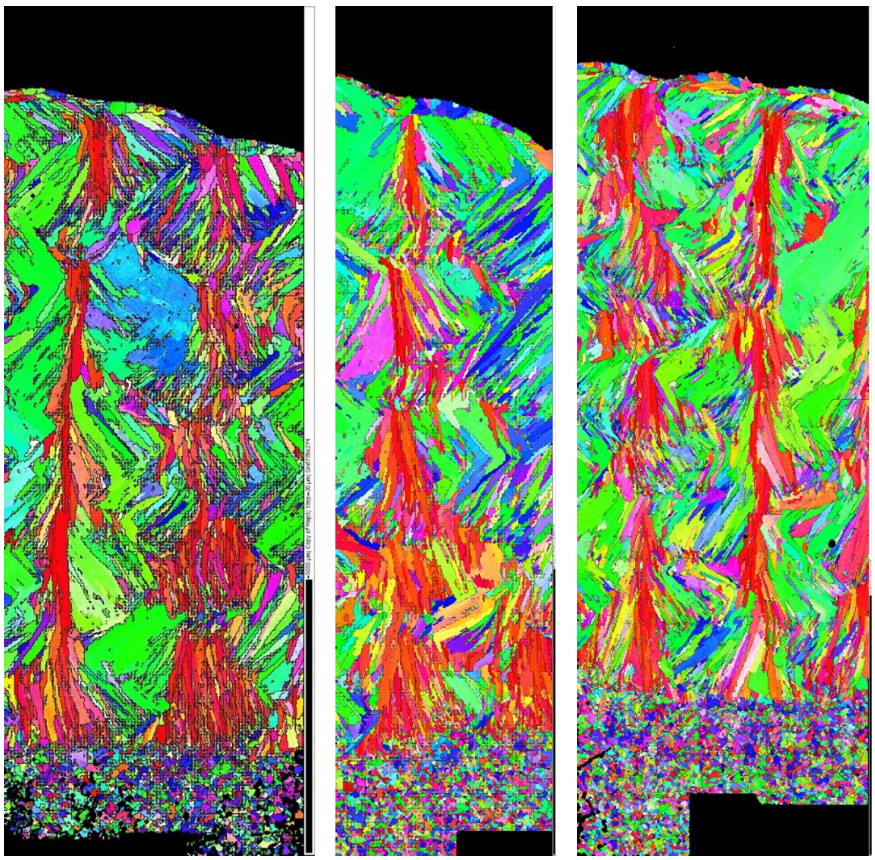

Figure 66: EBSD images for sample C in the XY plane; C1 (left), C2 (middle) and C3 (right).

Figure 63 demonstrates excessively large columnar grains within the predicted microstructure for sample B which is unlike the experimental microstructure witnessed. Repeats have been

run of this particular model to examine if this is due to the probabilistic aspects of the model. The various results are shown in Figure 67. The first two simulations show very similar structures, whilst the third shows the central columnar grain being broken up with other interspersed grains. The probabilistic aspects of the model clearly have some influence on the results, although over-prediction of the length of columnar grains in the scenario does not appear to be uncommon.

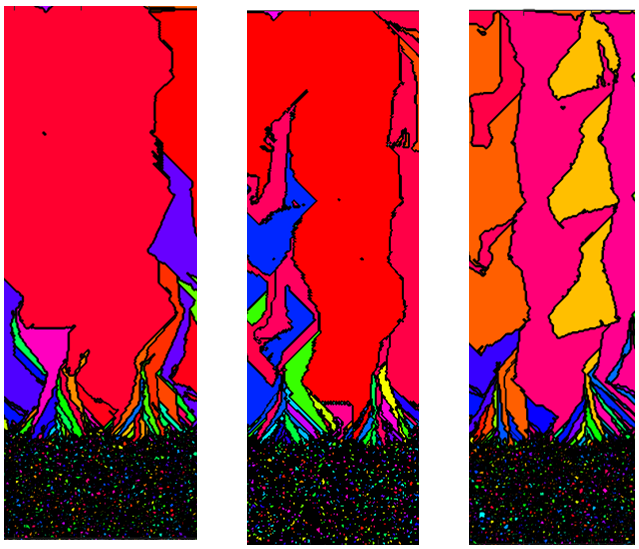

Figure 67: Effects of probabilistic aspects on sample B with no bulk nucleation.

As part of the comparison between simulated grain structures and those obtained experimentally, the angles of the elongated, epitaxial, grains that exhibit a zig-zag shape, within sample A, were measured. An average angle size of 105.9° was determined from the experimental EBSDs, as seen in Figure 68, compared to a value of 118.8° in the simulated microstructure, shown in Figure 69. This is an error of 12.1%, which demonstrated the model is capable of predicting the angle of the grain structure, as a result of the scan strategy and process parameters used here, to a suitable level of accuracy.

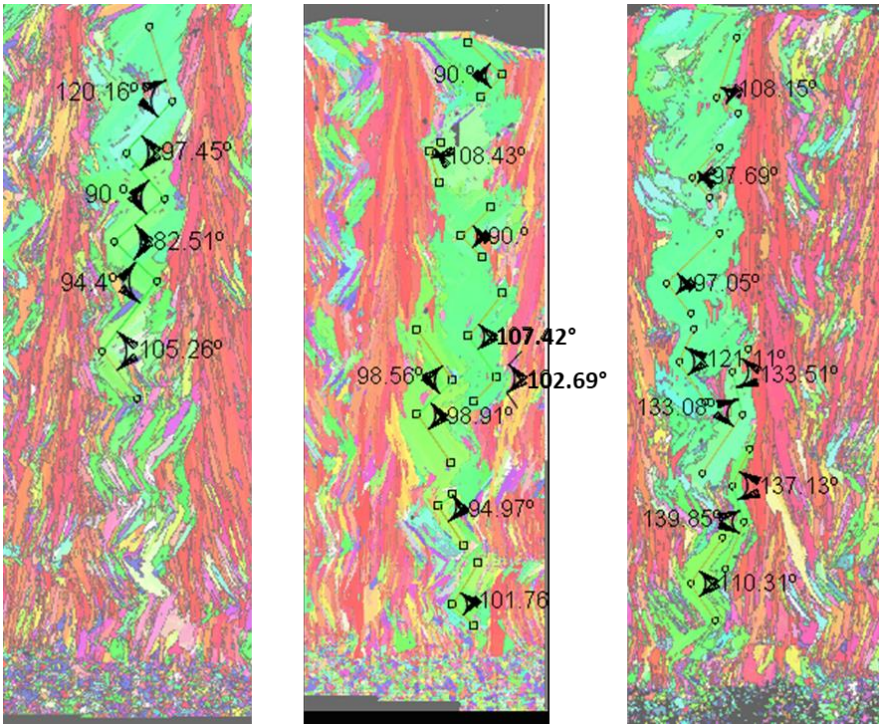

Figure 68: Experimental measurements of the large zig-zag structures in EBSD images for sample A.

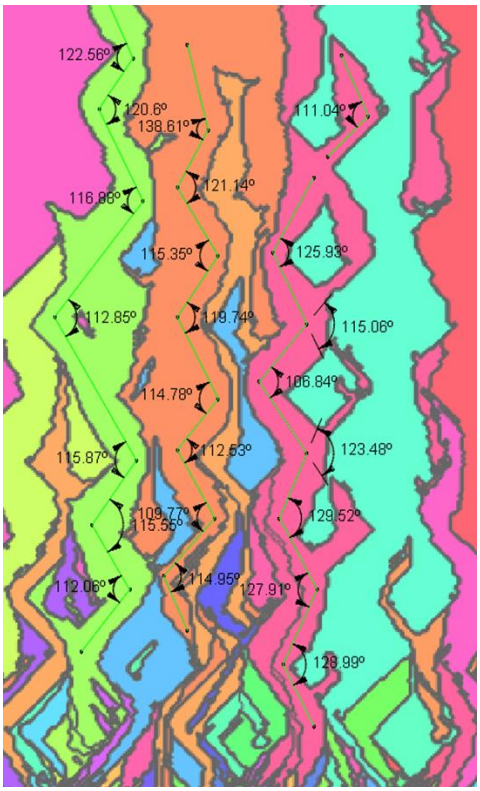

Figure 69: Measurement of the large zig-zag structures within the simulated results for sample A.

Unlike in powder bed fusion process, within direct energy deposition processes, when the material is deposited on top of existing material it is in a molten state. Hence, when solidification takes place, there is a lack of surrounding material on some surfaces of the melt

pool, particularly at the edges of the build. For this reason, when nucleation is not included within the CA models of the deposition process, large boundary effects can be experienced. This is particularly true when modelling the thermal model with conduction-based, heat transfer methods. These types of models are not capable of accurately modelling the fluid flow within the process and therefore do not accurately represent the expected bead shape within DED processes, especially on the edges of the shape where the molten material often exhibits signs of tapering. Moreover, due to the specific deposition strategy implemented within this work, that utilises an offset within the even layers to fill in the troughs of the previous layer, idealistic continuum scale models will ultimately simulate the deposition of material within the following odd layer on to material that was not activated within the previous layer. This is a direct result of more scans being deposited within odd layers than in even layers. This is obviously not representative of the physical effects that would be experienced in reality, such as gravitational force and fluid flow. Whilst this assumption, made early on within this work, is necessary to be able to undertake the modelling activities on the desired scale with a reasonable amount of computational efficiency, it is a contribution to the boundary effects experienced. This means the results are not reliable close to the boundary.

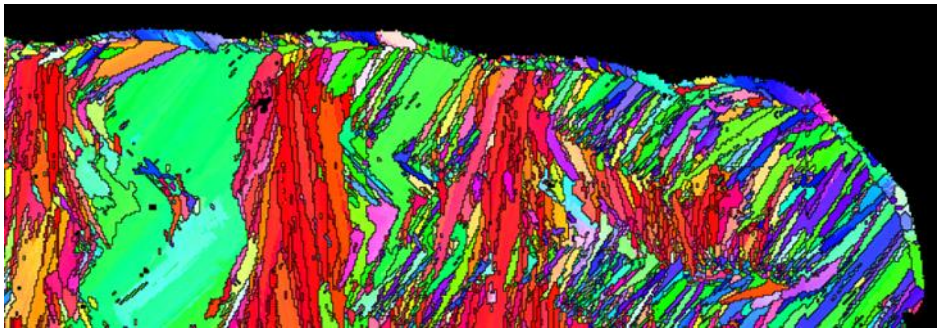

Figure 70: Equiaxed grains observed along the top surface of the deposit (taken from the XY EBSD for sample A1).

Bulk nucleation is applied within these models. The bulk nucleation applied within these simulations is expected to account for some of the introduction of new grains within the plane as a result of crystal growth from out of the plane (or surrounding material if a smaller domain is considered). These 3D effects are otherwise not accounted for within the 2D model. Furthermore, as can be seen in the experimental EBSD maps, a border of equiaxed grains is observed along the top surface of the deposited part. This is shown more closely in Figure 70. It is expected that this is as a result of bulk nucleation that takes place within the melt pool before epitaxial growth throughout the melt pool is complete, or again 3D growth from out of plane. Throughout the build the same formations are not witnessed, most likely because the re-melting of material due to subsequent passes erases this microstructure. This explains why this phenomena is only seen on the outer most surfaces of the deposit. Hence, this suggests

that the inclusion of bulk nucleation is a sensible conclusion. To address this observation and previous arguments about grain growth out of plane, two levels of nucleation density have been investigated; 1e2 and 1e4. These values were based on the value of nucleation density given by Lian et al (Lian, et al., 2019) of 1e6mm^{-3}. As the models undertaken here are in 2D this is reduced to 1e4mm^{-2}. A value of lower magnitudes have also been investigated for comparison purposes as part of a sensitivity study. The corresponding results for sample A, B and C are shown in Figure 71, Figure 72 and Figure 73 respectively. Repeats of the model with nucleation density of 1e2 are shown to demonstrate the effects of the probabilistic aspects of the model.

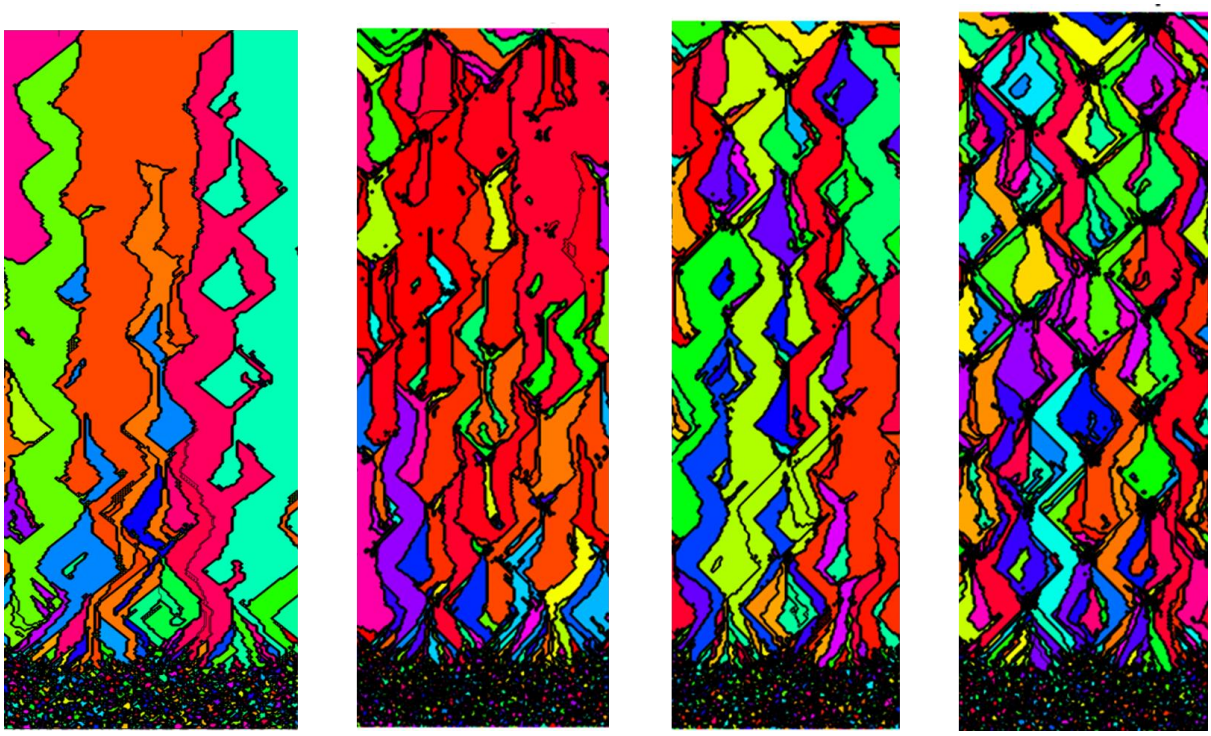

Figure 71: Microstructure simulations for sample A in the XY plane with a nucleation density of 0, 1e2, 1e2 and 1e4 from left to right.

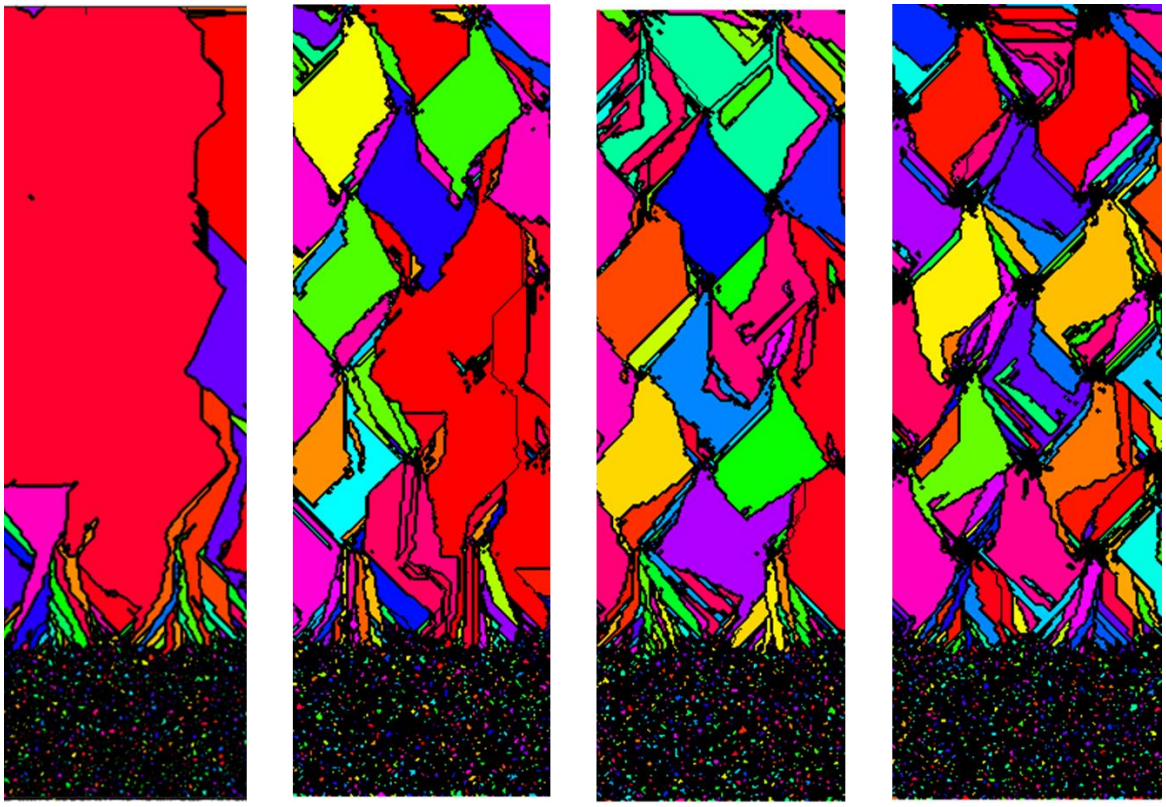

Figure 72: Microstructure simulations for sample B in the XY plane with a nucleation density of 0, 1e2, 1e2 and 1e4 from left to right.

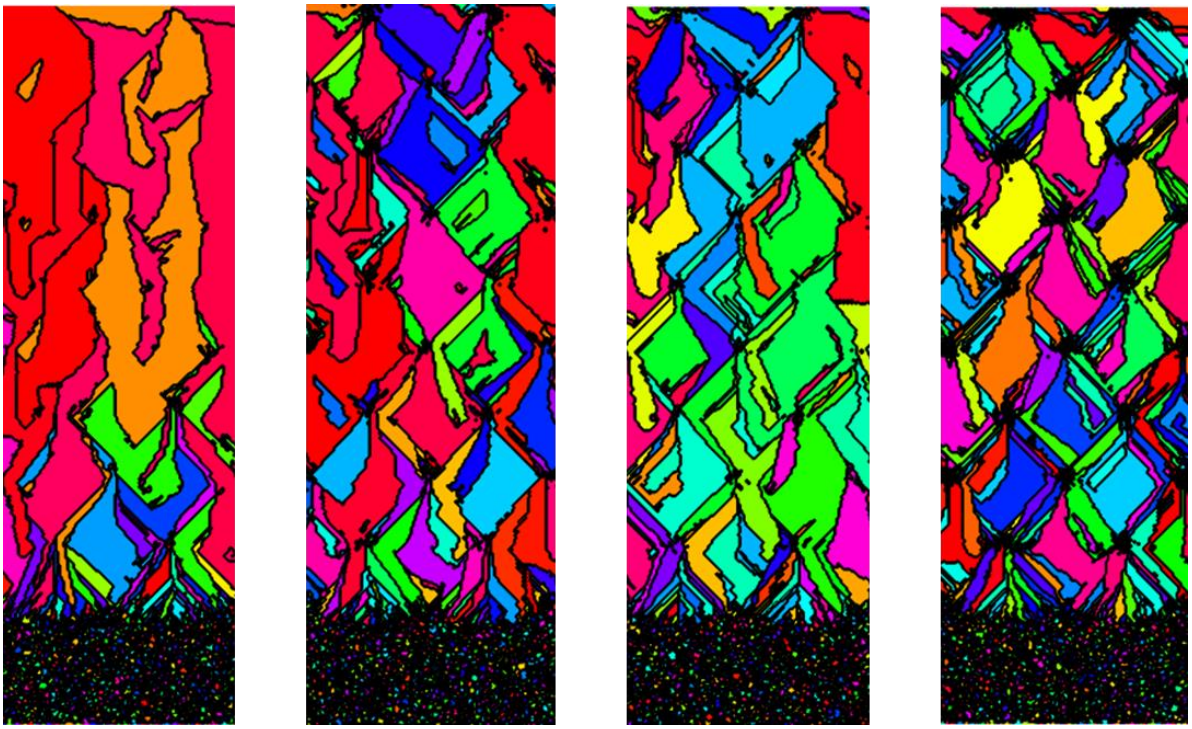

Figure 73: Microstructure simulations for sample C in the XY plane with a nucleation density of 0, 1e2, 1e2 and 1e4 from left to right.

A considerable change can be seen with the results as a consequence of the introduction bulk nucleation within the models. In particular, by including nucleation, more significant variations between the samples as a change in travel speed is demonstrated. Specifically, relatively thin elongated structures are seen within the simulations of sample A irrespective of nucleation density. Nevertheless, the length of these, elongated grains in the build direction, does become shorter as the nucleation density is increased and new grain orientation are introduced. On the other hand, wide diamond shaped grain morphologies are exhibited within sample B. By introducing nucleation, the long columnar grains seen in the initial simulations, that were not representative of the experimental morphology is suppressed. In fact, the microstructure is now more representative of the experimental EBSDs with the inclusion of shorter bulkier grains. Finally, sample C shows a combination of the diamond shaped wide grains as well as the thin elongated grains seen in the other two samples. This is particularly clear in the simulated microstructure with a nucleation density of 1e2. Again, this is expected as the travel speed is mid-way between that of sample A and B, and a similar phenomena is seen experimentally.

Another phenomena that is captured by the inclusion of nucleation is the clustering of equiaxed grains at the centre of the melt pool. This is shown clearly in all the simulations utilising a nucleation density of 1e4. Within these simulations clusters of nucleated grains can be seen at the centre of each melt pool, when bulk nucleation occurs within the undercooled material before epitaxial growth from surrounding grains is completed. This is representative of the equiaxed grains seen along the top surface of experimental samples, such as that seen in Figure 70. The introduction of these grains experimentally could also occur from epitaxial growth out of the plane.

6.6.2 XZ plane

Within this next section, the experimental and simulated microstructure of the planar cross section, XZ plane, are presented. Figure 74 shows the predicted solidification microstructure of all three samples without nucleation. It should be noted that this plane within the sample is more likely to be susceptible to epistemic uncertainty. Thus, the exact location of the EBSD cut, with respect to the build strategy, is subject to more uncertainty as the build strategy means that for various planes throughout the height of the build, different thermal profiles are experienced. This is not the case for the XY plane, as the build strategy is consistent through the travel direction. However, the EBSD results obtained will still be representative of the typical microstructures seen within these planes. In future work, multiple EBSD maps throughout the height of the sample would be beneficial to establish the influence of this uncertainty.

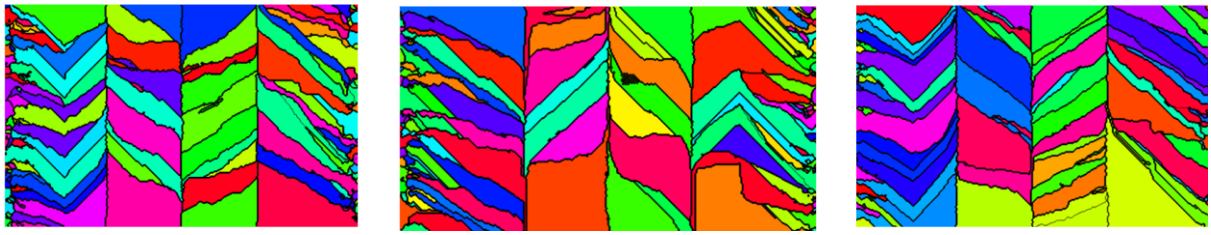

Figure 74: Simulated solidification microstructure within XZ plane, with no bulk nucleation; Sample A (left), B (middle) and C (right).

All of the predicted microstructures consistently show discrete tracks within the microstructure achieved by the bi-directional scan strategy. This feature is also observed within the experimental EBSD images shown in Figure 75 to Figure 77. Very little difference is seen within the simulated microstructures at this stage. The only slight variations, other than those that can be attributed to the probabilistic assignment of the initial microstructure, is the variation of the slope direction in the middle tracks of sample B compared to sample A and C. This is as a result of the reversed scanning direction within even layers due to the fact that each layer is deposited using one less scan. Moreover, these tracks appear to be slightly wider within this sample due to the increased track separation. It is also noted that occasionally within these models “a checker-boarding effect” between two grains is seen, this could suggest a finer incrementation or mesh may be beneficial.

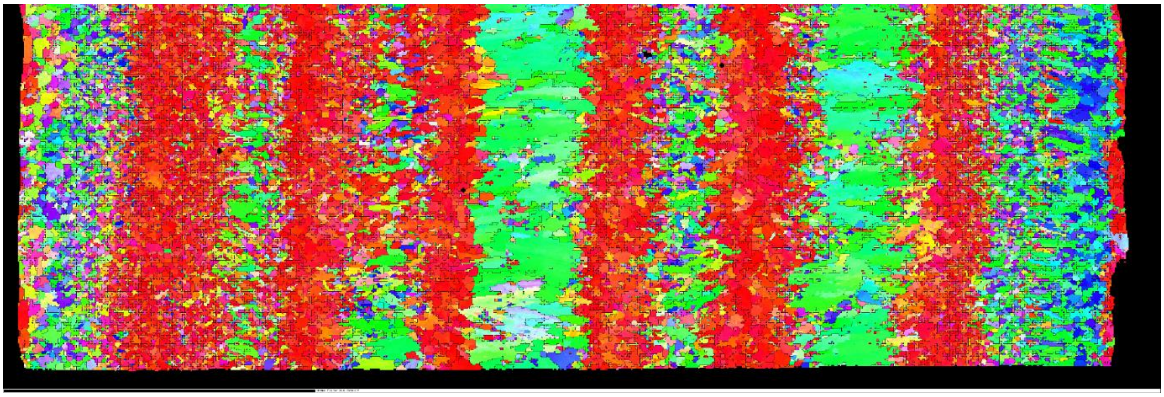

Figure 75: EBSD image of XZ plane for sample A2.

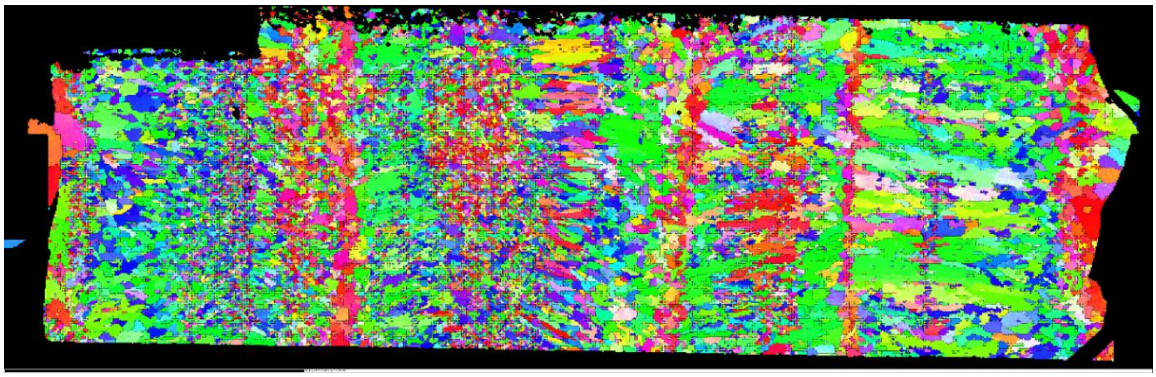

Figure 76: EBSD image of XZ plane for sample B2.

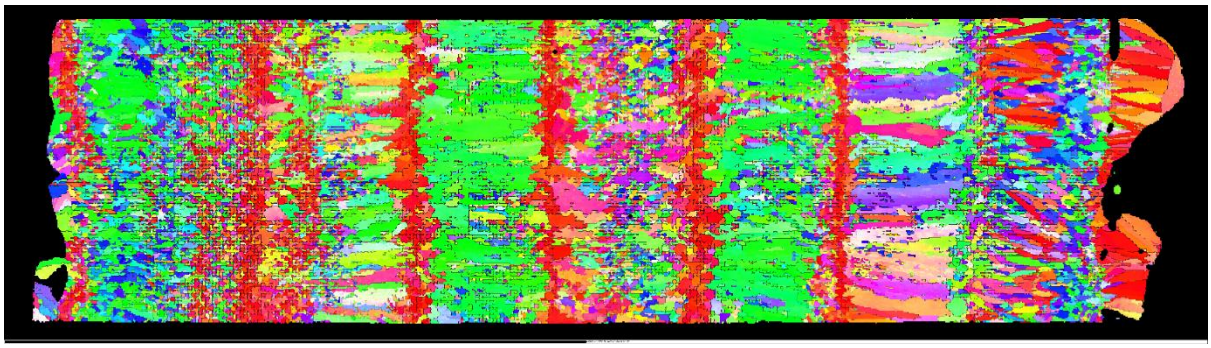

Figure 77: EBSD image of XZ plane for sample C2.

Experimentally, clear tracks can be seen in both sample A and C, but are less obvious in the sample B EBSD. It is believed that these are caused by the epitaxial growth of red grains in the build direction at the centre of the melt pool, whilst the green grains show grain growth with a horizontal component, from the sides of the melt pool inwards, as in the XY plane. It is expected that these are less clear within sample B as the red columnar grains are also less pronounced within the corresponding XY EBSD (Figure 65). Similarly the tracks of red grains are much wider within sample A, as they also are within the corresponding XY plane (Figure 64). As before, a sensitivity study considering the influence of bulk nucleation, has been included in the following results in an attempt to account for some of the epitaxial growth from out of the plane. These can be seen in Figure 78 to Figure 80.

Figure 78: Microstructure simulations for sample A in the XY plane with a nucleation density of 0, 1e1, 1e2 and 1e4 from left to right.

Figure 79: Microstructure simulations for sample A in the XY plane with a nucleation density of 0, 1e1, 1e2 and 1e4 from left to right.

Figure 80: Microstructure simulations for sample A in the XY plane with a nucleation density of 0, 1e1, 1e2 and 1e4 from left to right.

The introduction of bulk nucleation has a clear effect on the simulation results across all three samples. As in the XY plane, it predicts that the nucleation of new grains at the centre of the melt pool, prior to growth from the surrounding material taking place. This results in tracks of nucleated equiaxed grains surrounded by tracks of columnar elongated grains, that are relatively horizontal, although are angled towards the scanning direction. This is similar to the phenomena observed experimentally, although the horizontal tracks are more or less perpendicular to the scanning direction within the EBSD images as opposed to angled. Furthermore the tracks of red grains typically have a much larger grain size than those simulated. This is likely because the red grains within the experimental images are actually introduced to the plane through epitaxial growth out of the plane, when the thermal gradient in the build direction is stronger, so they are already growing from established grains. However, within the simulation these are new grains that are nucleated, so the growth envelope assigned to them is much smaller. Furthermore, as these are randomly nucleated grains this will affect the texture of the simulated microstructures, as predominantly red grains are seen within these tracks experimentally as this is the crystal orientation aligned with the build direction.

As a result of the nucleation within this model actually being more representative of crystal growth out of plane, rather than bulk nucleation within the melt pool, this suggest different nucleation densities may be more suitable for different process parameters, based on how prominently columnar growth within the build direction features within the XY plane. A high nucleation density would be required for sample A, compared to a much lower nucleation density for sample B.

6.6.3 YZ plane

Finally, the predicted microstructures for the longitudinal cross section, YZ plane, are shown. As with the previous comparisons, initial results without the inclusion of bulk nucleation are shown in Figure 81. Again, the exact location of the EBSD plane will have more effect on this analysis because of the variation of scan strategy out of plane. Again, due to epistemic

uncertainty, the exact location of the plane with respect to the build strategy is unknown, but the EBSD results are still indicative of the microstructure within this plane.

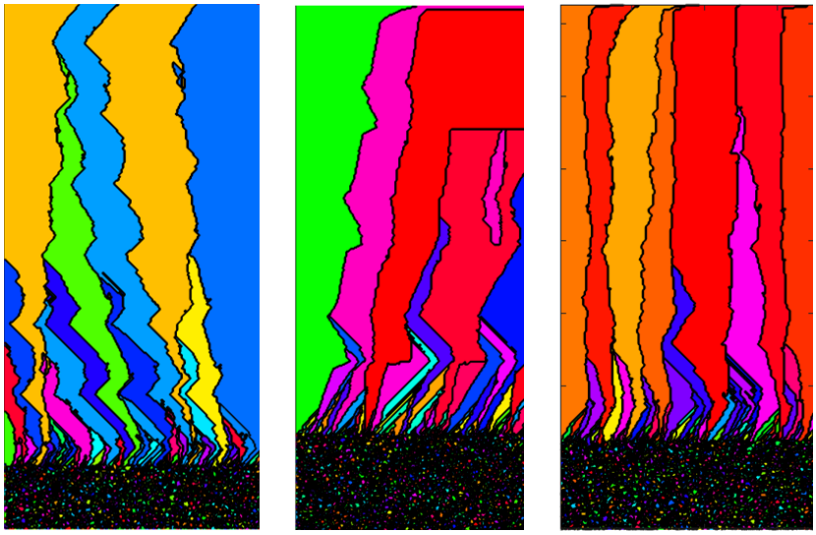

Figure 81: Simulated solidification microstructure within YZ plane, with no bulk nucleation; Sample A (left), B (middle) and C (right).

Elongated, columnar grains are predicted through the total build height of the samples. Zig zag formations are shown in sample A whilst vertical structures are shown for sample C. This is not representative of the structures seen experimentally. The EBSD maps within the YZ plane are shown in Figure 82.

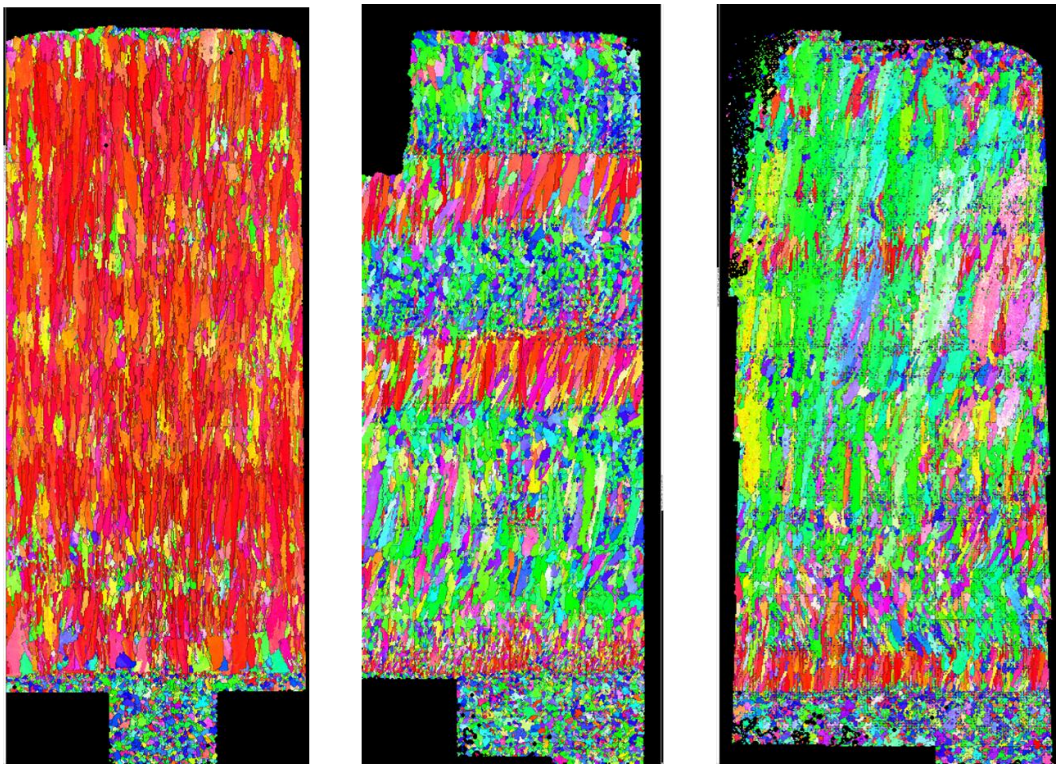

Figure 82: EBSD images of YZ plane for sample A2 (left), B2 (middle) and C2 (right).

The experimental microstructure within sample A shows consistently textured vertical columnar grains, aligned with the build direction. On the other hand, sample B and C show bands of different grains throughout the build height, although these are more prominent in sample B than sample C, which exhibits large regions of green grains which would be oriented at approximately 45 degrees to the build direction. The results of the simulations including nucleation with varying densities are presented in Figure 83 to Figure 85.

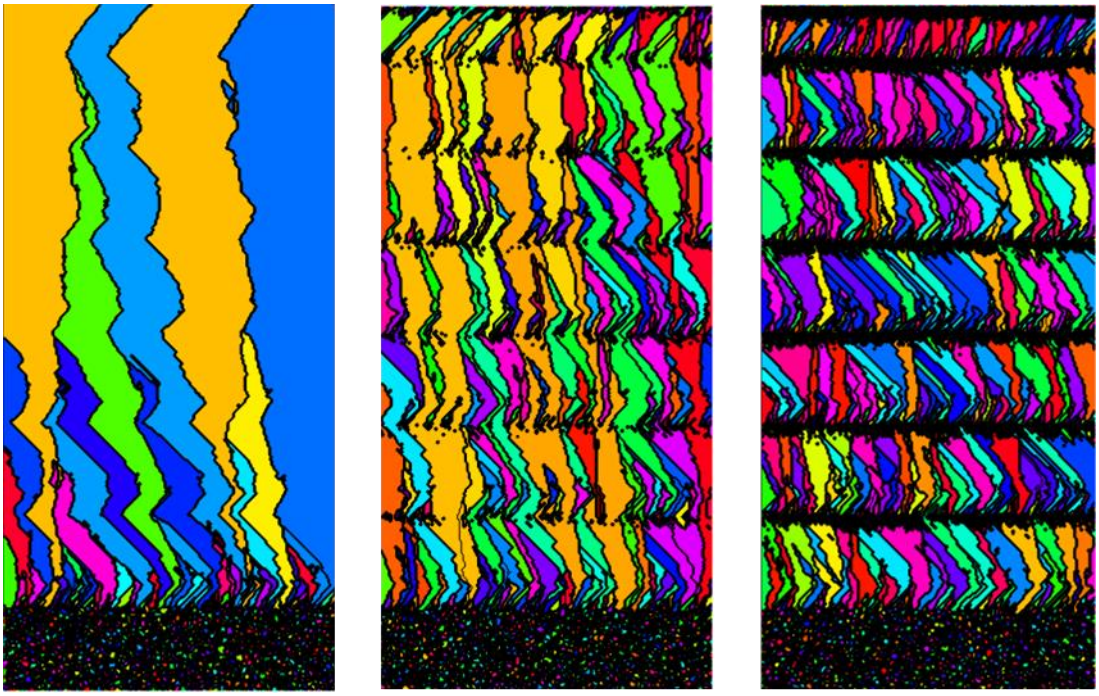

Figure 83: Microstructure simulations for sample A in the YZ plane with a nucleation density of 0, 1e1, 1e2 and 1e4 from left to right.

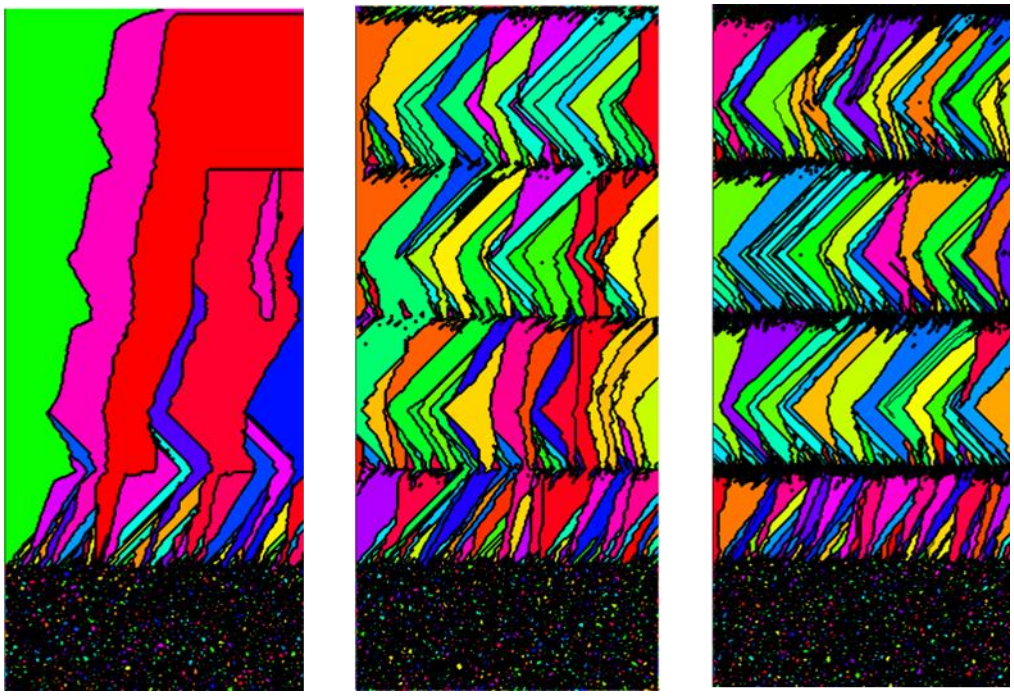

Figure 84: Microstructure simulations for sample B in the YZ plane with a nucleation density of 0, 1e1, 1e2 and 1e4 from left to right.

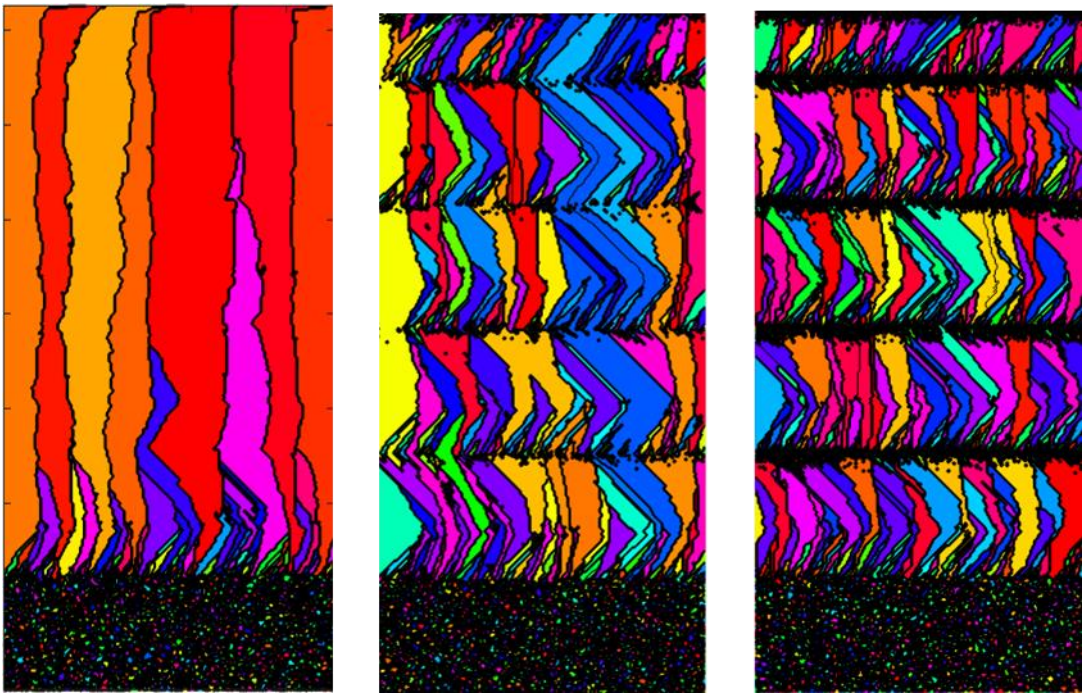

Figure 85: Microstructure simulations for sample C in the YZ plane with a nucleation density of 0, 1e1, 1e2 and 1e4 from left to right.

By including nucleation within the simulations, the models begin to predict the development of banded structures throughout the build height. These bands vary in size between samples based on the changes in layer height. As the nucleation density increased, the bands become more prominent across the simulations of all three samples. Between bands columnar grains are predicted, as is shown in the experimental EBSD images. However, distinct angles are simulated across all three samples within the elongated grains. This is not representative of the grains seen experimentally. It is thought that the nucleation here is again related to the epitaxial growth out of plane that is not captured by the 2D model. Particularly, because as with the XZ planes, different values of nucleation density appear to best suit different samples. For example, as columnar grains without much banding is observed within sample A, a low nucleation density is expected, however a high nucleation density was assumed within the XZ planes. Similarly, a high value of nucleation density is more suitable here for sample B, however a low nucleation density was chosen for the XZ plane. Therefore, it is concluded that the nucleation density is actually accounting for the significance of the thermal gradient out of plane. And hence a different value is required depending on the plane being simulated. This could be connected to the ratio of melt pool depth to length. This is expanded on further within the conclusions.

6.7 Conclusion

Within this case study three LMD IN718 samples have been deposited with varying values of travel speed, whilst all other key parameters remained fixed. EBSD images have been obtained to reveal the as deposited solidification structure within all three principal planes. Analytical thermal models have been implemented for efficiency, due to unforeseen circumstances limiting the computational resources available. The Rosenthal solution was implemented within the 2D CA model to determine if the microstructure modelling approach was capable of predicting variations in microstructure as a result of changes in process parameters. Simulations were undertaken within all three principal planes for each sample. Varying levels of nucleation were included within the models. Representations of the 3D microstructures using the simulated 2D planes can be seen in Figure 86 to Figure 88. Note, these images have been constructed to get an idea of the overall grain structure in 3D, they are not to scale. The corresponding nucleation density values that have been chosen for each plane are given in Table 22.

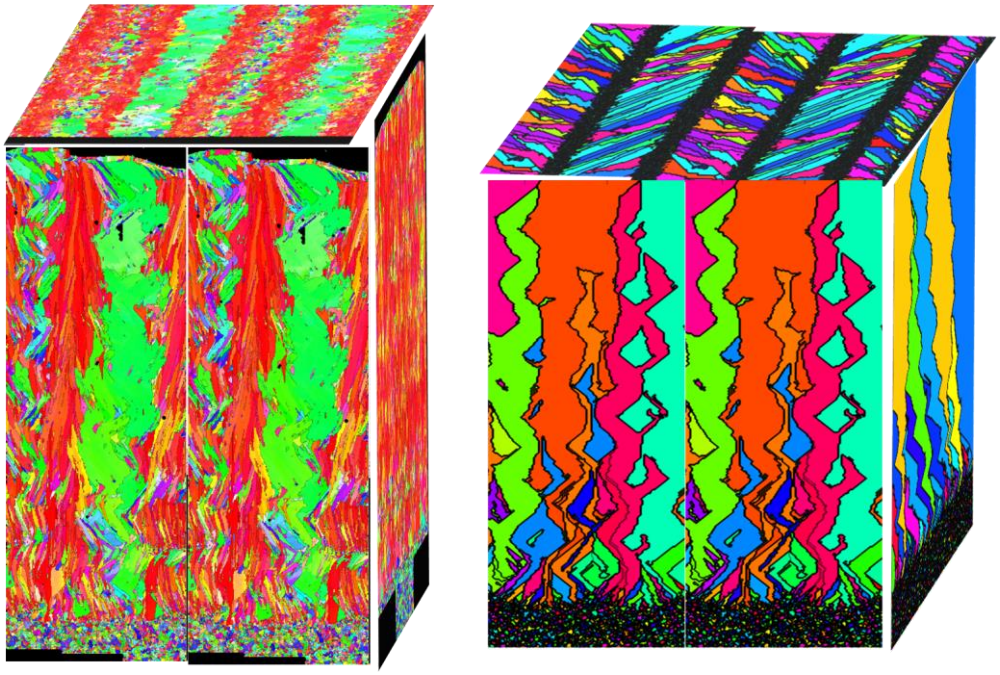

Figure 86: Comparison of representative 3D microstructure for sample A, constructed form 2D EBSD maps (left) and 2D simulations (right).

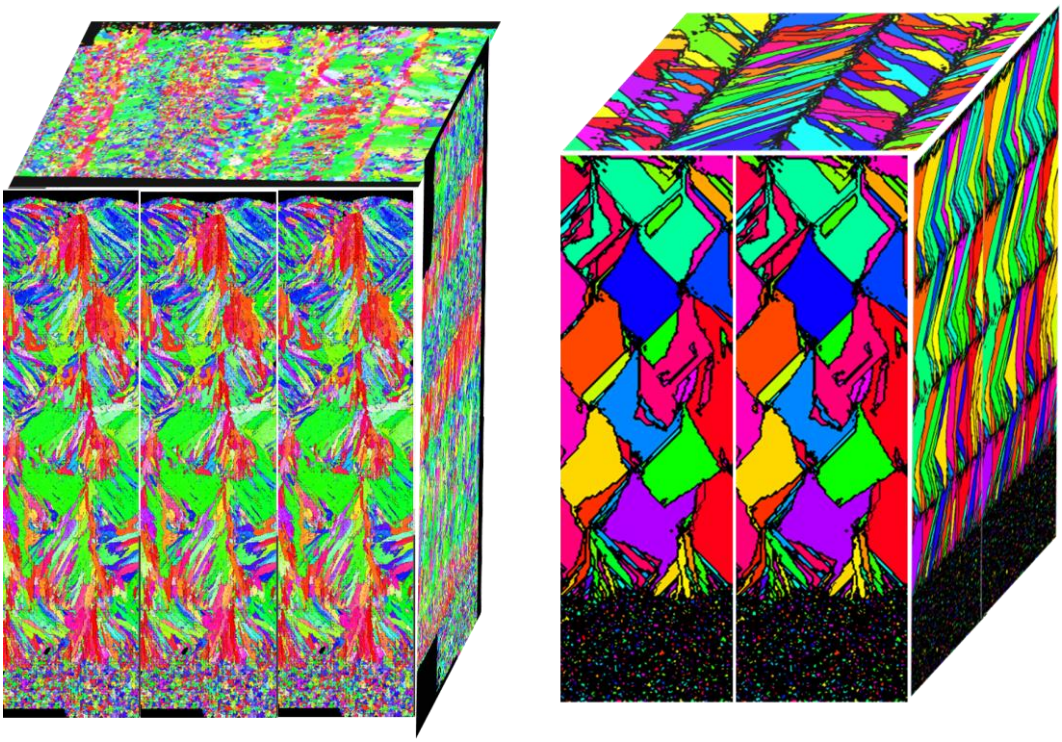

Figure 87: Comparison of representative 3D microstructure for sample B, constructed form 2D EBSD maps (left) and 2D simulations (right).

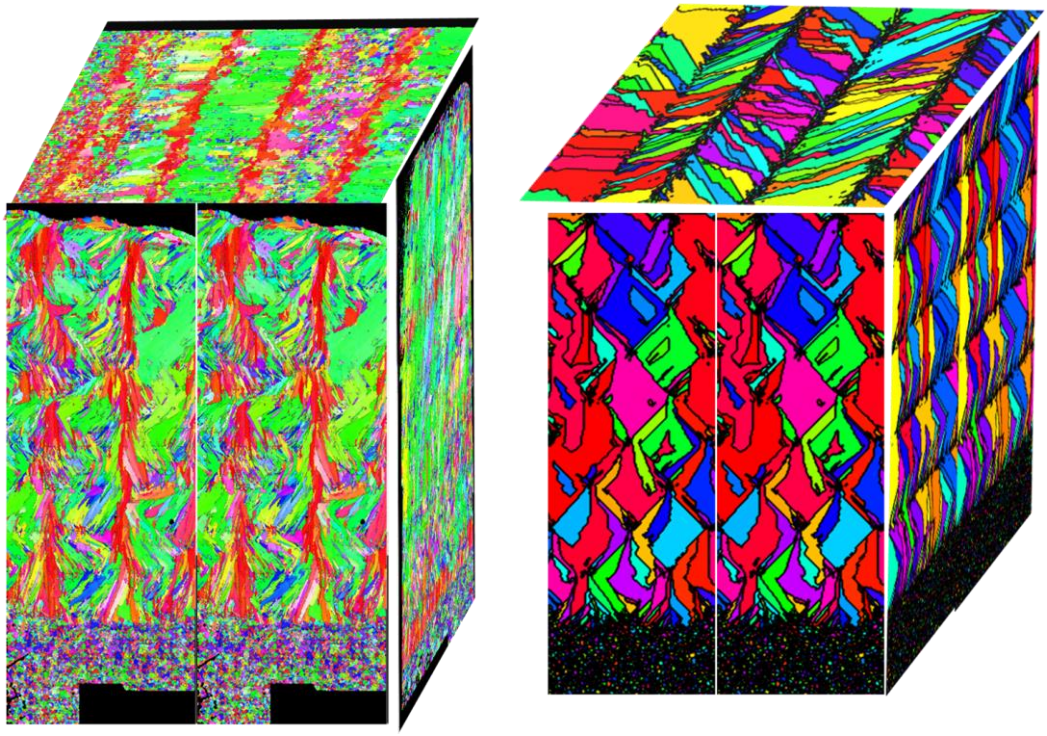

Figure 88: Comparison of representative 3D microstructure for sample C, constructed form 2D EBSD maps (left) and 2D simulations (right).

Sample	XY Plane	XZ Plane	YZ Plane
A	0	1e4	0
B	1e2	1e2	1e2
C	1e2	1e2	1e2

Table 22: Chosen nucleation densities (mm^{-3}).

Throughout the results shown in this work the effect of varying nucleation density within each plane has been discussed. As can be seen in Table 22, the most suitable nucleation density varies depending not only on the travel speed but also on the plane being investigated. It is thought that the nucleation within these models is more closely related to 3D crystal growth from out of the plane, than bulk nucleation within the melt pool. This is similar to the nucleation sites introduced by Akram et al. to account for 3D growth (Akram, et al., 2018). Hence, it is expected that the value of the density is determined by the strength of the growth from out of the plane. By looking at the ratio of the melt pool width and length, given in Table 20, we can begin to understand the relationship between the nucleation density and melt pool dimensions. For example, sample A has the smallest ratio, implying that the tail of the melt pool is much longer than the depth. Hence, it makes sense that when considering the XY plane growth out of plane is less likely to occur, as one could expect the thermal gradient through the depth of the melt pool to be much stronger than that through the length. This is supported by the more prominent columnar growth seen within the EBSD images. However, in the XZ plane a high nucleation density is used as growth perpendicular to this plane is more likely due to the stronger thermal gradient. The converse is true for sample B, as a larger ratio is seen. Therefore, increasing the likelihood of crystal growth perpendicular to the XY plane. However, whilst the inclusion of nucleation, with the appropriate density, helps account for these 3D aspects the size of the grains is not accurately predicted as the model assumes new growth, as opposed to epitaxial growth from existing grains.

Overall, the work presented within this chapter demonstrates the capabilities and the limitations of a 2D analytical-CA approach. The model was able to achieve a good level of agreement with EBSD images, including the simulation of a number of phenomena demonstrated within the experimental grain structures, including equiaxed growth at the top of the melt pool, and banding formations within the longitudinal plane. Whilst high fidelity models would provide deeper accuracy within the predictions, the modelling approach implemented here is sufficient to understand the expected solidification microstructure at a design level.

7 Fine to Coarse Microstructure Transitions

Following the validation of the modelling strategy, within the AMB2018-02 case study, and the application of the cellular automata method using the Rosenthal solution to assess the model's capability to predict microstructural changes as a result of changes in process parameters, work has been undertaken to apply the modelling approach to more complex additive manufacturing scenarios, including functionally graded materials. Introduced in section 1.1, functionally graded materials are highly desirable due to the added element of design they offer. This chapter focuses on the prediction of microstructure within multi-layer powder bed fusion systems involving an in situ process parameter change within the build process, causing a microstructure transition. Existing literature is used as the experimental validation within this study.

7.1 Experimental Paper

As mentioned within the literature review, one of the major benefits of additive manufacturing is the freedom of design. As understanding surrounding the physical processes increases, this extends to the tailoring of microstructures within the material through the alteration of process parameters. Such an example can be seen in the work presented by Popovich et al (Popovich, et al., 2017), which will be used as the source of experimental data for this case study. Within this piece of experimental work, the authors manufactured a number of samples using powder bed fusion of IN718, with different combinations of process parameters whilst maintaining energy density. This demonstrates that although energy density is an important factor in the design of additively manufactured parts, transitions in microstructure can be induced whilst maintaining a good quality of build. The sample of interest within this project was a 70 x 20 x 10 mm cuboid with alternating sections using two sets of parameters (Table 23) from which tensile samples were machined. It was stated that the parts were built using a scanning direction 45° between the X and Y axis, where the Z axis represents the build direction. Note, this coordinate system notation will be used in the model set up also. Although no detail is given within the paper, upon examination of the macrographs it appears that the scanning strategy rotated by 90° on alternate layers, therefore this rotation has been considered when undertaking the microstructure predictions. However, as the experimental detail is taken from literature there is minimal information by which to perform a thorough calibration of the thermal models.

Section	Power (W)	Scan Speed (mm/s)	Hatch Spacing (mm)	Layer Thickness (mm)	Beam Diameter (µm)	Beam Profile	Energy Density (J/mm^3)
1	250	700	0.12	0.05	80	Gaussian	59.5
2	950	320	0.5	0.1	100	Flat Top	59.4

Table 23: Experimental process parameters (Popovich, et al., 2017).

The sample seen within the EBSD map below (Figure 89), shows a tensile specimen extracted from a part built using predominantly section 1 parameters with two 6mm high section 2 regions within the build. This sample in particular is used as the subject of this study, as it is the only sample within the paper for which EBSD data is included. The EBSD shows a magnified region of a single transition from section 1 to section 2 parameters and back. Upon transition between sections a clear change is seen between fine and coarse grains. Section 2 exhibits large columnar grains, all of similar orientation within the EBSD map, whereas section 1 shows a more chaotic grains structure, showing smaller grains with varying orientations. Initial thoughts when considering the phenomena within this experimental work, was that an equiaxed grain structure was being achieved with the section 1 parameters, whilst the process parameters involved in section 2 were triggering a columnar growth formation on a G-R solidification diagram similar to that presented by DebRoy et al (Debroy, et al., 2018). However, upon analysis of the process parameters and comparison against a G-R diagram for IN718, it was determined that both structures are in fact likely to be columnar. The chaotic structure is actually the truncation of columnar growth due to the subsequently deposited layer.

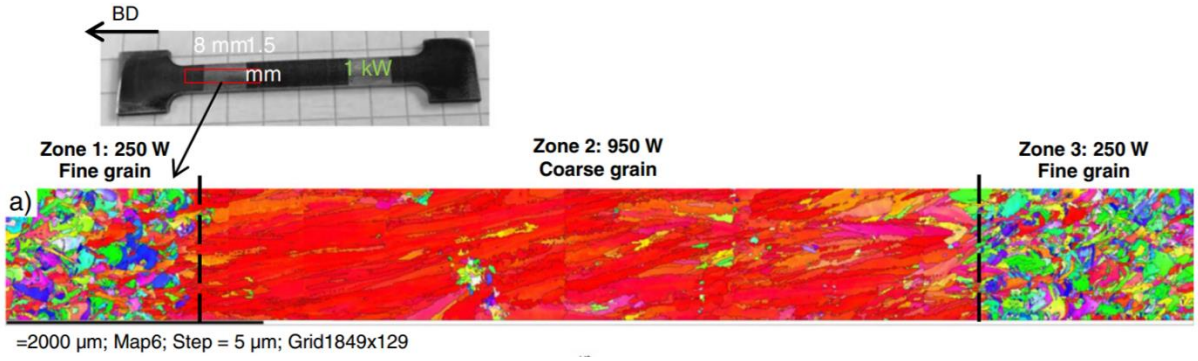

Figure 89: Experimental EBSD showing transition in microstructure upon change of process parameters. Figure 5 in (Popovich, et al., 2017).

7.2 Modelling Approach

Due to the relatively large size of the test parts built within the experimental study described above, it was impossible to efficiently model the entire build. In total there were over 800 layers in the original tensile samples builds and still 100 layers within the EBSD domain shown in Figure 89. Each layer had a dimension of 10mm by 20mm, which meant even the analysis of

a single layer on a fine enough scale to achieve accurate melt pool geometry and cooling rate through the use of a transient finite element model would be too computationally expensive. A number of approaches were taken to try and model a smaller domain. It was decided that as with the LMD study, the most suitable and computationally efficient approach would be to utilise an analytical thermal field to simulate the microstructural development within a 2D cross sectional plane. As this approach was capable of predicting changes in microstructure within the XY plane, it is expected that the same approach will be capable of demonstrating the changes in grain morphology as the result of in situ parameter changes.

The final modelling approach that was used is representative of 10 layers of the section 1 parameters followed by 10 of the section 2 layers, with an excess substrate layer at the base of the build, which was made to be 0.2mm thick. The width of the domain was chosen to allow sufficient material to model the solidification of three scans within the section 2 region, providing enough opportunity to witness the effects of the melt pool overlap as well as providing a suitable amount of the domain where there will be little influence from any boundary effects. A mesh size of 5μm was used as this was the same as the step size used within the experimentally obtained EBSD map.

The Rosenthal solution, as shown in section 6.4, has been used as an analytical thermal model, within this study, to represent the stable melt pool region. It was sensible to assume that the melt pool would be at steady state for this domain as the assumption was made that the simulations were predicting microstructure development from the centre of the build. The inherent assumption made by using the Rosenthal, which assumes the use of a steady-state point heat source, means the difference between the Gaussian and top hat laser distributions will not be specifically accounted for within this work. The same constant thermal properties were used for IN718 as previously specified in Table 19. Further detail on the calibration of the thermal model is given in the subsequent section.

The same validated modelling approach was used as that in the previous case study. However, adjustments to the model had to be made to represent the powder bed fusion process. Layers were activated in relation to the specified layer thicknesses. This was done through the use of the extra state variable values. Inactive material was assigned a physical state of -2, which stopped these cells being taken into account within the CA calculations. Once activated, the physical state was changed to -1 representing powder material. Powder already has an existing grain orientation within in the powder particles. This must be taken into consideration within the model as this introduces new grain orientations that would otherwise not exist. This is done by initialising the layers separately with an existing grain structure with a similar grain size to the particle size reported within the experimental work

(20-64 um). A similar approach can be seen in the work by Koepf et al (Koepf, et al., 2019; Koepf, et al., 2018). In addition, as the nucleation parameters featured heavily within the previous study and showed some beneficial contribution to the 2D predictions, simulations within this case study will be completed with and without nucleation. This helped to demonstrate the importance of their inclusion within powder bed fusion simulations. The same nucleation parameters for IN718 are used as before, a critical undercooling of 9.5 and a standard deviation of 2.0. A nucleation density of 1e2 has been assumed throughout.

7.3 Heat source

As stated earlier, the Rosenthal solution has been used as the thermal model within this study for computational efficiency. However, the efficiency of the heat source is an unknown parameter that requires determination. An alternative value to that within the previous study was to be expected because of the change in AM process and also the variation in process parameters. Two strategies were applied; first, a value of 0.4 was assumed for both parameter sets as this was found to be a typical value in literature for L-PBF processes (Irwin, et al., 2021; Lee & Zhang, 2016; King, et al., 2015), second an attempt was made to determine the melt pool dimensions from the available macrographs and use these to determine the efficiency of each parameter set individually. Efficiency values of approximately 0.21 and 0.68 were calculated for section 1 based on estimated melt pool width and depth respectively. Similarly, values of approximately 0.55 and 0.16 were determine for section 2 based on width and depth respectively. However, it should be noted that estimating the melt pool depth, or width, accurately from a macrograph is extremely difficult due to the overlap of melt pools, and angle of the scan strategy. Furthermore, the Rosenthal solution predicts a semi-circular melt pool, physically this is not always representative of the melt pool shape. Ultimately, a value of 0.3 was chosen for the section 1 parameters compared to a value of 0.55 for the section 2 parameters. These values ensured that no evidence of lack of fusion was witnessed and complete melting of the required material was achieved. The melt pool dimensions achieved are given in Table 24 for reference.

Section	Efficiency	Approx. Width (mm)	Approx. Length (mm)
1	0.3	0.146	0.799
2	0.55	0.571	5.564

Table 24: Resultant melt pool dimensions.

Moreover, the scan strategy used for the build of this part involved scanning at 45 degrees to the X and Y axes. Therefore, in order to simulate the microstructural development on a 2D cross section perpendicular to the Y axis, a coordinate transformation must be applied to the Rosenthal solution to account for this. Figure 90 shows the traditional Cartesian coordinate

system and the XZ plane representing the simulation domain. Another coordinate system (p,q) is also shown. This is a 2D coordinate system set up such that p is the scan direction at 45° to the X and Y axes, and q the normal to this. Through matrix calculations of this specific coordinate transformation, p and q are given as functions of x and y in Equation 27. This allows the Rosenthal solution to be defined in the (p,q) coordinate system with respect to the scan direction as it is traditionally defined and converted back into Cartesian coordinates for projection onto the XZ plane. Within Figure 90 the scan direction is defined as the p-axis, however the scan direction can also be changed from being parallel to the p-axis to parallel to the q-axis to account for the 90° rotation on even layers.

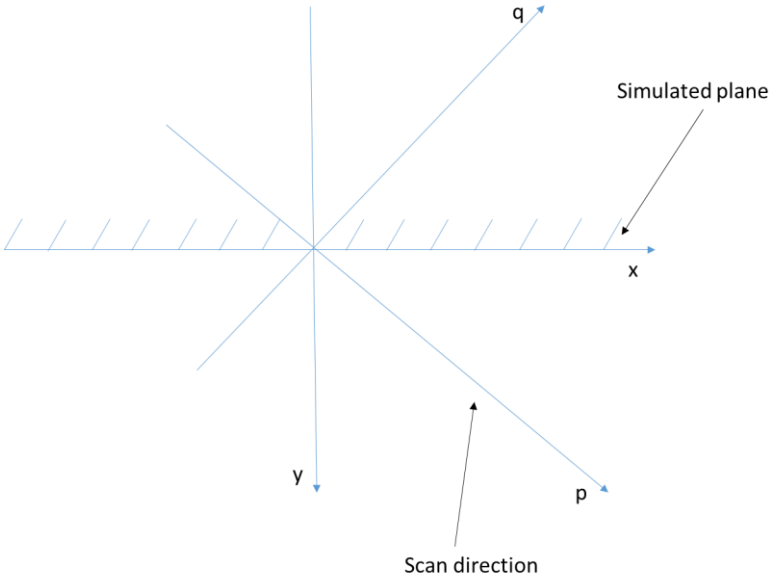

Figure 90 Visual representation of the coordinate transformation required to transform Rosenthal solution by 45°.

$$p = \frac{x + y}{\sqrt{2}}$$

$$q = \frac{x - y}{\sqrt{2}}$$

Equation 27 Coordinate transformations required to simulate Rosenthal solution at 45°.

A visual representation of the effects on the melt pool shape predicted by the Rosenthal simulation, within in the 2D cross-section, as a result of this transformation is shown in Figure 91.

Figure 91: Comparison of melt pool shape with and without 45 degree rotation.

7.4 Modelling Results

Unidirectional models, with a scanning direction along the y-axis, were initially set up for simplicity. These were representative of a part being built using the same process parameters without the assumed rotation between layers and without scanning at 45 degrees within the plane. The result of these simulations with and without bulk nucleation are shown in Figure 92. Note, within all the simulation results presented here, the bottom few layers shows the un-affected substrate, demonstrating the initial microstructure assumed for the substrate and powder material.

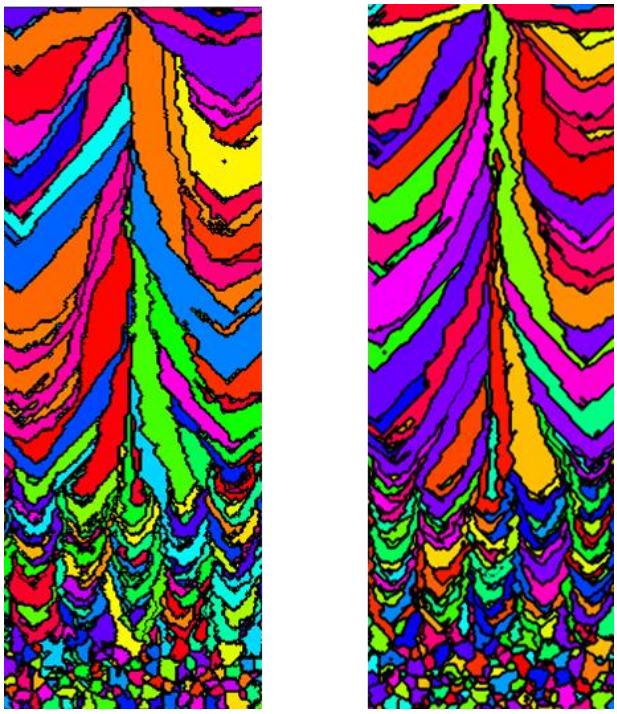

Figure 92: Unidirectional, scanning at 0°, microstructure prediction, with no nucleation (left) and nucleation (right).

Within the images shown here, the model domain has been reduced to be representative of a similar width of the build as that shown within the experimental EBSD, approximately 0.645mm

based on the step size and grid dimensions. Figure 92 clearly shows a transition in grain morphology upon transition between parameters. Similar to that in the experimental EBSDs, a fine structure is seen within section 1 region, changing to much more elongated grain structures within section 2 in the direction of the melt pool solidification. The grain morphology within section 1 frequently shows 'V' shape grains. These can also be seen in the experimental EBSD. This grain morphology is not seen within the section 2 region of the experimental EBSD, instead elongated grains are seen, with a very consistent texture. However, a slight slope is seen within the angle of the grain morphology. Elongated epitaxial growth is predicted within section 2 by the microstructure models, although the growth direction clearly follows the thermal gradient during melt pool solidification, resulting in angled grains towards the centre of the domain shown. The inclusion of nucleation within the results presented on the right of Figure 92 has little effect on the predicted morphology. Whilst there are some differences between the two images, it is expected this is more likely to be due to the probabilistic aspects of orientation assignment to both the substrate and unfused powder, than because of the inclusion of bulk nucleation.

The next step in increasing model complexity was to introduce the 90° rotation on alternate layers. Hence, within this simulation, on odd layers the scanning direction was along the y-axis, out of the plane, whilst on even layers it was along the x-axis, parallel to the plane. The results obtained with and without nucleation are shown in Figure 93.

Figure 93: Predicted solidification microstructure scanning at 0°, with 90° rotation on alternate layers, with no nucleation (left) and nucleation(right).

A clear visual difference is seen between the Figure 92 and Figure 93. Firstly, within the section 1 region the ‘V’ shape grains are still prominent, however, the introduction of the perpendicular scanning direction, on alternate layers, has resulted in the coarsening of these grains. This is a good demonstration of the models capability to pick up changes to the structure as a result of changes in scan strategy. Secondly, as a result of the introduction of perpendicular scans, the epitaxial growth within section 2 is much more columnar and elongated. This could be as a result of the lack of 3D effects that would capture out of plane grain growth. Specifically, within the layers where the scan direction is parallel to the 2D plane, there is a lack of new powder particles accounted for within the simulation for the introduction of new grains. However, the application of bulk nucleation that could contribute to the nucleation of new grains has been accounted for in the right hand image. Whilst, this result seems very similar to the EBSD, with the sloped columnar grains within section 2, the modelling set up is still not representative of the experimental set up as the 45° scanning direction between the x and y axis has not yet been accounted for. This is introduced in the following results in Figure 94 and Figure 95.

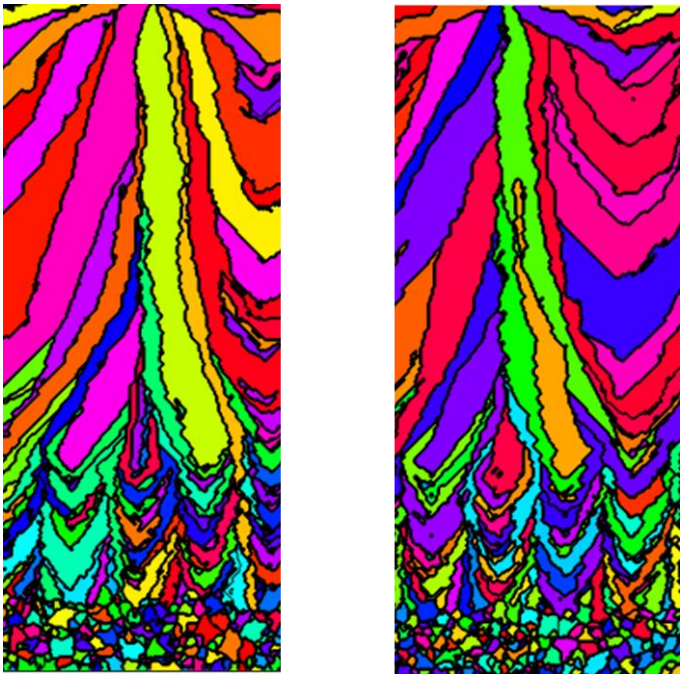

Figure 94: Unidirectional, scanning at 45°, microstructure prediction, with no nucleation (left) and nucleation (right).

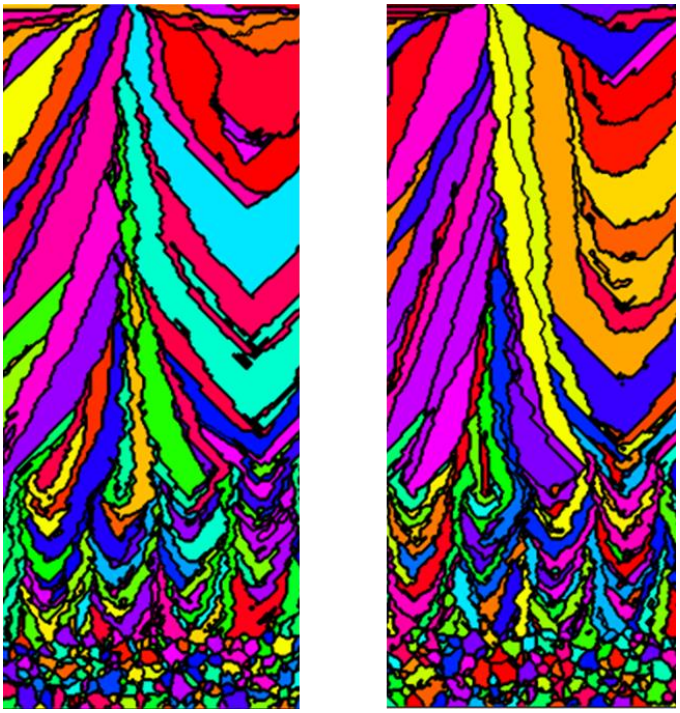

Figure 95: Predicted solidification microstructure scanning at 45°, with 90° rotation on alternate layers, with no nucleation (left) and nucleation(right).

Again the model is undertaken with and without the 90° rotation of the scan direction on alternate layers; Figure 94 and Figure 95 show the predicted grain morphology with and without this rotation, respectively. For both, simulating the inclusion of bulk nucleation had little effect as with the previous models within this study. Therefore, it is suggested that this highlights that the inclusion of nucleation is much less important for PBF processes, where nucleation of new grain orientations can be initiated from the surrounding powder material. Furthermore, there is much less variation between the predicted grain structures with and without the alternating scan direction, than that seen in Figure 92 and Figure 93. This is to be expected as a 90° rotation on alternate layers when a 45° scanning direction is applied results in a -45° scanning direction and therefore there is much less significance in the variation of the melt pool shape seen within the plane between layers, especially when compared to the variation between a scanning direction perpendicular to the plane and parallel to the plane. For this reason, the results shown utilising the 45° scan strategy are much more similar to the uni-directional, 0° scan strategy than with the alternate layer rotation applied. A comparison of the experimental EBSD and most representative microstructure simulation (45° scanning direction with a 90° rotation on alternate layers, without bulk nucleation) is shown in Figure 96.

Within this image the EBSD and simulations results have both been reduced to represent the same size domain of 1mm by 1.5mm.

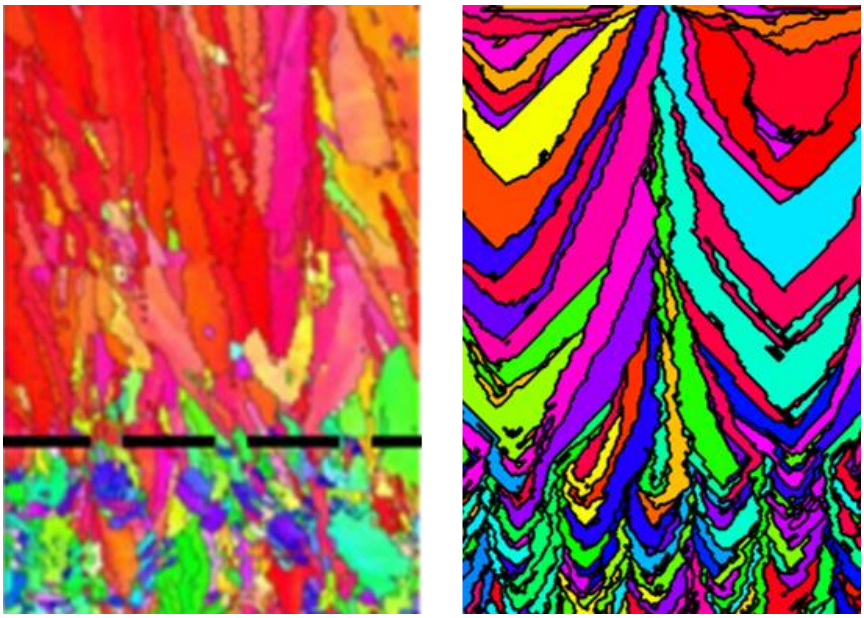

Figure 96: Comparison of microstructure predictions; Experimental EBSD, adapted from (Popovich, et al., 2017) (left) and simulation (right).

A strong agreement can be seen between the morphology in the EBSD and the simulated result, with a clear transition to larger, more elongated grains upon the in situ change of parameters. However, it is clear that the elongated grains within the simulation are much more angled than those in the experimental EBSD. It is unclear why this is, but it is suggested that this could be as a result of difference between the melt pool shape obtained experimentally and that simulated by the Rosenthal. Furthermore, due to the small size of EBSD data available it is likely that deeper experimental analysis would benefit this investigation.

7.5 Conclusion

Within this chapter, the previously validated modelling approaches were implemented for the application of functionally graded materials. Experimental data was taken from literature demonstrating the use of in situ parameter changes to initiate a microstructural transition within the deposition of L-PBF parts. These experimental details were used as the basis of microstructure simulations.

The complexity of the models was built up incrementally allowing for the comparison of the prediction of similar microstructures for variations on the scan strategy. A large change in microstructure is seen when comparing a constant scan strategy perpendicular to the plane with a scan strategy that introduces a 90 degree rotation on alternate layers, such that the scan direction becomes parallel to the plane. This is not seen when an alternating 90 degree

rotation is applied to a scanning direction at 45 degrees within the XY plane. Furthermore, the inclusion of bulk nucleation has little effect on the simulation throughout this study.

The final microstructure simulations achieved a good level of agreement with the experimental EBSD. Fine, textured grain structures were seen in the region deposited using the section 1 parameters both experimentally and within the model. Meanwhile, elongated grains were witnessed within the section 2 region. Whilst epitaxial growth within the model clearly shows the microstructural transition to elongated grains, the simulated grains seem to be slightly more angled than those witnessed experimentally. It is unknown why this is possibly the case, but it is suggested that further experimental data would be required to investigate this fully.

8 Conclusions

Within this work, microstructure modelling methods have been used as a method of increasing the understanding of the relationship between process parameters and the solidification microstructure for metal additive manufacturing. Ultimately, the work presented here aims to contribute to the process-structure-property relationships that are fundamental to understanding the behaviour, and increasing the reliability, of additively manufactured parts for use within industry. Cellular automata (CA) methods have been implemented due to their relative computational efficiency compared to other methods such as phase field modelling, whilst still being based on physical solidification laws and providing visual representations of the simulated microstructure. For the ease of the reader, the objectives identified for this work are reiterated here:

- Contribute to the smaller catalogue of work available for the application of cellular automata (CA) to direct energy deposition (DED) processes, particularly for multi-layer builds.
- Implement CA methods with experimentally-validated thermal models.
- Improve the computational efficiency of the required models to achieve sensible run times with practical hardware requirements, suitable for use in industry.
- Apply CA models to investigate the influence of process parameters, with experimental validation.

A 2D weakly-coupled CA model has been implemented throughout this work. Three case studies have been undertaken to investigate the capabilities of the modelling approach. Firstly, open source experimental data was used to validate the simulation approach for laser scans on a bare Inconel 625 substrate. A statistical analysis of the microstructure model was undertaken to determine the influence of probabilistic aspects of the model.

Secondly, the approach was applied to laser metal deposition (LMD) Inconel 718 deposits with 3 varying travel speeds. The aim of this case study was to evaluate the ability of the model to predict differences in microstructure as a result of changes in process parameters. Whilst unforeseen circumstances resulting in a lack of computational resources meant that the planned finite element models could not be completed, microstructure predictions were undertaken using an analytical Rosenthal solution. In fact, this provided an extremely computationally efficient approach to investigate the resultant microstructure as a result of process parameters. Simulated microstructures were undertaken in all 3 principal planes and showed strong agreement with the experimental EBSD maps. Varying levels of nucleation

density were investigated and it was observed that different levels of nucleation density were more suitable for different travel speeds and plane of simulation. It is suggested that this is linked to the ratio of melt pool dimensions, based on the likelihood of out of plane crystal growth.

Finally, this approach was applied to a powder bed fusion application, with an in situ change in parameters. This was based upon experimental data found within literature. This demonstrated the capability of the model to predict microstructure transitions for the application of functionally graded materials.

The main outcomes of this project are summarised here:

- Development of experimentally validated thermal models for additive manufacturing applications including, contributions to an NIST Benchmark award winning submission, that used the Abaqus AM plug-in to provide part level thermal models for residual stress predictions.
- Successful implementation of a 2D CA model weakly coupled to a finite element thermal model that was validated with experimental data. Probabilistic effects on the simulations were also investigated.
- An efficient method, that can be used at the design level, with minimal hardware requirements, has been established through the use of 2D CA with an analytical heat source within MATLAB.
- Whilst the 3D transient finite element models were unable to be completed within this work, an approach for a combined integrated and conical heat source was suggested. This aims to improve efficiency of fine level thermal models by allowing the analyst to change the spatial and temporal resolution of the model within regions of interest.
- Experimental Inconel 718 LMD samples have been manufactured with thermocouple recordings for thermal model validation. Furthermore, EBSD imaging has been undertaken to reveal the solidification structure in all 3 principal planes, for experimental validation of the microstructure predictions.
- Microstructure predictions have been undertaken on all 3 principal planes for multilayer LMD Inconel 718 deposits with varying values of travel speed. Certain features of the solidification microstructures have been captured well by the 2D models. The results have been compared to experimental EBSD images and show a good level of agreement.
- Different nucleation densities have been investigated. It is thought that the presence of nucleation within this work is related to crystal growth from out of the 2D plane. Links between this and the melt pool geometry have been proposed.

- The ability of the modelling approach to simulate microstructural transitions as a result of in situ changes in process parameter, within powder bed fusion (PBF) applications, was demonstrated. This was based on and compared to experimental results within literature.

It is suggested here that future work within this topic requires the establishment of reliable and widely accepted material parameters for microstructure models, including critical undercooling and nucleation density. For use at the design level, well established material properties must be available for a range of common alloys used for additive manufacturing. Increased understanding of how these parameters can be derived experimentally would also be useful. Further investigation of the link between process parameters and melt pool geometry could improve the efficient use of 2D models, whilst accounting for out of plane growth. If an established method of determining a reliable and appropriate correction factor for the nucleation density, which accounted for the contribution of out of plane growth within 2D models, this would increase the accuracy and practicality of 2D CA methods for industry. On the other hand, improvements on computational efficiency of 3D CA methods, that achieve suitable run times with practical hardware requirements, would be the ultimate goal within CA models, as they can more accurately account for crystallographic texture and 3D growth, without having to introduce any assumptions.

Moreover, the application of these approaches to more complex geometries representative of industrially relevant components would be beneficial. Currently, the majority of work is undertaken on test sample geometries such as walls and cubes. In order for this methodology to be used effectively within industry, application to industrial geometries is essential. Due to the large amount of process parameters available within AM processes, a wider investigation of various process parameter influences would also be suggested.

In addition, the implementation of the combined integrated and conical heat source approach to improve the efficiency of fine level finite element thermal models should be investigated. This approach provides the potential to increase efficiency of fine level thermal models that can be undertaken on a part scale but still provide a melt pool level thermal profile for implementation within CA models. Computational efficiency of accurate models is key to making models accessible and practical within industry.

Finally, further work is required to establish relationships between the outcomes of the simulated solidification microstructures, such as those presented here, to the behaviour and material properties within additively manufactured parts. This will complete the links between process, structure and properties, and hence provide greater understanding surrounding the

reliability of additively manufactured parts, ultimately resulting in an increase of AM parts within industry.

9 References

Acharya, R., Sharon, J. A. & Staroselsky, A., 2017. Prediction of microstructure in laser powder bed fusion process. *Acta Materialia,* Volume 124, pp. 360-371.

Additive Manufacturing Center of Excellence, 2020. *Strategic Roadmap for Research & Development,* Washington DC: ASTM International.

Agarwal, G., Gao, H., Amirthalingam, M. & Hermans, M., 2018. Study of solidification cracking susceptibility during laser welding in an advanced high strength automotive steel. *Metals,* 8(673).

Ahsan, M. N. & Pinkerton, A. J., 2011. An analytical-numerical model of laser direct metal deposition track and microstructure formation. *Modelling and Simulation in Materials Science and Engineering ,* 19(055003).

AK Steel Corporation, 2007. *Product data sheet: 304/304L stainless steel.* West Chester: AK Steel Corporation.

Akram, J., Chalavadi, P., Pal, D. & Stucker, B., 2018. Understanding grain evolution in additive manufacturing through modeling. *Additive Manufacturing,* Volume 21, pp. 255-268.

Alhuzaim, A., Imbrogno, S. & Attallah, M. M., 2021. Controlling microstructural and mechanical properties of direct laser deposited Inconel 718 via laser power. *Journal of Alloys and Compounds,* 872(159588).

Alimardani, M., Toyserkani, E. & Huissoon, J. P., 2007. A 3D dynamic numerical approach for temperature and thermal stress distributions in multilayer laser solid freeform fabrication process. *Optics and Lasers in Engineering,* Volume 45, pp. 1115-1130.

America Makes & ANSI Additive Manufacturing Standardization Collaborative (AMSC), 2017. *Standardization Roadmap for Additive Manufacturing,* Youngstown/New York: ANSI and NDCMM/America Makes.

AM-motion, 2016. *A strategic approach to increasing Europe's value proposition for additive manufacturing technologies and capabilities,* Brussels: AM-motion.

Andersson, J., 2011. *Weldability of precipitation hardening superalloys - Influence of microstructure.* Goteberg, Sweden: Chalmers University of Technology.

Andrews, G., 2008. *Cellular automata and applications.* Walla Walla: Whitman College.

Annaratone, D., 2010. *Engineering Heat Transfer.* 1st ed. Berlin: Springer.

Arisoy, Y. M., Criales, L. E. & Ozel, T., 2019. Modeling and simulation of thermal field and solidification in laser powder bed fusion of nickel alloying IN625. *Optics & Laser Technology ,* Volume 109, pp. 278-292.

ASTM International, 2013. *Standard Terminology for Additive Manufacturing Technologies: Designation F2792 - 12a,* West Conshohocken: ASTM International.

ASTM International, 2013. *Standard Test Methods for Determining Average Grain Size: Designation: E112 - 13,* West Conshohocken: ASTM International.

Attallah, M. M., Jennings, R., Wang, X. & Carter, L. N., 2016. Additive manufacturing of Ni-based superalloys: The outstanding issues. *Materials Research Society,* Volume 41, pp. 758-764.

Avrami, M., 1939. Kinetics of Phase Change. 1: General Theory. *Journal of Chemical Physics,* Volume 7, pp. 1103-1112.

Avrami, M., 1940. Kinetics of Phase Change. 2: Transformation-Time Relations for Random Distribution of Nuclei. *Journal of Chemical Physics,* Volume 8, pp. 212-224.

Avrami, M., 1941. Kinetics of Phase Change. 3: Granulation, Phase Change, and Microstructure. *Journal of Chemical Physics,* Volume 9, pp. 177-184.

AZO Materials, 2015. *Generating Orientation Maps to Present EBSD Data.* [Online] Available at: https://www.azom.com/article.aspx?ArticleID=11775 [Accessed 27 01 2022].

Babu, B., Lundback, A. & Lindgren, L.-E., 2019. Simulation of Ti-6Al-4V additive manufacturing using coupled physically based flow stress and metallurgical model. *Materials,* 12(3844).

Bai, X. et al., 2018. Numerical analysis of heat transfer and fluid flow in multilayer deposition of PAW-based wire and arc additive manufacturing. *International Journal of Heat and Mass Transfer,* Volume 124, pp. 504-516.

Bertoli, U. S., MacDonald, B. E. & Schoenung, J. M., 2019. Stability of cellular microstructure in laser powder bed fusion of 316L stainless steel. *Materials Science & Engineering A,* Volume 739, pp. 109-117.

Bhadeshia, H., 2022. *Lecture 9: Overall Transformation Kinetics.* Cambridge: University of Cambridge.

Bhadeshia, H. K. D. H., 2010. *Lecture 15: Phase Field Modelling.* Cambridge: Cambridge University.

Bonifaz, E. A., 2018. Thermo-mechanical analysis in SAE-AISI 1524 carbon steel gas tungsten arc welds. *Int. J. Computational Materials Science and Surface Engineering ,* 7(3/4).

Bonifaz, E. A. & Palomeque, J. S., 2020. A mechanical model in wire + Arc additive manufacturing process. *Progress in Additive Manufacturing .*

Bourell, D. et al., 2017. Materials for Additive Manufacturing. *CIRP Annals - Manufacturing Technology,* Volume 66, pp. 659-681.

Bourell, D. L., Beaman, J. J., Leu, M. C. & Rosen, D. W., 2009. *A brief history of additive manufacturing and the 2009 roadmap for additive manufacturing: Looking back and looking ahead.* US-TURKEY, Workshop on Rapid Technologies.

Bourrel, D. L., Leu, M. C. & Rosen, D. W., 2009. *Roadmap for additive Manufacturing: Identifying the future of freeform processing,* Austin: The University of Texas.

Bunge, H.-J., 1982. *Texture Analysis in Materials Science.* English ed. London, Boston: Butterworth & Co.

Burkardt, J., 2005. *Geometry.* [Online] Available at: https://people.sc.fsu.edu/~jburkardt/f_src/geometry/geometry.html [Accessed 29 01 22].

Carozzani, T., Digonnet, H. & Gandin, C.-A., 2012. 3D CAFE modeling of grain structures: application to primary dendritic and secondary eutectic solidification. *Modelling and Simulation in Materials Science and Engineering,* 20(015010).

Carozzani, T., Gandin, C.-A. & Digonnet, H., 2014. Optimized parallel computing for cellular automaton-finite element modeling of solidification grain structures. *Modelling and Simulation in Materials Science and Engineering ,* 22(015012).

Carozzani, T. et al., 2013. Direct simulation of a solidification benchmark experiment. *Metallurgical and materials transactions A,* Volume 44A, pp. 873-887.

Charles Murgau, C., 2016. *Microstructure model for Ti-6Al-4V used in simulation of additive manufacturing,* Luleå, Sweden: Luleå University of Technology.

Charles Murgau, C., Pederson, R. & Lindgren, L. E., 2012. A model for Ti-6Al-4V microstructure evolution for arbitrary temperature changes. *Modelling and Simulation in Materials Science and Engineering ,* 20(055006).

Charles, C., 2008. *Modelling microstructure evolution of weld deposited Ti-6Al-4V.* Lulea: Lulea University of Technology.

Chen, S., Guillemot, G. & Gandin, C.-A., 2016. Three-dimensional cellular automaton-finite element modeling of solidification grain structures for arc-welding processes. *Acta Materialia,* Volume 115, pp. 448-467.

CLLAIM, 2021. *CLLAIM: Homepage.* [Online] Available at: https://cllaimprojectam.eu/ [Accessed 12 November 2021].

Cruz-Mejia, O., Marquez, A. & Monsreal-Berrera, M. M., 2019. Product delivery and simulation for industry 4.0. In: M. M. Gunal, ed. *Simulation for industry 4.0 - Past, present, future.* Switzerland: Springer, pp. 81-95.

Dai, K. & Shaw, L., 2004. Thermal and mechanical finite element modeling of laser forming from metal and ceramic powders. *Acta Materialia,* Volume 52, pp. 69-80.

Dantzig, J. A. & Rappaz, M., 2016. *Solidification.* 2nd ed. Lausanne: EPFL Press.

Dassault Systèmes, 2015. *Abaqus User Subroutine Reference Guide.* Providence: Dassault Systèmes.

Dassault Systemes, 2019. *Thermomechanical simulation of additive manufacturing processes.* [Online] Available at: https://help.3ds.com/2019/english/dssimulia_established/simacaeanlrefmap/simaanl-c-amthermomechanical.htm?contextscope=all [Accessed 23 01 2022].

Dassault Systemes, 2019. *UEPACTIVATIONVOL.* [Online] Available at: https://help.3ds.com/2019/English/DSSIMULIA_Established/SIMACAESUBRefMap/simasub-c-uepactivationvol.htm?contextscope=all&id=f167fdb83da643a4bdea8d9826c61343 [Accessed 23 01 2022].

De Moraes, D. A. & Czekanski, A., 2017. *Thermal modeling of 304L stainless steel for selective laser melting: laser power input evaluation.* Tampa, Florida, Proceedings of the ASME 2017 International Mechanical Engineering Congress and Exposition, IMECE2017.

Debroy, T. et al., 2018. Additive Manufacturing of Metallic Components - Process, Structure and Properties. *Progress in Materials Science,* Volume 92, pp. 112-224.

Denlinger, E., Gouge, M., Irwin, J. & Michaleris, P., 2017. Thermomechanical model development and in situ experimental validation of the laser powder-bed fusion process. *Additive Manufacturing,* Volume 16, pp. 73-80.

Ding, D., Pan, Z., Cuiuri, D. & Li, H., 2015. A multi-bead overlapping model for robotic wire and arc additive manufacturing (WAAM). *Robotics and Computer-Integrated Manufacturing,* Volume 31, pp. 101-110.

Ding, H., He, Y., Liu, L. & Ding, W., 2006. Cellular automata simulation of grain growth in three dimensions based on the lowest-energy principle. *Journal of Crystal Growth ,* Volume 293, pp. 489-497.

Ding, J., 2012. *Thermo-mechanical Analysis of Wire and Arc Additive Manufacturing Process.* Swindon: Cranfield University.

Doux, A. & Philippe, V., 2019. Thermomechanical modeling of In718 alloy directed energy deposition process. *MATEC Web of Conferences,* 304(01023).

Dowling, L., Kennedy, J., O'Shaughnessy, S. & Trimble, D., 2020. A review of critical repeatability and reproducibility issues in powder bed fusion. *Materials and Design,* 186(108346).

Dwivedi, D. K., 2022. *Fundamentals of metal joining: Processes, mechanism and performance.* 1st ed. Singapore: Springer.

Eagar, T. W. & Tsai, N.-S., 1983. Temperature fields produced by traveling distributed heat sources. *Welding Research Supplement,* pp. 346-355.

Energetics Incorporated, 2013. *Measurement science roadmap for metal-based additive manufacturing,* Columbia: National Institute of Standards and Technology.

Engineer Educators, 2022. *Common Crystal Structures.* [Online] Available at: https://mypdh.engineer/lessons/common-crystal-structures/ [Accessed 01 10 2022].

European Commission: CORDIS, 2020. *Horizon 2020: Part specific process optimization in SLM (Grant agreement ID: 785562).* [Online] Available at: https://cordis.europa.eu/project/id/785562 [Accessed 28 01 2022].

Fan, D. & Chen, L.-Q., 1997. Computer simulation of grain growth using a continuum field model. *Acta mater.,* 45(2), pp. 611-622.

Felippa, C. A., 2004. Introduction to finite element methods. In: *Appendix O: The origins of the finite element method.* Boulder: University of Colorado.

Fielding, J. et al., 2016. *Department of Defense Additive Manufacturing Roadmap,* Washington, DC: Department of Defense USA.

Fish, J. & Belytschko, T., 2007. *A first course in finite elements.* Chichester: Wiley & Sons Ltd.

Foroozmehr, A., Badrossamay, M., Foroozmehr, E. & Golabi, S., 2016. Finite element simulation of selective laser melting process considering optical penetration depth of laser in powder bed. *Materials and Design,* Volume 89, pp. 255-263.

Fu, C. H. & Guo, Y., 2014. *3-dimensional finite element modeling of selective laser melting.* Austin, Texas, 25th Annual International Solid Freeform Fabrication Symposium.

Gandin, C.-A., Desbiolles, J.-L., Rappaz, M. & Thevoz, P., 1999. A three-dimensional cellular automaton - finite element model for the prediction of solidification grain structures. *Metallurgical and Materials Transactions A,* Volume 30A, pp. 3153-3165.

Gandin, C.-A. & Rappaz, M., 1994. A coupled finite element - cellular automaton model for the prediction of dendritic grain structures in solidification processes. *Acta metall. mater.,* 42(7), pp. 2233-2246.

Gandin, C.-A. & Rappaz, M., 1997. A 3D cellular automaton algorithm for the prediction of dendritic grain growth. *Acta mater.,* 45(5), pp. 2187-2195.

Gandin, C.-A., Schaefer, R. J. & Rappaz, M., 1996. Analytical and numerical predictions of dendritic grain envelopes. *Acta mater.,* 44(8), pp. 3339-3357.

Gan, Z. et al., 2019. Benchmark study of thermal behaviour, surface topography, and dendritic microstructure in selective laser melting of Inconel 625. *Integrated Materials and Manufacturing Innovation,* Volume 8, pp. 178-193.

Gatsos, T., Elsayed, K. A., Zhai, Y. & Lados, D. A., 2020. Review on computational modeling of process-microstructure-property relationships in metal additive manufacturing. *Journal of the Minerals, Metals & Materials Society,* Volume 72, pp. 403-419.

GE, 2018. *New manufacturing milestone: 30,000 additive fuel nozzles.* [Online] Available at: https://www.ge.com/additive/stories/new-manufacturing-milestone-30000-additive-fuel-nozzles
[Accessed 27 01 2022].

Ge, P. et al., 2019. An integrated modeling of process-structure-property relationship in laser additive manufacturing of duplex titanium alloy. *International Journal of Thermal Sciences,* Volume 140, pp. 329-343.

Ghobakhloo, M., 2018. The future of manufacturing industry: a strategic roadmap toward Industry 4.0. *Journal of Manufacturing Technology Management.*

Gibson, I., Rosen, D. & Stucker, B., 2015. *Additive manufacturing technologies: 3D printing, rapid prototyping, and direct digital manufacturing.* 2nd ed. New York: Springer.

Graf, M. et al., 2018. Thermo-mechanical modelling of wire-arc additive manufacturing (WAAM) of semi-finished products. *Metals,* 8(1009).

Graybill, B. et al., 2018. *Additive manufacturing of nickel-based superalloys.* TX, USA, ASME.

Groover, M. P., 2020. *Fundamentals of modern manufacturing: Materials, processes and systems.* 7th ed. Hoboken: Wiley.

Gu, C. et al., 2019. Three-dimensional cellular automaton simulation of coupled hydrogen porosity and microstructure during solidification of ternary aluminium alloys. *Scientific Reports,* 9(13099).

Guillemot, G., Gandin, C.-A., Combeau, H. & Heringer, R., 2004. A new cellular automaton - finite element coupling scheme for alloy solidification. *Modelling and Simulation in Materials Science and Engineering,* Volume 12, pp. 545-556.

Hamahmy, M. I. & Deiab, I., 2020. Review and analysis of heat source models for additive manufacturing. *The International Journal of Advanced Manufacturing Technology,* Volume 106, pp. 1223-1238.

Han, J.-C., 2012. *Analytical heat transfer.* 1st ed. Boca Raton: CRC Press.

Heigel, J., Michaleris, P. & Reutzel, E., 2015. Thermo-mechanical model development and validation of direct energy deposition additive manufacturing of Ti-6Al-4V. *Additive Manufacturing,* Volume 5, pp. 9-19.

Hejripour, F., Binesh, F., Hebel, M. & Aidun, D. K., 2019. Thermal modeling and characterization of wire arc additive manufactured duplex stainless steel. *Journal of Materials Processing Tech. ,* Volume 272, pp. 58-71.

Hekmatjou, H. et al., 2020. A comparative study of analytical Rosenthal, finite element and experimental approaches in laser welding of AA5456 alloy. *Metals,* 10(436).

Herriott, C. et al., 2019. A multi-scale, multi-physics modeling framework to predict spatial variation of properties in additive-manufactured metals. *Modelling and Simulation in Materials Science and Engineering ,* 27(025009), p. 23pp.

Hinsen, K., 2020. Chapter 2: Computation in Science. In: Anon, ed. *Computation in Science (Second Edition).* Bristol: IOP Publishing Ltd, pp. 2:1 - 2:30.

Hodge, N., Ferencz, R. & Solberg, J., 2014. Implementation of a thermomechanical model for the simulation of selective laser melting. *Comput. Mech. ,* Volume 54, pp. 33-51.

Holm, E. A. & Battaile, C. C., 2001. The computer simulation of microstructural evolution. *Journal of the Minerals, Metals & Materials Society,* 53(9), pp. 20-23.

Huang, Y., Yang, L., Du, X. & Yang, Y., 2016. Finite element analysis of thermal behaviour of metal powder during selective laser melting. *International Journal of Thermal Sciences,* Volume 104, pp. 146-157.

Hu, D. & Kovacevic, R., 2003. Modelling and measuring the thermal behaviour of the molten pool in closed-loop controlled laser-based additive manufacturing. *Proceedings of the Institution of Mechanical Engineers, Part B: Journal of Engineering Manufacture,* 217(4), pp. 441-452.

Hussein, A., Hao, L., Yan, C. & Everson, R., 2013. Finite element simulation of the temperature stress field in single layers built without-support in selective laser melting. *Materials and Design,* Volume 52, pp. 638-647.

Irwin, J. E. et al., 2021. Iterative simulation-based techniques for control of laser powder bed fusion additive manufacturing. *Additive Manufacturing,* 46(102078).

Irwin, J. et al., 2016. Predicting microstructure from thermal history during additive manufacturing for Ti-6Al-4V. *Journal of Manufacturing Science and Engineering,* 138(111007-1).

ISO, 2005. *ISO/TR 581: Weldability-Metallic materials-General principles,* Switzerland: ISO.

Jiji, L. M., 2009. *Heat convection.* 2nd ed. Verlag: Springer.

Keller, T. et al., 2017. Application of finite element, phase-field, and CALPHAD-based methods to additive manufacturing of Ni-based superalloys. *Acta Materialia,* Volume 139, pp. 244-253.

Kelly, S. & Kampe, S., 2004. Microstructural evolution in laser-deposited multilayer Ti-6Al-4V builds: Part 2. thermal modeling. *Metallurgical and Materials Transactions A,* Volume 35A, pp. 1869-1879.

Kelly, S. & Kampe, S. L., 2004. Microstructural evolution in laser-deposited multilayer Ti-6Al-4V builds: Part 1. microstructural characterization. *Metallurgical and Materials Transactions A,* Volume 35A, pp. 1861-1867.

Kelly, S. M., 2004. *Thermal and microstructure modeling of metal deposition processes with application to Ti-6Al-4V.* Blacksburg, Virginia: Virginia Polytechnic Institute and State University.

Khairallah, S. A. & Anderson, A., 2014. Mesoscopic simulation model of selective laser melting of stainless steel powder. *Journal of Materials Processing Technology,* Volume 214, pp. 2627-2636.

Khanpara, P. & Tanwar, S., 2020. Additive manufacturing: Concepts and technologies. In: A. Nayyar & A. Kumar, eds. *A roadmap to industry 4.0: Smart production, sharp business and sustainable development.* Switzerland: Springer, pp. 171-184.

King, W. et al., 2015. Overview of modelling and simulation of metal powder bed fusion process at Lawrence Livermore National Laboratory. *Materials Science and Technology,* 31(8), pp. 957-968.

Knapp, G. et al., 2017. Building blocks for a digital twin of additive manufacturing. *Acta materialia ,* Volume 135, pp. 390-399.

Koepf, J. A., Gotterbarm, M. R., Markl, M. & Korner, C., 2018. 3D multi-layer grain structure simulation of powder bed fusion additive manufacturing. *Acta Materialia,* Volume 152, pp. 119-126.

Koepf, J. et al., 2019. Numerical microstructure prediction by a coupled finite element cellular automaton model for selective electron beam melting. *Computational Materials Science,* Volume 162, pp. 148-155.

Kok, Y. et al., 2018. Anisotropy and heterogeneity of microstructure and mechanical properties in metal additive manufacturing: A critical review. *Materials and Design,* Volume 139, pp. 565-586.

Kollmannsberger, S., Carraturo, M., Reali, A. & Auricchio, F., 2019. Accurate prediction of melt pool shapes in laser powder bed fusion by the non-linear temperature equation including phase changes. *Integrating Materials and Manufacturing Innovation,* Volume 8, pp. 167-177.

Korner, C., Markl, M. & Koepf, J. A., 2020. Modeling and simulation of microstructure evolution for additive manufacturing of metals: A critical review. *Metallurgical and Materials Transactions 50th Anniversary Collection,* Volume 51, pp. 4970-4983.

Kou, S., 2003. *Welding metallurgy.* 2nd ed. Hoboken, New Jersey: John Wiley & Sons, Inc..

Krill III, C. & Chen, L.-Q., 2002. Computer simulation of 3-D grain growth using a phase-field model. *Acta Materialia,* Volume 50, pp. 3057-3073.

Kumara, C. et al., 2019. Predicting the microstructural evolution of electron beam melting of alloy 718 with phase-field modeling. *Metallurgical and Materials Transactions A,* Volume 50A, pp. 2527-2537.

Kumara, C. et al., 2019. Microstructure modelling of laser metal powder directed energy deposition of alloy 718. *Additive Manufacturing,* Volume 25, pp. 357-364.

Kumar, S. & Vedrtnam, A., 2018. Prediction of thermal history in laser metal deposition. *High Temperature Material Processes,* 22(1), pp. 47-62.

Kurz, W., Giovanola, B. & Trivedi, R., 1986. Theory of microstructural development during rapid solidification. *Acta. metall.,* 34(5), pp. 823-830.

Leblond, J. B. & Devaux, J., 1984. A new kinetic model for anisothermal metallurgical transformations in steels including effect of austenite grain size. *Acta metall.,* 32(1), pp. 137-146.

Lee, Y. S. & Zhang, W., 2015. *Mesoscopic simulation of heat transfer and fluid flow in laser powder bed additive manufacturing.* Austin, Texas, 26th Solid Freeform Fabrication Symposium.

Lee, Y. & Zhang, W., 2016. Modeling of heat transfer, fluid flow and solidification microstructure of nickel-base superalloy fabricated by laser powder bed fusion. *Additive Manufacturing,* Volume 12, pp. 178-188.

Levine, L. et al., 2020. Outcomes and conclusions from the 2018 AM-bench measurements, challenge problems, modeling submissions and conference. *Integrating Materials and Manufacturing Innovation,* 9(1).

Lian, Y. et al., 2019 . A cellular automaton finite volume method for microstructure evolution during additive manufacturing. *Materials and Design ,* 169(107672).

Lienhard IV, J. H. & Lienhard V, J. H., 2019. *A heat transfer textbook.* 5th ed. Cambridge, Massachusetts: Phlogiston Press.

Li, J. et al., 2020. Solidification microstructure simulation of Ti-6Al-4V in metal additive manufacturing: A review. *Additive Manufacturing ,* 31(100989).

Li, L. et al., 2020. Temperature and residual stress distribution of FGM parts by DED process: modeling and experimental validation. *The International Journal of Advanced Manufacturing Technology,* Volume 109, pp. 451-462.

Lindgren, L.-E.et al., 2016. Simulation of additive manufacturing using coupled constitutive and microstructure models. *Additive Manufacturing,* Volume 12, pp. 144-158.

Li, Q., Gnanasekaran, B., Fu, Y. & Liu, G., 2020. Prediction of thermal residual stress and microstructure in direct laser metal deposition via a coupled finite element and multiphase field framework. *The Minerals, Metals & Materials Society,* 72(1), pp. 496-508.

Li, R., Xiong, J. & Lei, Y., 2019. Investigation on thermal stress evolution induced by wire and arc additive manufacturing for circular thin-walled parts. *Journal of Manufacturing Processes,* Volume 40, pp. 59-67.

Liu, G. & Quek, S., 2014. *The finite element method: A practical course.* Second ed. Oxford/Waltham: Elsevier.

Liu, S. & Shin, Y. C., 2020. Integrated 2D cellular automata-phase field modeling of solidification and microstructure evolution during additive manufacturing of Ti6Al4V. *Computational Materials Science,* 183(109889).

Liu, S. et al., 2018. Microstructure prediction of selective laser melting AlSi10Mg using finite element analysis. *Materials and Design,* Volume 142, pp. 319-328.

Li, X. & Tan, W., 2018. Numerical investigation of effects of nucleation mechanisms on grain structure in metal additive manufacturing. *Computational Materials Science,* Volume 153, pp. 159-169.

Lloyd's Register Foundation, 2016. *Roadmap for additive manufacturing: Safe adoption of additive manufacturing for safety-critical assets,* London: Lloyd's Register Foundation.

Lopez-Botello, O. et al., 2017. Two-dimensional simulation of grain structure growth within selective laser melted AA-2024. *Materials and Design,* Volume 113, pp. 369-376.

Lundbäck, A. & Lindgren, L.-E., 2011. Modelling of metal deposition. *Finite Elements in Analysis and Design,* Volume 47, pp. 1169-1177.

Lu, X., Li, M. V. & Yang, H., 2021. Simulation of precipitates evolution driven by non-isothermal cyclic thermal history during wire and arc additive manufacturing of IN718 superalloy. *Journal of Manufacturing Processes,* Volume 65, pp. 258-270.

Lu, Y., 2021. *A systematic methodology to develop scaling laws for thermal features of temperature field induced by a moving heat source,* Edmonton: University of Alberta.

Malinov, S., Guo, Z., Sha, W. & Wilson, A., 2001. Differential scanning calorimetry study and computer modeling of beta to alpha phase transformation in a Ti-6Al-4V alloy. *Metallurgical and Materials Transactions A,* Volume 32A, pp. 879-887.

Malinov, S., Markovsky, P., Sha, W. & Guo, Z., 2001. Resistivity study and computer modelling of the isothermal transformation kinetics of Ti-6Al-4C and Ti-6Al-2Sn-4Zr-2Mo-0.08Si alloys. *Journal of Alloys and Compounds ,* Volume 314, pp. 181-192.

Marion, G., 2008. *An introduction to mathematical modelling.* Edinburgh: Bioinformatics and Statistics Scotland.

MathWorks, 2021. *hsv.* [Online] Available at: https://www.mathworks.com/help/matlab/ref/hsv.html [Accessed 23 01 2022].

McLean, M., 1995. Nickel-base superalloys: Current status and potential. *Philosophical Transactions of the Royal Society of London. Series A: Physical and Engineering Sciences,* Volume 351, pp. 419-433.

Michaleris, P., 2014. Modeling metal deposition in heat transfer analyses of additive manufacturing processes. *Finite Elements in Analysis and Design ,* Volume 86, pp. 51-60.

Mi, G. et al., 2014. A coupled thermal and metallurgical model for welding simulation of Ti-6Al-4V alloy. *Journal of Materials Processing Technology,* Volume 214, pp. 2434-2443.

Moatamedi, M. & Khawaja, H. A., 2018. *Finite element analysis.* 1st ed. Boca Raton: CRC Press.

Mohebbi, M. S. & Ploshikhin, V., 2020. Implementation of nucleation in cellular automaton simulation of microstructural evolution during additive manufacturing of Al alloys. *Additive Manufacturing ,* Issue 101726.

Montevecchi, F., Venturini, G., Scippa, A. & Campatelli, G., 2016. Finite element modelling of wire-arc-additive-manufacturing process. *Procedia CIRP,* Volume 55, pp. 109-114.

Moshtagh, N., 2005. Minimum volume enclosing ellipsoids. *Convex optimization,* Volume 111, pp. 1-9.

Mukherjee, T., Zhang, W. & DebRoy, T., 2017. An imporved prediction of residual stresses and distortion in additive manufacturing. *Computational Materials Science,* Volume 126, pp. 360-372.

Naterer, G. F., 2022. *Advanced heat transfer.* 3rd ed. Boca Raton: CRC Press.

National Institute of Standards and Technology, 2013. *Measurement science roadmap for metal-based additive manufacturing,* Columbia: Energetics Incorporated.

National Institute of Standards and Technology, 2018. *AMB2018-01 Description.* [Online] Available at: https://www.nist.gov/ambench/amb2018-01-description

National Institute of Standards and Technology, 2018. *AMB2018-02 Description.* [Online] Available at: https://www.nist.gov/ambench/amb2018-02-description [Accessed 2019].

National Institute of Standards and Technology, 2019. *Benchmark Test Data.* [Online] Available at: https://www.nist.gov/ambench/benchmark-test-data [Accessed 2019].

Navid, A. H. F. & Aghababa, A. B., 2013. Cellular Learning Automata and Its Applications. In: A. Salcido, ed. *Emerging Applications of Cellular Automata.* London: IntechOpen, pp. 85-111.

Ngo, T. D. et al., 2018. Additive manufacturing (3D printing): A review of materials, methods, applications and challenges. *Composites Part B,* Volume 143, pp. 172-196.

Ogino, Y., Asai, S. & Hirata, Y., 2018. Numerical simulation of WAAM process by a GMAW weld pool model. *Welding in the World,* Volume 62, pp. 393-401.

Olleak, A. & Xi, Z., 2019. Simulation of layer-by-layer selective laser melting process with an efficient remeshing technique. *Procedia Manufacturing,* Volume 34, pp. 613-618.

Ou, W. et al., 2018. Fusion zone geometries, cooling rates and solidifcation parameters during wire arc additive manufacturing. *International Journal of Heat and Mass Transfer,* Volume 127, pp. 1084-1094.

Parimi, L. L., G., A. R., Clark, D. & Attallah, M. M., 2014. Microstructural and texture development in direct laser fabricated IN718. *Materials Characterization,* Volume 89, pp. 102-111.

Pepper, D. W. & Heinrich, J. C., 2017. *Finite element methods: Basic concepts and applications with MATLAB, MAPLE and COMSOL.* Third ed. United States: CRC Press.

Peter, N., Pitts, Z., Thompson, S. & Saharan, A., 2020. Benchmarking build simulation software for laser powder bed fusion of metals. *Additive Manufacturing ,* 36(101531).

Peyre, P., Dal, M., Pouzet, S. & Castelnau, O., 2017. Simplified numerical model for the laser metal deposition additive manufacturing process. *Journal of Laser Applications,* 29(2).

Pinkerton, A. J., 2015. Advances in the modeling of laser direct metal deposition. *Journal of Laser Applications ,* 27(S1).

Popovich, V. A. et al., 2017. Functionally graded Inconel 718 processed by additive manufacturing: Crystallographic texture, anisotropy of microstructure and mechanical properties. *Materials & Design,* Volume 114, pp. 441-449.

Promoppatum, P., Yao, S.-C., Pistorius, P. C. & Rollett, A. D., 2017. A comprehensive comparison of the analytical and numerical prediction of the thermal history and solidification microstructure of Inconel 718 products made by laser powder-bed fusion. *Engineering,* Volume 3, pp. 685-694.

Rai, A., Markl, M. & Körner, C., 2016. A coupled cellular automaton-lattice boltzmann model for grain structure simulation during additive manufacturing. *Computational Materials Science,* Volume 124, pp. 37-48.

Rao, S. S., 2005. *The finite element method in engineering.* 4th ed. Oxford: Elsevier.

Rappaz, M., 1989. Modelling of microstructure formation in solidification processes. *International Materials Reviews,* 34(3), pp. 93-123.

Rappaz, M. & Gandin, C.-A., 1993. Probabilistic modelling of microstructure formation in solidification processes. *Acta metall. mater.,* 41(2), pp. 345-360.

Rappaz, M., Gandin, C.-A., Desbiolles, J.-L. & Thevoz, P., 1996. Prediction of grain structures in various solidification processes. *Metallurgical and Materials Transactions A,* Volume 27A, pp. 695-705.

Rappaz, M. & Thevoz, P., 1987. Solute diffusion model for equiaxed dendritic growth. *Acta metall. ,* 35(7), pp. 1487-1497.

Recktenwald, G., 2011. *Finite difference approximations to the heat equation.* Portland: Portland State University.

Reese, Z. C., Fox, J., Taylor, J. & Evans, C., 2018. *Evolution of cooling length in parts created through laser powder bed fusion additive manufacturing.* Berkley, CA, ASPE Summer Topical Meeting: Advancing Precision in Additive Manufacturing.

Roberts, I. et al., 2009. A three-dimensional finite element analysis of the temperature field during laser melting of metal powders in additive manufacturing. *International Journal of Machine Tools & Manufacture,* Volume 49, pp. 916-923.

Robichaud, J., Vincent, T., Schultheis, B. & Chaudhary, A., 2019. Integrated computational materials engineering to predict melt-pool dimensions and 3D grain structures for selective laser melting of Inconel 625. *Integrating Materials and Manufacturing Innovation,* Volume 8, pp. 305-317.

Rodgers, T., Madison, J., Tikare, V. & Maguire, M., 2016. Predicting mesoscale microstructural evolution in electron beam welding. *Journal of the Minerals, Metals & Materials Society,* 68(5).

Rodgers, T. M., Lim, H. & Brown, J. A., 2020. Three-dimensional additively manufactured microstructures and their mechanical properties. *Journal of the Minerals, Metals & Materials Society,* Volume 72, pp. 75-82.

Rodgers, T. M., Madison, J. D. & Tikare, V., 2017. Simulation of metal additive manufacturing microstructures using kinetic Monte Carlo. *Computational Materials Science,* Volume 135, pp. 78-89.

Rodgers, T. M., Mitchell, J. A. & Tikare, V., 2017. A Monte Carlo model for 3D grain evolution during welding. *Modelling and Simulation in Materials Science and Engineering,* 25(064006).

Rodic, B., 2017. Industry 4.0 and the New Simulation Modelling Paradigm. *Organizacija,* Volume 50.

Roehling, T. T. et al., 2017. Modulating laser intensity profile ellipticity for microstructural control during metal additive manufacturing. *Acta Materialia,* Volume 128, pp. 197-206.

Rolchigo, M. & LeSar, R., 2019. Application of alloy solidification theory to cellular automata modeling of near-rapid constrained solidification. *Computational Materials Science,* Volume 163, pp. 148-161.

Sabau, A. S. et al., 2020. Fluid dynamics effects on microstructure prediction in single-laser tracks for additive manufacturing of IN625. *Metallurgical and Materials Transactions B,* Volume 51B, pp. 1263-1281.

Safdar, S. et al., 2013. An anisotropic enhanced thermal conductivity approach for modelling laser melt pools for Ni-base super alloys. *Applied Mathematical Modelling,* Volume 37, pp. 1187-1195.

Sahoo, S. & Chou, K., 2016. Phase-field simulation of microstructure evolution of Ti-6Al-4V in electron beam additive manufacturing process. *Additive Manufacturing,* Volume 9, pp. 14-24.

Salerno, G. et al., 2018. On the interaction between welding residual stresses: a numerical and experimental investigation. *International Journal of Mechanical Sciences,* Volume 144, pp. 654-667.

Seetharaman, S. et al., 2016. Research updates on the additive manufacturing of nickel based superalloys. *Solid Freeform Fabrication 2016: Proceedings of the 27th Annual International Solid Freeform Fabrication Symposium - An Additive Manufacturing Conference,* pp. 469-486.

Shahabad, S. I. et al., 2020. Heat source model calibration for thermal analysis of laser powder-bed fusion. *The International Journal of Advanced Manufacturing Technology,* Volume 106, pp. 3367-3379.

Sher, D., 2020. *Additive manufacturing history in the making as Boeing 77X makes maiden flight with GE9X engines.* [Online] Available at: https://www.3dprintingmedia.network/additive-manufacturing-history-in-the-making-as-boeing-777x-makes-maiden-flight-with-ge9x-engines/ [Accessed 27 01 2022].

Shiffman, D., 2012. Chapter 7. Cellular Automata. In: S. Fry & Z. Marsh, eds. *The Nature of Code.* New York: D. Shiffman.

Shrestha, S. & Chou, K., 2018. Computational analysis of thermo-fluid dynamics with metallic powder in SLM. In: L. Nastac, et al. eds. *CFD modeling and simulation in materials processing 2018. TMS 2018. The Minerals, Metasl & Materials Series.* Cham: Springer , pp. 85-95.

Sieradzki, L. & Madej, L., 2013. A perceptive comparison of the cellular automata and Monte Carlo techniques in application to static recrystallization modeling in polycrystalline materials. *Computational Materials Science,* Volume 67, pp. 156-173.

Singamneni, S. et al., 2019. Additive manufacturing for the aircraft industry: A review. *Journal of Aeronautics & Aerospace Engineering,* 8(1).

Singh, N., 2015. *Phase field modeling: A report submitted on the completion of summer internship at Bhabha atomic research centre,* Mumbai: Bhabha Atomic Research Centre.

Special Metals, 2007. *Inconel Alloy 718.* [Online] Available at: https://www.specialmetals.com/documents/technical-bulletins/inconel/inconel-alloy-718.pdf
[Accessed 02 November 2021].

Special Metals, 2013. *Inconel Alloy 625.* [Online] Available at: https://www.specialmetals.com/documents/technical-bulletins/inconel/inconel-alloy-625.pdf
[Accessed 02 November 2021].

Spittle, J. A. & Brown, S. G. R., 1989. A computer simulation of the influence of processing conditions on as-cast grain structures. *Journal of Materials Science,* Volume 23, pp. 1777-1781.

Spittle, J. A. & Brown, S. G. R., 1989. Computer simulation of the effects of alloy variables on the grain structures of castings. *Acta metall.,* 37(7), pp. 1803-1810.

StatEase, 2022. *Design-Expert v12.* [Online] Available at: https://www.statease.com/docs/v12/
[Accessed 28 01 2022].

Stavropoulos, P. & Foteinopoulos, P., 2018. Modelling of additive manufacturing processes: a review and classification. *Manufacturing Review,* 5(2).

Steinbach, I. et al., 1996. A phase field concept for multiphase systems. *Physica D,* Volume 94, pp. 135-147.

Steuben, J. C., Nirnbaum, A. J., Michopoulos, J. G. & Iliopoulos, A. P., 2019. Enriched analytical solutions for additive manufacturing modeling and simulation. *Additive Manufacturing,* Volume 25, pp. 437-447.

Suarez, A. et al., 2011. Modeling of phase transformation of Ti6Al4V during laser metal deposition. *Physics Procedia,* Volume 12, pp. 666-673.

Tadmor, E., 2012. A review of numerical methods for nonlinear partial differential equations. *Bulletin (New Series) of the American Mathematical Society,* 49(4), pp. 507-554.

Tang, M., 2017. *Inclusions, porosity and fatigue of AlSi10Mg parts produced by selective laser melting ,* Pittsburgh: Carnegie Mellon University .

Tang, Y. T. et al., 2021. Alloys-by-design: Application to new superalloys for additive manufacturing. *Acta Materialia,* Volume 202, pp. 417-436.

Teferra, K. & Rowenhorst, D. J., 2021. Optimizing the cellular automata finite element model for additive manufacturing to simulate large microstructures. *Acta Materialia,* 213(116930).

UC Riverside, Central Facility for Advance Microscopy and Microanalysis, 2013. *Introduction to EBSD.* [Online] Available at: https://cfamm.ucr.edu/media/226/download [Accessed 28 01 2022].

Vakili-Tahami, F. & Ziaei-Asl, A., 2013. Numerical and experimental investigation of T-shape fillet welding of AISI 304 stainless steel plates. *Materials & Design,* Volume 47, pp. 615-623.

Vastola, G., Zhang, G., Pei, Q. X. & Zhang, Y.-W., 2016. Modeling the microstructure evolution during additive manufacturing of Ti6Al4V: A comparison between electron beam melting and selective laser melting. *The Minerals, Metals & Materials Society,* 68(5).

Velten, K., 2009. 1.1 A complex world needs models. In: *Mathematical modeling and simulation: Introduction for scientists and engineers.* Weinheim: WILEY-VCH Verlag GmbH & Co. KGaA, pp. 1-3.

Venkatkumar, D. & Ravindran, D., 2016. 3D finite element simulation of temperature distribution, residual stress and distortion on 304 stainless steel plates using GTA welding. *Journal of Mechanical Science and Technology ,* 30(1), pp. 67-76.

Versteeg, H. K. & Malalasekera, W., 2007. Chapter four: The finite volume method for diffusion problems. In: *An introduction to computational fluid dynamics: The finite volume method.* Harlow: Pearson Education Limited, pp. 115-134.

Walker, T. B. C., Lee, T. & Clare, A., 2019. A validated analytical-numerical modelling strategy to predict residual stress in single-track laser deposited IN718. *International Journal of Mechanical Sciences,* Volume 151, pp. 609-621.

Walker, T., Bennett, C., Lee, T. & Clare, A., 2020. A novel numerical method to predict the transient track geometry and thermomechanical effects through in-situ modification of the process parameters in direct energy deposition. *Finite Elements in Analysis and Design,* 169(103347).

Wang, L., 2021. Prediction of the microstructural grain evolution during selective laser melting by a cellular automata method. *Journal of Physics: Conference Series,* 2090(012056).

Wang, X. & Wang, A., 2016. Three-dimensional finite element analysis with clamping in wire and arc additive manufacturing. *2016 European Modelling Symposium (EMS),* pp. 104-108.

Wei, H. et al., 2021. Mechanistic models for additive manufacturing of metallic components. *Progress in Materials Science,* 116(100703).

Williams, S. et al., 2016. Wire + Arc Additive Manufacturing. 32(7).

Wolfram, S., 1994. Cryptography with cellular automata. In: *Cellular automata and complexity.* USA: Westview Press, pp. 487-490.

Wolfram, S., 2002. *A New Kind of Science.* Champaign: Wolfram Media, Inc..

Xiong, J., Lei, Y. & Li, R., 2017. Finite element analysis and experimental validation of thermal behavior for thin-walled parts in GMAW-based additive manufacturing with various substrate preheating temperatures. *Applied Thermal Engineering,* Volume 126, pp. 43-52.

Xu, X., Ding, J., Ganguly, S. & Williams, S., 2019. Investigation of process factors affecting mechanical properties of Inconel 718 superalloy in wire + arc additive manufacture process. *Journal of Materials Processing Tech.,* Volume 265, pp. 201-109.

Yang, J. et al., 2018. Prediction of microstructure in selective laser melted Ti-6Al-4V alloy by cellular automaton. *Journal of Alloys and Compounds,* Volume 748, pp. 281-290.

Yang, X. et al., 2020. Prediction of microstructure evolution for additive manufacturing of Ti-6Al-4V. *Procedia Manufacturing,* Volume 47, pp. 1178-1183.

Yang, Y., Allen, M., London, T. & Oanceas, V., 2019. Residual strain predictions for a powder bed fusion Inconel 625 single cantilever part. *Integrating Materials and Manufacturing Innovation,* Volume 8, pp. 294-304.

Yang, Y., Zhou, X., Li, Q. & Ayas, C., 2021. A computationally efficient thermo-mechanical model for wire arc additive manufacturing. *Additive Manufacturing ,* 46(102090).

Yan, L. et al., 2018. Fast prediction of thermal history in large-scale parts fabricated via a laser metal deposition process. *Solid Freeform Fabrication 2018: Proceedings of the 29th Annual International Solid Freeform Fabrication Symposium - An Additive Manufacturing Conference,* pp. 517-526.

Yan, W. et al., 2018. An integrated process-structure-property modeling framework for additive manufacturing. *Computer Methods in Applied Mechanics and Engineering,* Volume 339, pp. 184-204.

Yap, C. et al., 2015. Review of selective laser melting: Materials and applications. *Applied Physics Reviews,* 2(041101).

Yongjie, Z., Gang, Y. & Xiuli, H., 2012. Numerical study of thermal history in laser aided direct metal deposition process. *Science China-Physics, Mechanics & Astronomy,* 55(8), pp. 1431-1438.

Zavala-Arredondo, M. et al., 2019. Use of power factor and specific point energy as design parameters in laser powder-bed-fusion (L-PBF) of AlSi10Mg. *Materials & Design,* 182(108018).

Zhang, D. et al., 2017. Modeling of temperature field evolution during multilayer direct laser metal deposition. *J Therm Spray Tech,* Volume 26, pp. 831-845.

Zhang, J., Li, W., Yan, L. & Liou, F., 2018. A two-dimensional simulation of grain structure growth within the substrate and the fusion zone during direct metal deposition. *Comptes Rendus Mecanique,* Volume 346, pp. 1072-1086.

Zhang, Q. et al., 2019. A metallurgical phase transformation framework applied to SLM additive manufacturing processes. *Materials and Design,* 166(107618).

Zhang, X. & Liang, E., 2019. Metal additive manufacturing in aircraft: current application, opportunities and challenges. *IOP Conf. Series: Materials Science and Engineering ,* Volume 493.

Zhan, M. et al., 2019. Numerical and experimental investigation on laser metal deposition as repair technology for 316L stainless steel. *Optics and Laser Technology,* Volume 118, pp. 84-92.

Zhan, X. et al., 2018. Modeling and simulation of the columnar-to-equiaxed transition during laser melting deposition of Invar alloy. *Journal of Alloys and Compounds,* Volume 755, pp. 123-134.

Zhan, X. et al., 2015. The numerical and experimental investigation of the multi-layer Laser-MIG hybrid welding for Fe36Ni Invar alloy. *Journal of Materials Engineering and Performance,* 24(12), pp. 4948-4957.

Zinovieva, O., Zinoviev, A. & Ploshikhin, V., 2018. Three-dimensional modeling of the microstructure evolution during metal additive manufacturing. *Computational Materials Science,* Volume 141, pp. 207-220.

Zinovieva, O. et al., 2015. A solution to the problem of the mesh anisotropy in cellular automata simulations of grain growth. *Computational Materials Science,* Volume 108, pp. 168-176.

Zinovieva, O. et al., 2015. Two dimensional cellular automata simulation of grain growth during solidification and recrystallization. *IOP Conf, Series: Materials Science and Engineering,* 71(012073).

Zinoviev, A. et al., 2016. Evolution of grain structure during laser additive manufacturing. Simulation by a cellular automata method. *Materials and Design ,* Volume 106, pp. 321-329.

Appendix

NIST AM Benchmark submission

Integrating Materials and Manufacturing Innovation (2019) 8:294–304
https://doi.org/10.1007/s40192-019-00144-5

THEMATIC SECTION: ADDITIVE MANUFACTURING BENCHMARKS 2018

Residual Strain Predictions for a Powder Bed Fusion Inconel 625 Single Cantilever Part

Yangzhan Yang[1] · Madie Allen[2,3] · Tyler London[4] · Victor Oancea[1]

Received: 14 January 2019 / Accepted: 23 May 2019 / Published online: 03 July 2019

Abstract
The laser powder bed fusion (LPBF) process involves using a laser beam to selectively melt metal powder with a desired shape on a substrate to create a part layer-by-layer. As an Additive Manufacturing (AM) process, laser powder bed fusion (commonly referred to as selective laser melting—SLM) offers superior design freedom over conventional manufacturing methods and enables the production of complex, lightweight geometries with applications in the aerospace, automotive, and biomedical industries. In addition to enhanced design freedom, AM technologies provide improved material utilization and allow for reduced assembly needs. However, the reliability and repeatability of additively manufactured parts is a challenge to the wide-scale adoption of the technology for safety critical parts. A critical limitation of process optimization is the prediction and control of residual stresses, distortion, and microstructure evolution. This work focuses on the development and implementation of a numerical modeling technique for the prediction of residual strains within an Inconel 625 LPBF part. The model, using the SIMULIA Additive Manufacturing Scenario App, based on the Abaqus 2018 finite element solver, was developed and analyzed as part of a submission for the NIST AM Benchmark 2018. A sequentially coupled thermo-mechanical analysis was adopted to replicate the building conditions of a single cantilever beam built at the NIST laboratories. The results of the blind study were compared to X-ray diffraction (XRD) measurements of the physical build. The predicted three-dimensional residual strain field showed a high level of accuracy and the submission described in this paper received joint first prize in the residual elastic strain category of the NIST AM Benchmark 2018. The results presented in this paper reflect only findings before the benchmark measurements were posted on the NIST website.

Keywords Additive manufacturing · Selective laser melting · Numerical modeling · Residual strain

Introduction

Additive manufacturing (AM) has been of interest from as early as the 1980s [1]. The process requires that the desired shape be divided into relatively thin layers (or slices) and added consecutively on top of each other. Initially used to produce rapid prototypes, significant research and development over the past decade means that AM can now be used as a near net shape method of manufacture. The technique boasts a wide range of applications from weight-reduced aerospace parts [2] to bespoke artificial joints [3]. Between 1990 and 2015, the growth rate of the worldwide revenues generated from all AM products or services was 25.4% [4]. This increase in interest was due to the wide range of benefits the technique has to offer. AM provides methods of waste reduction [5], customization opportunities [6], and part repair [7]. Furthermore, it eradicates the need for the creation of geometry specific dies and provides new methods of creating even more complex geometries.

One particular AM process that offers the capability of the production of complex structures is laser powder bed fusion (LPBF), which is also commonly referred to as selective laser melting (SLM). SLM is a powder bed fusion process that uses a laser as a heat source as opposed to an electron beam or wire arc. The use of a powder bed enables the fabrication of lattice structures; features that could not be manufactured by

✉ Madie Allen
madie.allen@affiliate.twi.co.uk

[1] Dassault Systèmes SIMULIA Corp, Johnston, RI, USA
[2] NSIRC, TWI Ltd, Cambridge, UK
[3] Brunel University, London, UK
[4] TWI Ltd, Cambridge, UK

traditional methods such as casting. SLM is one technique that can also be used to reduce the weight-to-strength ratio of a part by manufacturing topology optimized parts. However, due to the relative infancy of the technology, there are still a number of challenges with the process that are preventing its widespread introduction into industry.

The procedure has a number of limitations, some of which challenge the reliability of the build parts and others that constrain the manufacture process itself. For example, certain AM procedures such as SLM are limited by the size of the build chamber. These processes can also exhibit very long manufacture times, due to the slow scan speeds and small layer heights. Other issues that can be more widely applied to all AM procedures include surface roughness, lack of fusion, and distortion.

Primarily, the main challenge with all AM procedures is the reliability and repeatability of parts [8, 9]. Due to the thermal cycles that are experienced by the part during the build process, residual stresses are induced, resulting in part distortions. In addition, the thermal field induces changes within the microstructure of the material, resulting in altered material properties. These factors cause unreliability in additively manufactured parts. Alterations in mechanical properties and unknown residual stresses mean that the suitability of the part is unknown until tested. Therefore, non-destructive testing methods are required to determine the material properties of the built part and any possible defects, such as pores caused by lack of fusion; however, the lack of inspectability of complex parts by means other than computed tomography limits scalability.

The key to unlocking the potential of this new technology is understanding every aspect of the process and its effect on the material behavior, so that parts can be manufactured in a fit-for-purpose state. Numerical modeling plays a large part in enabling this by providing a method of testing the effect of physical parameters without the cost of experimental trials. Once a validated model that can predict the impact of these parameters has been established, it can be used to investigate of the tailoring process parameters to achieve desirable material properties and minimize distortion and residual stress.

Previous work on additive manufacturing has included the research of modeling methods to predict distortion and residual stresses [10–14], melt pool geometry and energy penetration depth [15, 16], microstructure [17, 18], or to determine the effect of different process parameters [19, 20]. Due to the complexity of the process, simulation techniques vary a great deal, depending on which particular AM process is being implemented and what feature or parameter is the central interest of the study. A relatively detailed review of existing modeling approaches was recently summarized by Luo and Zhao [21].

In this study, the focus is on a method of prediction of residual stresses for the selective laser melting process. In order to model residual stresses, first a sufficiently representative thermal model is required.

A number of heat source models have been used to model the laser. Song et al. [22] undertook an investigation into residual stresses and microstructure using powder bed methods with a nickel superalloy. A Goldak double ellipsoidal model was used to represent the moving heat source. Meanwhile, Hussein et al. [23] use the more common Gaussian model in their analysis of temperature and stress fields. While Hussein et al. [23] use only a single layer in their model, simulations which include multiple layers must exhibit a method of material deposition. Song et al. [22] use the element birth and death technique, in which sets of elements are activated/deactivated within new steps. This method is implemented by many others including Fu et al. [24]. Alternative methods include the quiet element method demonstrated by Michaleris [25].

Material properties, specified within the analysis, should also be temperature and state dependent [26]. For example, Huang et al. [27] establish an effective thermal conductivity for powder particles, and also use a linear mixing rule to take porosity of the powder into account within its density.

When considering the simulation of residual strains, a number of approaches are available. Li et al. [11, 12] have developed a multi-scale model. Multi-scale models have become of increasing interest due to their computational efficiency. The model shows the implementation of a Gaussian heat distribution on a micro, meso, and macro scale. The benefit of this method is that it allows for the implementation of specific scan strategies. Other approaches include an analytical method, demonstrated by Fergani et al. [10]. Furthermore, Wu et al. [13] implement a sequentially coupled thermo-mechanical analysis through Abaqus, similar to the work presented here. Sequentially coupled analyses save a significant amount of computational time [26] without sacrificing a reasonably accurate representation of the underlying physics. Denlinger et al. [28] also use a sequentially coupled analysis in their model of electron beam direct manufacture and again in reference [29]. In this analysis, the weak coupling was used as the plastic strain energy was significantly small in comparison to laser energy. More recently, Williams et al. [14] have also used a sequentially coupled analysis through Abaqus, using a 'block dump' approach for material deposition that will be used within this work. This is an efficient tool that also reduces computational cost of the analysis.

In this paper, a specific approach for simulating residual strains within an Inconel 625 part created by SLM is described. This was undertaken as part of the AM Benchmark 2018, challenge 1 to (AMB201801). In section "The Challenge", an outline of the challenge is provided, followed

by a description of the modeling approach in section "Modeling Approach". Finally, a discussion of the results is presented in section "Results and Discussion".

The Challenge

For this section, note that all details regarding the design and setup of the experiment have been sourced from reference [30], along with some independent correspondence with the challenge coordinators.

The part geometry for this challenge was a simple single cantilever structure of dimension 75 mm, 5 mm, and 12.5 mm in length, width, and height, respectively. A depiction of the geometry can be seen in Fig. 1.

For each build process, four parts were built on the same substrate. A full schematic of the layout and dimensions can be found in reference [30]. However, as spacing is sufficient between parts such that the build of an adjacent part has a negligible effect on the thermal history of the current part, the model is reduced to a single part, saving on computation time. Nevertheless, it is important to consider the entire build layout when calculating the cooling time between layers, as this will have a first-order impact on the thermal history of the part and consequently the residual strain field. The reduced model is a single part, mounted on a section of the substrate. The section is taken to be 81 mm × 12.7 mm × 11 mm (length × height × width).

Within the benchmark, the part was built in IN625 and 15-5PH Stainless Steel as part of the experimental tests held at the NIST laboratories. The substrate in both cases was the same alloy as the build part. In this study, IN625 was chosen as the build material. The material properties used within the model can be found in section "Material Properties".

The manufacture of parts, within the benchmark, was undertaken on two different machines: an NIST-built machine and an EOS M270. It is assumed from here on out in this analysis that the EOS M270 is used. The exact build parameters used during the process can be seen in Table 1.

Table 1 Build parameters [30]

Build parameter (units)	Value
Infill laser power (W)	195
Contour laser power (W)	100
Laser diameter (μm)	50 *(estimated)*
Infill scan speed (mm/s)	800
Contour scan speed (mm/s)	900
Infill hatch distance (μm)	100
Layer height (μm)	20

The scan strategy used is outlined in great detail within the challenge description, including laser on and off times. Firstly, each layer begins with a contour scan, creating only the outline of a single part. An infill scan of the current part then occurs, before moving on to the next part within the build. From Table 1, it can be seen that the infill and contour scans have different laser properties. In addition, the infill scan strategy alternates, between horizontal and vertical scans, depending on whether an odd or even layer is being completed. This is a common technique used within AM in order to reduce lack of fusion within the build.

The parts described above were built to these specific parameters at the NIST laboratories. This was in preparation for experimental testing as comparative data for simulations.

Multiple tests were undertaken on the completed build part and many features observed, including distortion, residual strain, and microstructure properties. This paper focuses solely on the prediction of the residual strain measurements.

The evaluation of residual strain was undertaken using X-ray diffraction (XRD) measurements across the central plane of the build. Additionally, measurements were only taken along the thickest legs. The measurement plane can be seen in Fig. 2.

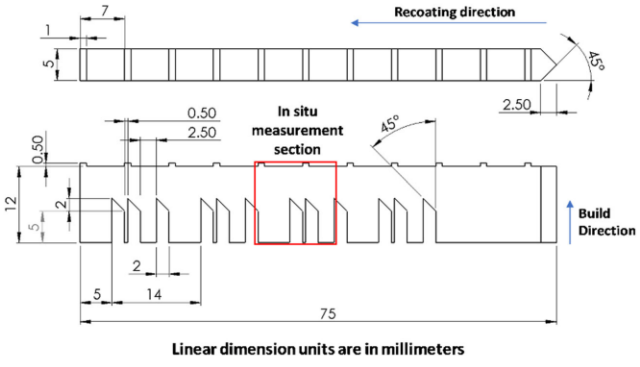

Fig. 1 The full geometry of the build part as given by NIST [30]

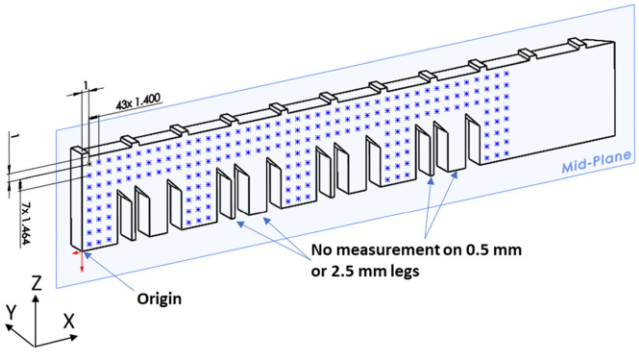

Fig. 2 Plane for XRD measurement [30]

For additional information on the experimental measurement procedure, please refer to reference [31].

Modeling Approach

In order to achieve the prediction of residual strains, a numerical simulation was undertaken using the additive manufacturing process Apps from DASSAULT SYSTEMES [22]. Details of the modeling approach in the software package can be found below in section "Software". The software offers several modeling approaches including thermo-mechanical and eigenstrain/inherent strain methods. In this particular work, the authors have adopted the sequentially coupled thermo-mechanical procedure.

Sequentially coupled analyses rely on the fact that the first analysis is independent of the second. Hence, in this particular case, the thermal history of the build can be assumed to be independent of its mechanical response [29]. This form of analysis is preferential to a fully coupled analysis as it saves a considerable amount of computational time and cost. Sections "Thermal Simulation" and "Mechanical Simulation" outline the approach to each part of the analysis.

Software

Initially, the DELMIA Powder Bed Fabrication App was used to generate the slicing, recoating, and laser trajectories of the part. This was done to comply with the specifications of the challenge, including laser speed, power, and infill pattern. The actual analysis was completed in the SIMULIA Additive Manufacturing Scenario App, based on the Abaqus 2018 finite element solver. The app offers the ability to use either a thermo-mechanical method or an eigenstrain based method. Within this study, we used the thermo-mechanical approach.

As implemented in Abaqus 2017 [32], key features of the physics-based framework that facilitate a more representative analysis of additive manufacturing processes include (1) the ability to use finite element meshes that do not conform to the actual powder layer thickness; (2) explicit use of the spatial and temporal data associated with laser scan paths and powder recoating for defining material activation in the model and integration of the moving heat source; (3) an "intersection module" that slices the laser scan path within the finite element mesh to distribute the heat source over a given increment of time; (4) progressive element activation to track the specific volume of an element that is either completely or partially filled with material (integration points) that are active within a given time increment; and (5) progressive heat loss through convection and radiation by determining the evolving lateral and vertical free surfaces as a consequence of the layer-by-layer activation process. These specific features and their application within the current finite element model are described in more detail in subsequent sections.

Geometry and Mesh

The single cantilever used in this study can be seen earlier in Fig. 1. In order to replicate this geometry exactly within the model, the STL file was taken directly from the challenge description [30] and converted into a solid part within the Abaqus model. A second part was created in the model to represent the build plate. This is an important aspect that must be accounted for in order to achieve a reasonable thermal history prediction, due to the large heat sink effect induced by the relatively large size of the substrate in comparison to the build. The substrate dimensions were given by NIST in the task description [30]. However, to model the entire build plate would have been computationally expensive, especially as four parts were built on each build plate. Moreover, each part was thermally isolated from the other parts; that is, the spacing is sufficient such that the build of an adjacent part has a negligible effect on the thermal history of any other part. Therefore, within this model, a reduced substrate was used

and only a single part was modeled. The reduced substrate was still sufficiently large (with the actual through-wall thickness modeled) to account for the heat sink effect of the substrate. The dimensions of this section can be found above in section "The Challenge". The two parts were connected by a mesh "gluing" technique constraint within the interaction model. This ensures that the heat transfer flows from the build material through to the build plate directly.

In order to achieve a regular, structured mesh, the build part was partitioned. Throughout the thermal analysis, linear hexahedron (DC3D8) elements were used. An identical mesh was used in the structural analysis, to allow the analysis to take place on a compatible mesh (see section "Mechanical Simulation"). The characteristic element size of the build was 0.20 mm (Fig. 3). Hence, each element accounted for approximately 10 real layers. Single element layers were unfeasible due to the large number of layers within the model. The element size was chosen as compromise between accuracy and run time. The partial integration and homogenization modeling techniques in the Abaqus 2018 solver were leveraged to mitigate the discrepancy between element size and layer thickness.

Material Properties

As described previously, IN625 was the build material in this study. Due to the abundant use of this nickel superalloy within industry, material property data is widely available for this particular alloy. However, within this application to a powder bed process, temperature-dependent data is required. The large thermal gradients that take place in the manufacturing process mean that the material experiences a wide range of temperatures and physical states.

Table 2 Temperature-independent material properties

Density (kg/m^3)	8440
Solidus temperature (°C)	1290
Liquidus temperature (°C)	1350
Latent heat for phase transformation (J/kg)	272E+3

The above (Table 2) gives the values of some temperature-independent properties of the material. The temperature-dependent data used for the thermal conductivity, specific heat capacitance, Young's modulus, Poisson's ratio, and coefficient of thermal expansion can all be seen in Fig. 4a–e [33]. In general, for manufacturing process simulations, one accounts for the temperature-dependent plasticity behavior of the material under consideration. For example, temperature-dependent stress-strain curves would be implemented in the finite element solver to accurately account for the softening response at elevated temperatures. However, due to the range of temperatures that are experienced by the material, as a result of the time integration method used, the plastic behavior exhibits only a small dependency on temperature. Moreover, Li et al. [11, 12] and Wu et al. [13] have shown that for similar materials and geometric configurations, the temperature-dependent behavior is of second-order importance. Wen et al. [34] have also shown reasonable success predicting

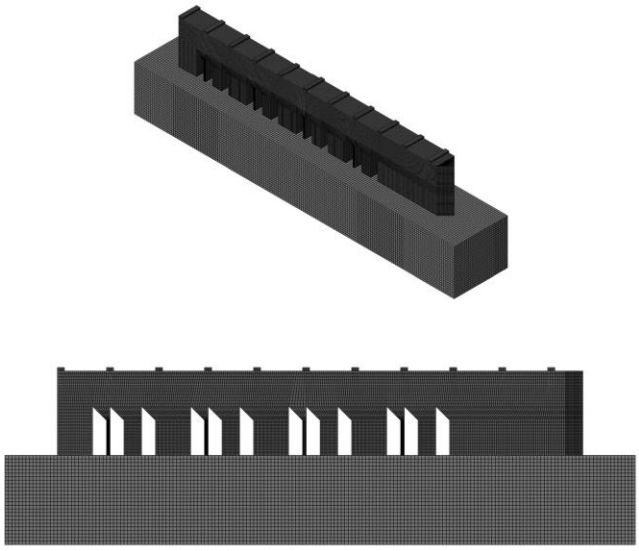

Fig. 3 Finite element mesh of part in 2 directions

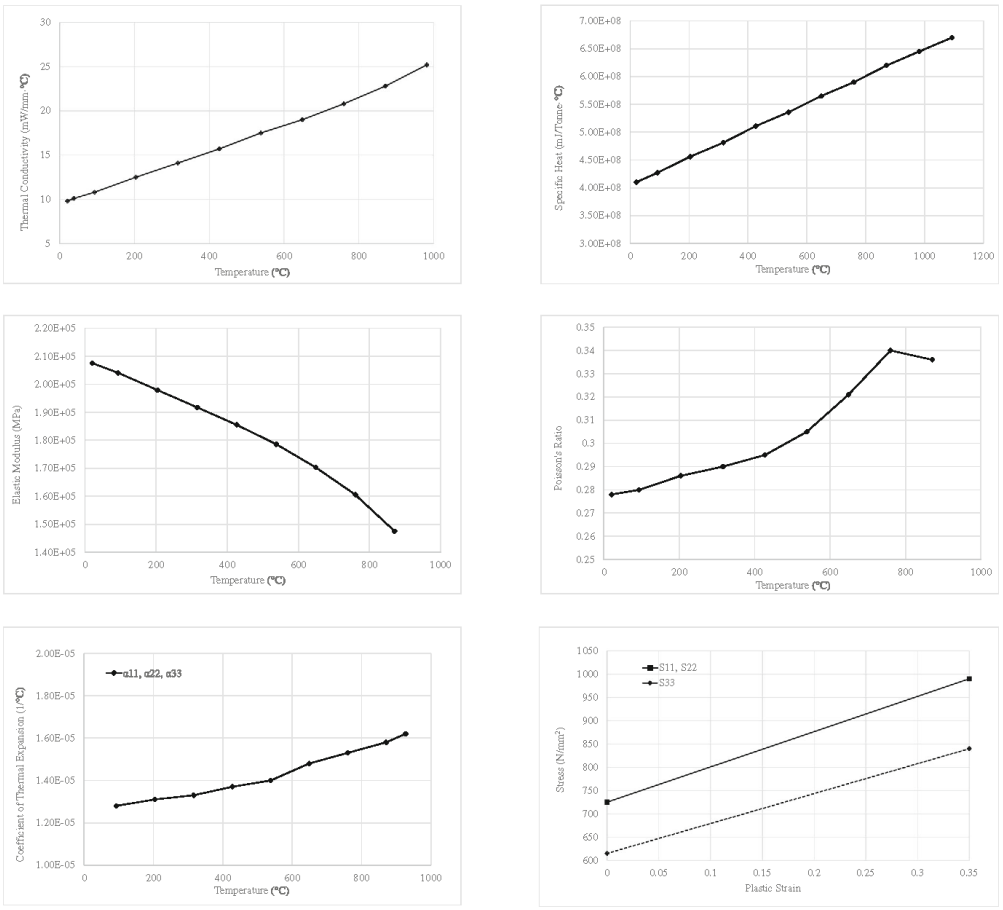

Fig. 4 Temperature-dependent material properties and plasticity: **a** thermal conductivity, **b** specific heat, **c** elastic modulus, **d** Poisson's ratio, **e** coefficient of thermal expansion, **f** orthotropic plasticity

residual stress with temperature-independent properties. Therefore, for the simulations in this work, temperature-independent yielding behavior was implemented, with a bilinear, orthotropic plasticity hardening model as shown in Fig. 4f [35]. The material's yield stress is 725 MPa in the horizontal x- and y-directions and 615 MPa in the vertical z-direction. The stress ratio is 0.8483. The stress corresponding to a plastic strain of 0.35 is 990 MPa in the horizontal directions, and the stress in the vertical direction is scaled with the same stress ratio as that used for the yield stress. This modeling assumption—using a temperature-independent yield behavior—has been justified by the accuracy of the predictions presented herein.

Thermal Simulation

The initial step of the analysis was to simulate the thermal history of the process. This is important as it is used to drive the mechanical responses and development of residual strains within the build. In order to do so, a number of important features of the additive manufacturing process had to be modeled effectively. Firstly, the moving laser heat source needs to be modeled in such a way that is representative of the shape, the power, and the movement of the laser.

In this model, a single thermal analysis step, with duration slightly larger than the total build time of the part, is

undertaken. This is to allow some extra time, for cooling, post build. The laser is modeled by a moving concentrated point heat source. This method applies the heat flux at a singular moving point, and the heat is then dissipated through the model by the underlying rules of conduction. This approach is valid when the size of the heat source (or melt pool) is small relative to the characteristic element size. In such a case, the shape of the heat source is not as important as the total magnitude of heat flux; however, it is important that the precise temporal and spatial locations of the heat flux are taken into account within the modelling approach. The energy deposition into the system is computed by taking into account the actual path of the heat source. The toolpath-mesh intersection module provides the information pertaining to the energy deposition. Thus, for any given solution increment of time duration dt, the mesh intersection calculation identifies all elements (and their associated mass properties) through which the laser passes. The concentrated point heat source is then distributed according to the mass properties of all of the intersected elements. The movement of the heat source was implemented with the use of an event series replicating exactly the movement of the scanning strategy. For more detail on this approach, please see references [36, 37] where the thermal approach is fully described. Images of the scan strategy used can be seen in Fig. 5.

Another key attribute of the selective laser melting process is the material deposition. The arrival of material needs to be accounted for as it has a large impact on the heat loss effects within the system. The simulation of material deposition has been achieved in the past through the implementation of one of two main methods: element birth techniques or quiet element methods. The former of the two methods uses a model change within each new step to introduce a new set of elements. The quiet element method assigns all elements with suppressed material properties until activated by the laser.

Within this simulation, material deposition was achieved via the element birth technique within the ABAQUS AM app. This technique allows material to be added to the model within a single step. An event series was developed detailing the movement of the recoater blade and implemented within the app. The material is progressively activated using the inbuilt progressive element activation techniques, according to the recoat times given while leveraging spatial and temporal homogenization techniques mentioned above.

Further details were taken into account using boundary and initial conditions. In order to replicate the substrate heating within the model, the substrate was assigned an initial temperature of 80 °C, along with a boundary condition on the bottom surface at 80 °C to maintain this temperature. Moreover, the build part was assigned an initial temperature of 40 °C as this was taken as the chamber temperature.

Heat loss was taken into account through convection and radiation, given, respectively, by the equations below.

$$q_{conv} = h(T - T_\infty) \quad [1a]$$
$$q_{rad} = \varepsilon\sigma\left(T^4 - T_\infty{}^4\right) \quad [1b]$$

Eqn.1 **a** Heat loss due to convection.**b** Heat loss due to radiation

Here, h is the heat transfer coefficient taken to be 18 W/m^2 K [29] and ε is the emissivity taken to be 0.45. T_∞ is the ambient chamber temperature and σ is the Stefan-Boltzman constant. These conditions were assigned to the evolving lateral and vertical free surfaces (calculated based on the specific activated elements for a given solution increment). Heat loss through the evolving lateral surfaces to the surrounding powder was assigned the same convective heat transfer coefficient as the evolving top surface of the part. In preparing the model, a number of sensitivity studies were undertaken and it was observed that the assumptions with regards to heat loss to the surrounding powder (which in reality would be lower than the top surface) only weakly influenced the results. This is likely a consequence of the thermal model analyzing relatively large solution increments. A thermal model focusing on melt pool size predictions would require smaller time incrementation and therefore would experience a larger influence of these heat loss considerations.

When running the thermal simulation, to reduce required memory and computational time, the time points feature within Abaqus was used. Time points use a list of specified values to create a bespoke range of times within

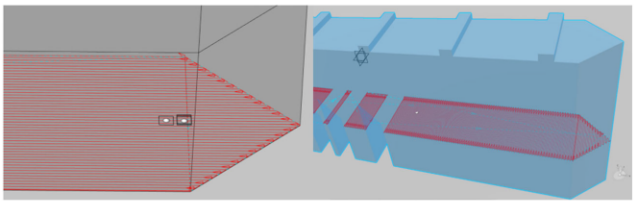

Fig. 5 Event series defining the laser movement

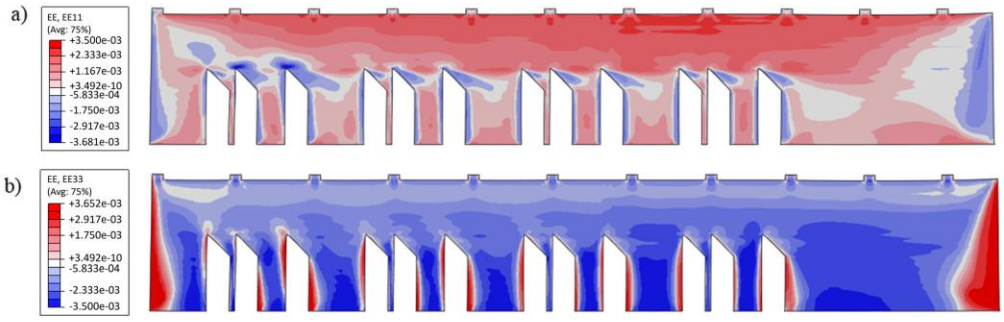

Fig. 6 Results of the mechanical simulation **a** EE11 and **b** EE33

the analysis at which to output the solution. Note: time points are different to time increments, many increments may occur but only certain ones are written to the output file. It is used as a tool to reduce computational space required and does not affect the accuracy of the analysis. The total step time was taken as the entire build time and a single time point was used to output the thermal history for each elemental layer (e.g., each simulated, aggregation of actual build layers). A total of 79 frames were outputted within the thermal analysis.

Mechanical Simulation

Although not a numerical requirement, the mesh geometry is automatically copied from the thermal model and used in the mechanical model. This ensures mesh compatibility and minimizes any further interpolation required between nodes. The thermal elements are automatically replaced with 3D stress elements in the App. Similarly, the heat transfer step in the original heat transfer analysis was replaced with a single, static general step. The same step time and time points sequence were used, although a smaller time increment was used to ease convergence. Further details on this can be found in references [36, 37].

The thermal history was imported into the mechanical model as a predefined field. Temperatures are automatically mapped between the thermal analysis and structural analyses, thermal expansion then drives deformation. These values essentially act as the load within the analyses and can be used to determine the build-up of residual strain within the model.

The initial temperature of the build part represents a relaxation temperature (not room temperature) above which thermal straining induces negligible thermal stress. Upon material

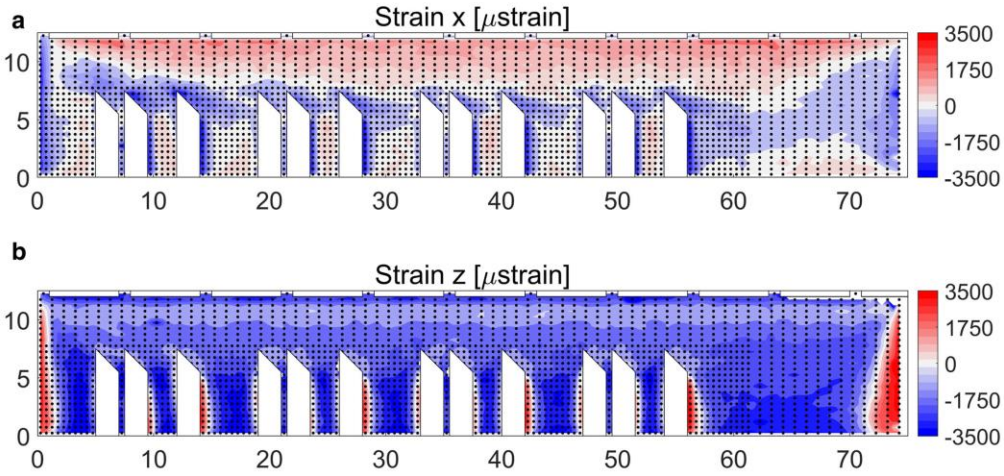

Fig. 7 XRD measurements from NIST **a** EE11 and **b** EE33 [38]

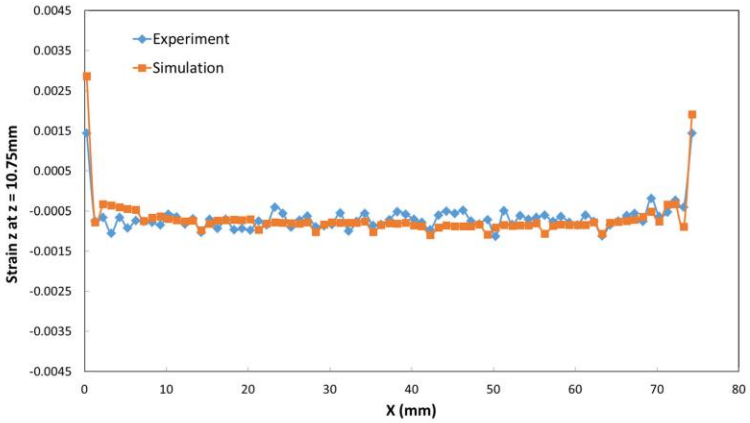

Fig. 8 XRD measurement and simulation result of strain z along the $z = 10.75$ mm path

activation, it represents the temperature from which the initial thermal contraction occurs. In this analysis, the initial temperature of the bridge is set to 750 °C. The initial temperature for the build plate is 80 °C.

The thermal results for each increment during the previous transient heat transfer analysis are applied to the structural analysis as predefined fields. Abaqus automatically maps the nodal values of temperature by interpolation (both in space and time) of the previous results.

In addition to this, the base of the substrate is assigned an encastre boundary to ensure no movement. Therefore, we can determine from this that any displacement caused within the build is as a direct result of the build-up of residual stresses.

Results and Discussion

The thermal simulation, though done on a coarse scale, shows reasonable accumulation of heat among the layers and accounts for the cooling period between layers.

The results of the mechanical simulation are shown in Fig. 6. Figure 6a shows the contour plot of the residual strain in the x direction. Likewise, Fig. 6b shows the simulation result of the residual strain along the z direction.

When compared to the results produced by NIST [31], a few main features show strong agreement between the simulation and experimental results.

Firstly, in a comparison of the simulation and experimental contour plots in the x direction (Fig. 6a and Fig. 7a), one can see that both results show tensile strains across the main body

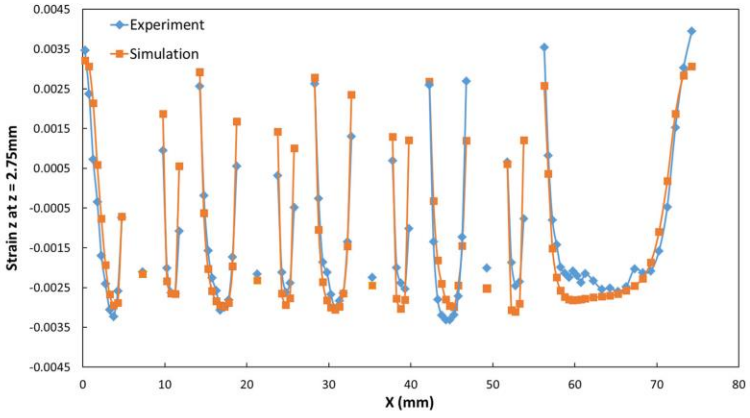

Fig. 9 XRD measurement and simulation result of strain z along the $z = 2.75$ mm path

of the part, with compressive strains being seen on the left hand side of each leg. Furthermore, there appears to be an accumulation of compressive strains around the peaks where the legs join. The magnitude in both cases is on a very similar scale, showing values in the region of 3.5e-03 and − 3.5e-03. Another prominent feature that can be seen in both contour plots is the change from tensile to compressive strains within the middle region of the far right support.

The comparison of the contour plots in the z direction (Fig. 6b and Fig. 7b) again shows a very good level of agreement. Both contours show almost a reversal image to that in the x-direction. Compressive strains can be seen throughout the body of the build with tensile strains down the length of some of the legs, in particular the wider ones. Again, magnitudes are very similar, with a peak value of 3.652e-3 being shown in the simulations and 3.5e-3 in the experimental data.

Figure 8 and Fig. 9 show the comparison between X-ray diffraction measurements and simulation result of the strain in the z direction along the $z = 10.75$ mm and $z = 2.75$ mm paths in the center plane. The predicted results show good correlation with the benchmark test data.

It is suggested by the results above that the model implemented here has delivered a reasonably accurate prediction of the residual strains within the build. The magnitudes of the strains are correct across the plane examined and the distribution of the strains shows visual agreement between the two sets of contour plots. Additionally, Figs. 8 and 9 show very clearly an agreement in measurements throughout the build height of the part.

Conclusion

Within this study, a single cantilever was simulated and experimentally built and tested. This was undertaken as part of the Additive Manufacturing Benchmark 2018. Experimental data was supplied courtesy of the NIST laboratories.

A thermo-mechanical sequentially coupled analysis was undertaken in order to predict the residual strain values within the selectively laser melted part. The results show a very good level of agreement with the XRD measurements taken of the built part in this blind benchmark. From this, we can conclude that the simulation technique developed within this document is a sufficient method for the prediction of residual strain measurements. The model described in this paper received joint first prize in the residual elastic strain category of the NIST AM Benchmark 2018.

Acknowledgments The authors would like to thank NIST for the organization of this benchmark and for the undertaking of the physical validations, as well as their cooperation throughout the process. Furthermore, the authors would like to acknowledge the support of the Lloyd's Register Foundation and Jan Przydatek. Lloyd's Register Foundation helps to protect life and property by supporting engineering-related education, public engagement, and the application of research.

This work was also enabled through, and partly undertaken at, the National Structural Integrity Research Centre (NSIRC), a postgraduate engineering facility for industry-led research into structural integrity established and managed by TWI through a network of both national and international Universities.

Compliance with Ethical Standards

Conflict of Interest The authors declare that they have no conflict of interest.

References

1. Guo N, Leu MC (2013) Additive manufacturing: technology, application and research needs. Front Mech Eng 8(3):215–243
2. Reddy KVP, Mirzana IM, Reddy AK (2018) Application of additive manufacturing technology to an aerospace component for better trade-off's. Materials Today: Proceedings 5(2):3895–3902
3. Vandenbroucke B, Kruth JP (2007) Selective laser melting of biocompatible metals for rapid manufacturing of medical parts. Rapid Prototyp J 13:196–203
4. Huang Y, Leu MC, Mazumder J, Donmez A (2015) Additive manufacturing: current state, future potential, gaps and needs, and recommendations. J Manuf Sci Eng 137:014001
5. Rejeski D, Zhao F, Huang Y (2018) Research needs and recommendations on environmental implications of additive manufacturing. Addit Manuf 19:21–28
6. Maresch, D., Technological Forecasting & Social Change (2018), https://doi.org/10.1016/j.techfore.2018.02.009
7. Le VT, Paris H, Mandil G (2018) The developmpent of a strategy for direct part reuse using additive and subtractive manufacturing technologies. Addit Manuf 22:687–699
8. Bae C-J, Diggs AB, Ramachandran A (2018) Quantification and certification of additive manufacturing materials and processes. In: Zhang J, Jung Y (eds), Additive Manufacturing. Butterworth-Heinemann, Oxford, pp 181–213
9. Ngo TD, Kashani A, Imbalzano G, Nguyen KT, Hui D (2018) Additive manufacturing (3D printing): a review of materials, methods, applications and challenges. Compos Part B 143:172–196
10. Fergani O, Berto F, Welo T, Liang SY (2017) Analytical modelling of residual stress in additive manufacturing. Fatigue Fract Eng Mater Struct 40:971–978
11. Li C, Fu C, Guo YB, Fang FZ (2016) A multiscale modeling approach for fast prediciton of part distortion in selective laser melting. J Mater Process Technol 229:703–712
12. Li C, Liu J, Guo YB (2016) Prediction of residual stress and part distortion in selective laser melting. Procedia CIRP 45:171–174
13. Wu J, Wang L, Xuguang A (2017) Numerical analysis of residual stress evolution of AlSi10Mg manufactured by selective laser melting. Optik 137:65–78
14. Williams RJ, Davies CM, Hooper PA (2018) A pragmatic part scale model for residual stress and distortion prediction in powder bed fusion. Addit Manuf 22:416–425
15. Cheng B and Chou K (2013) 24th International SFF symposium An Additive Manufacturing Conference, SFF 2013, pp 644–654

16. Foroozmehr A, Badrossamay M, Foroozmehr E, Golabi S (2016) Finite element simulation of selective laser melting process considering optical penetration depth of laser in powder bed. Mater Des 89:255–263
17. Lopez-Botello O, Martinez-Hernandez U, Ramírez J, Pinna C, Mumtaz K (2017) Two-dimensional simulation of grain structure growth within selective laser melted AA-2024. Mater Des 113: 369–376
18. Rai A, Markl M, Korner C (2016) A coupled cellular automaton-lattice Boltzmann model for grain structure simulation during additive manufacturing. Comput Mater Sci 124:37–48
19. Heeling T, Cloots M, Wegener K (2017) Melt pool simulation for the evaluation of process parameters in selective laser melting. Addit Manuf 14:116–125
20. Parry L, Ashcroft IA, Wildman RD (2016) Understanding the effect of laser scan strategy on residual stress in selective laser melting through thermo-mechanical simulation. Addit Manuf 12:1–15
21. Luo Z, Zhao Y (2018) A survey of finite element analysis of temperature and thermal stress fields in powder bed fusion additive manufacturing. Addit Manuf 21:318–332
22. Song X, Xie M, Hofmann F, Illston T, Connolley T, Reinhard C, Atwood RC, Connor L, Drakopoulos LF, Korunsky AM (2015) Residual stresses and microstructure in powder bed direct laser deposition (PB DLD) samples. Int J Mater Form 8:245–254
23. Hussein A, Hao L, Yan C, Everson R (2013) Finite element simulation of the temperature and stress fields in single layers built without-support in selective laser melting. Mater Des 52:638–647
24. Fu CH and Guo YB 3-dimensional finite element modeling of selective laser melting TI-6AL-4V alloy 2014, 25th Annual International Solid Freeform Symposium, pp. 1129-1144
25. Michaleris P (2014) Modeling metal deposition in heat transfer analyses of additive manufacturing processes. Finite Elem Anal Des 86:51–60
26. Schoinochoritis B, Chantzis D, Salonitis K (2017) Simulation of metallic powder bed additive manufacturing processes with the finite element method: a critical review. J Eng Manuf 231(1):96–117
27. Huang Y, Yang LJ, Du XZ, Yang Y (2016) Finite element analysis of thermal behaviour of metal powder during selective laser melting. Int J Therm Sci 104:146–157
28. Denlinger ER, Heigel JC, Michaleris P (2015) Residual stress and distortion modeling of electron beam direct manufacturing Ti-6Al-4V. J Eng Manuf 229(10):1803–1813
29. Denlinger ER, Michaleris P (2016) Effect of stress relaxation on distortion in additive manufacturing process modeling. Addit Manuf 12:51–59
30. NIST, "AMB2018–01 Description," (2018). [Online]. Available: https://www.nist.gov/ambench/amb2018-01-description. [Accessed December 2018]
31. Phan T, Strantza M, Hill M, Gnaeupel-Herold TH, Heigel J, D'Elia C, DeWald AT, Clausen B, Pagan D, Brown DW, Levine LE (2019) Elastic strain and stress measurements and corresponding part deflections of 3D AM builds of 15–5 and IN625 AM-bench artifacts using neutron diffraction, synchrotron X-ray diffraction, and mechanical measurements. IMMI
32. DASSAULT SYSTEMES, "Additive Manufacturing," [Online]. Available: https://www.3ds.com/products-services/simulia/trends/digital-additive-manufacturing/
33. Special Metals, Inconel Alloy 625 http://www.specialmetals.com/assets/smc/documents/alloys/inconel/inconel-alloy-625.pdf?ContextScope=all [Accessed 29 January 2018]
34. Wen S, Hilton P, Farrugia D (2001) Finite element modelling of a submerged arc welding process. J Mater Process Technol 119:203–209
35. EOS, EOS NickelAlloy IN625 http://www.eos.info/material_m/werkstoffe/download/NickelAlloy_IN625.pdf?ContextScope [Accessed 29 January 2018]
36. Zhang Q, Xie J, Gao Z, London T, Griffiths D, Oancea V (2019) A metallurgical phase transformation framework applied to SLM additive manufacturing processes. Mater Des 166:107618
37. Zhang Q, Xie J, London T, Griffiths D, Bhamji I, Oancea V (2019) Estimates of the mechanical properties of laser powder bed fusion Ti-6Al-4V parts using finite element models. Mater Des 169: 107678
38. NIST, "Results for CHAL-AMB2018–01-RS: Part Residual Strains," December 2018. [Online]. Available: https://www.nist.gov/ambench/results-chal-amb2018-01-rs-part-residual-strains. [Accessed December 2018]

Materials and Design 182 (2019) 108018

Contents lists available at ScienceDirect

Materials and Design

journal homepage: www.elsevier.com/locate/matdes

Use of power factor and specific point energy as design parameters in laser powder-bed-fusion (L-PBF) of AlSi10Mg alloy

Miguel Zavala-Arredondo *, Tyler London, Madie Allen, Tomaso Maccio, Sam Ward, David Griffiths, Amanda Allison, Paul Goodwin, Carl Hauser

TWI Ltd, Cambridge, UK

HIGHLIGHTS

- Characterisation of porosity formation with varying process parameters in laser powder-bed-fusion of AlSi10Mg alloy.
- Quantitative melt-pool indicators for optimal additive manufacturing of as-built AlSi10Mg components.
- L-PBF experiments and simulations for optimised calculation of point-to-point speed in a pulsed-mode laser system.
- Novel approach for characterising optimal process conditions using the power factor model and specific point energy.

GRAPHICAL ABSTRACT

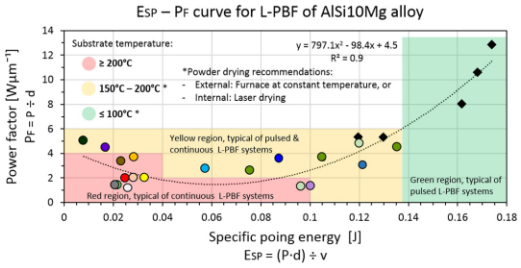

ARTICLE INFO

Article history:
Received 24 April 2019
Received in revised form 14 June 2019
Accepted 4 July 2019
Available online 06 July 2019

Keywords:
Laser powder-bed-fusion (L-PBF)
Energy density
Power factor
Specific point energy
Melt-pool aspect ratio

ABSTRACT

The densification mechanism in L-PBF of AlSi10Mg alloy with varying process parameters has been investigated. The suitability of using volumetric [Jmm^{-3}], areal [Jmm^{-2}] and linear [Jmm^{-1}] energy density as design parameters is discussed. To compare process conditions between continuous and pulsed laser systems, the jump speed v_j of a pulsed L-PBF system is calculated by means of an experimentally validated FE thermal model previously developed at TWI. The importance of using v_j in scan speed calculations is demonstrated. This allowed calculation of accurate energy levels comparable to optimal conditions reported in literature. The power factor (P_F) model and the specific point energy (E_{SP}), used to describe and replicate the laser welding process in different laser systems, have been adapted to describe the L-PBF process. E_{SP} - P_F curve is introduced, showing optimal processing windows applicable to different L-PBF systems with powers ranging from 175 to 967 W and laser focus diameter from 75 to 300 µm. Quantitative indicators for hatch spacing and layer thickness optimisation are presented for processing AlSi10Mg alloy: 1) melt-width overlapping coefficient ≥ 30%, 2) width-to-depth ratio ≥ 0.8 (using the measured half width) and 3) melt-depth limit <410 µm.

1. Introduction

Laser powder-bed-fusion (L-PBF), also known as selective laser melting (SLM) or direct metal laser sintering (DMLS, trade name by EOS) is a laser additive manufacturing (AM) technology that offers high geometrical flexibility and accuracy with minimal material waste

* Corresponding author.
E-mail address: miguel.zavala@twi.co.uk (M. Zavala-Arredondo).

https://doi.org/10.1016/j.matdes.2019.108018

as well as topology optimisation potential for improving engineering components [1]. Aerospace and automotive manufacturers are increasingly adopting L-PBF as an industrial manufacturing technique for production and topology optimisation of AlSi10Mg components due to the material's high strength-to-weight ratio and its good mechanical properties [2]. However, Aluminium alloys are corrosion susceptible and easily oxidised, which increase material welding complexities [3]. Thermomechanical and optical properties of Aluminium play a very important role in its welding capabilities. The energy balance of the process can be described by the relationship between the material's thermal conductivity (k) and its laser absorption rate (A): k/A [4]. Aluminium's characteristic 5% absorption coefficient (in cold material) at the typical L-PBF laser wavelength 1.064 μm [5] and its high thermal conductivity promote energy imbalance which limits laser processing. The need of high laser power (e.g. 500 W – 1000 W) in L-PBF of Aluminium [11] and Aluminium alloys can be more critical compared to corrosion resistant materials or materials with higher absorptivity and lower thermal conductivity (e.g. stainless steel, titanium alloys, nickel alloys etc.), as the use of higher power can help disrupting oxides and improving the process energy balance. Absorptivity in laser welding of Aluminium alloys can significantly increase from <20% to >80% when increasing linear energy density from 33 Jm^{-1} to 100 Jm^{-1} [6]. L-PBF process is similar to the laser welding process with the difference that L-PBF works with powder feedstock rather than solid dense material. In L-PBF, apparent density of powder, particle morphology and size distribution define the absorptivity of a powder bed which can be higher than that of solid dense materials [7]. In turn, thermal conductivity of a powder bed can be one to two orders of magnitude lower than that of the solid material [8]. Lower energy levels are thus typically used in L-PBF compared to laser welding for manufacturing near full-density components.

Volumetric energy density (V_{ED}) is typically used in L-PBF to characterise optimal parameters for minimum porosity in a specific material. V_{ED} is defined by the laser power, scan speed, hatch spacing and layer thickness as described in Eq. (1).

$$V_{ED} = \textit{laser power} \div (\textit{scan speed}\cdot\textit{hatch spacing}\cdot\textit{layer thickness}) \quad \left[Jmm^{-3}\right] \tag{1}$$

Critical $V_{ED} = 60\ Jmm^{-3}$ was identified [9] for AlSi10Mg whilst processing 50 μm layer thickness and varying hatch spacing, laser power and scan speed. A maximum part density of 99.2% was reported (measured from cross-section micrographs using optical microscope). In [10], two-dimensional (2D) expression of energy density was used. This is described in Eq. (1) where A_{ED} is the areal energy density in the 2D plane.

$$A_{ED} = \textit{laser power} \div (\textit{scan speed}\cdot\textit{hatch spacing}) \quad \left[Jmm^{-2}\right] \tag{2}$$

In [10], A_{ED} processing window ranging from 1.2 to 1.8 Jmm^{-2} was identified for high-density AlSi10Mg parts with 30 μm layer thickness and varying hatch spacing, laser power and scan speed (acquiring a maximum 99.07% density measured based on the Archimedes' principle). The densification mechanism of high power (HP) L-PBF of AlSi10Mg was investigated in [11], using up to 1 kW laser power to achieve a maximum 99.8% density (measured using optical microscope). The effect of linear energy density L_{ED} in the densification mechanism was presented. L_{ED} is defined by Eq. (3).

$$L_{ED} = \textit{laser power} \div \textit{scan speed} \quad \left[Jmm^{-1}\right] \tag{3}$$

From work conducted in [11], optimal L_{ED} ranging from 0.2 to 0.7 Jmm^{-1} can be identified with 50 μm layer thickness and varying power and speed with fixed hatch spacing. A 'pre-sinter' scan strategy was used in [12] to obtain 99.8% part density, similar to the HP L-PBF approach. The pre-sinter strategy consisted on a first scan of the layer using half the power followed by a second scan with full power (100 W) at 0.2 Jmm^{-1} with 50 μm hatch spacing and 40 μm layer thickness (i.e. $V_{ED} = 100\ Jmm^{-3}$). The use of pre-sintering strategies tends to significantly decrease build rates resulting in longer processing time. Build rate is defined by the divisor factor in Eq. (1) and is typically given in $mm^3\ s^{-1}$. Build rate of the pre-sinter strategy is therefore 1 $mm^3\ s^{-1}$ which is then divided by the number of scanning per/layer (i.e. build rate = 0.5 $mm^3\ s^{-1}$), whilst HP L-PBF can build at 9.75 $mm^3\ s^{-1}$ achieving same maximum density of 99.8%. Furthermore, build rates of 21 $mm^3\ s^{-1}$ were reported in [11] for 99.5% density parts. The use of higher powers can increase the laser absorptivity of the material [7]. HP L-PBF of AlSi10Mg can thus improve the energy balance of the material promoting a more efficient densification mechanism whilst increasing build rates simultaneously.

Following the linear energy density approach, single-track parametric analysis is reported in [13], characterising melt-pool dimensions and weld bead homogeneity. Low L_{ED} was observed to result in droplet formation and bad wetting to previous layers (or to the baseplate for the first layer) whereas too high L_{ED} caused distortions and irregularities due to large melt-pool volumes and balling. In their work they defined a process window in the power-velocity (P-v) graph ranging from 0.13 to 0.21 Jmm^{-1} for samples >99% density. Single tracks within the process window were characterised by the conduction welding mechanism as well as uniform and continuous track beads. Keyhole welding modes resulted in gas porosity formed at the bottom of the melt pool and non-uniform tracks resulted in bead disruptions that ultimately promoted higher levels of porosity. The process window in the P-v graph was broader when using higher powers possibly due to the more efficient densification mechanism promoted by an optimised energy balance. The maximum density acquired was ~99.3% (measured by the Archimedes' method) using 200 W power with a build rate ~4.4 $mm^3\ s^{-1}$. The effect of L_{ED} in porosity development of L-PBF parts was investigated in [14]. Strong correlation between part density and single track morphology, melt pool dimensions and welding mode (conduction or keyhole) was observed. They concluded that melt pool characterisation using different L_{ED} levels can provide valuable information to define optimal processing windows for near full-density components. The present work investigates the suitability of using energy density as a design parameter to describe L-PBF. The use of V_{ED}, A_{ED} and L_{ED} to characterise optimal L-PBF parameters is analysed. An alternative approach using the specific point energy as design parameter is presented.

2. Background

This section presents consolidation defects typically observed in L-PBF of AlSi10Mg components that limit the densification mechanism. Also presented are the role of laser energy density in parameter optimisation and processing windows reported in literature for this material. Characteristics of the two different laser irradiation mechanisms used in L-PBF, pulsed and continuous, are briefly described as well as the two different approaches used in literature to characterise pulsed-mode laser speeds. Finally, the power factor model used in laser welding is presented. The present work investigates the use of the power factor model and specific point energy concept to characterise the densification mechanism in L-PBF. To the authors' knowledge, no work has been reported previously in literature investigating the use of power factor and specific point energy as design parameters in L-PBF.

2.1. Porosity and oxidation in L-PBF of AlSi10Mg

Porosity and lack of fusion are typical defects in L-PBF AlSi10Mg components. Large oxides (several microns to tens of microns large) are known to be associated with such defects, promoting formation of fatigue cracks [15]. The oxide particles prevent consolidation of the molten alloy causing the formation of large pores and incomplete

consolidation (lack of fusion). Porosity along the edges of melt pool widths are typically caused by lack of fusion. Such defects can be eliminated by reducing hatch spacing which increases the number of local melting cycles. In [15], oxidation-promoted lack of fusion and porosity was predominant in L-PBF of AlSi10Mg using 370 W. Spherical gas pores were only occasionally observed which were not associated with crack nucleation, unlike the large oxidation-promoted pores. High laser powers can be used to disrupt such oxides in order to minimise porosity and eliminate lack of fusion defects [16]. In [17] it is reported that 96% of the gas content within spherical gas pores in L-PBF of AlSi10Mg is hydrogen. Only gas (hydrogen) porosity was observed using 910 W in HP L-PBF of AlSi10Mg and no lack of fusion was detected. Hydrogen porosity can be controlled using different powder drying mechanisms as reported in [17]. HP L-PBF can thus be used to manufacture AlSi10Mg components with minimum porosity and no lack-of-fusion defects.

2.2. The role of laser diameter in porosity formation

Laser beam diameter has a very important role in porosity formation. Porosity can increase significantly when using larger diameters [17] possibly due to decrease in power density. Power density is defined as the power per unit area, usually expressed in $MWcm^{-2}$. Lower power density requires slower scanning speeds to manufacture samples without imperfections. In turn, slower speeds can cause larger and deeper melt pools which can promote the formation of keyhole porosity. Large beam diameters with slow speeds can thus limit the process window for manufacturing high density components.

2.3. Defining processing windows of optimal energy density

As described in Section 1, V_{ED}, A_{ED} and L_{ED} are typically used as design parameters to manufacture near full-density AlSi10Mg L-PBF components. However, processing windows for same material can show different energy values in literature especially with varying power, scan speed and laser focus diameter. For instance, optimal 58 Jmm^{-3} was reported in [9] using 175 W whilst 185 Jmm^{-3} was reported in [18] with 400 W. In [10], optimal 55 Jmm^{-3} was identified at 195 W whilst 36 Jmm^{-3} was reported in [17] using 910 W. Near-full density was achieved at 72 Jmm^{-3} in [11] with 700 W and in [19] 67 Jmm^{-3} and 250 W were used to manufacture defect-free L-PBF components. Finally, 500 Jmm^{-3} was used in [32] to obtain optimal metallurgical bonding between neighbouring (50 μm) layers and in [33] uniform scan tracks with no irregularities and well-consolidated layers, free of satellites and balling, were produced at 160 Jmm^{-3}. The different energy density values reported in literature resulted from different combinations of laser power with the other V_{ED} parameters (see Eq. (1)). It has to be noted that all the aforementioned studies were conducted in different L-PBF systems (i.e. different machine manufacturers) featuring different laser focus diameters. Table 1 presents different powers, laser diameters and energy densities used in literature for manufacturing near full-density L-PBF AlSi10Mg components.

Table 1
Different powers, laser focus diameters, V_{ED}, S_{ED} and L_{ED} used in literature for manufacturing near full-density L-PBF AlSi10Mg components.

Power [W]	Laser diameter [μm]	V_{ED} [Jmm^{-3}]	A_{ED} [Jmm^{-2}]	L_{ED} [Jmm^{-1}]	Reference
910	300	40	2	0.4	[17]
195	100	55	1.6	0.28	[10]
175	150	58	1.8	0.17	[9]
250	200	67	3.3	0.50	[19]
700	195	72	3.6	0.54	[11]
400	135	131	3.3	0.43	[18]
100	20	160	8	0.4	[33]
250	70	500	25	1.25	[32]

Table 1 shows that optimal energy density can range from 40 to 500 Jmm^{-3}, depending on power and laser focus diameter. Such wide range complicates transferring parameters from one L-PBF system to another, which results in a long and resource consuming parameter development process. As shown in Eqs. (1)–(3), the calculation of V_{ED}, A_{ED} and L_{ED} does not take into account laser diameter. Defining process power density for a given laser diameter is crucial for energy density optimisation. Investigating the role of laser focus diameter in L-PBF densification mechanism may help transferring optimal parameters between different L-PBF systems with higher accuracy.

2.4. Pulsed and continuous L-PBF laser systems

Lasers in commercial L-PBF systems can be operated by two different energy deposition modes: continuous or pulsed. The main difference between the two is the approach used to deliver the power along the scan track in terms of speed. In pulsed L-PBF systems, the laser does not fire continuously, but in a discrete (point-by-point) manner. While continuous lasers use a single parameter that define the scan speed, pulsed lasers use two different parameters that have to be investigated independently, namely: point distance (P_d, distance between two consecutive points) and exposure time (T_e, elapsed laser firing time at each point). Usually, the speed (v) at which the pulsed laser moves across the powder bed is defined by the ratio of these two parameters as shown in Eq. (4) [18]. However, in such approach the speed at which the laser moves from point to point is not considered (i.e. speed of the scanning mirrors that control the point-to-point movement of the laser). A more detailed definition of scan speed in a pulsed L-PBF system is presented in [20] as described in Eq. (5).

$$v = P_d \div T_e \quad [mms^{-1}] \tag{4}$$

$$v = P_d \div (T_e + (P_d \div v_j)) \quad [mms^{-1}] \tag{5}$$

where v_j is the jump speed from point to point. In a pulsed system, the scan speed can be obtained by combination of different P_d and T_e values, but not all are suitable for use even when the combined values are identical. Same speeds with different combination of P_d and T_e can deliver completely different results, from near-full density components to very high levels of porosity or build failure. In [18] it was shown that P_d similar to the laser diameter can be used to achieve high-density AlSi10Mg components. The size of the melt pool may not be able to cover the distance between consecutive points if P_d is too large, resulting in high porosity or even disrupted melt tracks. In turn, too large exposures can develop keyhole welding mode which is detrimental for the density of the part whilst too short exposures can result in unconsolidated material. Therefore, each parameter has to be carefully selected. The use of v_j in pulsed laser systems may provide a more accurate representation of the process scanning speed which facilitates transferring optimal parameters from a pulsed to a continuous L-PBF system.

2.5. The use of specific point energy and the power factor model

In laser welding, an empirical model is presented in [21] to characterise the melt pool formation mechanism taking into account laser diameter. The model uses the fundamental laser-material interaction parameters (FLMIP), power density (q_p), interaction time (t_i) and specific point energy (E_{SP}), to replicate the welding process in different laser systems. These parameters are described in Eqs. (8)–(10). It was reported that power density and specific point energy control the depth of penetration whilst interaction time controls the weld width. The power factor (P_F) (see Eq. (11)) is used as design parameter to control constant melt pool depth with varying beam diameter. In [6] the

model was used to characterise laser welding process of Aluminium and in [22] the role of power density in the transition from conduction to keyhole welding mode was investigated. Also, the relationship between power density and porosity build-up within the melt pool is presented. The model used to describe the densification mechanism and characterise melt pool dimensions in laser welding can potentially be used to investigate the L-PBF densification process as both technologies use similar joining mechanism of laser melting of metallic feedstock. As mentioned above, E_{SP} and P_F empirical model is used in laser welding to control melt depth, independent of laser beam size. A similar approach is presented in [23] where a novel method is proposed for selecting optimal parameters in L-PBF of AlSi10Mg, based on the laser penetration depth.

$$q_p = P_L \div A_S \quad [\text{typically MWcm}^{-2}] \tag{8}$$

$$t_i = d \div v \quad [s] \tag{9}$$

$$E_{SP} = q_p t_i A_S = P_L \cdot d \div v \quad [J] \tag{10}$$

$$P_F = q_p d = P_L \div d \quad [\text{Wμm}^{-1}] \tag{11}$$

In Eqs. (8)–(11), P_L refers to laser power, A_S is laser spot area, d is laser diameter and v is welding speed.

2.6. Motivation and limitations of the present work

This work investigates the effect of energy density parameters such as scan speed (i.e. exposure time and point distance), hatch spacing and layer thickness in the densification mechanism of HP L-PBF of AlSi10Mg alloy. The results are compared with optimal parameters reported in literature for same material, using different laser systems (i.e. different machine manufacturers). An empirical model used to characterise laser welding process has been adapted to describe L-PBF densification mechanism of as-built AlSi10Mg components, independent of laser system. A well-defined specific point energy range characterising optimal L-PBF process conditions is proposed in the present investigation. Only energy density parameters (see Eq. (1)) and laser focus diameter are considered in this work. Other L-PBF parameters such as gas flow, scan strategy, etc., are not investigated. However, it has to be noted that such parameters are fundamental for controlling mechanical properties of the as-built component. For instance, optimal gas flow can help removing laser spatter particles, preventing them from landing on the powder bed and minimising the number of imperfections in the process layer, which ultimately improves the density of the part. On the other hand, optimal scan strategies can be developed in order to control local cooling rates and residual stresses and improve mechanical properties [34]. If a scan strategy is poorly chosen, it can cause local thermal accumulation which can lead to part deformation [35]. The scope of the present work is to optimise and homogenise L-PBF FLMIP in order to identify optimal energy maps, independent of laser system used. Process parameters such as gas flow, scan strategy, etc. can be investigated in future work using optimal laser-material interaction parameters.

3. Experimental methodology

In order to investigate the effect of process parameters in the densification mechanism of HP (1 kW) L-PBF of AlSi10Mg, two builds, B1 and B2, of different process layer thickness were conducted with varying exposure time and hatch spacing. The samples were $10 \times 10 \times 10$ mm^3 cubes for density and microstructure analysis. Low and high layer thickness levels were used in B1 and B2 respectively, namely: a) 50 μm (B1) and (b) 100 μm (B2). Laser power was fixed to 967 W and point distance $P_d = d$ was used in all B1 and B2 samples. Both B1 and B2 were designed in a full factorial 5×5 design with varying exposure time and hatch spacing. Exposure times in B1 and B2 were chosen in order to maintain consistent V_{ED} ranges between both builds of varying layer thickness according to Eq. (1). Hatch spacing range 0.12–0.24 mm, typical of HP L-PBF of AlSi10Mg, was used in both builds. As layer thickness is a fixed value that cannot be varied within the same build, using two full factorial design builds (i.e. B1 and B2) allows identification of representative density trends with varying characteristic V_{ED}, A_{ED} and L_{ED} parameters, namely: layer thickness, hatch spacing and scan speed (or exposure time in pulsed-mode laser) respectively. As V_{ED} is the typical design parameter used in L-PBF, the experimental approach used in the present research allows investigating same V_{ED} range in the different layer thickness investigated, adjusting exposure time accordingly. One additional build was conducted with $P_d = 2d$, adjusting exposure time in order to maintain same V_{ED} range. However, larger point distance promoted weld bead disruptions, leading to build failure. This build is therefore not discussed in the present investigation.

3.1. L-PBF system

All experiments were conducted in a one-off Renishaw AM250 specially equipped with a 1 kW IPG pulsed-mode laser. A focus test was conducted in order to use laser focus diameter that resulted in uniform and consistent tracks at typical HP L-PBF scan speed. The test consisted of multiple laser scan tracks on Aluminium solid substrate using fixed speed and power, and varying machine focus parameter. Focus parameter is a numerical value in mm that defines alignment of the powder bed with the laser focal z-location. Commercial L-PBF systems can

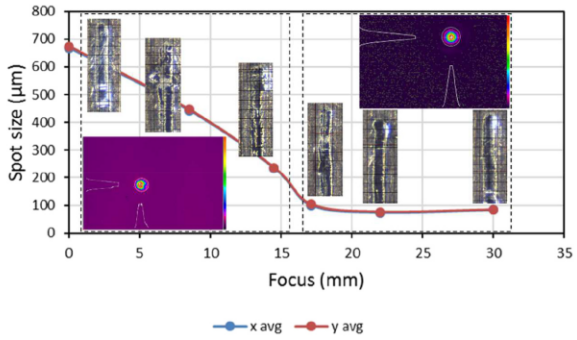

Fig. 1. Average laser spot size with varying machine focus parameter. Regions of two different intensity distribution are shown within black dashed lines. Top view images of scan tracks conducted at different laser spot size and focus are shown.

Table 2
Chemical composition of AlSi10Mg powder in weight %.

Al	Cu	Fe	Mg	Mn	N	Ni	Pb	O	Si	Sn	Ti	Zn	Other
Bal.	<0.01	0.1	0.33	<0.01	<0.01	<0.01	<0.01	0.05	9.87	<0.01	0.01	<0.01	0.02

have different focus at which the laser spot is at its focal position on the process layer. Periodical focus characterisation is recommended in L-PBF systems to confirm spot size and intensity distribution. Spot size and intensity distribution of varying focus parameter were measured using an Ophir Spiricon camera-based beam profiler. Fig. 1 shows focus values plotted against average laser spot diameter. Two regions of different laser intensity distribution are highlighted within dashed lines in Fig. 1. A uniform Gaussian distribution was observed within spot size range 75–100 μm. Larger diameters with non-uniform intensity distribution resulted in disrupted tracks of varying width along the scan direction. The 75 μm focused laser diameter resulted in uniform tracks with constant width along the scan direction. In the present work, all samples were conducted using 75 μm laser diameter. Additionally, a water-cooled Ophir Spiricon power sensor was used to measure laser power delivered at the powder bed. Effective 967 W was measured when using 1 kW output. Therefore, 967 W is used in calculations for higher accuracy.

3.2. Material

Gas atomised AlSi10Mg powder sorted by LPW with 20–63 μm particle size distribution was used. Table 2 shows the chemical composition of the material in weight % according to LPW Test Certificate. Fig. 2 shows scanning electron microscope (SEM) images of the powder morphology and cross-sectional density. A large amount of elongated and satellite particles were observed. The light density of Aluminium may have caused such defects to form during the gas atomisation process. Elongated and satellite particles can have a detrimental effect on powder flowability (especially during deposition of layers) and apparent density of the powder bed, limiting the densification process. No apparent porosity/defects or contamination inside powder particles were observed in the cross section powder morphology. Only occasional small scale porosity was observed within the particles.

A particle size analysis was conducted using the laser diffraction method according to BS ISO 13320-2009 standard. Fig. 3 shows the particle size distribution (PSD) graph. A table embedded in Fig. 3 shows values for D_{10}, D_{50} and D_{90}. Sieving of powder is critical as PSD analysis showed a small volume fraction below and above the declared size. Sieving was conducted using 63 μm sieve.

3.3. L-PBF process parameters

Fig. 4 shows the parameters used in B1 and B2. A pre-heat temperature of 80 °C, meander scan strategy and 67° rotation of subsequent layers were used in both builds. X-marked samples in Fig. 4 were used as reference for thermal monitoring and metallography. The reference samples were specially selected to account variations in hatch spacing and exposure time.

3.4. Thermal monitoring

The temperature evolution of reference samples was measured in-situ using a bespoke 13 mm-thick thermocouple substrate. The substrate is composed of multiple adjustable bolt-holders that locate the

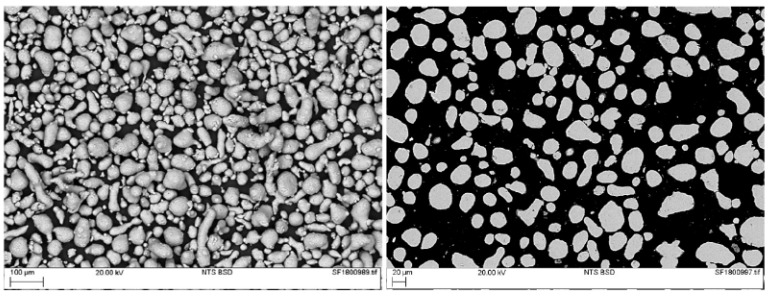

Fig. 2. Scanning electron microscope (SEM) images showing (a) powder morphology and (b) cross-sectional density.

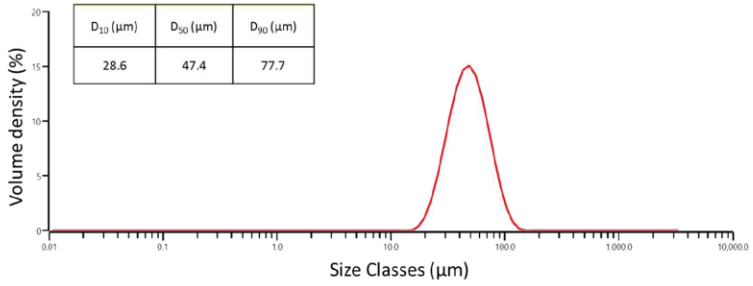

Fig. 3. Particle size distribution (PSD) of AlSi10Mg powder showing D_{10}, D_{50} and D_{90} values.

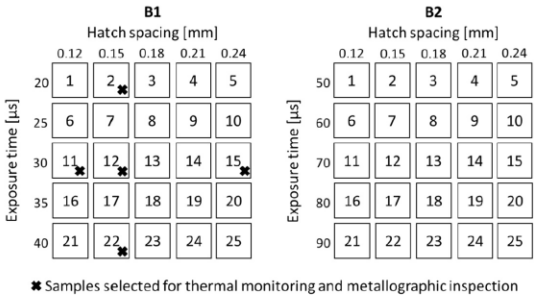

Fig. 4. Parameters used in B1 (50 µm layer thickness) and B2 (100 µm layer thickness). X-marked samples were selected for thermal monitoring and metallography.

thermocouple probes at the bottom of the substrate in a fixed position and known distance from the top surface of the substrate. The thermocouple probes are surrounded by the substrate material and are in solid contact with the measuring surface. Fig. 5a shows a schematic representation of the temperature measurement approach of a single reference sample and Fig. 5b shows a bottom view of the thermocouple substrate with spatially-defined thermocouple probe bolt-holders.

Multiple samples of varying hatch spacing and exposure time were monitored as described in Fig. 4. For proper alignment between measuring points and sample location on substrate, the substrate geometry was embedded on an STL file, superposed to the sample array in Magics Software. The samples of interest were located superposed to the substrate measuring points. The substrate geometry was then removed from the STL file and the sample array was built without superposing geometries. The thermocouple data was acquired using a 500 Hz data logger to account for the rapid thermal evolution of the laser melting process. Time events were recorded describing representative temperature evolution plots.

3.5. L-PBF modelling

In order to use a more accurate pulsed scan speed in the calculations, experimentally acquired thermal evolution of AlSi10Mg reference samples were used to calibrate an FE model capable of adjusting jump speed v_j. The FE approach used in the present investigation leverages a new physics-based framework from a general-purpose finite element code (ABAQUS). The moving laser heat source was modelled through the implementation of a DFLUX user subroutine, which accessed data regarding the location and power of the laser from an event series. The event series was created to define the whereabouts and properties of the laser throughout time and took both the exact scan strategy and scan speed, as defined in Eq. (5), into consideration. This allowed for the inclusion of jump speed within the simulation. Furthermore, material deposition was modelled through the implementation of element birth techniques. This is a common procedure in the modelling of AM processes and allows for new material to be added throughout the simulation. The model has been previously developed and validated in research conducted at TWI for Ti6Al4V alloy [24,25]. Further validation was conducted in the present work modelling the thermomechanical properties of AlSi10Mg.

3.6. Porosity and melt pool size measurement

Porosity in XZ and XY planes was measured using optical microscopy. XZ plane provides information of porosity build-up within multiple layers, showing porosity development in melt pool widths and depths. XY plane investigates porosity development within a single layer. B1 and B2 samples were cross-sectioned across the scanning direction to characterise melt pool width and depth. Optical micrographs were taken at different locations across the sample covering 25% of the total cross-sectional area. The micrographs were converted to binary images where black pixels represented sample porosity. Statistical pore pixel count was conducted using ImageJ software to calculate % density of samples. B1 cross-sectioned reference samples (X-marked

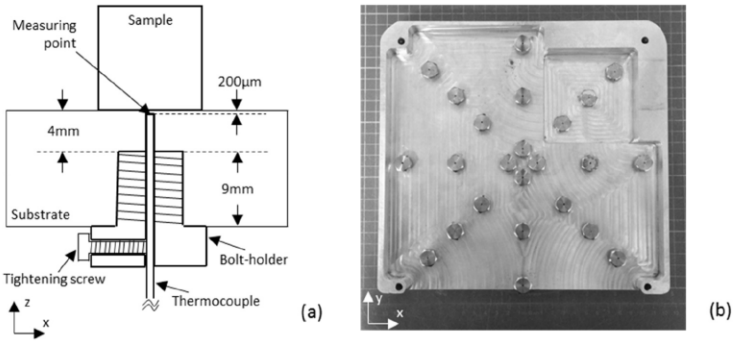

Fig. 5. (a) Schematic representation of the thermocouple substrate design showing the holding mechanism used to fix the thermocouple in solid contact with the measuring point and surrounding substrate material. Not scaled. (b) Bottom view of thermocouple substrate showing spatially-defined thermocouple probe bolt-holders.

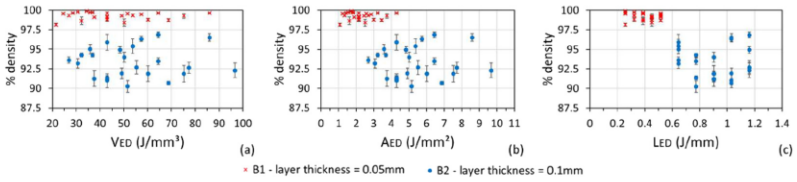

Fig. 6. XZ density of B1 (50 μm) and B2 (100 μm) samples with varying (a) V_{ED}, (b) A_{ED} and (c) L_{ED}.

samples in Fig. 4) of varying exposure time and hatch spacing were used for metallography analysis. Reference samples were etched with Keller's reagent to reveal melt pools. Melt pool dimensions were measured by pixel count in micrographs using ImageJ software.

4. Results

The effect of varying process parameters in melt-pool dimensions and part density is presented in this section. Also presented are experimental thermal measurements which were used to validate and calibrate the FE model for v_j simulation.

4.1. Density

Volumetric energy density range 20–100 Jmm^{-3} (identified from literature) was used for investigating the L-PBF densification mechanism of AlSi10Mg powder. In the present section, 967 W power was fixed in all samples in order to investigate the effect of exposure time, hatch spacing and layer thickness in porosity development. Scan speed of the pulsed laser was obtained using Eq. 4 as is typically used in literature. In all samples, point distance was fixed to 75 μm (i.e. $P_d = d$). Fig. 6 shows B1 and B2 samples XZ density with varying V_{ED}, A_{ED} and L_{ED}. Standard deviations are represented by error lines. Fig. 6a–c show that energy density ranges of 'good' (higher % density) samples are being gradually set apart from 'bad' (lower % density) samples when reducing dimensional expression of energy input from 3D to 1D respectively. As shown in Fig. 6, layer thickness has a strong influence on the density of AlSi10Mg components as different thickness levels can result in very different part densities even at same energy range. High power factor (i.e. high laser power, e.g. 1 kW, focused onto a small beam diameter, e.g. < 100 μm) can lead to improper closure of the melt pool especially when processing thicker layers [36]. Thick (e.g. 100 μm) layers typically lead to deeper melt pools. Residual gas at the bottom of deep melt pools cannot escape in time during rapid solidification, promoting keyhole porosity formation [37]. Fig. 7 shows a B2-7 sample micrograph (n.b. XZ density of B2–7 sample is 90.3%). Several aspects observed in all 100 μm layer samples are represented in Fig. 7, namely: 1) melt pool depths in excess of layer thickness can develop, suggesting that subsequent layers can be fully consolidated; 2) too deep melt pools promote keyhole porosity; 3) sufficient overlapping between melt depths can be observed; 4) keyhole porosity is the governing factor limiting part densification as lack of fusion was only occasionally observed. These B2 samples' characteristics indicate that the laser energy range investigated is sufficient to process large (100 μm) layer thickness. However, Fig. 7 provides information indicating that thicker layers of AlSi10Mg alloy might require less laser energy than expected. This could be due to typical Aluminium material properties. Different layer thickness in L-PBF of Aluminium can develop different Oxygen content during the build process. In [39] it was observed that lower layer thickness (i.e. 50 μm) in Aluminium alloy can develop higher amounts of oxide content than thicker (i.e. 75 μm) layers, as thicker layers reduce Oxygen by enhancing temperature and stirring within the melt pool. Lower laser energy might thus be required in thicker layers since thicker layers reduce cooling rates, increase exothermic reaction and produce larger melt pools [39]. Layer-thickness-based process instabilities might thus limit the use of V_{ED} as design parameter. In L-PBF process, layer thickness has typically constant value during the build process and is selected in advance based in productivity (i.e. build rate), surface roughness, etc. Using A_{ED} or L_{ED} (i.e. removing the effect of layer thickness from energy calculations) can simplify

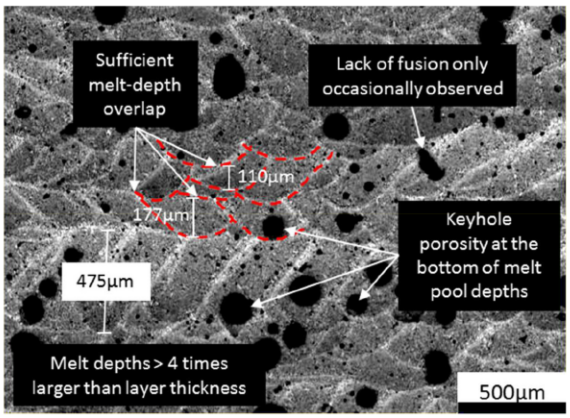

Fig. 7. Representative Micrograph of 100 μm layer thickness B2-7 sample showing melt-pool and porosity characteristics. Keyhole porosity is shown as the governing factor limiting part densification which might be an indication of excessive laser energy.

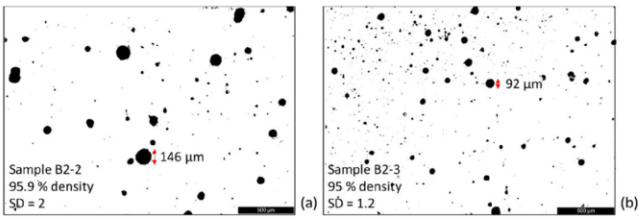

Fig. 8. Optical binary micrographs of B2 samples of similar XZ density showing (a) large and (b) small pore sizes at different standard deviation (SD) values, extracted from porosity measurement data.

identification of optimal process energy levels as long as a good range of layer thickness levels is identified for manufacturing near-full density components. If layer thickness vary during L-PBF process (e.g. for increasing build rates, control microstructure, etc.), multiple lasers with different size and power might be required to process each layer thickness at optimal power factor and energy conditions [38]. Layer thickness is therefore a fundamental parameter that defines energy input requirements. Fig. 8 shows a comparison of two B2 samples of similar % density (95.9% and 95%) and different standard deviations (2 and 1.2 respectively). It was observed that average pore-size distribution and maximum individual pore dimensions were correlated with standard deviation values. A well-defined energy range differentiating high from low % density was observed when analysing linear energy density L_{ED}. In contrast, V_{ED} and A_{ED} scenarios showed "good" and "bad" samples merged along the energy axis. This was especially observed in V_{ED}, where all "good" and "bad" samples shared the same energy range. A well-defined L_{ED} region of high-density components with small spherical pores was identified ranging from 0.2 to 0.6 Jmm^{-1}. Porosity in all samples was observed to be either gas or keyhole porosity as evidenced by the spherical morphology of individual pores. No lack of fusion defects were detected and only small amounts of irregular pores were observed in B2 samples, where multiple spherical pores merged together. Standard deviations <1 were observed in high-density samples which resulted in <60 µm pores. In contrast, standard deviations >1 were associated with larger pores, reaching even values >200 µm with SD > 2.

Figs. 9 and 10 show XZ density and standard deviations (SD) of B1 and B2 micrographs with varying exposure time and hatch spacing. It can be seen in Fig. 9 that most of B1 samples were > 99% density with only small spherical pores. Porosity and standard deviation increased only in samples with hatch spacing 0.24 mm with 20–30 µs exposures. Melt pool dimensions of lower exposure times may have not been large enough to overcome porosity formation in regions along the edges of melt pools widths, promoting higher porosities in samples with larger hatch spacing. Fig. 10 shows larger spherical pores reaching diameters >200 µm in B2 samples with 70–90 µs exposures and 0.12 mm hatch spacing. In B2 samples, higher energy densities with longer exposure times promoted deeper melt pools, which led to keyhole porosity. Increasing hatch spacing may have decreased the number of local melting cycles which helped reducing standard deviations and smaller pore dimensions. However, large quantities of smaller pores limited the densification mechanism in B2 samples even with increased hatch spacing, resulting in densities <95%.

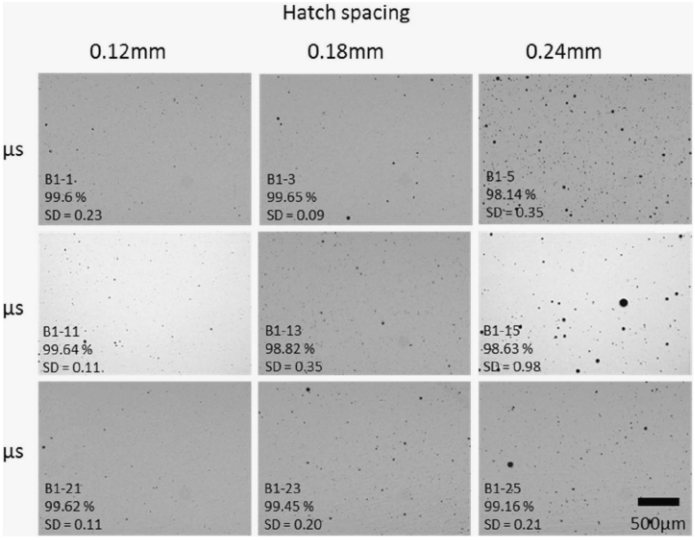

Fig. 9. Optical micrographs showing XZ density and standard deviation of B1 samples with varying exposure time and hatch spacing.

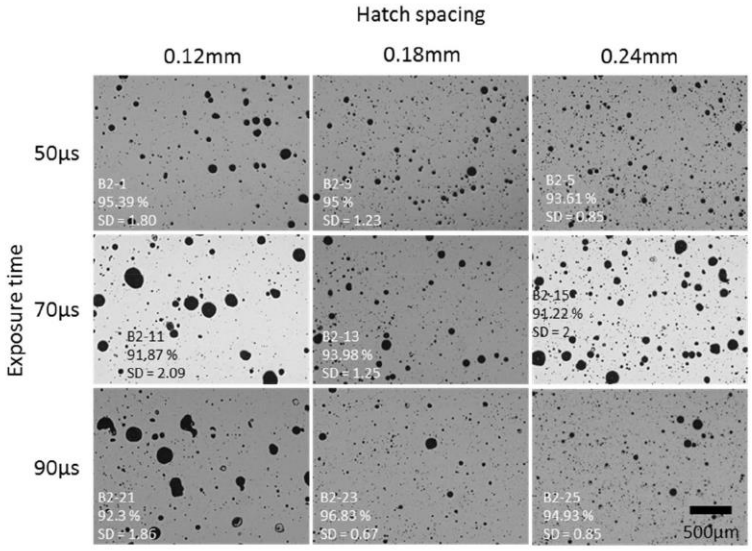

Fig. 10. Optical micrographs showing XZ density and standard deviation of B2 samples with varying exposure time and hatch spacing.

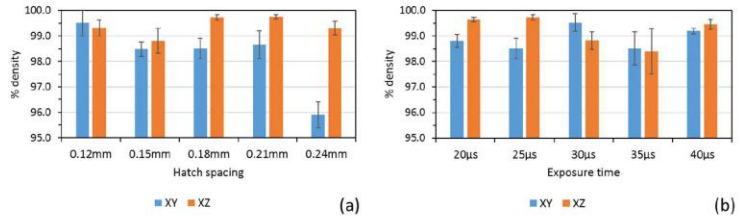

Fig. 11. (a) XY and XZ % density of B1 samples with varying hatch spacing and constant 25 µs exposure time. (b) XY and XZ % density of B1 samples with varying exposure time and constant 0.18 mm hatch spacing.

Fig. 11 shows XY and XZ densities of a) B1-6-10 samples (i.e. 25 µs exposure time with varying hatch spacing) and b) B1-3, 8, 13, 18 and 23 samples (i.e. 0.18 mm hatch spacing with varying exposure time). It can be seen in Fig. 11a that XY density can decrease steeply with increasing hatch spacing, leading to large differences between XY and XZ densities. XY density analysis accounts for porosity development in-between laser tracks as shown in Fig. 11a where 0.12 mm hatch spacing shows minimum difference between XY and XZ densities whilst 0.24 mm hatch spacing shows XY density < 96% and XZ density > 99%. Better agreement between XY and XZ densities were observed with

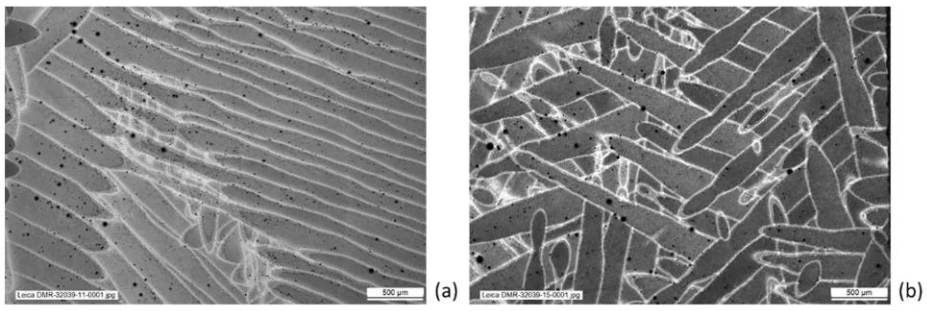

Fig. 12. Representative XY micrographs of (a) B1–11 and (b) B1–15 samples with (a) 0.12 mm hatch spacing and (b) 0.24 mm hatch spacing respectively.

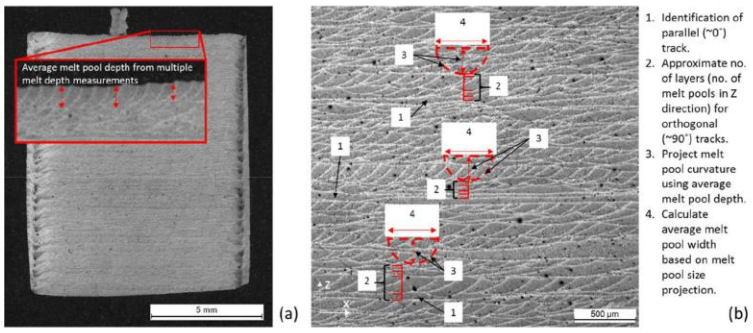

Fig. 13. (a) Low and (b) high magnification XZ micrographs of reference sample showing (a) melt pool depths at the top of the sample, used to calculate average melt depth; and (b) progressive melt pool width measurement approach based on average melt depth.

constant hatch spacing and varying exposure time especially at longer exposures, as shown in Fig. 11b. Longer exposures usually lead to wider melt tracks which can improve overlapping between melt pools along the melt-width direction, improving part density especially in larger hatch spacing values (smaller hatch spacing might exhibit good melt-width overlapping at shorter exposure times). Fig. 12 shows XY micrographs depicting melt pool tracks along scanning directions of a) 0.12 mm hatch spacing and b) 0.24 mm hatch spacing with constant exposure time. It can be seen in Fig. 12 that the amount of overlapping between melt pools can decrease when increasing hatch spacing with constant exposure time. Lower overlapping can be detrimental to the density of the part, especially in the XY plane.

4.2. Microstructure

Microstructure of reference samples was investigated using XZ cross-section micrographs of the whole sample (see Fig. 13a). Fig. 13 shows the melt-pool-size measurement approach used in the present research. Scanning vectors were rotated 67° every subsequent layer in the present work. It is assumed that melt tracks parallel to the X direction, represent ~0° rotation. This is represented by continuous longitudinal melt tracks in Fig. 13b. From the ~0° base track, the fourth layer in the build direction should have rotated ~270° (i.e. 268°) which is equivalent to ~90° orthogonal scan tracks. Orthogonal tracks are differentiated from oblique tracks as they show narrower melt pool widths. The angle of rotation of scan vectors within layers does not affect melt pool depths. Therefore, melt depth can be measured from melt pools at the top of the sample, independent of the layer rotation angle (see Fig. 13a). From Fig. 13a, average melt depth is calculated from multiple top-melt-pool measurements along the sample. Then, from high magnification micrographs, parallel (~0°) scan tracks are identified. Melt pools are counted along the build direction (i.e. Z direction) to identify orthogonal ~90° tracks. The curvature of orthogonal melt pools is projected assuming typical L-PBF parabolic melt pool shapes. Melt pool widths are measured at the corresponding average melt depth calculated (see Fig. 13a). Melt widths are thus measured from multiple layers along the build direction to calculate average melt pool width. Average depths and widths are used to calculate width-to-depth ratios. Fig. 14 shows melt pools and XZ porosity development of B1 reference samples with increasing (a) exposure time and (b) hatch spacing.

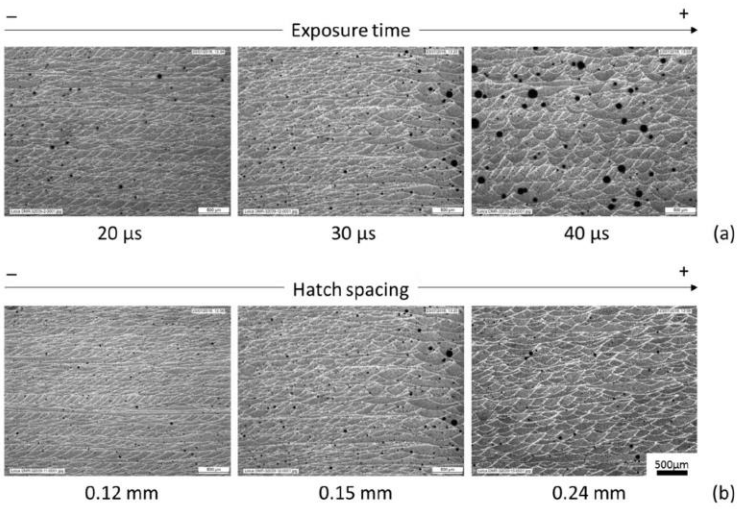

Fig. 14. Melt pools and XZ porosity development of B1 samples at increasing (a) exposure time and (b) hatch spacing.

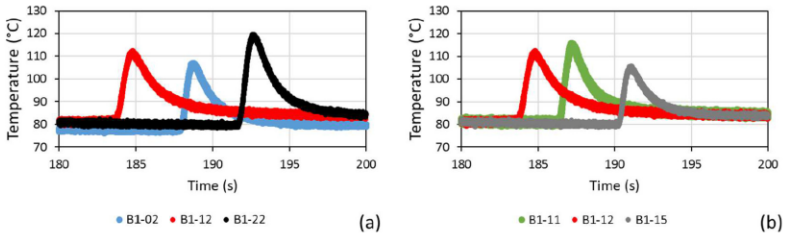

Fig. 15. Temperature evolution of reference samples of (a) varying exposure time and (b) varying hatch spacing. (a) Exposure values of B1-02, B1-12 and B1-22 samples are 20, 30 and 40 μs respectively. (b) Hatch spacing of B1-11, B1-12 and B1-15 are 0.12, 0.15 and 0.24 mm respectively.

Longer exposures were observed to promote overall porosity and larger individual pores. Longer exposures are associated with slower scan speeds and therefore higher energy levels. Excessive local energy deposition may have promoted dynamic instabilities within the melt pool, promoting inclusion of gas and formation of larger pores.

Melt pool overlapping can be determined based on XZ cross-sections at the top of the sample. Based on pixel count (using the melt-pool-size measurement approach shown in Fig. 13), the melt pool width (using the measured half width) and depth of samples of varying exposure time are 253 ± 30 μm and 232 ± 15 μm; 332 ± 25 μm and 308 ± 15 μm; and 358 ± 30 μm and 472 ± 15 μm for exposures 20, 30 and 40 μs respectively. Width-to-depth ratio was observed to decrease with increasing exposure time. Critical width-to-depth ratio 0.8 was identified. Below the critical value keyhole porosity developed, limiting the densification mechanism. Such instabilities were more critical in B2 samples with exposures >40 μs. In samples of varying hatch spacing, melt pool width and depth were 332 ± 25 μm and 308 ± 15 μm respectively. Hatch spacing did not influence melt pool dimensions. It was observed that porosity increased proportionally with hatch spacing. Densities ≥99% were attained in samples with ≥30% melt-pool width overlap between neighbouring scan tracks. Lower overlapping coefficients promoted porosity formation especially in regions along the melt-pool width.

4.3. Thermal monitoring and FE simulation

Sensitivity studies were conducted in order to calibrate and validate the L-PBF FE model. Calibration involved performing parameter matching exercises that result in the model predictions agreeing with physical measurements. Simulation iterations were conducted to calibrate the jump speed v_j of scanning mirrors. Validation involved using the calibrated model to (blindly) predict physical measurements. To calibrate and validate the model, experimental thermal monitoring of reference samples (see Fig. 3) was conducted using the thermocouple substrate described in Section 3.4. The samples were instrumented and in situ temperature measurements were recorded for a range of different process parameter combinations. Fig. 15 shows thermal evolution at the measuring point, 200 μm below the top surface of the substrate. Fig. 15a shows thermal evolution of reference samples with varying exposure time and Fig. 15b shows thermal evolution of reference samples with varying hatch spacing. It was observed that peak temperatures at the measuring point increased with increasing exposure time (exposure values of B1-02, B1-12 and B1-22 samples are 20, 30 and 40 μs respectively) and decreasing hatch spacing (hatch spacing of B1-11, B1-12 and B1-15 are 0.12, 0.15 and 0.24 mm respectively). Longer exposures and smaller hatch spacing induced higher peak temperatures.

Temperature histories experimentally acquired (recorded at 500 Hz sampling frequency) were compared with model that simulated the production of the same samples with a "digital" thermocouple placed at the same location as in the real experiment (i.e. measuring point 200 μm below the top surface of the substrate). The first simulations were used to calibrate the heat source efficiency. Once the heat source efficiency was calibrated, the model predictions were compared against additional physical measurements. Jump speed $v_j = 500\ mms^{-1}$ resulted in good agreement between model prediction and experimental measurements. Fig. 16 shows simulated thermal evolution against experimental measurements of a) multiple layers and b) single layer. The black curve (digital thermocouple in the simulation) and the red curve (physical measurement) showed strong agreement. The peak temperatures and cooling rates were predicted within 15% error accuracy.

5. Discussion

5.1. Effect of process parameters in sample density

Density and standard deviations of B1 and B2 samples have been presented in Section 4.1. It has been shown that standard deviations are directly correlated with the size of individual pores. Spherical pore morphology in all samples suggested the predominance of gas and keyhole porosity as the only defects limiting the densification mechanism.

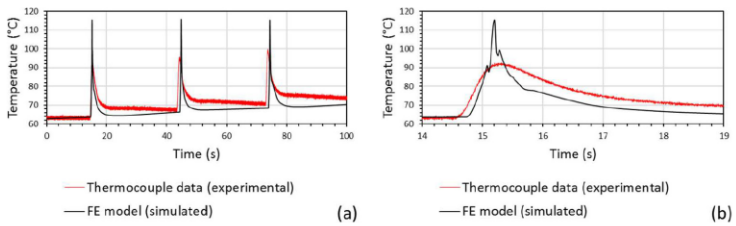

Fig. 16. Simulated and experimental thermal evolution at the measuring point located 200 μm below the top surface of the substrate; a) multiple layers; b) single layer.

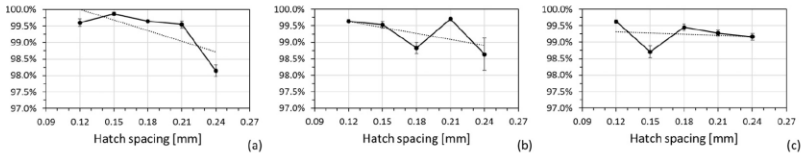

Fig. 17. XZ density of B1 samples with (a) 20 μs, (b) 30 μs and (c) 40 μs exposure time and varying hatch spacing.

In the present section, the effect of hatch spacing, exposure time and layer thickness in % density is presented. Fig. 17a–c show XZ B1 densities with varying hatch spacing for (a) 20, (b) 30 and (c) 40 μs exposures. A decreasing density trend was observed with increasing hatch spacing. This is more evident at shorter exposure 20 μs compared to 30 and 40 μs (see steeper trend in Fig. 17a in comparison with trends in Fig. 15b and c).

Longer exposures led to larger melt-pool widths which promoted re-melting of regions along edges of the melt-pool width, reducing pore formation. Shorter exposures produced thinner melt widths which were incapable of disrupting porosity in-between tracks. Fig. 18a–c show XZ density trends with L_{ED} for (a) 0.15 mm, (b) 0.21 mm and (c) 0.24 mm hatch spacing. L_{ED} is directly correlated with exposure time, i.e. the longer the exposure the higher the energy. Again, a decreasing density trend was observed with increasing L_{ED} when using lower hatch spacing 0.15 and 0.21 mm in Fig. 18a and b respectively. Deeper melt pools formed at higher energy levels which may have induced melt instabilities promoting keyhole porosity. In contrast, hatch spacing 0.24 mm showed an increasing % density trend with increasing L_{ED} (see Fig. 18c). This can be explained in terms of the melt-width to hatch-spacing ratio. Thinner melt pools, typical of lower L_{ED} levels, were not capable of re-melting regions along the edges of the melt when processing larger hatch spacing. Wider melt pools are required to reduce porosity in-between tracks when processing larger hatching. Fig. 19 shows density of samples with varying hatch spacing for (a) 50 μm and (b) 100 μm layer thickness. Similar exposure times are compared in Fig. 19a–b, namely (a) 40 and (b) 50 μs respectively. It was observed that larger layer thickness limited the densification mechanism, possibly due to the development of deeper melts promoting keyhole porosity. Longer exposures used in B2 with 100 μm layer thickness may have increased instabilities within the melt promoting gas entrapment and larger pores as shown in Fig. 14a with increasing exposure time. It has to be noted that longer exposures were used in B2 in order to process similar V_{ED} levels at both 50 μm and 100 μm layer thickness scenarios.

5.2. Power factor model and specific point energy – transferring parameters between different laser systems

In Section 4.1, it was observed that characterising % density using L_{ED} as design parameter resulted in well-defined regions of high-density samples. Using V_{ED} and A_{ED} resulted in high and low % density merged within same energy levels. It can be concluded that porosity formation within melt pools is governed by the amount of energy per unit length applied to the process. Characterising the densification mechanism using V_{ED} or A_{ED} can be a misleading approach for selecting optimal parameters especially when varying exposure time (i.e. scan speed), hatch spacing or layer thickness as demonstrated in the present investigation. In laser welding, the power factor model is used to characterise porosity formation in terms of the process specific-point-energy, taking into account laser diameter. In L-PBF, the specific point energy is the product of L_{ED} and laser diameter d: $E_{SP} = L_{ED} \times d$. Therefore, E_{SP} can be used to characterise the densification mechanism in L-PBF, taking into account laser diameter. In the present section, the scan speed used to characterise optimal E_{SP} was calculated using Eq. (5), with jump speed $v_j = 500$ mms^{-1} obtained from simulations. Fig. 20a shows XZ % density trends of B1 and B2 samples (50 μm and 100 μm layer thickness respectively) with varying E_{SP}. The $R^2 = 0.8$ trend crossing 99% density threshold at ~ 0.173 J shows that $E_{SP} > 0.173$ J can result in density < 99% when processing layers >50 μm. Therefore, $E_{SP} < 0.173$ J is suggested for layers >50 μm. In the present work, $P_F = 12.9$ $Wμm^{-1}$ remained constant for B1 and B2 samples. It was observed that E_{SP} controlled melt depth as depicted in Fig. 20b. Melt depth increased with increasing E_{SP} whilst % density increased with decreasing E_{SP}. Critical $E_{SP} = 0.18$ J was observed above which density dropped <99% in B1 (50 μm layer thickness) samples (see crossing point highlighted in Fig. 20b). As shown in Fig. 20b,

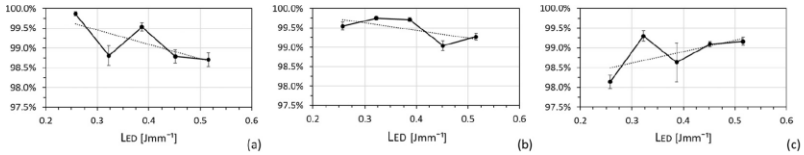

Fig. 18. XZ density of B1 samples with (a) 0.15 mm, (b) 0.21 mm and (c) 0.24 mm hatch spacing and varying exposure time.

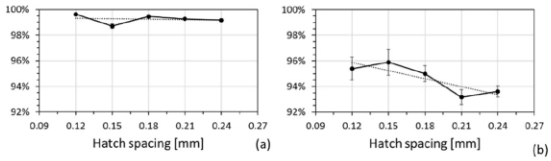

Fig. 19. XZ density of (a) B1 and (b) B2 samples with (a) 50 μm and (b) 100 μm layer thickness, (a) 40 μs and (b) 50 μs exposure time and varying hatch spacing.

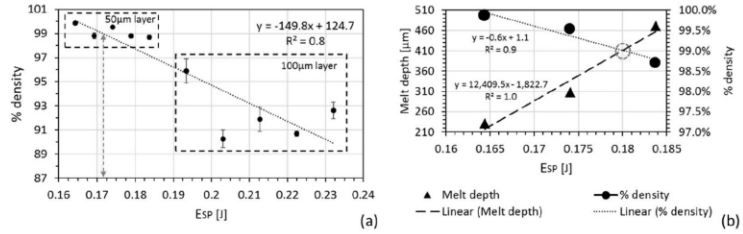

Fig. 20. (a) XZ density trend with varying specific point energy in B1 (50 µm layer) and B2 (100 µm layer) samples. (b) Melt depth and % XZ density of B1 samples with varying E_{SP}, highlighting critical energy and melt depth limit point for >99% density.

melt depth > 410 µm resulted in <99% density due to keyhole porosity development within deeper melts. It can be concluded that melt depths <410 µm, width-to-depth ratio ≥ 0.8 (using the measured half width) and melt width overlap ≥30% (see Section 4.2) are required for achieving near full density AlSi10Mg parts whilst processing within optimal energy levels.

E_{SP} values that resulted in highest % density were compared to optimal parameters reported in literature for manufacturing near full-density AlSi10Mg components. A specific point energy range of 0.017–0.18 J was identified with varying laser focus diameter and processing parameters. It is reported in literature that (a) P_F controls laser penetration depth independent of laser beam diameter, and (b) melt depth can be used as a design parameter to select optimal process conditions in L-PBF of AlSi10Mg. In the present work, E_{SP} was observed to control melt depth at fixed P_F. The use of E_{SP} and P_F as design parameters controlling melt depth, can thus provide processing windows for manufacturing near full-density L-PBF components. In order to investigate the role of P_F in the densification mechanism of AlSi10Mg parts in the present section, multiple samples were manufactured with power ranging from 400 to 800 W, constant 75 µm laser focus diameter and E_{SP} < 0.18 J. The samples manufactured with densities >99% are shown in Fig. 21. A clear trend of optimal parameters in the E_{SP} - P_F curve was identified. This is shown in Fig. 21 along with optimal parameters reported in literature for the same material. The data plotted in Fig. 21 (extracted from [2,9-11,17-19,23,26-33]) corresponds to different processing conditions with laser focus diameter and power ranging from 75 µm to 300 µm and 175 W to 967 W respectively; as well as substrate temperatures and layer thickness ranging from <100 °C to >200 °C and 25 µm to 50 µm respectively. The broad range of process parameters would complicate identification of optimal processing windows especially if V_{ED} was used as design parameter. The use of jump speed in calculations resulted in pulsed-mode energy levels comparable to values reported in literature for continuous-mode laser systems (see $R^2 = 0.9$ in $E_{SP} - P_F$ trend). Fig. 22 shows comparison of trends corresponding to different pulsed-mode scan speed scenarios, i.e. with and without jump speed in energy calculations. Trend behaviour comparable to continuous-mode data reported in literature is observed when using jump speed in calculations as well as higher R^2 in trend. The $E_{SP} - P_F$ curve proposed in the present investigation provides a clear trend of optimal process energy conditions taking into account substrate temperature recommendations (according to literature and complemented with the present research) depending on E_{SP} and P_F values. For instance, substrate pre-heating temperature ≥ 200 °C is recommended when processing at $P_F \leq 2$ W/µm^{-1} and $E_{SP} = 0.1$ J, or $E_{SP} < 0.04$ J and $P_F \leq 4$. On the other hand, $P_F \geq 8$ W/µm^{-1} or $E_{SP} \geq 0.16$ J may require <100 °C substrate pre-heating. Laser absorptivity and thermal conductivity are temperature dependant material properties that can vary with different substrate preheating temperatures. Such properties will ultimately affect melt pool depths. Therefore, optimal combination of E_{SP}, P_F and substrate preheating temperature has to be used to control melt depth and improve part density. Higher energy and power promote disruption of oxides and improves the energy balance (k/A) in HP L-PBF. As E_{SP} and P_F control melt depth, deeper melts promoted by higher energy and power levels may cause over-melting and formation of keyhole welding-mode if higher substrate temperatures are used. For higher E_{SP} and P_F, alterative powder drying mechanism are proposed as reported in literature, namely: a) external, using a furnace at constant temperatures during a specific period of time; and/or b) internal, using laser pre-sintering strategies to dry the powder locally at each layer. The $E_{SP} - P_F$ curve in Fig. 21 provides optimal energy required

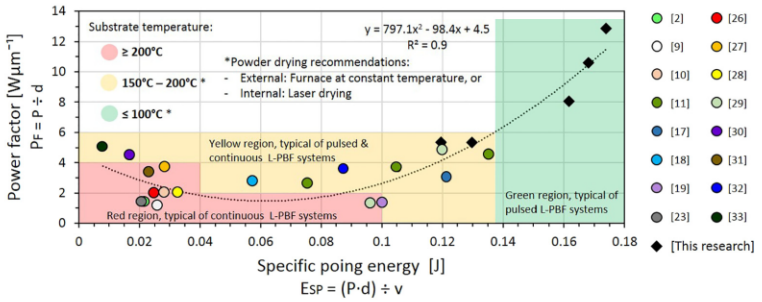

Fig. 21. $E_{SP} - P_F$ curve of L-PBF parameters for manufacturing near full density AlSi10Mg components showing recommended regions of substrate preheating temperature ranges and powder drying techniques for higher E_{SP} and P_F to avoid over-melting. Data points represent optimal parameters that resulted in highest densities as reported in literature, along with those obtained in the present investigation. Different laser focus diameters and laser powers are considered, ranging from 75 µm – 300 µm and 175 W – 967 W respectively. The data plotted corresponds to layer thickness ranging from 25 µm – 50 µm as reported in literature and in the present research. The curve might not be applicable to thicker layers.

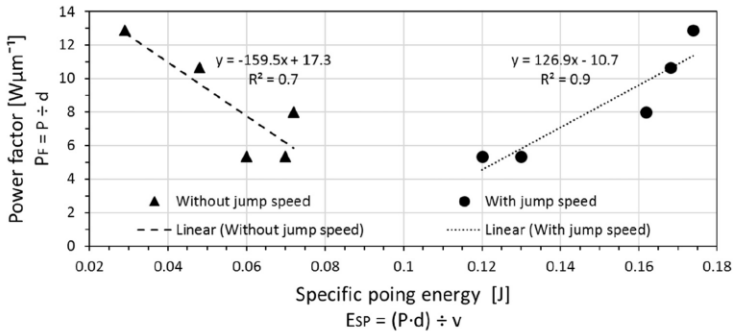

Fig. 22. E_{SP} – P_F curve of L-PBF parameters for manufacturing >99% AlSi10Mg components showing trends of pulsed-mode scan speeds with and without jump speed v_j for energy calculations.

for a given power level and laser focus diameter to manufacture near full-density AlSi10Mg components. With this information, single track experiments can be conducted at optimal energy conditions in order to obtain melt pool dimensions. The quantitative indicators for process optimisation reported in the present research, namely: 1) melt-width overlapping, 2) melt-depth limit and 3) width-to-depth ratio; can be used to choose layer thickness and hatch spacing for a) productivity (i.e. build rate) and/or b) surface roughness optimisation.

6. Conclusion

The densification mechanism in L-PBF of AlSi10Mg has been investigated in the present work. The role of processing parameters in part density and melt pool dimensions has been characterised. Optimal process conditions have been quantitatively defined and a new method for selecting process parameters based on empirical model used to characterise laser welding process has been proposed. The following can be concluded:

- Volumetric (Jmm^{-3}) and areal (Jmm^{-2}) energy density ranges typically used to characterise processing windows in L-PBF can be ambiguous approaches to define optimal processing windows, especially when using laser systems with different power, laser spot diameter and irradiation mode (i.e. pulsed or continuous). Varying layer thickness (characteristic parameter of V_{ED}) can increase process instabilities, especially with thicker layers, that might require varying laser spot size, and adapting power levels accordingly (i.e. changing power factor). Such process optimisation can be a more a complex approach than just varying V_{ED} levels within same power factor (i.e. laser power to beam size ratio). Even though A_{ED} can be used to simplify the volumetric analysis, different power factors can result in different melt pool sizes even with same A_{ED} levels (i.e. same A_{ED} values can have different laser spot sizes in different machines which results in different power intensities). V_{ED} and A_{ED} can be used as design parameters if the same machine is used. However, a more holistic approach, taking into account different laser systems, can be defining E_{SP} – P_F curves (using L_{ED} and laser diameter) and quantitative melt pool size indicators to use as design parameters for process optimisation of a given material.
- Porosity formation was observed to be controlled by the amount of energy per unit length (Jmm^{-1}) rather than by the volumetric (Jmm^{-3}) or areal (Jmm^{-2}) energy expressions. Density characterisation of samples using L_{ED} as design parameter resulted in well-defined regions of high and low-density components.
- The use of specific point energy E_{SP} as design parameter has incorporated the use of laser diameter into the L_{ED} approach, which can be applicable to different L-PBF systems featuring different laser diameters.
- Jump speed v_j (i.e. speed of scanning mirrors controlling the point-to-point movement) in pulsed lasers is a very important factor that has to be taken into account in E_{SP} calculations especially when transferring parameters from pulsed to continuous L-PBF systems. If v_j is not considered, optimal parameters developed in a pulsed L-PBF system can be misinterpreted and only applicable to specific L-PBF systems.
- In the present work, $v_j = 500\ mms^{-1}$ was obtained from experimental thermal measurements and simulation iterations. This resulted in well-defined range of parameters comparable to optimal conditions reported in literature using pulsed and continuous laser systems. It is suggested that v_j is taken into account in scan speed calculations for higher accuracy.
- E_{SP} was observed to control melt pool dimensions. Higher E_{SP} levels resulted in deeper melts. Critical width-to-depth ratio 0.8 was identified, using the measured half width. Width-to-depth values <0.8 promoted development of keyhole porosity.
- Melt pool dimensions were characterised against E_{SP} levels. An inverse correlation between melt pool depth and part density was observed and a critical melt depth value of 410 μm was identified. Densities ≥99% corresponded to <410 μm melt depths.
- Hatch spacing values that resulted in ≥30% overlap between neighbouring melt tracks were observed to promote densities ≥99%. Lower overlapping resulted in increased porosity in regions along the edges of the melt pool width.
- The E_{SP} - P_F curve has been presented in order to identify optimal E_{SP} values for different power ratings and laser focus diameters. Regions of substrate preheating temperatures were recommended based on E_{SP} and P_F values. Higher power and energy levels may cause overmelting if higher substrate temperatures are used.
- The use of E_{SP} - P_F curves as design parameter for process optimisation in L-PBF of AlSi10Mg has been proposed in the present work. This provided processing windows that can be applicable to L-PBF machines featuring different powers, laser focus diameters and laser irradiation mode (i.e. pulsed or continuous) as well as varying layer thickness.

Data statement

The raw/processed data required to reproduce these findings cannot be shared at this time as the data also forms part of an ongoing study.

CRediT authorship contribution statement

Miguel Zavala-Arredondo: Formal analysis, Methodology, Investigation, Resources. **Tyler London:** Methodology, Resources, Data curation, Conceptualization. **Madie Allen:** Software, Validation. **Tomaso Maccio:** Investigation. **Sam Ward:** Investigation. **David Griffiths:**

Formal analysis, Resources. **Amanda Allison:** Writing - review & editing. **Paul Goodwin:** Writing - review & editing. **Carl Hauser:** Supervision.

Acknowledgments

This work was funded by TWI's Core Research Programme (funded by TWI Industrial Members) and by EU's framework programme Horizon 2020 for research and innovation under H2020-EU.3.4.5.4, grant agreement ID 785562. The authors would like to thank Paul Hilton for his technical advisory regarding laser energy deposition mechanisms.

References

[1] Miguel Seabra, José Azevedo, Aurélio Araújo, Luís Reis, Elodie Pinto, Nuno Alves, Rui Santos, João Pedro Mortágua, selective laser melting (SLM) and topology optimization for lighter aerospace componentes, Procedia Structural Integrity, 1, 2016, pp. 289–296 , ISSN 2452-3216 https://doi.org/10.1016/j.prostr.2016.02.039.

[2] K. Kempen, L. Thijs, J. Van Humbeeck, J.-P. Kruth, Mechanical properties of AlSi10Mg produced by selective laser melting, Phys. Procedia 39 (2012) 439–446 , ISSN 1875-3892 https://doi.org/10.1016/j.phpro.2012.10.059.

[3] E.O. Olakanmi, Selective laser sintering/melting (SLS/SLM) of pure Al, Al–Mg, and Al–Si powders: effect of processing conditions and powder properties, J. Mater. Process. Technol. 213 (8) (2013) 1387–1405 , ISSN 0924-0136 https://doi.org/10.1016/j.jmatprotec.2013.03.009.

[4] I. Yadroitsev, A. Gusarov, I. Yadroitsava, I. Smurov, Single track formation in selective laser melting of metal powders, J. Mater. Process. Technol. 210 (12) (2010) 1624–1631 , ISSN 0924-0136 https://doi.org/10.1016/j.jmatprotec.2010.05.010.

[5] R.M. Mahamood, Laser basics and laser material interactions, Laser Metal Deposition Process of Metals, Alloys, and Composite Materials. Engineering Materials and Processes, Springer, Cham, 2018.

[6] J. Coroado, S. Meco, S. Williams, et al., Int. J. Adv. Manuf. Technol. 93 (2017) 3165, https://doi.org/10.1007/s00170-017-0702-6.

[7] Johannes Trapp, Alexander M. Rubenchik, Gabe Guss, Manyalibo J. Matthews, In situ absorptivity measurements of metallic powders during laser powder-bed fusion additive manufacturing, Appl. Mater. Today 9 (2017) 341–349 , ISSN 2352-9407 https://doi.org/10.1016/j.apmt.2017.08.006.

[8] M. Zavala-Arredondo, K.M. Groom, K. Mumtaz, Int. J. Adv. Manuf. Technol. 94 (2018) 2563, https://doi.org/10.1007/s00170-017-1040-4.

[9] Noriko Read, Wei Wang, Khamis Essa, Moataz M. Attallah, Selective laser melting of AlSi10Mg alloy: process optimisation and mechanical properties development, Mater. Des. 65 (2015) 417–424 , ISSN 0261-3069 https://doi.org/10.1016/j.matdes.2014.09.044.

[10] Manickavasagam Krishnan, Eleonora Atzeni, Riccardo Canali, Flaviana Calignano, Diego Manfredi, Elisa Paola Ambrosio, Luca Iuliano, On the effect of process parameters on properties of AlSi10Mg parts produced by DMLS, Rapid Prototyp. J. 20 (6) (2014) 449–458, https://doi.org/10.1108/RPJ-03-2013-0028.

[11] D. Buchbinder, H. Schleifenbaum, S. Heidrich, W. Meiners, J. Bültmann, High power selective laser melting (HP SLM) of aluminum parts, Phys. Procedia 12 (Part A) (2011) 271–278 , ISSN 1875-3892 https://doi.org/10.1016/j.phpro.2011.03.035.

[12] Nesma T. Aboulkhair, Nicola M. Everitt, Ian Ashcroft, Chris Tuck, Reducing porosity in AlSi10Mg parts processed by selective laser melting, Addit. Manuf. 1–4 (2014) 77–86 , ISSN 2214-8604 https://doi.org/10.1016/j.addma.2014.08.001.

[13] K. Kempen, L. Thijs, J. Van Humbeeck, J.-P. Kruth, Processing AlSi10Mg by selective laser melting: parameter optimisation and material characterisation, Mater. Sci. Technol. 31 (8) (2015) 917–923, https://doi.org/10.1179/1743284714Y.0000000702.

[14] J.J.S. Dilip, S. Zhang, C. Teng, et al., Prog. Addit. Manuf. 2 (2017) 157, https://doi.org/10.1007/s40964-017-0030-2.

[15] P. Ming Tang, Chris Pistorius, Oxides, porosity and fatigue performance of AlSi10Mg parts produced by selective laser melting, Int. J. Fatigue 94 (Part 2) (2017) 192–201 , ISSN 0142-1123 https://doi.org/10.1016/j.ijfatigue.2016.06.002.

[16] Eleftherios Louvis, Peter Fox, Christopher J. Sutcliffe, Selective laser melting of aluminium components, J. Mater. Process. Technol. 211 (2) (2011) 275–284 , ISSN 0924-0136 https://doi.org/10.1016/j.jmatprotec.2010.09.019.

[17] Christian Weingarten, Damien Buchbinder, Norbert Pirch, Wilhelm Meiners, Konrad Wissenbach, Reinhart Poprawe, Formation and reduction of hydrogen porosity during selective laser melting of AlSi10Mg, J. Mater. Process. Technol. 221 (2015) 112–120 , ISSN 0924-0136 https://doi.org/10.1016/j.jmatprotec.2015.02.013.

[18] Lin-zhi Wang, Sen Wang, Jiao-jiao Wu, Experimental investigation on densification behavior and surface roughness of AlSi10Mg powders produced by selective laser melting, Opt. Laser Technol. 96 (2017) 88–96 , ISSN 0030-3992 https://doi.org/10.1016/j.optlastec.2017.05.006.

[19] Erhard Brandl, Ulrike Heckenberger, Vitus Holzinger, Damien Buchbinder, Additive manufactured AlSi10Mg samples using selective laser melting (SLM): microstructure, high cycle fatigue, and fracture behaviour, Mater. Des. 34 (2012) 159–169 , ISSN 0261-3069 https://doi.org/10.1016/j.matdes.2011.07.067.

[20] Abdullah Yahia Alfaify, James Hughes, Keith Ridgway, Critical evaluation of the pulsed selective laser melting process when fabricating Ti64 parts using a range of particle size distributions, Addit. Manuf. 19 (2018) 197–204 , ISSN 2214-8604 https://doi.org/10.1016/j.addma.2017.12.003.

[21] W.J. Suder, S. Williams, Power factor model for selection of welding parameters in CW laser welding, Opt. Laser Technol. 56 (2014) 223–229 , ISSN 0030-3992 https://doi.org/10.1016/j.optlastec.2013.08.016.

[22] Goncalves Assuncao, Eurico, Investigation of Conduction to Keyhole Mode Transition, PhD Thesis, Cranfield University, **http://dspace.lib.cranfield.ac.uk/handle/1826/7842**

[23] E.W. Hovig, H.D. Holm, K. Sørby, Effect of processing parameters on the relative density of AlSi10Mg processed by laser powder bed fusion, in: K. Wang, Y. Wang, J. Strandhagen, T. Yu (Eds.), Advanced Manufacturing and Automation VIII. IWAMA 2018. Lecture Notes in Electrical Engineering, vol 484, Springer, Singapore, 2019https://doi.org/10.1007/978-981-13-2375-1_34.

[24] S. Tripathy, C. Chin, T. London, U. Ankalkhope, V. Oancea, Process modeling and validation of powder bed metal additive manufacturing, NAFEMS World Congress, 2017 , *(Stockholm, Sweden)*.

[25] Qi Zhang, Jiawen Xie, Zhenyuan Gao, Tyler London, David Griffiths, Victor Oancea, A metallurgical phase transformation framework applied to SLM additive manufacturing processes, Mater. Des. 166 (2019) 107618 , ISSN 0264-1275 https://doi.org/10.1016/j.matdes.2019.107618.

[26] D. Manfredi, R. Bidulsky, Laser powder bed fusion of aluminium alloys, Acta Metall. Slovaca 23 (3) (2017)https://doi.org/10.12776/ams.v23i3.988.

[27] A.H. Maamoun, Y.F. Xue, M.A. Elbestawi, S.C. Veldhuis, Effect of selective laser melting process parameters on the quality of Al alloy parts: powder characterization, density, surface roughness, and dimensional accuracy, Materials 11 (2018) 2343.

[28] G. Marchese, A. Aversa, M. Lorusso, D. Manfredi, F. Calignano, M. Lombardi, S. Biamino, M. Pavese, Development and characterisation of aluminium matrix nanocomposites AlSi10Mg/$MgAl_2O_4$ by laser powder bed fusion, Materials 8 (2018) 175.

[29] D. Buchbinder, W. Meiners, K. Wissenbach, Selective laser melting of aluminium die-cast-alloy – correlatinos between process parameters, solidification conditions, and resulting mechanical properties, J. Laser Appl. 27 (2015), S29205. https://doi.org/10.2351/1.4906389.

[30] A.A. Raus, M.S. Wahab, Z. Shayfull, K. Kamarudin, M. Ibrahim, The influence of selective laser melting parameters on density and mechanical properties of AlSi10Mg, MATEC Web Conf 78 (2016), 01078. https://doi.org/10.1051/matecconf/20167801078.

[31] Edward Stugelmayer, Characterization of Process Induced Defects in Laser Powder Bed Fusion Processed AlSi10Mg Alloy, 2018 157 , Graduate Theses & Non-Theses **https://digitalcommons.mtech.edu/grad_rsch/157**.

[32] Yali Li, Gu Dongdong, Parametric analysis of thermal behavior during selective laser melting additive manufacturing of aluminum alloy powder, Mater. Des. 63 (2014) 856–867 , ISSN 0261-3069 https://doi.org/10.1016/j.matdes.2014.07.006.

[33] Nesma T. Aboulkhair, Ian Maskery, Chris Tuck, Ian Ashcroft, Nicola M. Everitt, On the formation of AlSi10Mg single tracks and layers in selective laser melting: microstructure and nano-mechanical properties, J. Mater. Process. Technol. 230 (2016) 88–98 , ISSN 0924-0136 https://doi.org/10.1016/j.jmatprotec.2015.11.016.

[34] Haider Ali, Hassan Ghadbeigi, Kamran Mumtaz, Effect of scanning strategies on residual stress and mechanical properties of selective laser melted Ti6Al4V, Mater. Sci. Eng. A 712 (2018) 175–187 , ISSN 0921-5093 https://doi.org/10.1016/j.msea.2017.11.103.

[35] Cheng Bo, Subin Shrestha, Kevin Chou, Stress and deformation evaluations of scanning strategy effect in selective laser melting, Addit. Manuf. 12 (Part B) (2016) 240–251 , ISSN 2214-8604 https://doi.org/10.1016/j.addma.2016.05.007.

[36] X. Shi, S. Ma, C. Liu, C. Chen, Q. Wu, X. Chen, J. Lu, Performance of high layer thickness in selective laser melting of Ti6Al4V, Materials 9 (2016) 975.

[37] Mingming Ma, Zemin Wang, Ming Gao, Xiaoyan Zeng, Layer thickness dependence of performance in high-power selective laser melting of 1Cr18Ni9Ti stainless steel, J. Mater. Process. Technol. 215 (2015) 142–150 , ISSN 0924-0136 https://doi.org/10.1016/j.jmatprotec.2014.07.034.

[38] H. Schleifenbaum, A. Diatlov, C. Hinke, et al., Prod. Eng. Res. Devel. 5 (2011) 359, https://doi.org/10.1007/s11740-011-0331-0.

[39] Sasan Dadbakhsh, Liang Hao, Effect of layer thickness in selective laser melting on microstructure of Al/5 wt.%Fe_2O_3 powder consolidated parts, Sci. World J. 2014 (2014), 106129 , 10 pages https://doi.org/10.1155/2014/106129.